2007

SEMI-EMPIRICAL METHOD FOR DESIGNING EXCAVATION SUPPORT SYSTEMS BASED ON DEFORMATION CONTROL

David G. Zapata-Medina
University of Kentucky, david.zapata@uky.edu

ABSTRACT OF THESIS

SEMI-EMPIRICAL METHOD FOR DESIGNING EXCAVATION SUPPORT
SYSTEMS BASED ON DEFORMATION CONTROL

Due to space limitations in urban areas, underground construction has become a common practice worldwide. When using deep excavations, excessive lateral movements are a major concern because they can lead to significant displacements and rotations in adjacent structures. Therefore, accurate predictions of lateral wall deflections and surface settlements are important design criteria in the analysis and design of excavation support systems. This research shows that the current design methods, based on plane strain analyses, are not accurate for designing excavation support systems and that fully three-dimensional (3D) analyses including wall installation effects are needed.

A complete 3D finite element simulation of the wall installation at the Chicago and State Street excavation case history is carried out to show the effects of modeling: (i) the installation sequence of the supporting wall, (ii) the excavation method for the wall, and (iii) existing adjacent infrastructure. This model is the starting point of a series of parametric analyses that show the effects of the system stiffness on the resulting excavation-related ground movements. Furthermore, a deformation-based methodology for the analysis and design of excavation support systems is proposed in order to guide the engineer in the different stages of the design. The methodology is condensed in comprehensive flow charts that allow the designer to size the wall and supports, given the allowable soil distortion of adjacent structures or predict ground movements, given data about the soil and support system.

KEYWORDS: Excavation; Excavation Support Systems; Wall Installation Effects; Ground Movements, 3D Finite Element Simulation.

David G. Zapata-Medina

07/25/2007

SEMI-EMPIRICAL METHOD FOR DESIGNING EXCAVATION SUPPORT
SYSTEMS BASED ON DEFORMATION CONTROL

By

David G. Zapata-Medina

L. Sebastian Bryson, Ph.D., P.E.
Director of Thesis

Kamyar Mahboub, Ph.D.
Director of Graduate Studies

07/25/2007

RULES FOR THE USE OF THESES

Unpublished theses submitted for the Master's degree and deposited in the University of Kentucky Library are as a rule open for inspection, but are to be used only with due regard to the rights of the authors. Bibliographical references may be noted, but quotations or summaries of parts may be published only with the permission of the author, and with the usual scholarly acknowledgments.

Extensive copying or publication of the thesis in whole or in part also requires the consent of the Dean of the Graduate School of the University of Kentucky.

A library that borrows this thesis for use by its patrons is expected to secure the signature of each user.

Named   Date

_____

_____

_____

_____

_____

_____

_____

_____

_____

_____

THESIS

David G. Zapata-Medina

The Graduate School

University of Kentucky

2007

SEMI-EMPIRICAL METHOD FOR DESIGNING EXCAVATION SUPPORT SYSTEMS BASED ON DEFORMATION CONTROL

THESIS

A thesis submitted in partial fulfillment of the
requirements for the degree of Masters of Science
in Civil Engineering in the College of Engineering
at the University of Kentucky

By

David G. Zapata-Medina

Lexington, Kentucky

Director: Dr. L. Sebastian Bryson, Assistant Professor of Civil Engineering

Lexington, Kentucky

2007

MASTER'S THESIS RELEASE

I authorize the University of Kentucky
Libraries to reproduce this thesis in
whole or in part for purposes of research.

Signed: David G. Zapata-Medina

Date: 07/25/2007

To my darling wife: Paula A. Betancur-Montoya
For her patience and understanding throughout this endeavor

To my beloved Parents: J. Guillermo Zapata-Alvarez and Martha L. Medina-Agudelo,
For their unconditional love and support

To my dear sister: Martha E. Zapata-Medina
For her love and support

Their love and encouragement made this a reality.

ACKNOWLEDGMENTS

First, I would like to thank the LORD JESUS for all the blessings I have received during these two years. I thank HIM because HE never moved the mountain, but gave me strength to climb it.

I would like to express my deepest gratitude to my advisor, Professor L. Sebastian Bryson, for his continued support during my studies, for his mentoring, for being a great source of inspiration, and for his guidance and encouragement throughout this endeavor. Working with Professor Bryson has been an intense and memorable learning experience.

Lastly but most importantly, I would like to thank my family. This would have not been possible without their vision, support and sacrifice under very difficult circumstances. Especially, I would like to thank Paula, my wife and closest friend, she has been the best and most complete distraction from science one could possible ask for. That she has chosen to spend her life with me is the single thing which I am most proud.

TABLE OF CONTENTS

List of Tables

List of Figures

ix

CHAPTER 1

1   INTRODUCTION

1.1   Synopsis of the Problem

Underground construction has become a common practice worldwide. This is primarily because space for construction activities in urban areas is typically constrained by the proximity of adjacent infrastructure. Stiff excavation support systems (i.e., secant pile walls, diaphragm walls, tangent pile walls) have been employed successfully in protecting adjacent infrastructure from excavation-related damage. In particular, several case histories are presented in the literature where stiff excavation support systems have been used for construction of subway stations (Finno et al., 2002); cut-and-cover tunnel excavations (Koutsoftas et al., 2000); and deep basement excavations (Ou et al., 2000; and Ng, 1992); among others. However, for most underground construction projects in urban areas, excessive excavation-induced movements are major concerns. This is because these can lead to significant displacements and rotations in adjacent structures, which can cause damage or possible collapse of such structures. Therefore, accurate predictions of lateral wall deflections and surface settlements are important design criteria in the analysis and design of excavation support systems.

Conventionally, excavation support systems are designed based on structural limit equilibrium. Although these approaches will prevent structural failure of the support wall, they may result in excessive wall deformations and ground movements. Their design is often based on anticipated earth pressures calculated from the apparent earth pressure diagrams developed by Peck (1969) or Tschebotarioff (1951). These diagrams are semi-empirical approaches back-calculated from field measurements of strut loads and represent

1

conservative enveloped values. Using this approach, the support system design becomes a function of the maximum anticipated earth pressure and is governed by overall structural stability as opposed to maximum allowable horizontal or vertical deformation.

Current design methods, which relate ground movements to excavation support system stiffness and basal stability, are based on plane strain analyses. Additionally, these were developed using a limited number of wall types and configurations, and do not include considerations for soil types; excavation support types and materials; excavation geometry; wall installation effects; construction techniques; and construction sequencing.

A new deformation-based design methodology is proposed in order to overcome the deficiencies of the current design methods.

1.2   Proposed Concept

Direct and quantitative analyses of the performance of excavation supports systems are not easy tasks. This is not only because of the complexity of the system itself, but also because of the difficulty in modeling the wall installation and excavation processes. Three-dimensional (3D) finite element models are required for a realistic analysis of the interaction between the soil and the excavation support system.

This research proposes a new deformation-based design methodology based on both observation of 30 case histories reported worldwide and fully three-dimensional analyses that realistically model the excavation support system and the excavation activities. This semi-empirical approach allows for the design of excavation support systems based on deformation criteria including the influences of the inherent three-dimensional behavior of the excavation support system and the associated excavation.

2

1.3   Objectives of the Research

The objective of this research is to develop a deformation-based design methodology that will protect adjacent infrastructure from excavation-related ground movements.

The specific objectives of this work included:

- Develop a three-dimensional model of the wall installation at the Chicago and State excavation case history reported by Finno et al. (2002) using the software package PLAXIS 3D FOUNDATION.

- Develop a new deformation-based design methodology, based on three-dimensional finite element analyses, that shows the effects of the excavation support system stiffness on the resulting excavation-related ground movements.

- Develop design flow charts that will guide the engineer through the entire process of deformation-based design. This will allow the designer to size the wall and supports, given the allowable soil distortion or predict the ground movements, given data about the soil and support system.

- Develop a database of case histories that document the field performance of a variety of excavation support system types and site conditions. These data will be used to aid in methodology validation and calibration.

1.4   Relevance of Research

Recent studies (Ou et al., 2000; Lin et al., 2003; Zdravkovic et al., 2005; Finno et al., 2007) have shown that the complicated soil-structure interaction of excavation support systems and the excavation-induced ground movements are three-dimensional in nature. Nevertheless, limited data has been reported in the literature presenting a fully three-dimensional finite element analysis of deep excavations. In addition, no one has presented a

3

design methodology for excavation support systems that relates system stiffness to excavation-related ground movements incorporating the three-dimensional nature of the excavation and the effects of constructing the retaining wall. This research presents the three-dimensional finite element analysis of a benchmark case history and provides a deformation-based design methodology for the analysis and design of excavation support systems. It is expected that the proposed deformation-based methodology will save millions of dollars typically expended in repairs and mitigation of excavation-induced damage to adjacent infrastructure.

1.5   Content of Thesis

Chapter 2 of this document presents technical background concerning analysis and design of excavation support systems. This chapter discusses the available methods in the literature for determining earth pressures and calculating factors of safety against basal heave. It also reviews methods for predicting perpendicular and parallel excavation-related ground movements and discusses several attempts for quantifying wall installations effects on the performance of excavation support systems. Lastly, this chapter provides a review and discussion of the available deformation based design methods and three-dimensional finite element analyses of excavations.

Chapter 3 focuses on wall installation effects. Analyses for quantifying such effects are based on previously presented works and three-dimensional finite element simulations of the Chicago and State excavation case history.

Chapter 4 shows the influences of the system stiffness on the excavation-related ground movements. The deficiencies of the existing methods and charts are shown and a parametric

study based on fully three-dimensional finite element analyses is performed. Finally, a new index is presented which relates deformation and three-dimensional system stiffness.

Chapter 5 presents a semi-empirical method for designing excavation support systems. It allows the designer to predict the ground movements, given data about the support system or size of the wall and supports, given the allowable soil distortion of adjacent infrastructure.

Chapter 6 summarizes this work and presents conclusions and recommendations.

CHAPTER 2

2   TECHNICAL BACKGROUND

2.1   Lateral Earth Pressure

It is well-known that an incorrect implementation in the design earth pressure may lead to uneconomical or even unsafe designs. Traditionally, apparent earth pressure diagrams are used for designing excavation support systems. These diagrams are semi-empirical approaches back-calculated from field measurements of strut loads which do not represent the actual earth pressure or its distribution with depth. Therefore, apparent earth pressure diagrams are only appropriate for sizing the struts. As previously mentioned, the use of these diagrams yield support systems that are adequate with regards to preventing structural failure, but may result in excessive wall deformations and ground movements.

2.1.1   Peck's (1969) Apparent Earth Pressure Diagrams

The most commonly used apparent earth pressure diagrams are those presented by Peck (1969). He presented pressure diagrams for three different categories of soil: sands (Figure 2.1.a); soft to medium clays (Figure 2.1.b), applicable when the stability number ($N_b = \gamma H_e / s_u$) > 6; and stiff clays (Figure 2.1.c), applicable for the condition of $N_b \leq 4$. These pressure diagrams were back-calculated from field measurements of strut loads in braced excavations located at Chicago, Oslo, and Mexico. The clay diagrams assumed undrained conditions and only consider total stresses; and in sand diagrams, drained sands are assumed.
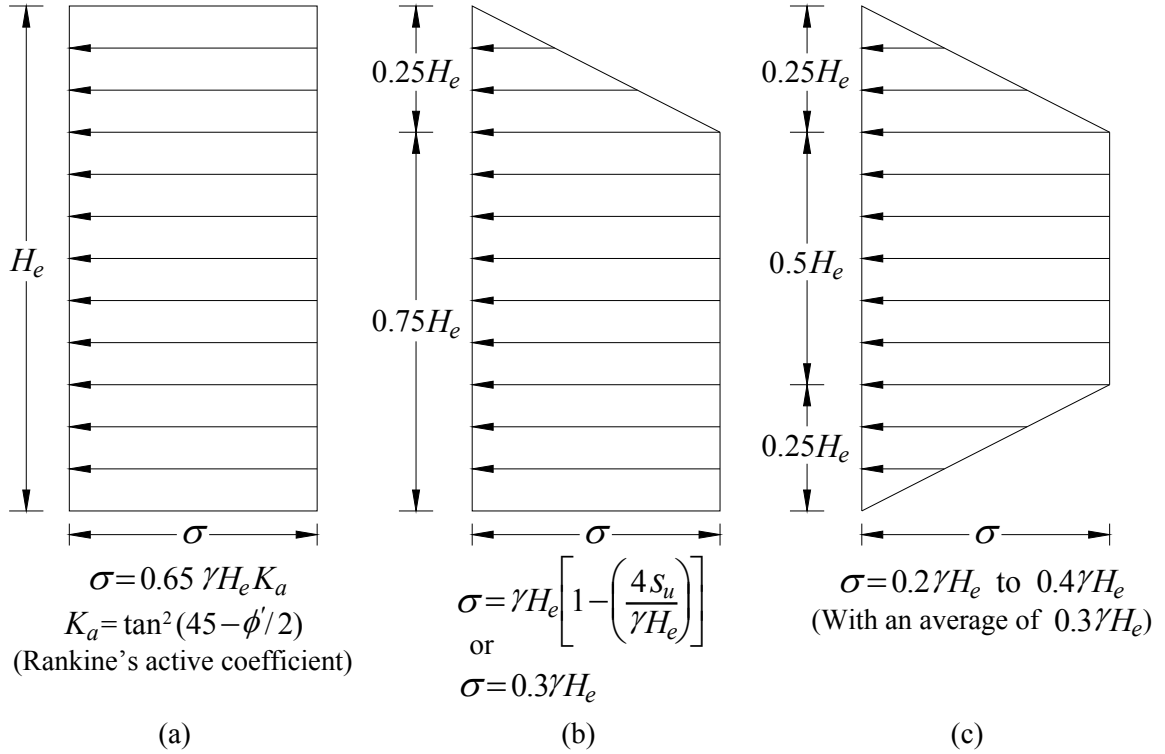
Figure 2.1 - Peck's (1969) Apparent Pressure Envelopes: (a) Cuts in Sand; (b) Cuts in Soft to Medium Clay; and (c) Cuts in Stiff Clay (After Peck, 1969).

It is noted that some researchers (Ou, 2006; Das, 2007) presented the soft to medium clay diagram applicable for the case of $N_b > 4$ and the apparent earth pressure, σ, as the larger of:

$$\sigma = \gamma H_e \left(1 - m \frac{4 s_u}{\gamma H_e} \right) \quad \text{or} \quad \sigma = 0.3 \gamma H_e \qquad (2\text{-}1)$$

where m is an empirical coefficient related to the stability number N_b. For $N_b \leq 4$, $m = 1$; and for $N_b > 4$, $m = 0.4$. However, for reaching the condition of $\sigma = 0.3\gamma H_e$, one would have to assume $N_b = 5.7$, which is nothing more than Terzaghi's (1943a) bearing capacity factor for clays, $N_c = 5.7$, implying a factor of safety against basal heave, $FS_{(heave)}$, equal to 1.0. Consequently, the condition $\sigma = 0.3\gamma H_e$ would never control because the reduction

7

factor m (=0.4 for $N_b > 4$) makes $\sigma = \gamma H_e[1 - m(4s_u / \gamma H_e)]$ the larger of both. Furthermore, when $N_b \leq 4$ the condition for soft to medium clays is not applicable and the stiff clay diagram must be used.

When there is a layered soil profile, which is quite common in deep excavations, one can either determine which layer of soil is the dominant within the depth of the excavation and use those properties for design, or one can apply Peck's (1943) equivalent undrained shear strength, $s_{u,av}$, and unit weight, γ_{av}, parameters for use in the pressure envelopes presented in Figure 2.1.

For two alternating layers of sand and clay as shown in Figure 2.2.a, $s_{u,av}$ and γ_{av} can be calculated as:

$$s_{u,av} = \frac{1}{2H_e}\left[\gamma_s K_s H_s^2 \tan\phi_s + 2(H_e - H_s)n' s_u\right] \tag{2-2}$$

$$\gamma_{av} = \frac{1}{H_e}\left[\gamma_s H_s + (H_e - H_s)\gamma_c\right] \tag{2-3}$$

where

$K_s =$ coefficient of lateral earth pressure

$n' =$ coefficient of progressive failure (ranging from 0.5 to 1.0; average value 0.75)

$H_e =$ height of the excavation

$H_s =$ thickness of sand layer

$H_c =$ thickness of clay layer

$\phi_s =$ angle of friction of sand layer

$s_u =$ undrained shear strength of clay layer

γ_s = unit weight of sand layer

γ_c = unit weight of clay layer

Similarly, for layered clay strata (Figure 2.2.b), $s_{u,av}$ and γ_{av} can be calculated as:

$$s_{u,av} = \frac{1}{H_e}\left(s_{u,1}H_1 + s_{u,2}H_2 + ... + s_{u,i}H_i + ... + s_{u,n}H_n\right) \tag{2-4}$$

$$\gamma_{av} = \frac{1}{H_e}\left(\gamma_1 H_1 + \gamma_2 H_2 + ... + \gamma_i H_i + ... + \gamma_n H_n\right) \tag{2-5}$$

where

H_e = height of the excavation

$s_{u,i}$ = undrained shear strength of ith layer

H_i = thickness of ith layer

γ_i = unit weight of ith layer
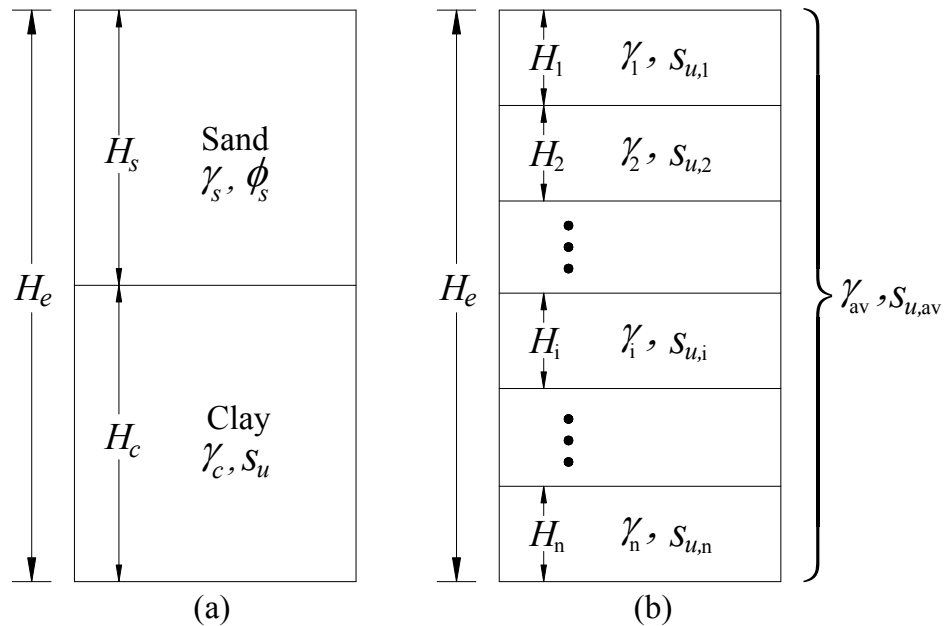
Figure 2.2 - Layered Soil in Excavations: (a) Sand and Clay; and (b) Multilayered Clay (Adapted from Ou, 2006 and Das, 2007).

9

Ou (2006) affirmed that the apparent earth pressure diagrams must only be used to calculate the strut loads and that it is incorrect to use them for calculating the stress or bending moments in the retaining wall. Furthermore, he questioned the application of such apparent earth pressure diagrams to deep excavations (over 20 m) and limited their use to excavations less than 10-m-deep.

2.1.2 Rankine's Earth Pressure

Rankine (1857) presented a solution for lateral earth pressures in retaining walls based on the theory of plastic equilibrium. He assumed that there is no friction between the retaining wall and the soil, the soil is isotropic and homogenous, the friction resistance is uniform along the failure surface, and both the failure surface and the backfilled surface are planar.

When the retaining wall in Figure 2.3.a moves from AB to A'B' the horizontal stresses in back of and in front of the retaining wall will decrease and increase, respectively, while the vertical stresses remain constant. Rankine called the stresses in back of and in front of the retaining wall active earth pressure and passive earth pressure, respectively.

For a soil exhibiting both effective cohesion, c', and effective angle of internal friction, ϕ', the Rankine earth pressures are given by:

Active case:

$$\sigma'_a = \sigma'_v K_a - 2c' \sqrt{K_a} \qquad (2\text{-}6)$$

where: $K_a = tan^2\left(45° - \phi'/2\right)$ (2-7)

Passive case:

$$\sigma'_p = \sigma'_v K_p + 2c' \sqrt{K_p} \qquad (2\text{-}8)$$

where: $K_p = tan^2\left(45° + \phi'/2\right)$ (2-9)

10

The above expressions are adequate for evaluating long-term lateral unloading conditions, which are the most critical conditions in excavations.

For evaluating short-term conditions undrained parameter must be used and soil strength parameters must be developed from CU or UU triaxial tests. In this case, $c' = s_u$ and $\phi' = 0$. Therefore, the active and passive coefficients equal unity ($K_a = K_p = 1$) and the Rankine earth pressures are given by:

Active case:

$$\sigma'_a = \sigma'_v K_a - 2s_u \tag{2-10}$$

Passive case:

$$\sigma'_p = \sigma'_v K_p + 2s_u \tag{2-11}$$

Rankine also defined the active and passive failure zones (Figure 2.3.b) According to the Mohr-Coulomb failure theory. The angle between the active failure surface and the horizontal plane is $(45° + \phi'/2)$ and that between the passive failure surface and the horizontal plane is $(45° - \phi'/2)$.
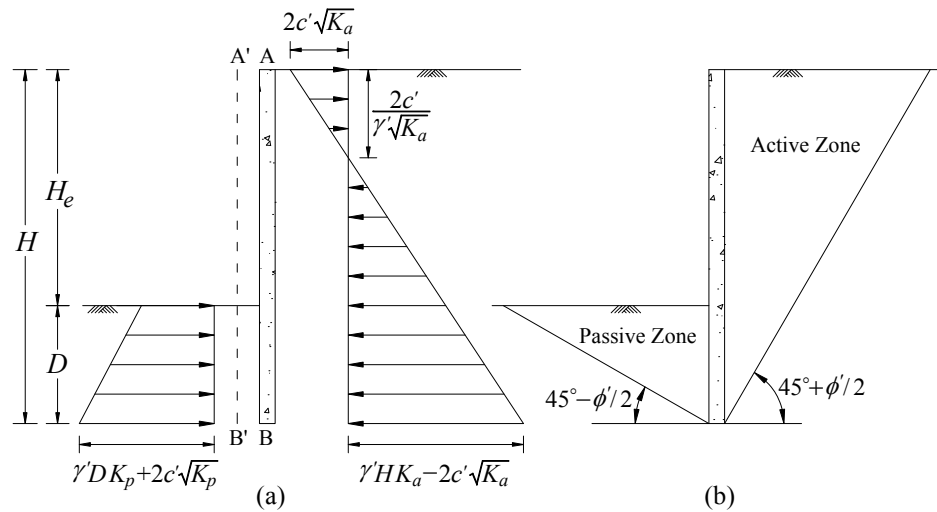
Figure 2.3 - (a) Rankine's Earth Pressure Distributions; and (b) Passive and Active Zones.

Since friction exists between the retaining wall and the soil, the active and passive failure surfaces are both curved rather than planar. The less the friction is between the wall and the soil, the more plane the failure surface. For cast-in-place retaining walls, there is significant friction between the wall and the soil. Consequently, this effect must be included.

2.1.3   Caquot and Kerisel (1948)

Caquot and Kerisel (1948) included the friction factor, δ, between the retaining wall and the soil and assumed an elliptical curved failure surface which is recognized to be very close to the actual failure surface. The active and passive coefficients presented by Caquot and Kerisel (1948) were developed for cohesionless soils. However, they can be used for evaluating long-term conditions in cohesive soils where complete dissipation of pore water pressure occurs.

Figure 2.4 and Figure 2.5 present the Caquot and Kerisel (1948) coefficients for the active and passive conditions, respectively. These coefficients were developed assuming horizontal backfill and vertical wall. Rankine's coefficients, which do not include the friction effect between wall and soil and are applicable for both cohesive and cohesionless soil, are also plotted in Figure 2.4 and Figure 2.5 for comparison.
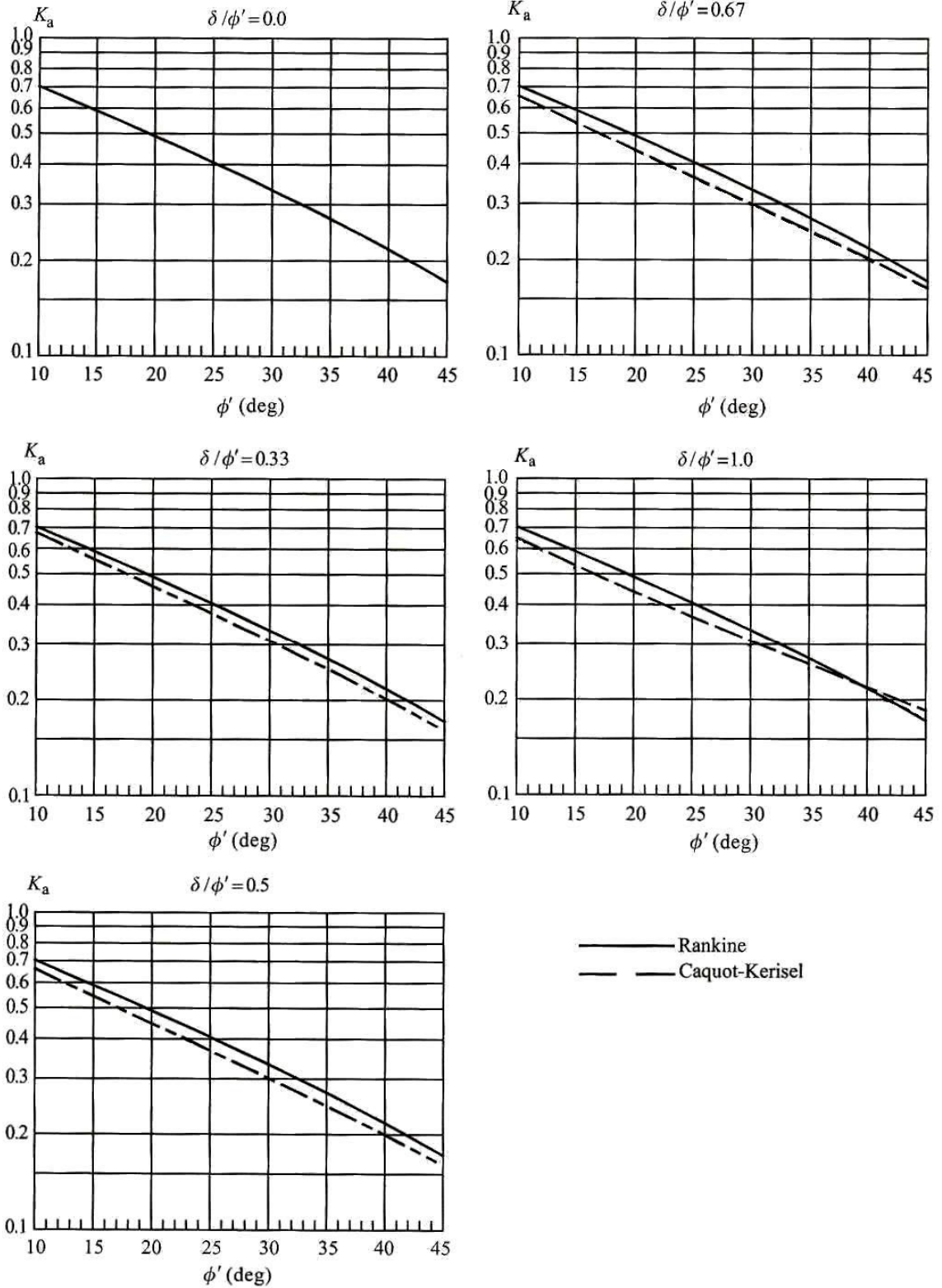
Figure 2.4 - Coefficients of Caquot-Kerisel Active Earth Pressure. Horizontal Component $K_{a.h} = K_a \cos\delta$ (Adapted from Ou, 2006).
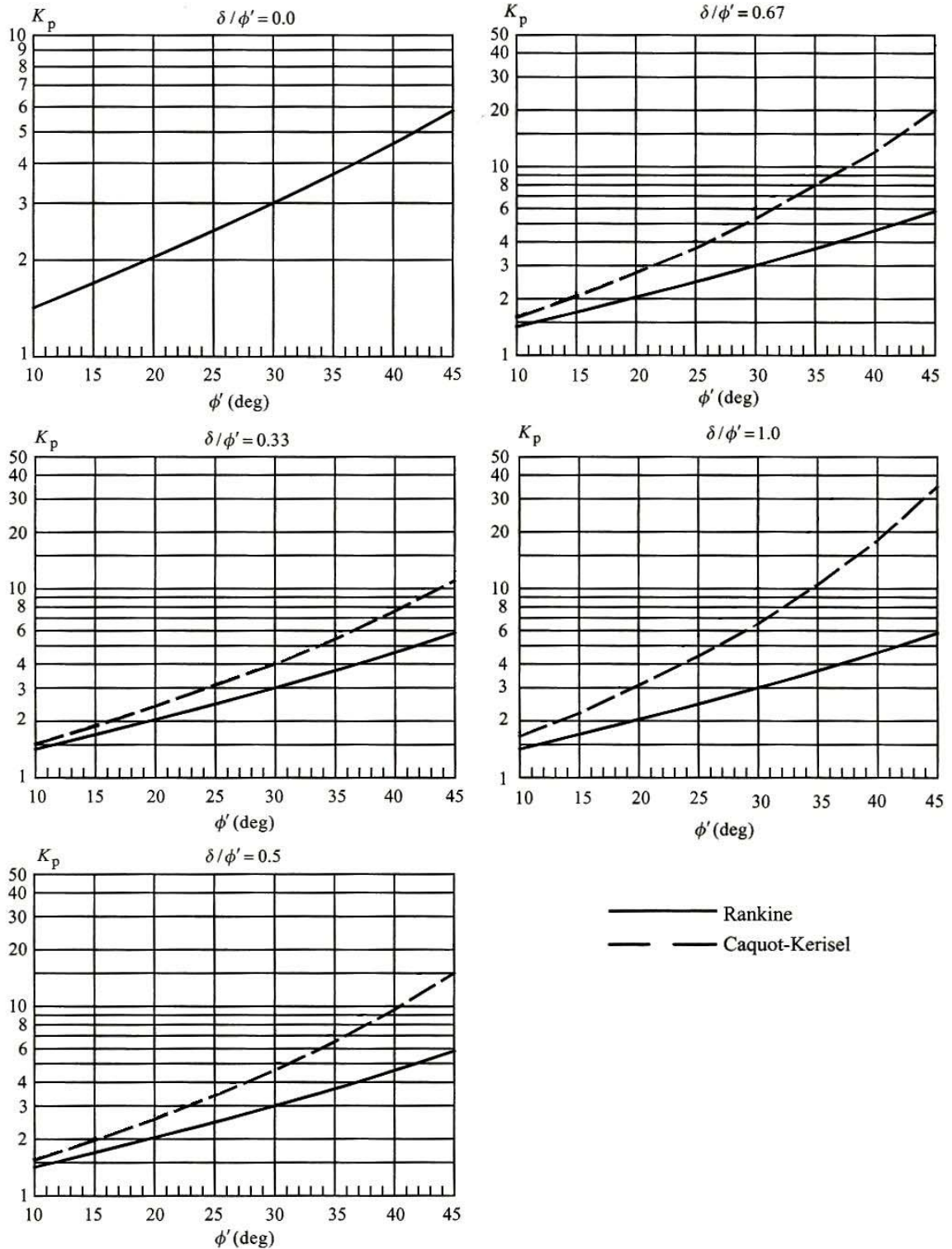
Figure 2.5 - Coefficients of Caquot-Kerisel Passive Earth Pressure. Horizontal Component $K_{p.h} = K_p\cos\delta$ (Adapted from Ou, 2006).

14

2.1.4   Earth Pressure for Design

Ou (2006), following Padfield and Mair's (1984) suggestions, adopted Rankine's earth pressure theory and Caquot-Kerisel's coefficients of earth pressure to calculate earth pressures in excavation support systems for short and long term conditions, respectively.

For short-term conditions, as presented in Section 2.1.2, undrained shear parameter must be used in the calculations of earth pressures. Padfield and Mair (1984) presented Equations (2-12 to 2-15) which take into account the adhesion between the retaining wall and the soil, overcoming the limitations of Rankine's theory.

$$\sigma_a = \sigma_v K_a - 2cK_{ac} \tag{2-12}$$

$$K_{ac} = \sqrt{K_a\left(1 + c_w/c\right)} \tag{2-13}$$

$$\sigma_p = \sigma_v K_p + 2cK_{pc} \tag{2-14}$$

$$K_{pc} = \sqrt{K_p\left(1 + c_w/c\right)} \tag{2-15}$$

where

σ_a = total active earth pressure (horizontal) acting on the retaining wall

σ_p = total passive earth pressure (horizontal) acting on the retaining wall

c = cohesion intercept

ϕ = angle of friction, based on the total stress representation

c_w = adhesion between the retaining wall and soil

K_a = Rankine's coefficient of active earth pressure

K_p = Rankine's coefficient of passive earth pressure

15

Under completely saturated conditions, $\phi = 0$ and $c = s_u$. Then, $K_a = K_p = 1$ and

$K_{ac} = K_{pc} = \sqrt{1 + c_w/s_u}$ where c_w can be found from:

$$c_w = \alpha \cdot s_u \tag{2-16}$$

where α is the adhesion factor (American Petroleum Institute, 1987) defined as:

$$\alpha = 0.5 \left(s_u/\sigma'_v \right)^{-0.50} \qquad \text{for} \qquad s_u/\sigma'_v \leq 1.0 \tag{2-17}$$

$$\alpha = 0.5 \left(s_u/\sigma'_v \right)^{-0.25} \qquad \text{for} \qquad s_u/\sigma'_v > 1.0 \tag{2-18}$$

Note that the factor, α, comes from studies on adhesion between piles and soil. Ou (2006) stated that it may be feasible to apply the studies on pile foundations to deep excavations because of the similar nature of retaining walls and foundation piles.

For long-term conditions in cohesive soils, drained shear parameters must be used for the analysis. The governing assumption is that complete dissipation of pore water pressure will occur. Ou (2006) suggested that the distribution of earth pressure for long-term conditions in cohesive soils can be estimated using the earth pressure theory for cohesionless soil presented by Padfield and Mair (1984):

$$\sigma'_a = K_a \left(\sigma_v - u \right) - 2c' K_{ac} \tag{2-19}$$

$$K_{ac} = \sqrt{K_a \left(1 + c'_w/c' \right)} \tag{2-20}$$

$$\sigma_a = \sigma'_a + u \tag{2-21}$$

$$\sigma'_p = K_p \left(\sigma_v - u \right) - 2c' K_{pc} \tag{2-22}$$

$$K_{pc} = \sqrt{K_p \left(1 + c'_w/c' \right)} \tag{2-23}$$

$$\sigma_p = \sigma'_p + u \tag{2-24}$$

where

16

$\sigma'_a =$ effective active earth pressure acting on the retaining wall

$\sigma'_p =$ effective passive earth pressure acting on the retaining wall

$\sigma_a =$ total active earth pressure

$\sigma_p =$ total passive earth pressure

$K_a =$ Caquot-Kerisel's coefficient of active earth pressure

$K_p =$ Caquot-Kerisel's coefficient of passive earth pressure

$c' =$ effective cohesion intercept

$\phi' =$ effective angle of friction

$c'_w =$ effective adhesion between the retaining wall and soil

$u =$ porewater pressure

To obtain the horizontal component of active and passive earth pressures ($\sigma_{a,h}$ and $\sigma_{p,h}$), K_a and K_p must be substituted for $K_{a.h}$ and $K_{p.h}$ respectively, where $K_{a.h} = K_a \cos \delta$ and $K_{p.h} = K_p \cos \delta$.

It can be seen in Figure 2.6.a that there is a zone behind the wall where the soil will be in tension and most likely tension cracks will form. The depth of the tension cracks is given by:

$$z_c = \frac{2c}{\gamma \sqrt{K_a}} \qquad\qquad (2\text{-}25)$$

A conservative approach in the design of excavation support systems is to assume that tension cracks already exist and most likely will be filled with water and moisture generating a hydrostatic pressure (Ou, 2006) (Figure 2.6.a.). Consequently, the lateral earth pressure for design is redistributed as shown in Figure 2.6.b.

17
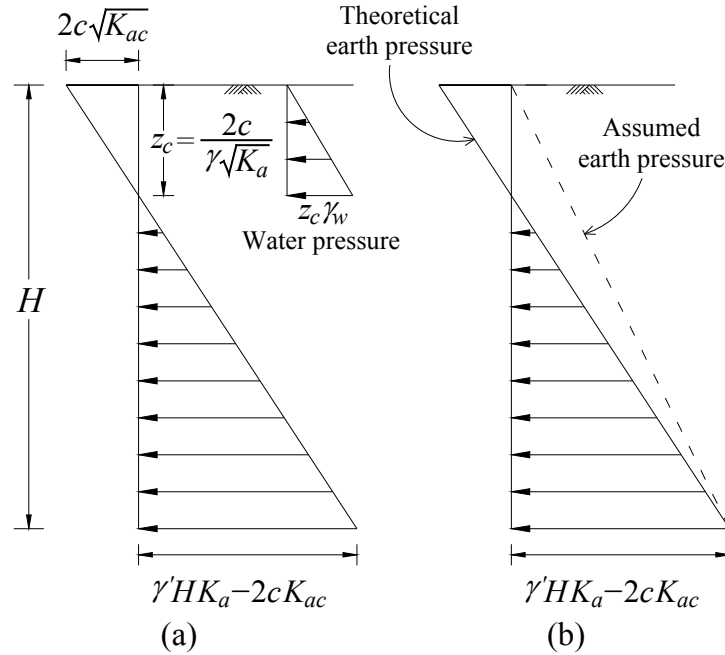
Figure 2.6 - (a) Distribution of Lateral Earth Pressure for Cohesive Soil under Short-Term Conditions; and (b) Assumed Design Earth Pressure (Adapted from Ou, 2006).

2.2   Stability Analysis (Basal Heave)

Stability considerations often play an important role in the design of excavation support systems in clay. If the factor of safety is low, considerable ground movements can be expected (Mana and Clough, 1981; Clough et al., 1989) and expensive modifications may be necessary.

Basal stability analyses can be carried out using limit equilibrium methods or nonlinear finite element methods. The former methods are most typically used in the initial phases of the design because of their simplicity compared to nonlinear finite element methods, which require the determination of many input parameters and a high level of expertise for the simulation processes.

Limit equilibrium methods assume two-dimensional conditions and are based on bearing capacity (Terzaghi, 1943a; Bjerrum and Eide, 1956) or overall slope stability (using circular or noncircular arc failure surfaces). However, bearing capacity methods ignore both the effects

of the depth of wall penetration below the base of excavation and soil anisotropy. The accuracy of overall stability methods is questioned because of the approximations used to solve equilibrium calculations (interslice force assumptions) and the difficulties for analyzing soil-structure interaction for embedded walls and support systems with tiebacks.

2.2.1   Terzaghi Method

Terzaghi (1943a) assumed a failure surface (jihg in Figure 2.7.a) of infinite length ($L = \infty$) for wide excavations. The factor of safety against bottom heave is given by:

$$FS_{(heave)} = \frac{s_u N_c}{\gamma_s H_e + q_s - s_u H_e / B'} = \frac{s_u N_c}{(\gamma_s + q_s / H_e - s_u / B')H_e} \tag{2-26}$$

where B' is limited to $B / \sqrt{2}$ or T, the thickness of the clay below the base of the excavation, whichever is smaller. Note that Equation (2-26) is the factor of safety used by Clough et al. (1989) for relating maximum lateral movement to system stiffness.

Additional modifications have been made to Terzaghi (1943a) for including the effect of the depth of wall penetration below the base of excavation (Figure 2.7.b). Ukritchon et al. (2003) proposed a modified version of the Terzaghi (1943a) factor of safety against basal heave for including the wall embedment factor. The expression is given by:

$$FS_{(heave)} = \frac{s_u N_c + \sqrt{2} s_u (H/B) + 2 s_u (D/B)}{\gamma_s H_e} \tag{2-27}$$

where the terms $s_u N_c$ and $\sqrt{2} s_u (H/B)$ represents the shear capacity and the shear resistance of the soil mass, respectively and $2 s_u (D/B)$ represents the adhesion along the inside faces of the wall assuming a rough surface.

Note that Terzaghi (1943a) uses $N_c = 5.7$, which originally assumed resistance at the interface of the base of the footing and the soil (i.e., perfectly rough foundation). For basal

19

calculations, this implies some restraint at the base of the excavation. However, it is assumed that the base of the excavation is a restraint-free surface. Thus, $N_c = 5.14$ (i.e., perfectly smooth footing) is appropriated.
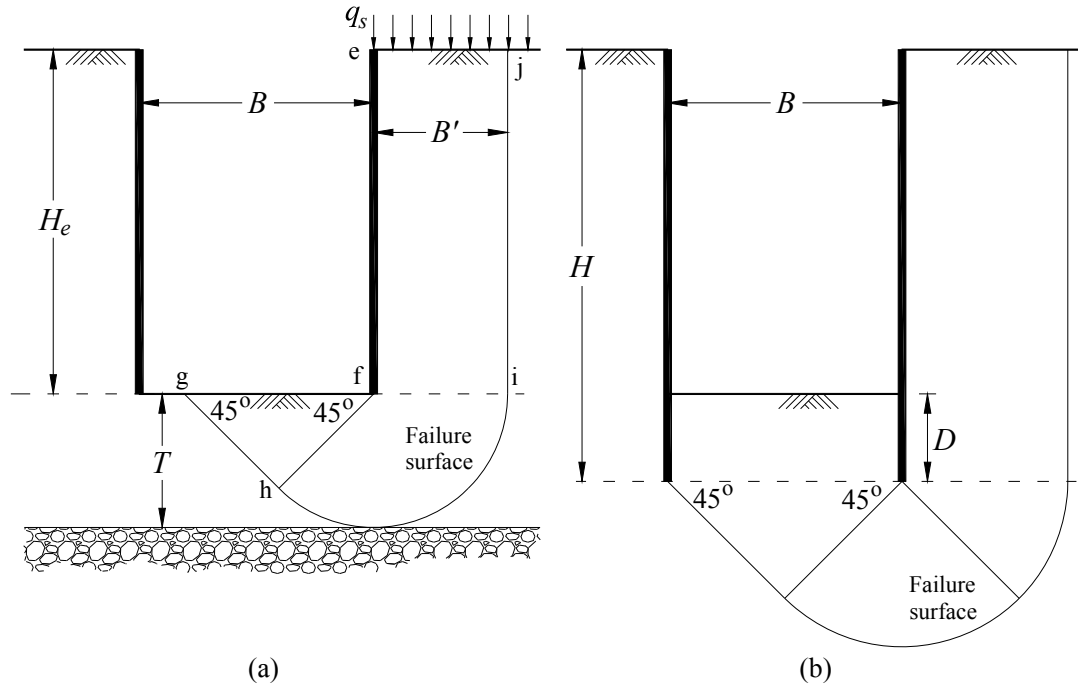
Figure 2.7 - Factor of Safety against Bottom Heave Based on Terzaghi (1943a): (a) without Wall Embedment; and (b) with Wall Embedment (Adapted from Ukritchon et al., 2003).

2.3   General Deflection Behavior of an Excavation Support System

Lateral wall deformations and ground surface settlements represent the performance of excavation support systems. These are closely related to the stiffness of the supporting system, the soil and groundwater conditions, the earth and water pressures, and the construction procedures.

Excavation activities generally include three main stages: (i) installation of retaining wall, (ii) excavation of soil mass and installation of lateral support elements, and may or may not include (iii) removal of the supports and backfill.

Figure 2.8 shows the general deflection behavior of the wall in response to the excavation presented by Clough and O'Rourke (1990). Figure 2.8.a shows that at early phases of the excavation, when the first level of lateral support has yet to be installed, the wall will deform as a cantilever. Settlements during this phase may be represented by a triangular distribution having the maximum value very near to the wall. As the excavation activities advance to deeper elevations, horizontal supports are installed restraining upper wall movements. At this phase, deep inward movements of the wall occur (Figure 2.8.b). The combination of cantilever and deep inward movements results in the cumulative wall and ground surface displacements shown in Figure 2.8.c.

Clough and O'Rourke (1990) stated that if deep inward movements are the predominant form of wall deformation, the settlements tend to be bounded by a trapezoidal displacement profile as in the case with deep excavations in soft to medium clay; and if cantilever movements predominate, as can occur for excavations in sands and stiff to very hard clay, then settlements tend to follow a triangular pattern. Similar findings were presented by Ou et al (1993) and Hsieh and Ou (1998), who based on observed movements of case histories in clay, proposed the spandrel and concave settlement profiles (see 2.5.1).
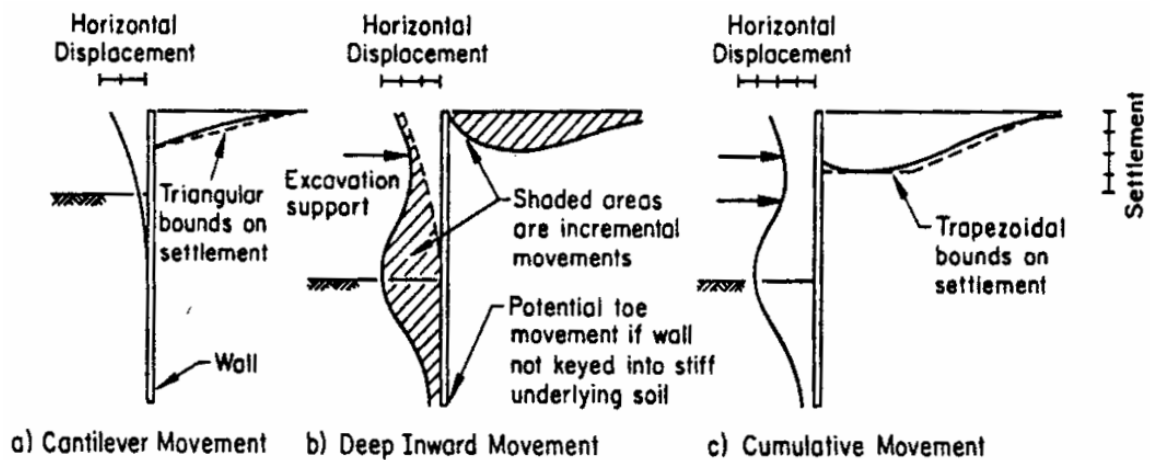
Figure 2.8 - Typical Profiles of Movement for Braced and Tieback Walls (After Clough and O'Rourke, 1990).

It has to be noted that Figure 2.8 only describes the general wall deflection behavior in response to the excavation and neglects important factors such as soil conditions, wall installation methods, and excavation support system stiffness, which have been shown to influence the magnitude and shape of both lateral wall movements and ground settlements.

2.4   Excavation Support System Stiffness

As mentioned in 2.3, lateral wall movements and ground settlements are influenced by several factors including wall installation, soil conditions, factor of safety against basal heave, support system stiffness, and methods of support system installation. The stiffness of an excavation support system is a function of the flexural rigidity of the wall element; the vertical and horizontal spacing of the supports; and the structural stiffness of the support elements and the type of connections between the wall and supports. Walls that are considered stiff on the basis of the rigidity of the wall element include secant and tangent pile walls and diaphragm walls. Walls that are considered flexible on the basis of the rigidity of the wall element include steel sheet pile walls and soldier pile and lagging walls.

Mana and Clough (1981) were the first to introduce the well-known effective system stiffness parameter which is given by:

$$S = \frac{EI}{h^4 \gamma} \tag{2-28}$$

where EI is the wall flexural stiffness per horizontal unit of length (E is the modulus of elasticity of the wall element and I is the moment of inertia per length of wall), h is the average vertical spacing between supports, and γ is the total unit weight of the soil behind the wall. Afterward, Clough et al. (1989) modified Equation (2-28) by replacing the unit weight of soil with the unit weight of water, γ_w.

Clough et al. (1989) presented a design chart for clays which allows the user to estimate lateral movements in terms of effective system stiffness and the factor of safety against basal heave presented by Terzaghi (1943a) [Equation (2-26)]. The system stiffness combines the effects of the wall stiffness (EI) and the average spacing of the struts. Figure 2.9 was created from parametric studies using plane strain finite element analyses of sheet piles and slurry walls and expanded on the work done by Mana and Clough (1981) to stiffer types of walls. Figure 2.9 illustrates the influence of basal stability on movements and can be used to estimate maximum lateral wall movements in circumstances where displacements are primarily due to the excavation and support process.
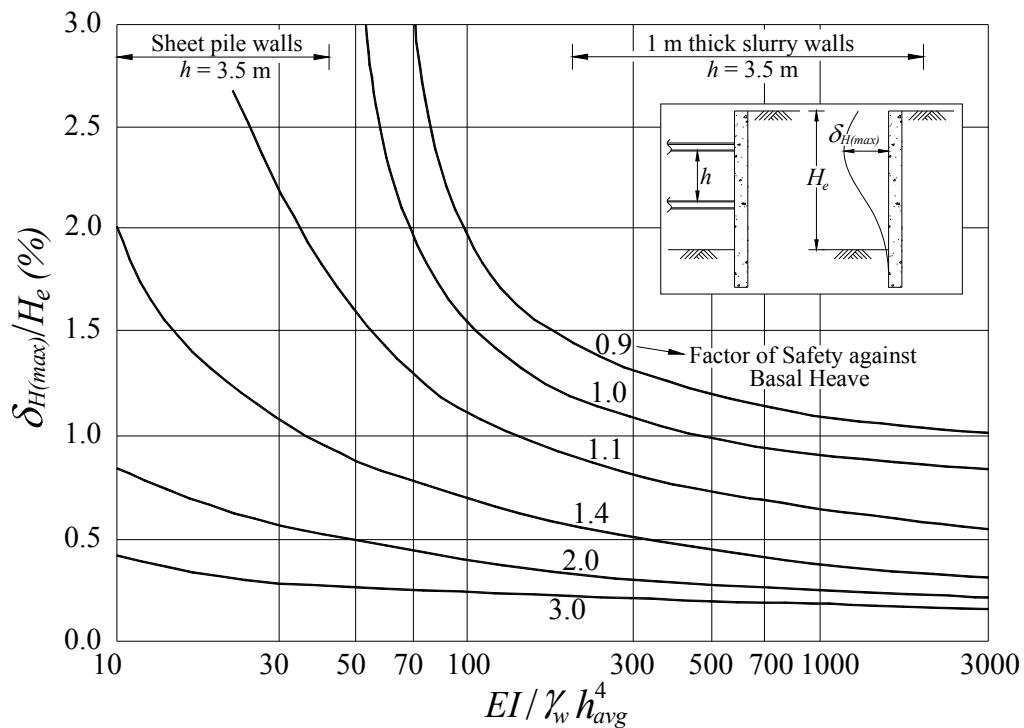
Figure 2.9 - Maximum Lateral Wall Movements and Ground Surface Settlements for Support Systems in Clay (After Clough et al., 1989).

Clough and O'Rourke (1990), based on Figure 2.9 and available data from different case histories, concluded that for stiff clays, where basal stability is typically not an issue, wall stiffness and support spacing have a small influence on the predicted movements. This is

23

because in most circumstances these soils are stiff enough to minimize the need of stiff support systems. They found that for these soils the soil modulus and coefficient of lateral earth pressure have a more significant impact on the ground movements. Their results suggested that in a stiff soil, variations in soil stiffness have a more profound effect on wall behavior than system stiffness.

For soft to medium clays, where basal stability may be an issue, Clough and O'Rourke (1990) found that the resulting deformations are most influenced by the support system stiffness, and thus, is the key design parameter used to control ground movements.

It is important to note that Figure 2.9 and other existing methods that relate lateral wall movements to excavation support system stiffness and basal stability were developed using a limited number of wall types and configurations. Furthermore, these do not include the three-dimensional nature of the excavation, the three-dimensional effects of the wall construction, the effects of different support types, the influences of the excavation geometry and sequencing, and the effects of complex site geology.

2.5   Ground Movement Predictions Adjacent to Excavations

The stresses in the ground mass change during excavation activities. These changes are evidenced in the form of vertical and horizontal ground movements whose magnitude and distribution are closely related to factors such as: (i) soil conditions; (ii) excavation geometry; (iii) stability against basal heave; (iv) type and material of retaining wall; (v) stiffness and spacing of vertical and horizontal supports; (vi) construction procedures; and (vii) workmanship. A direct and quantitative analysis of excavation-related ground movements is not an easy task. It requires an analysis of the complex interaction between the aforementioned parameter in a three-dimensional way.

24

2.5.1 Perpendicular Profile

Ou et al. (1993) proposed a procedure to estimate excavation-induced ground settlement profile normal to the excavation support wall. Their work was based on observation of 10 case histories in soft soils (Taipei, Taiwan). From these data, they developed a trilinear settlement profile (Figure 2.10) called spandrel-type settlement, which presents the maximum settlement very near to the wall. The spandrel type of settlement profile occurs if a large amount of wall deflection occurs at the first phase of excavation when cantilever conditions exist and the wall deflection is relatively small due to subsequent excavation (as presented in 2.3). The data presented in Figure 2.10 is normalized settlement, $\delta_V/\delta_{V(max)}$, where $\delta_{V(max)}$ is the maximum ground surface settlement, versus the square root of the distance from the edge of the excavation, d, divided by the excavation depth, H_e.
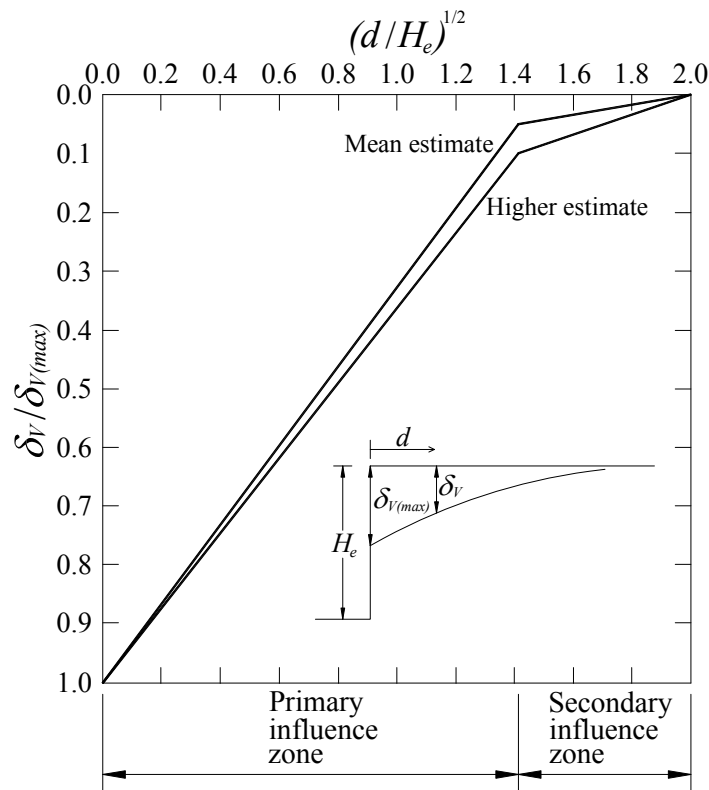
Figure 2.10 - Shape of "Spandrel" Settlement Profile (After Ou et al., 1993).

Hsieh and Ou (1998), based on nine case histories worldwide, extended the work done by Ou et al. (1993) by proposing the concave settlement profile (Figure 2.11) induced by deep excavations. From Figure 2.11, it can be seen that the maximum settlement occurs at a distance of $H_e/2$ from the wall and that the settlement at the wall can be approximated to $0.5\delta_{V(max)}$. The case history data also showed that the extent of the primary influence zone is approximately two excavation depths ($2H_e$) and after a distance of $4H_e$ the settlement is basically negligible.
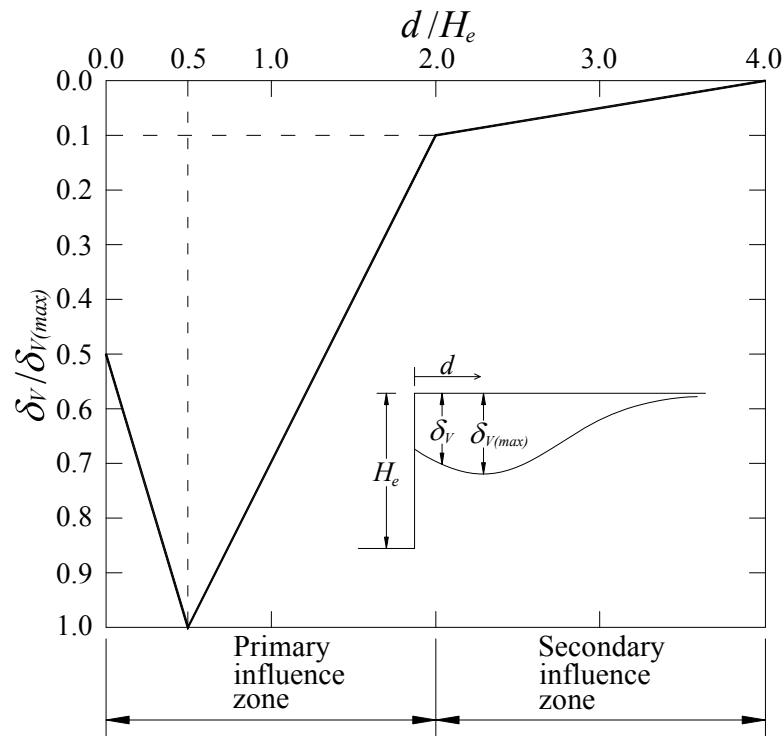
Figure 2.11 - Proposed Method for Predicting Concave Settlement Profile (After Hsieh and Ou, 1998).

Hsieh and Ou (1998) also established the relationship of cantilever area and deep inward area of wall deflection, similar to the one proposed by O'Rourke (1981), as a first approximation to predict the type of settlement profile. They suggested the following procedures for predicting the settlement profile: (1) predict lateral deformations using finite

element or beam on elastic foundation methods; (2) determine the type of settlement profile by calculating the areas of the cantilever and inward bulging of the wall displacement profile; (3) estimate the maximum ground surface settlement as $\delta_{V(max)} \approx 0.5\delta_{H(max)}$ to $1.0\delta_{H(max)}$; and (4) plot the surface settlement profile using Figure 2.10 for spandrel settlement profile or Figure 2.11 for concave settlement profile.

2.5.2   Parallel Profile

Finno and Roboski (2005) and Roboski and Finno (2006) proposed parallel distributions of settlement and lateral ground movement for deep excavations in soft to medium clays. The parallel distribution profiles were based on optical survey data obtained around a 12.8-m-deep excavation in Chicago supported by a flexible sheet pile wall and three levels of regroutable anchors.

They found that when using the complementary error function ($erfc$), just geometry and maximum movement parameters are necessary for defining the parallel distributions of ground movement. The complementary $erfc$ function is defined as:

$$\delta(x) = \delta_{max}\left\{1 - \frac{1}{2}erfc\left[\frac{2.8\left(x + L\left[0.015 + 0.035\,ln\dfrac{H_e}{L}\right]\right)}{0.5L - L\left[0.015 + 0.035\,ln\dfrac{H_e}{L}\right]}\right]\right\} \tag{2-29}$$

where δ_{max} can be either maximum settlement or maximum lateral movement, L is the length of the excavation, and H_e the height of the excavation as presented in Figure 2.12.

Although Equation (2-29) was derived from observations of flexible wall excavations, it has been reported by Roboski and Finno (2006) that it can predict with reasonable agreement the ground movement profiles for stiffer walls.

27
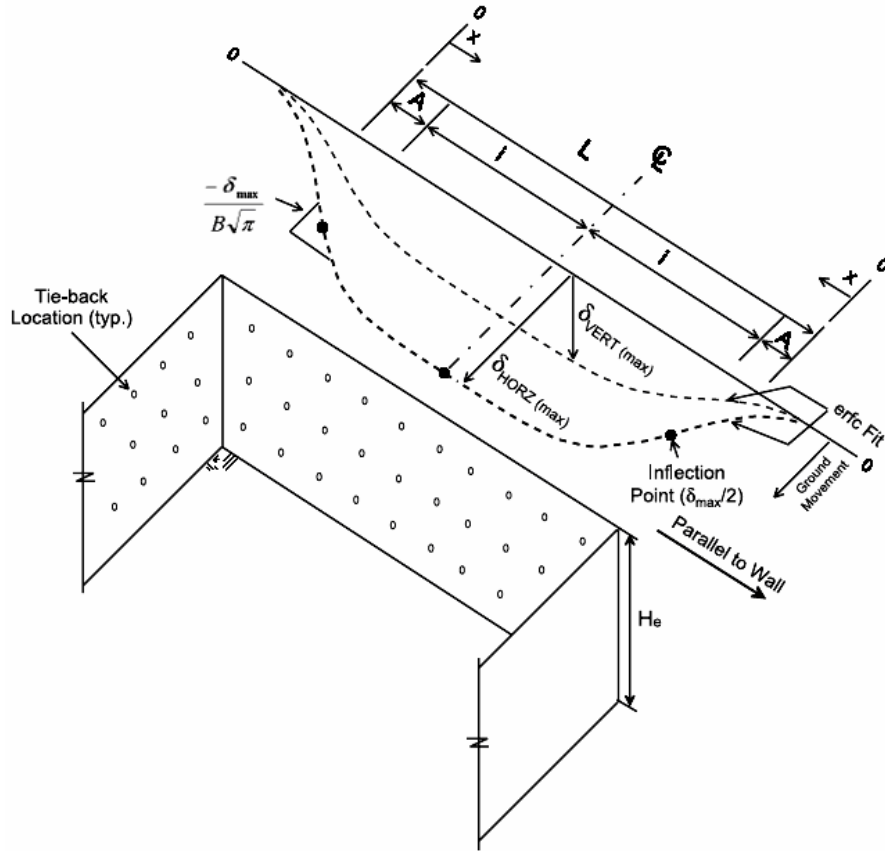
Figure 2.12 - Derived Fitting Parameters for the Complementary Error Function. δ_{VERT}, settlement; δ_{HORZ}, lateral movement (After Roboski and Finno, 2006).

Special attention is needed in excavations where there are larger diameter utility pipes, buildings with stiff floor systems, buildings supported on deep foundations, and deep foundations between the building and the excavation because they provide restraint for the movements and consequently will affect their distribution. Roboski and Finno (2006) concluded that the complementary error function approach is applicable to excavations where the induced ground movements can develop with little restraint.

2.5.3   Relation between $\delta_{H(max)}$ and $\delta_{V(max)}$

In general, the maximum ground surface settlement, $\delta_{V(max)}$, can be estimated by referring to the value of the maximum wall deflection, $\delta_{H(max)}$. Figure 2.13 presents

maximum wall deflection versus maximum ground surface settlement normalized both with respect to the height of the excavation, H_e. The data presented in the figure was reported by Mana and Clough (1981), Ou et al. (1993), and Hsieh and Ou (1998) from several case histories around the world. It can be seen in Figure 2.13 that $\delta_{V(\max)}$ relates to $\delta_{H(\max)}$ as:

$$\delta_{V(max)} \approx 0.5\delta_{H(max)} \ to \ 1.0\delta_{H(max)} \tag{2-30}$$
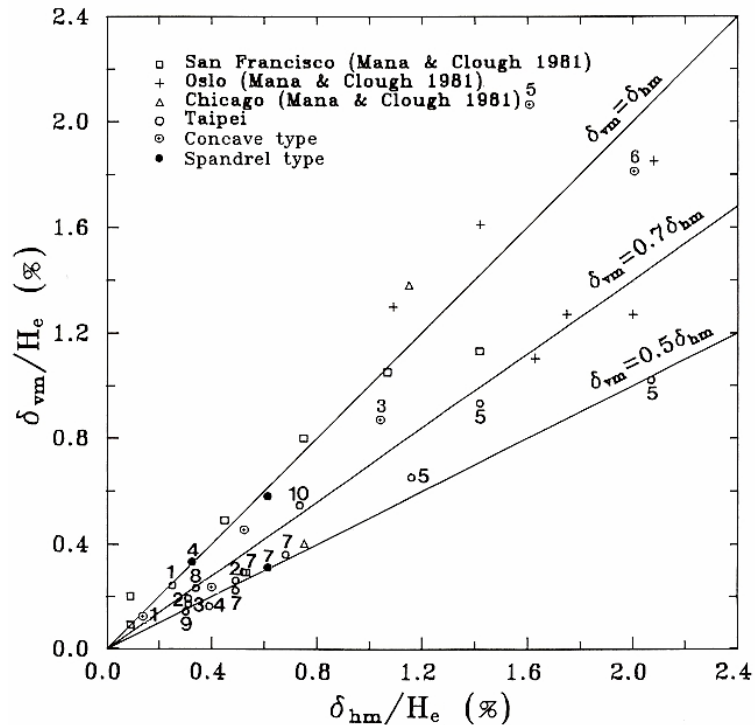
Figure 2.13 - Relationship between Maximum Ground Settlement and Maximum Lateral Wall Deflection (Adapted from Ou et al., 1993; and Hsieh and Ou, 1998).

2.6   Wall Installation Effects

A common practice for the analysis and design of excavation support systems consisting of insitu wall elements such as diaphragm and secant pile walls is to assume that the walls are "wished-in-place." This implies that the construction of the wall itself does not cause any changes in the insitu stress state and consequently does not yield any ground movements. However, several researchers (O'Rourke, 1981; Poh and Wong, 1998; Bryson, 2002) have

29

found this not to be the case. In fact, it has been reported that deformations associated with wall installation can comprise a significant percent of the total excavation-induced movements observed and significantly affect the insitu effective stresses (Ng, 1992; Ng and Yan, 1999; Gourvenec and Powrie, 1999).

2.6.1   Field Observations

O'Rourke (1981) noted that excavation-induced settlement in soft clays and sands occurred as a result of ground loss when excavating the trench for a diaphragm wall or when drilling shafts for secant and tangent pile walls. He reported case histories where 50 to 70 percent of the total recorded settlement were associated with the construction of the insitu wall.

Ng (1992) reported the top-down construction performance of a 10-m-deep multi-propped excavation in stiff fissured Gault Clay in Cambridge, United Kingdom. The excavation was retained by a 17-m-deep, 0.6-m-thick concrete diaphragm wall constructed under bentonite in panels typically 8.5 m in length. Field monitoring during the wall installation showed a significant reduction in lateral stresses associated with only small ground movements.

Poh and Wong (1998) reported the performance of a diaphragm wall panel during construction for investigating the effects of wall installation on ground movements, soil stresses and pore water pressures. They closely monitored lateral and vertical movements on the ground; soil and pore water pressures; and ground water table variations during the stages of trenching, holding time before concreting, variation of slurry pressure, and concreting of the panel. Later, Poh et al. (2001) presented four additional case histories where lateral soil movements and soil settlements due to the construction of diaphragm wall

panels were monitored. It was found that lateral soil movements caused by the construction of wall panels increased with increasing wall dimension and therefore their magnitude could be minimized by reducing the dimensions of the wall panels. Additionally, they found that the use of high slurry levels during the construction of the wall panels would help to minimize the magnitude of lateral soil movements.

Bryson (2002), Finno and Bryson (2002), and Finno et al. (2002) presented the excavation performance of a stiff support system in soft to medium stiff Chicago clay. The excavation was 13-m-deep and supported by a 0.9-m-thick secant pile wall, one level of cross-lot bracing, and two levels of tiebacks. Most of the secant pile wall was installed in just 10 days by first drilling primary shafts located 1.5 m apart; setting a wide-flange section into the hole; and placing grout from concrete trucks. Secondary shafts were installed between the primary shafts providing 150 mm overlap. Field performance data showed that 9.0 of the 38.1 mm of maximum lateral movement recorded at the end of the excavation, occurred during wall installation activities.

2.6.2   Numerical Analyses

Numerical analyses of insitu walls in which the effects of wall installation are neglected by modeling the wall as "wished-in-place," overestimate strut loads and fail to estimate the general ground deformation pattern (Ng and Lings, 1995 and Ng et al., 1998). It is because there is a stress relief in the soil mass caused by the construction of the insitu wall.

Ng and Yan (1998) and Ng et al. (1995) investigated the three-dimensional effects of diaphragm wall installation in Gault clay at Lion Yard Cambridge (United Kingdom). They found that the stress reduction in the soil mass around the wall panel is dominated by two distinct mechanisms: horizontal arching and downward load transfer, which only can be

31

modeled using three-dimensional techniques that permit stress redistribution. These mechanisms were later confirmed by Ng and Yan (1999), who conducted a three-dimensional back-analysis of the construction sequence of three diaphragm wall panels. They found that these two mechanisms act simultaneously and result in an average reduction of horizontal stress directly behind the wall above the toe but an increase of horizontal stress in neighboring soil beyond the wall in the longitudinal direction and below the toe of the wall.

Gourvenec and Powrie (1999) investigated the effect of the sequential installation of a number of adjoining panels to form a complete wall and the impact of panel length on the significance of three-dimensional ground movements and changes in lateral stresses. They reported that the magnitude and extent of lateral stress reduction in the vicinity of a diaphragm wall during construction depend on the panel length and are overpredicted in analyses assuming plane strain conditions. Three-dimensional effects tend to reduce lateral soil movements during installation of a diaphragm wall in panels compared with the plane strain case.

Several finite element analyses of insitu retaining wall installation have been reported in the literature. Table 2.1 lists and discusses some of them by (i) type of analysis, (ii) soil stratigraphy, (iii) wall model and dimensions, (vi) soil model and software, and (v) drained conditions. As can be seen in Table 2.1, all analyses generally differ in ground conditions and wall geometries, and all present their results in different ways. It is therefore difficult to draw any general conclusions.

Table 2.1 - Numerical Analyses of Wall Installation Effects.

Reference	Type of Analysis	Soil Stratigraphy	Wall Model	Soil Model and Software	Drained Conditions
De Moor (1994)	Plane strain FE[a] of a plan horizontal section	15 m London clay	Linear elastic Diaphragm wall 1.2 m thick	Mohr-Coulomb CRISP	Undrained
Ng et al. (1995)	Pseudo 3D[b]	3-4 m of fill/gravel and 38 m of Gault clay layers overlaying a greensand	Linear elastic Diaphragm wall 0.6 m thick, 8.5 m wide, 17 m deep	Mohr-Coulomb SAFE	-
Ng and Lings (1995)	Plane strain FE	same as Ng et al. (1995)	same as Ng et al. (1995)	Mohr-Coulomb, Nonlinear "Brick" model SAFE	Undrained
Ng et al. (1998)	Plane strain FE	same as Ng et al. (1995)	same as Ng et al. (1995)	Mohr-Coulomb, Nonlinear "Brick" model SAFE	Undrained
Ng and Yan (1998)	3D elastoplastic FD[c]	same as Ng et al. (1995)	same as Ng et al. (1995)	Mohr-Coulomb FLAC3D	Gravel: drained Clay: undrained
Ng and Yan (1999)	3D FD	same as Ng et al. (1995)	same as Ng et al. (1995)	Mohr-Coulomb FLAC3D	-
Gourvenec and Powrie (1999)	3D FE	Homogeneous stiff Lias clay in England	Isotropic elastic Diaphragm wall 1 m thick, 15 m deep, L varied	Mohr-Coulomb CRISP	Undrained
Gourvenec et al. (2002)	3D FE	4 m of Midford sand layer overlaying a stiff Lias clay layer	Isotropic elastic 1)22.85 m deep, 1.5 m thick and 7.5 m long; 2)12.87 m deep, 1 m thick and 5 m long	Mohr-Coulomb CRISP	Drained
Schafer and Triantafyllidis (2004)	3D FE	3-4 m of miscellaneous fill and 30 m of soft clay overlaying a bedrock stratum	Linear elastic Diaphragm wall 1 m thick, 5 m wide, 28 m deep	Mohr-Coulomb, and Modified Cam–Clay	-

[a] FE means Finite Element Analysis

[b] 3D means Three-dimensional Analysis

[c] FD means Finite Difference Analysis

2.6.3   Lateral Pressures and Critical Depth during Concreting

Lings et al. (1994) examined the lateral pressure exerted by wet concrete in diaphragm wall panels cast under bentonite. They found that there is a critical depth, above which the full fluid concrete pressures apply, and below which pressures increase with depth following the slope of the bentonite line. They reported that the critical depth was approximately one-third of the wall depth. They suggested that wet concrete pressure diagrams adopted in analyses of wall installation effects should use the bilinear shape as shown in Figure 2.14.
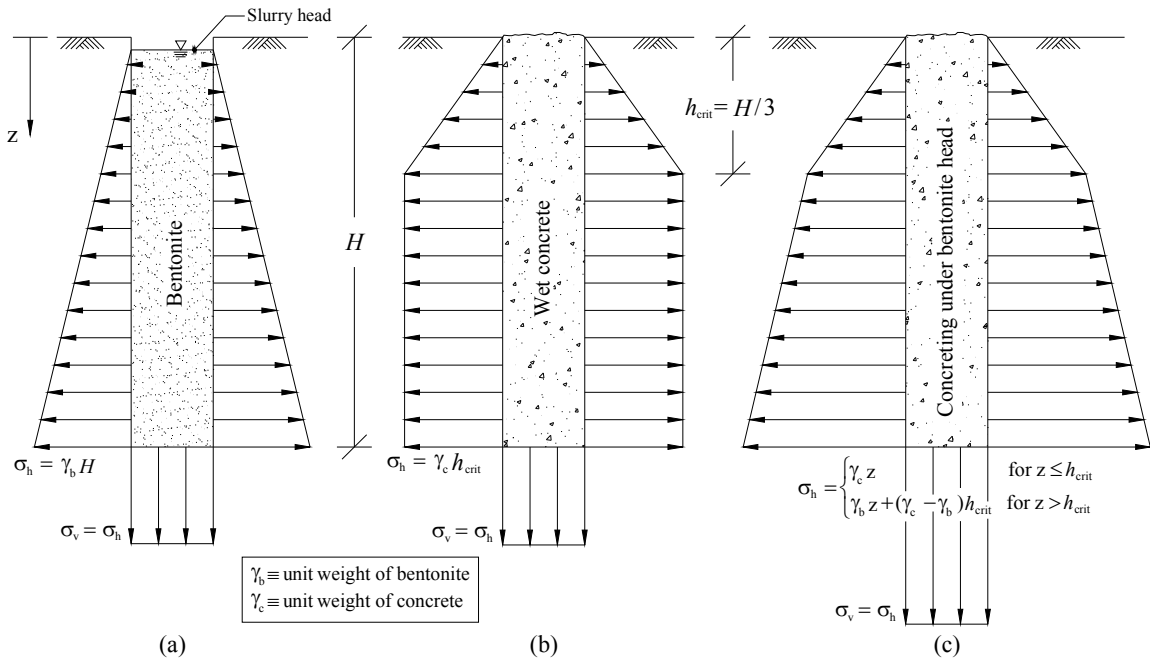
Figure 2.14 - Lateral Pressures and Critical Depth: (a) under Bentonite; (b) under Wet Concrete; and (c) Concreting under Bentonite.

2.6.4   Design Aids for Calculating Ground Movements and Stresses

Few prediction tools for estimating horizontal movements and stresses are found in the literature. Thorley and Forth (2002) presented predictions for settlement caused by the excavation and concreting of a diaphragm wall under slurry bentonite. Figure 2.15, which was estimated using empirical data measured in similar ground conditions in Hong Kong,

34

relates settlement to the distance from the wall, and lateral ground movements and settlements to the effective slurry pressures maintained in the trench respectively.
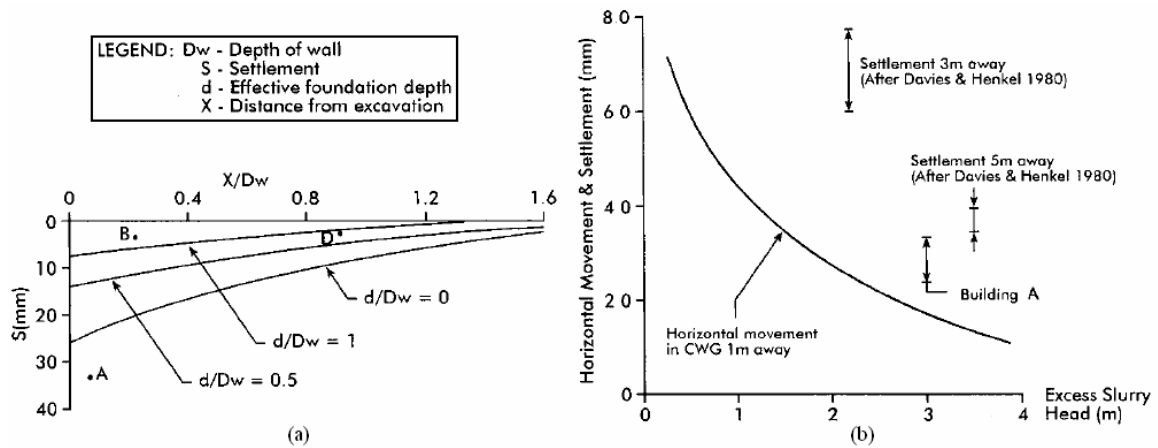
Figure 2.15 - Diaphragm Wall and Excavation Estimate Curves (Adapted from Thorley and Forth, 2002).

Ng and Lei (2003) presented Figure 2.16 and Figure 2.17 for calculating horizontal stress changes and displacements caused by the excavation for a diaphragm wall panel. Computed results are given in a normalized form in terms of aspect ratio (length to width) of a diaphragm wall panel. By using the theoretical solution, the calculated horizontal stress changes are found to be dependent on the aspect ratio λ_0 $(=l/w)$ and the lateral pressure changes ΔP on the sidewalls of the trench, which are mainly controlled by the initial stress of the soil, K_0. The calculated horizontal displacements are further dependent on the soil properties (i.e. Young's modulus E and Poisson's ratio υ).

Figure 2.16 and Figure 2.17 are useful for obtaining informative results for preliminary predictions and for capturing key features induced during the installation of a diaphragm wall panel. They can easily and rapidly provide stress distributions and displacements that would exist prior to yielding of the soil and helps designers to put forward measures to control the displacements induced during installation of a diaphragm wall panel. In addition,

35

they can be used to verify complicated numerical computations such as the ones in finite element methods.
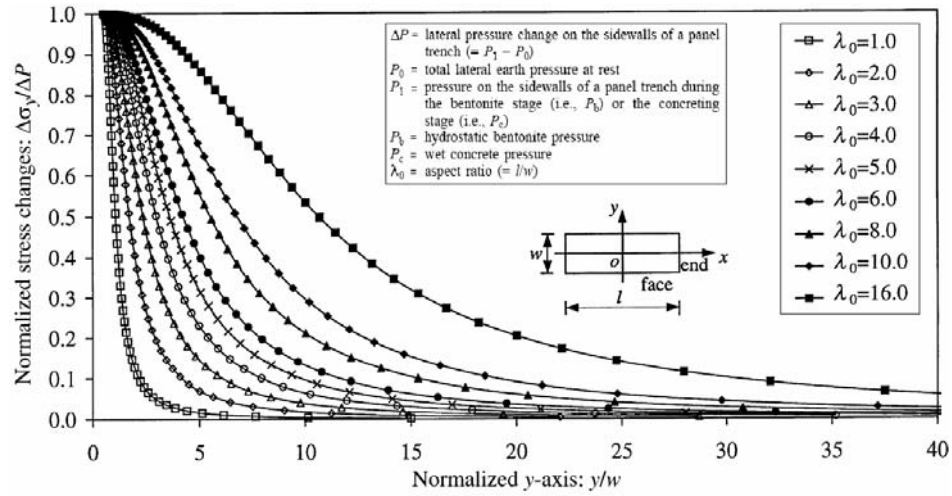
Figure 2.16 - Normalized Horizontal Stress Changes, $\Delta\sigma_y/\Delta P$, on Normalized y Axis (Adapted from Ng and Lei, 2003).
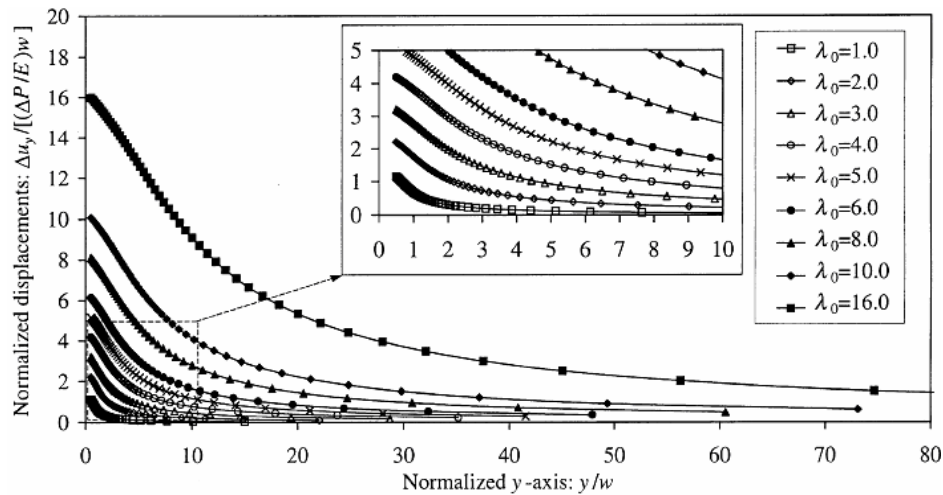
Figure 2.17 - Normalized Horizontal Displacements, $\Delta_{uy}/[(\Delta P/E)w]$, on Normalized y Axis for $\nu = 0.5$ (After Ng and Lei, 2003).

2.7   Deformation Based Design Methods

Osman and Bolton (2004, 2006a and 2006b) proposed a new approach, called Mobilizable Strength Design (MSD) method, for estimating ground movements around braced excavations in clays. It incorporates the actual undrained shear strength profile of the soil and stress-strain data deduced from a direct simple shear test on a representative sample.

36

The method is based on the assumption of a plastic deformation mechanism local to a braced excavation, and which avoids any slippage on shear surfaces.

The authors stated that the outcome is a prediction based on simple calculations that can satisfy both safety and serviceability in a single step of calculation without the need for elaborate constitutive modeling and finite element analyses. However, the method neglects both the three-dimensional nature of the excavation and the effects of installing the supporting walls; and does not include the stiffness of the support system which has been demonstrated by Clough et al (1989) to be an important factor in the prediction for ground movements.

2.8   Three-Dimensional Numerical Modeling

When excavating in an urban environment, the prediction of the magnitude and distribution of ground movements adjacent to the excavation is an important part of the analysis and design process. Numerical techniques, indisputably, have played an important role for such purpose.

In the common practice, analyses based on finite element methods assuming plane strain conditions are widely used. Two-dimensional analyses fail to capture the stiffening effect of the corners and generally overestimate the ground movements. It is intuitive that three-dimensional finite element models are required for a realistic analysis of the interaction between the soil and the excavation support system. However, full three-dimensional analyses have rarely been carried out because of their complexity and time-cost constraints.

Ou et al. (2000), Ou and Shiau (1998), and Ou et al. (1996) all used three-dimensional analyses to study geometric effects on surface settlement and lateral movements. Ou (1996) introduced the plane-strain ratio (PSR) as an indicator of restraint provided by three-

dimensional geometry in a numerical analysis. The plane-strain ratio is defined as the ratio between the maximum soil deformation observed (or calculated) with a three-dimensional geometry and the soil deformation calculated under plane-strain conditions. A PSR value approaching unity would signify an excavation configuration approaching plane-strain conditions; whereas a low PSR value would indicate significant restraining effects due to geometry and support stiffness. Ou and his co-workers all used the hyperbolic Duncan-Chang model for the soil and used conventional three-dimensional finite elements inside the excavation zone and infinite elements outside the zone. The hyperbolic model is a pseudo-elastic non-linear model that captures inelasticity by distinguishing between loading and unloading stiffness moduli. It is noted that the hyperbolic approximation does not capture shear-induced volume change. As a result, the model tends to under predict vertical displacements adjacent to the excavation. Infinite elements were implemented in an attempt to decrease the distance of the boundary elements, thereby reducing the number of elements required. Unfortunately, the computational efficiency gained by employing infinite elements does not outweigh the added complexity. Lee et al. (1998) also used three-dimensional analyses to study the effects of an irregular shaped excavation on movements. But, they used the modified Cam Clay model to represent the soil. They noted that the Cam Clay model was unable to capture the anisotropy and creep behavior as well as the small strain nonlinearity below the state boundary surface. Thus, a full spectrum of soil behavior was not reflected by the finite element analyses. However, their primary objective was to asses the significance of the geometry effects by comparing two-dimensional and three-dimensional analyses. Therefore, they determined that using a more sophisticated soil model was not necessary to their study.

38

In order to capture complex soil behavior, it is necessary to use a soil constitutive model that can closely represent the anticipated stress-strain behavior. Factors related to soil behavior include small strain non-linearity, anisotropy, volume change, stress path, loading and unloading characteristics, and strain softening or hardening. It is acknowledged that the vertical displacements adjacent to the excavation support system are more strongly affected by the soil models used than wall lateral movements. This is because the vertical displacements are mainly governed by the unload-reload stiffness properties of the soil mass. Wall lateral movements are mainly a function of structural stiffness of the support system and lateral earth pressure.

An attempt to use a more advance soil model for three-dimensional analyses was made by Zdravkovic et al. (2005). They used the non-linear elasto-plastic Mohr-Coulomb model (Potts and Zdravkovic, 1999) in which the non-linearity below yield is simulated with the Jardine et al. (1986) small-strain stiffness model. The purpose of the study was to investigate the three-dimensional effects of wall stiffness in different coordinate directions and the rotational fixity in the corner of the excavation for both square and rectangular excavations. The chosen geometry, construction sequence and soil conditions were based on the proposed deep excavation at Moorgate in London. Although the study shows the importance of three-dimensional analyses for producing realistic predictions of wall and ground movements and structural forces, the excavation was hypothetical. Thus, the efficacy of the advanced soil model could not be ascertained.

Blackburn (2005) used the Isotropic Hardening Soil model (HSM) to perform a three-dimensional finite element analysis of the Ford Engineering Design Center (FEDC) excavation in Evanston, Illinois. The analysis was performed to determine the influence of properly modeling the excavation sequence and to determine the degree of corner restraint

provided by three-dimensional geometries in deep excavations. His results show a good match between the predicted behavior and the observed behavior. In addition, Blackburn re-evaluated the PSR for the FEDC site and found good agreement with the results presented by Ou (1996).

Table 2.2 presents a summary of several numerical analyses which examined three-dimensional restraining effects on the magnitude and distribution of deep horizontal and vertical soil displacement along an excavation wall. It includes analyses previously listed by Roboski (2004) and Blackburn (2005), and some analyses not reported by them.

Table 2.2 - Summary of Three-dimensional Numerical Analyses.

Case	Support System	Geometry	Soil Stratigraphy	Constitutive Model	Summary of Findings
Hai-Hua Building Taipei, Taiwan Ou and Chiou (1993) and Ou et al. (1996)	Diaphragm wall (1.1 m, 42 m depth); Top down construction method (floors used as lateral support)	H_e = 20.3 m L x B 80 x 45 m (1/4 modeled)	Alternating layers of silty clay and silty sand	Hyperbolic, Drained behavior for sands, Undrained for clays	2D Analysis correct for (L/He=3.8) but overpredicted for (L/He=1.4). 3D Analysis correctly predicted movements for (L/He=1.4)
Hypothetical Excavation Taipei, Taiwan Ou et al. (1996)	Diaphragm wall (0.7 m, 32 m depth); Floor slabs provide lateral restraint	H_e = 16 m L x B Varied	Uniform layer of low to medium plasticity clay	Undrained hyperbolic stress strain model	Derived a Plane Strain Ratio (PSR) based on the ratio of B/L (shorter wall length to longer wall length of a rectangular excavation)
Commercial Building Central Business District Singapore Chew et al. (1997)	Sheet pile wall (FSP IV, 28 m depth); 1 level of struts	H_e = 6 m L x B 50 x 40 m (1/4 modeled)	6 m fill; 20 m soft to firm marine clay; 5 m loose to medium dense silty sand; 6 m firm marine clay; 12 m stiff sandy silt	Elasto-plastic with Mohr-Coulomb failure criteria for stiff sandy silt; Modified Cam Clay for marine clay, and sand layer	2D Analysis overpredicted maximum deflection at center of wall; 3D Analysis more accurately predicted max movement
Equivalent Hypothetical Excavation Singapore Chew et al. (1997)	Sheet pile wall (FSP IV, 28 m depth); 1 level of struts	H_e = 6 m L x B 51 x 40 m (1/4 modeled)	Added grout layer just below excavation level to stratigraphy above	Elasto-plastic with Mohr-Coulomb failure criteria for stiff sandy silt; Modified Cam Clay for marine clay, and sand layer	Added stiff layer altered wall deformation pattern. Reduction of movement from center to corner is less than for similar 3D analysis without stiff layer. 3D profile closer to 2D profile at center of wall with added stiff layer.
Immigration Building (IMM) Singapore Lee et al. (1998)	Diaphragm wall (1000 mm, 24 to 35 m depth); 5 levels of struts	H_e = 17.3 m L x B 75.6 x 50.4 m (1/4 modeled)	3 m sandy fill; 15 m marine clay; 10 m loose to medium dense clayey silt/sand; stiff silty clay	Modified Cam Clay; Diaphragm wall (Von Mises); Struts (3D spring elements)	Field data at center of each wall well modeled by 3D analysis; 2D analysis over predicted the maximum deflection. At the corners, 3D and 2D analyses over predicted by 30% and 200%, respectively.

41

Table 2.2 - (Continued) Summary of Three-dimensional Numerical Analyses.

Case	Support System	Geometry	Soil Stratigraphy	Constitutive Model	Summary of Findings
1) Hypothetical; 2) Central Insurance Building; 3) Chi-Ching Building. Taipei Ou and Shiau (1998)	Three support levels and diaphragm wall. 1) 0.6 m, 24 m depth; 2) 0.6 m, 23 m depth; 3) 0.7 m, 28 m depth	1) H_e = 12 m 20 x 20m 2) H_e = 9.45 m 51.9 x 33.7 m 3) H_e = 13.9 m 80 x 33 m	1) 36 m CL over hard soil; 2) Six alternating CL and SM layers overlaying a gravel formation; 3) 12 m SM, 3 m CL, 8 m CL, 26 m SM, gravel	Hyperbolic Duncan-Chang model (CUT3D)	Further verified the corner effect on the excavation behavior reported by Ou et al. (1996)
Taipei National Enterprise Center (TNEC) Ou et al. (2000)	Diaphragm wall (0.9 m, 35 m depth); Top down construction method (floors used as lateral support)	H_e = 19.7 m Irregular shape idealized as a rectangle 105 x 41 m	5.6 m CL; 2.4 m SM; 25 m CL; 4.5 m dense fine sand and CL; 8.5 m dense silt or SM; gravel formation	Hyperbolic Duncan-Chang model (CUT3D)	Soil outside the excavation tends to move toward the excavation center increasing with excavation depth. The settlement near the corners is less than that near the center due to the corner effects.
Bangkok, Thailand Lin et al. 2003	Diaphragm wall (0.8 m, 20 m depth); internally braced	H_e = 18.3 m L x B Varied	2 m weathered clay; 9 m very soft to soft clay; 4 m medium clay; 9 m stiff clay; 12 m sand	Mohr Coulomb, undrained; Finite Difference Method (FLAC 3D)	Quantitative relationship established for estimating 3D lateral movement using a 2D numerical result.
Robert H. Lurie Center Chicago, IL Roboski (2004)	Sheet pile wall (PZ27, 17.5 m depth); 3 level strut	H_e = 12.8 m L x B Varied	Fill deposit overlying clays of increasing shear strength: 9.2 m sand and fill; 7.5 m soft clay; 8.5 m stiff clay; hard clay	Sand/Fill-Mohr Coulomb Clays - Modified Cam Clay Model	Determined relationship between excavation geometry parameters and PSR

Table 2.2 - (Continued) Summary of Three-dimensional Numerical Analyses.

Case	Support System	Geometry	Soil Stratigraphy	Constitutive Model	Summary of Findings
Hypothetical Excavation (Central London, UK) Zdravkovic et al. (2005)	Wall stiffness varied. (46.7 m depth) 7 prop levels	$H_e = $ 40.7 m L x B 1) 35 x 35 m 2) 70 x 35 m 3) 140 x 35 m (1/4 modeled)	3.7 m made ground; 3.5 m terrace gravel; 28.5 m London clay; 18 m Lambeth group caly; 13 m Thanet sand; chalk	Non-linear Elasto-Plastic Mohr–Coulomb Model using the Imperial College Finite Element program (ICFEP)	The moment connections at the excavation corners were Examined. To obtain realistic results, the axial and bending stiffness of the wall along its perimeter must be reduced (wall is unlikely to be a continuous membrane and full moment is not transmitted at the corners)
Ford Engineering Design Center in Evanston, IL. Finno and Blackburn (2006), Blackburn and Finno (2006)	Sheet pile wall (XZ85, 14.4 m depth); 2 levels of internal bracings. 3 diagonal braces at each corner and 2 cross-lot braces	$H_e = $ 8.6 m L x B 44.2 x 36.6 m	5.2 m sand/fill; 1 m clay crust; 4 m soft clay; 8.1 m medium clay; 3.7 m stiff, silty clay; and hard clay, sand, gravel.	Isotropic hardening soil model (PLAXIS 3D FOUNDATION)	Illustrated the effects of the connections between braces, walers and wall; and show the effects of sheeting flexibility parallel to the wall.
Hypothetical Excavation Chicago, IL Finno et al. (2007)	Wall stiffness varied. (18.3 m depth) 4 levels of struts	$H_e = $ 9.8 to 16.3 m L x B Varied (1/4 modeled)	Same as Robert H. Lurie Center Chicago, IL Roboski (2004)	Isotropic hardening soil model (PLAXIS 3D FOUNDATION)	Determined relationship between geometry, wall system stiffness, factor of safety, and PSR. When L/H_e >6, plane strain and 3D simulations yield the same displacements in the center of the excavation.

CHAPTER 3

3　WALL INSTALLATION EFFECTS OF EXCAVATION SUPPORT SYSTEMS

3.1　Introduction

Construction projects involving deep excavations are prevalent in many urban areas around the world. Stiff excavation support systems, which typically imply the construction of insitu retaining walls such as secant and tangent pile walls and diaphragm walls, are widely used to minimize lateral and vertical ground movements. The common practice for excavation support system design is to use a limit equilibrium approach and to assume that the complete support system is "wished-in-place" (WIP). This implies that the construction of the insitu wall component and the installation of the supports do not cause any movements or changes in the insitu stress state. However, the installation process can cause significantly movements in the surrounding ground, which result in appreciable changes in the insitu soil stress conditions (Ng, 1992; Ng and Yan, 1999; Gourvenec and Powrie, 1999).

Finno et al. (2002) observed this to be the case during the excavation for the Chicago and State Subway Renovation Project in Chicago, Illinois. This project included the installation of a secant pile wall with three levels of support, to maintain a 13-m excavation in soft to medium Chicago clay. The lateral displacements observed at end of wall installation and at end of excavation are presented in Figure 3.1. The lateral displacement and depth are normalized with respect to the maximum lateral displacement recorded at end of excavation ($\delta_{H max(ii)}$ = 38.1 mm) and to the wall depth (H = 18.3 m), respectively.

As can be seen in Figure 3.1, the deformations recorded during wall installation were approximately 25 percent of the total displacement. This becomes a significant observation in that these deformations were observed prior to the start of the excavation. This case

44

shows that the assumption of a WIP system can lead to a significant underestimation of excavation-related lateral movements. It is also apparent that lateral movements of this magnitude cannot be neglected and must be taken into account when designing support systems, especially when sensitive structures are nearby.
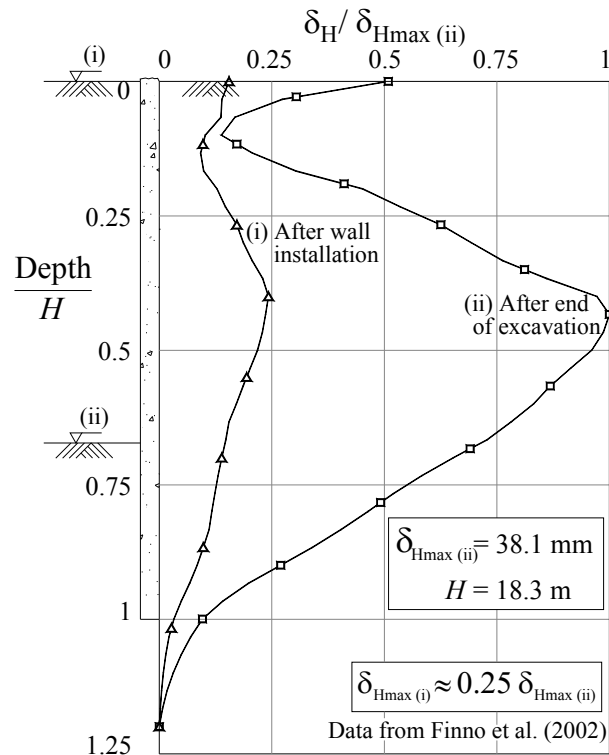
Figure 3.1 - Lateral Displacements vs. Depth after Wall Installation and after End of Excavation.

3.2   Evaluation of Wall Installation Effects

This section presents a comprehensive evaluation of insitu wall installation effects on the performance of excavation support systems. The evaluation includes field observations of deformations (lateral and vertical), pore water pressure changes, and lateral earth pressures resulting from wall installation. The evaluation also reports on several efforts to include wall installation effects in various numerical models. Particular emphasis is placed on techniques used to simulate the construction methods. In addition, this section evaluates the influences

45

of: (i) the analysis type (i.e. two-dimensional plane strain, three-dimensional and pseudo three-dimensional finite elements and finite difference); (ii) the soil and wall constitutive models employed in the simulation; and (iii) the drainage conditions (drained or undrained) assumed in the analysis, on the performance of the numerical models.

3.2.1 Finite Element Analysis of Excavation with and without Wall Installation Effects Included

Ng (1992) specifically investigated the effects of wall installation by performing a finite element analysis of the Lion Yard excavation in Cambridge, England. The analysis simulated the top-down construction of a 10-m deep, multi-supported excavation in the overconsolidated, stiff fissured Gault clay at Lion Yard. Ng (1992) analyzed conditions with and without wall installation effects included and utilized the nonlinear "brick model" (Simpson, 1992) to represent the soil behavior. Figure 3.2.a and Figure 3.2.b show an idealization of the "wished-in-place" model (WIP) and the wall installation model (WIM), respectively. In the WIM, the construction sequence of the retaining wall is modeled as: (i) excavating the soil under slurry head by removing the soil and applying lateral pressures to the faces of the trench; (ii) concreting under slurry by changing the pressure distribution as presented in Figure 2.14; and (iii) installing the concrete wall panels by removing the lateral pressures and filling with concrete grout the trenches. Ng (1992) evaluated the effects of modeling the wall installation on predicted lateral deformations and soil stresses by comparing numerical results with measured data. These results are shown in Figure 3.2.c and Figure 3.2.d. In the figures, horizontal stresses were inferred from strut loads and rotations of the wall, and were estimated using K_0 values obtained from pressuremeter tests. It is noted in Figure 3.2.c that the total horizontal stresses are normalized with respect to the

46

effective vertical stress at the bottom of the wall. In Figure 3.2.d, the lateral deformations are normalized with respect to the maximum lateral deformation recorded at end of excavation ($\delta_{H\,max}$ = 12.7 mm). In both Figure 3.2.c and Figure 3.2.d, the depths are normalized with respect to the wall depth (H = 17 m).
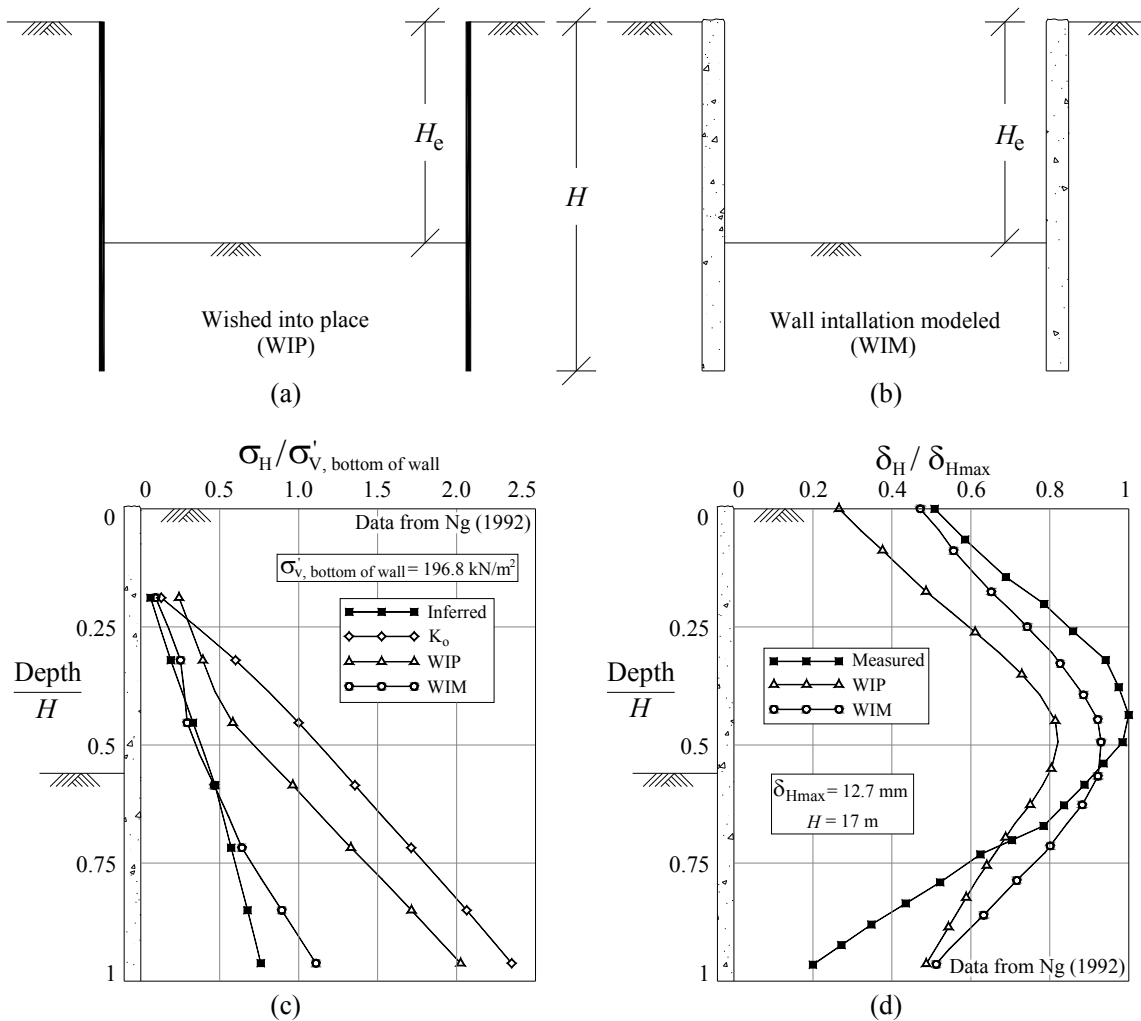
Figure 3.2 - Model Excavation: (a) Wall Wished into Place; (b) Wall Installation Modeled; (c) Total Horizontal Stress vs. Depth; and (d) Lateral Displacements vs. Depth.

Ng (1992) found that the model that included the wall installation procedures (i.e. WIM) produced results that closely matched the inferred horizontal stress data and the lateral deformation at the excavation level. However, the assumption of the wall being "wished in

place" overestimated the horizontal stresses at the excavation level by approximately 100 percent and underestimates the lateral deformations by approximately 20 percent.

3.2.2   Two-Dimensional and Three Dimensional Finite Element Models

While Ng (1992) utilized a two-dimensional (2D) plane strain finite element model to investigate wall installation effects, other efforts have been made to model the full wall construction sequence using three-dimensional (3D) finite element analyses. The two most common approaches to three-dimensional modeling are the pseudo 3D and the "true" 3D models. Figure 3.3 shows a comparison of the three model types. It can be seen that the pseudo 3D and plane strain analyses are simplifications of the "true" 3D analysis. The pseudo 3D analyses (Figure 3.3.b) consider two orthogonal plane strains analyses (A-A' and B-B' sections, see Figure 3.3.a), while plane strain analyses (Figure 3.3.c) only consider the A-A' section.
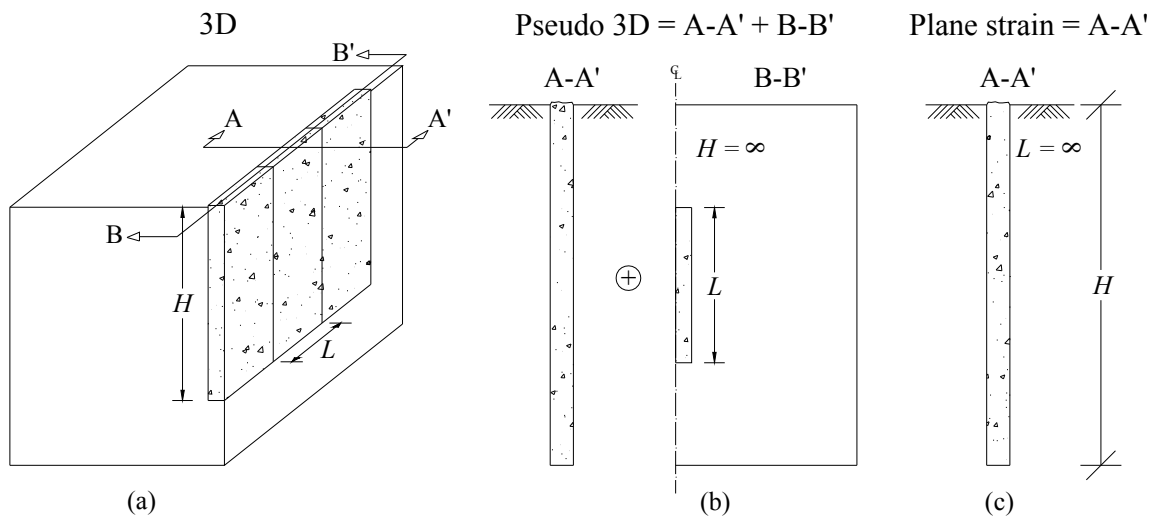
Figure 3.3 - (a) 3D Analysis; (b) Pseudo 3D Analysis; and (c) Plane Strain Analysis.

Ng and Yan (1999) compared the pseudo 3D analysis of a diaphragm wall installation with the "true" 3D analysis. Figure 3.4.a shows the results of this effort. It can be seen from the figure that the results differ in the vicinity of the bottom of the wall, especially below the

wall toe. Ng and Yan (1999) suggested that this was due to the stress reduction, which was attributed to both downward load transfer and horizontal arching mechanisms. They concluded that this behavior can only be modeled by the 3D analysis. Gourvenec and Powrie (1999) also compared 3D model results with those obtained from plane strain analyses. Figure 3.4.b shows the variation of the earth pressure coefficient at rest (K_0) with the depth at 5 m from the wall. It is apparent from Figure 3.4 that the "true" 3D analyses yield results that more closely match the field data, than the plane strain or pseudo 3D analyses.
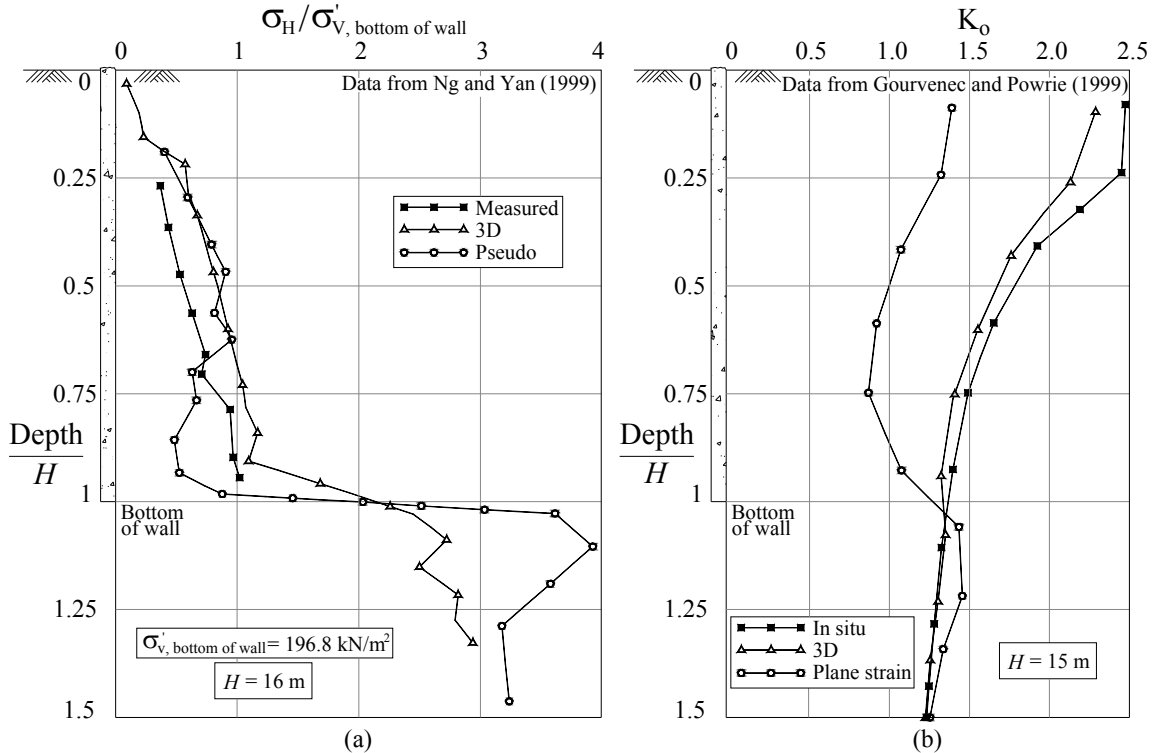
Figure 3.4 - (a) Plane Strain vs. 3D; and (b) Pseudo vs. 3D.

3.2.3   Influence of Panel Length and Construction Sequence

In addition to comparing K_0 predictions from plane strain and 3D analyses, Gourvenec and Powrie (1999) also investigated the influence of panel length and construction sequence

49

on predicted lateral deformations of a diaphragm wall. Figure 3.5 shows the lateral displacements, normalized with respect to the maximum lateral displacement corresponding to the plane strain case ($\delta_{H\,max}$ = 12.4 mm), versus depth, normalized with respect to the wall depth (H =15 m), for different panel lengths. It can be seen in the figure that the maximum lateral displacements for panel lengths of 2.5, 3.75, 5 and 7.5 m are approximately 90, 75, 65 and 40 percent of the displacements obtained for plane strains conditions ($L = \infty$), respectively.
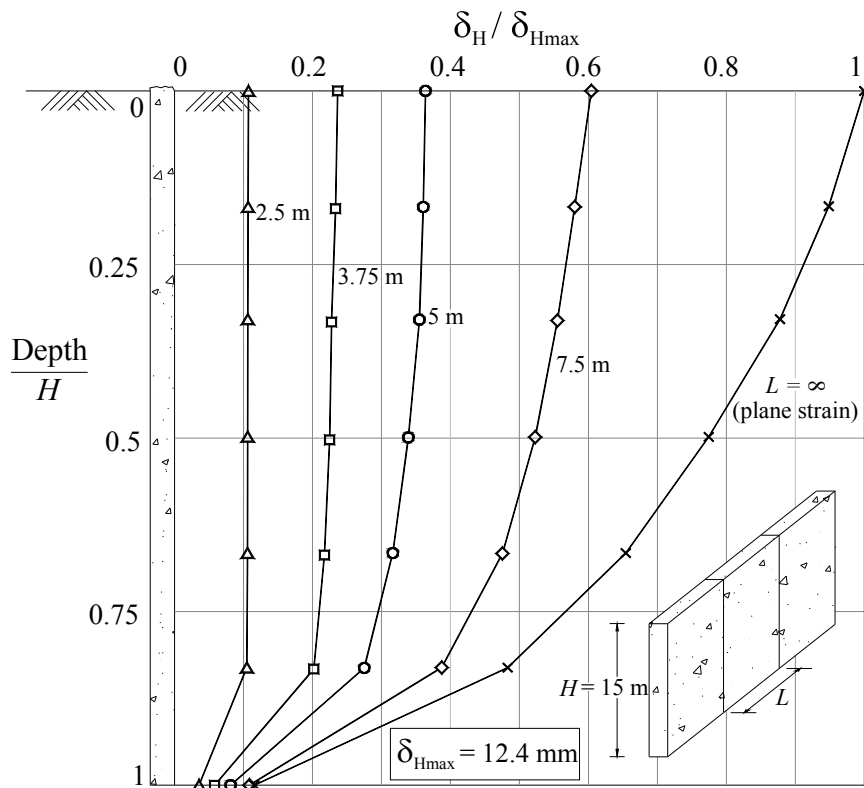
Figure 3.5 - Influence of Panel Length on Lateral Displacements (Data from Gourvenec and Powrie, 1999).

3.2.4   Effects of Slurry Head Variation and Holding Time

Poh and Wong (1998) investigated the influence of specific construction methods utilized to install the diaphragm wall on the magnitude of lateral displacements. Figure 3.6 presents the lateral displacements versus depth for a variation of the slurry head (Figure

3.6.b) and holding time stages (Figure 3.6.c). The lateral displacements are normalized with respect to the maximum lateral displacement recorded at the beginning of slurry variation ($\delta_{H\,max}$ = 12.7 mm, slurry head = $0.002\,H$) and the maximum lateral displacement recorded after trenching. The depths are normalized with respect to the wall depth (H = 55.5 m).
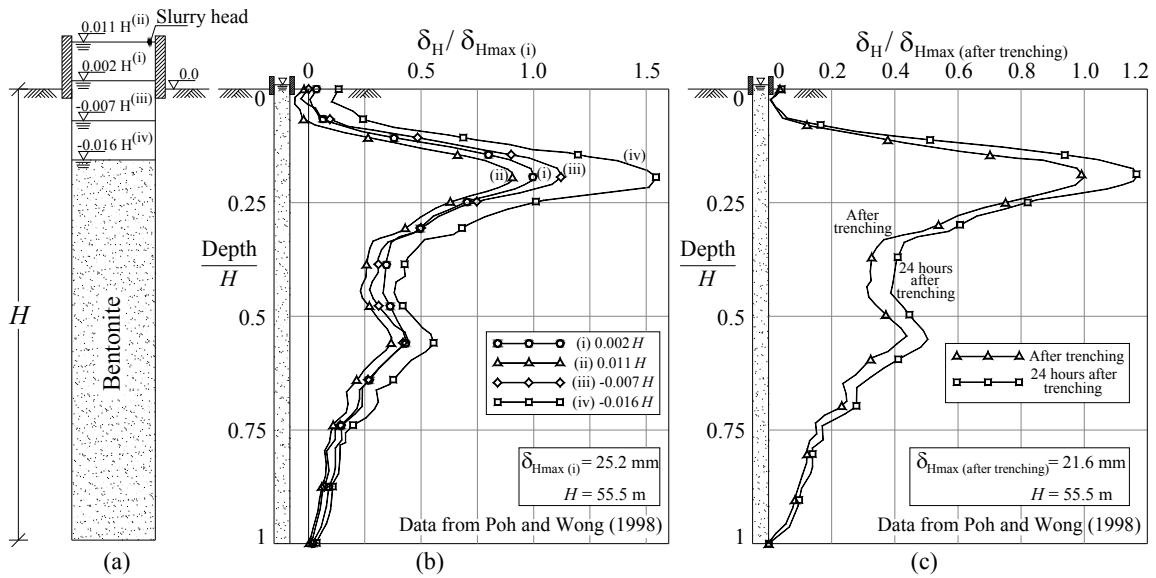
Figure 3.6 - (a) Slurry Heads; (b) Effects of Slurry Head Variation on Lateral Displacements; and (c) Effects of Holding Time on Lateral Displacements.

It can be seen in Figure 3.6.b that by increasing the slurry level, the lateral displacements decreased only slightly (approximately 10 percent), while decreasing the slurry level increases the lateral displacements by approximately 50 percent. From Figure 3.6.c, it can be seen that by increasing the holding time (i.e. time after the completion of the trench, but before concreting) only slightly increased the lateral soil movements (approximately 20 percent).

3.2.5 Design Aids

Figures 3.7 and 3.8 present settlement distributions and maximum horizontal ground movements due to wall installation, respectively. The figures show data calculated using the design aids presented by Thorley and Forth (2002) and by Ng and Lei (2003) (Section 2.6.4).

51

Also, measured data from several case histories previously presented in Section 2.6.1 is included in the figures. It can be seen in Figure 3.7 that there is a remarkable difference between the predicted and measured settlement distributions. Most likely, this is because the settlement distributions proposed by Thorley and Forth (2002) were estimated using empirical data from several excavations in Hong Kong. Consequently, they just apply to excavation sites on Hong Kong's soils or with similar characteristics. Figure 3.8 shows the horizontal displacements during the bentonite stage for the case history presented by Poh and Wong (1998) and compares it with the analytical solution proposed by Ng and Lei (2003) (Figure 2.17). In addition, it presents the required input parameters for the analytic calculations. The negative values in Figure 3.8 denote that the displacements are inward to the trench. In spite of the good correlation between the analytical and measured data, it has to be noted that the analytical solution fails in capturing the nonlinearity of the soil stress-strain behavior and the dependency of the soil stiffness to the stress history. Furthermore, it is only applicable to plane strain conditions and does not capture the three-dimensional nature of the problem.
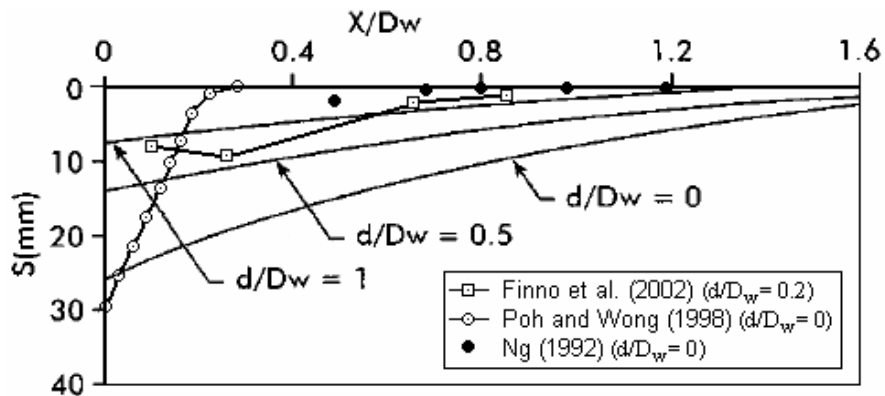
Figure 3.7 - Settlement Distribution Due to Wall Installation.

52
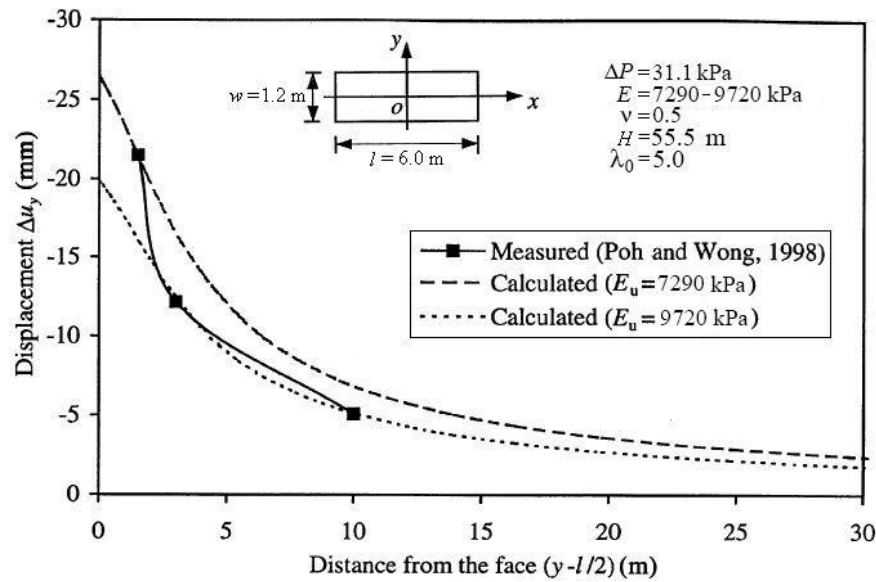
Figure 3.8 - Maximum Horizontal Ground Movements Due to Wall Installation (Adapted from Ng and Lei, 2003).

3.3   Wall Installation Finite Element Analysis of the Chicago and State Excavation

This section presents the results of the finite element analysis of the wall installation for the Chicago and State excavation case history reported by Bryson (2002), Finno and Bryson (2002), and Finno et al. (2002). Subsurface conditions, adjacent structures, and excavation support system are described in detail. This section also presents features and assumptions made in the finite element model and discusses on the several attempts to simulate the installation and behavior of the retaining wall.

3.3.1   Description of the Site

The Chicago Avenue and State Street Subway renovation project in Chicago, IL included the excavation of 12.2 m of soft to medium clay to expose the existing subway station and tunnels. Extensive monitoring of ground and structural movements associated with the excavation, to monitor the vertical movements of the adjacent school and to assess the potential for structural damage to the adjacent buildings, was performed. The adjacent

53

buildings of most concern were the Frances Xavier Warde School and the Holy Name Cathedral. The structural response of the Warde School to the excavation was of particular interest because of its close proximity to the excavation.

Figure 3.9 shows a plan view of the Chicago and State subway renovation project site including instrument locations, temporary wall types and strut locations. The temporary wall support along State Street consisted of two levels of tieback anchors and one level of cross-lot braces; and along Chicago Avenue, it consisted of just one level of cross-lot braces.
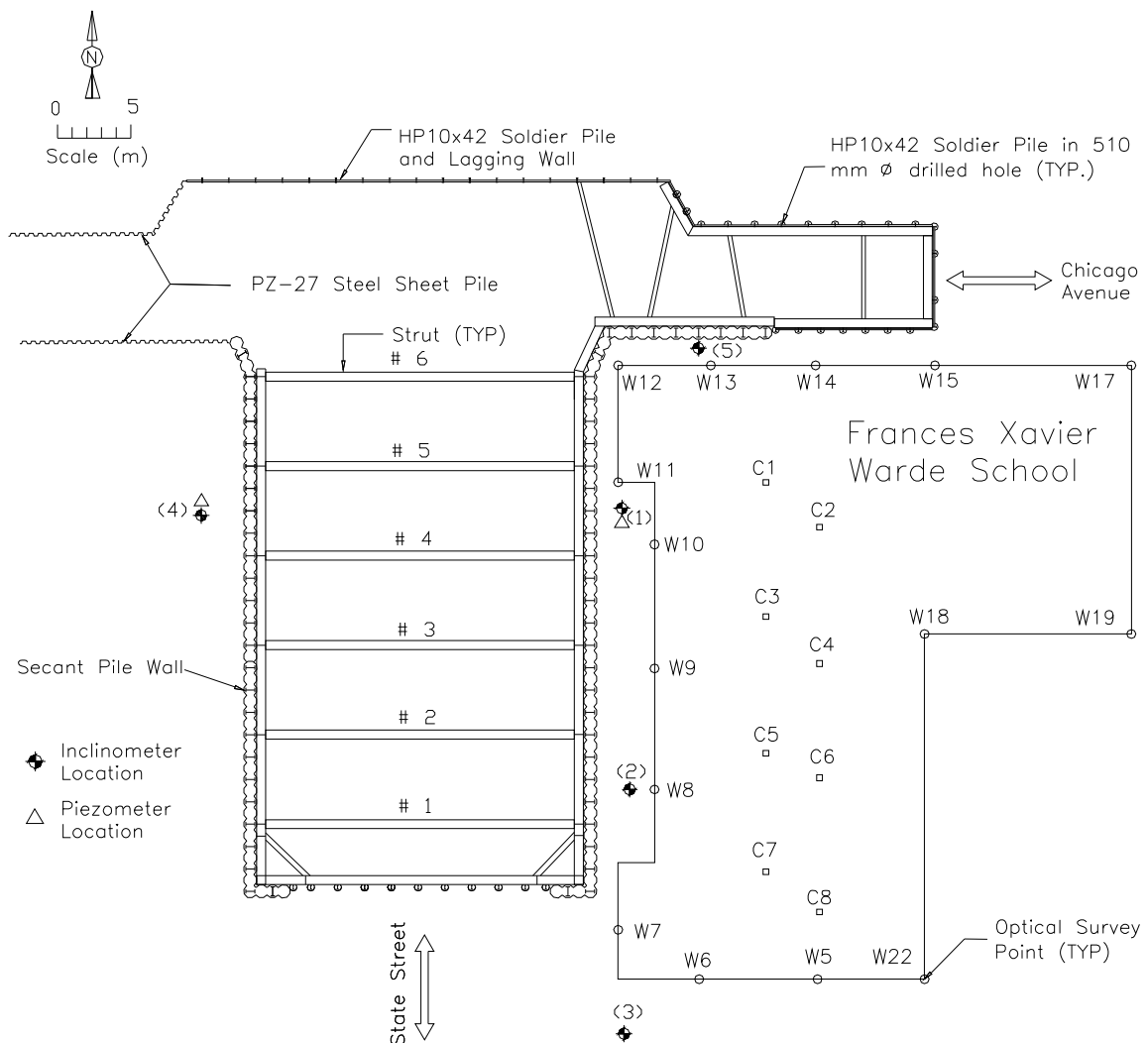
Figure 3.9 - Plan View of Excavation Site (After Bryson, 2002).

As shown in Figure 3.9, lateral movements of the soil behind the secant pile wall were recorded using five inclinometers located around the site. Vertical movements were obtained from optical survey points located along the outside walls of the school, on the roof, and on eight interior columns. Measurements of the different instruments were taken before the installation of the wall and at frequent intervals during construction.

Figures 3.10 and 3.11 show different views of the excavation site, support system, and exposed tunnel tubes. Figure 3.10 shows a detailed view of the secant pile wall with the struts and the two levels of tiebacks installed. Figure 3.11 was taken from the roof of the Frances Xavier Warde School (looking north) at the end of the excavation activities. Note that, because of the presence of the tunnel tubes, the final depth of the excavation was only reached in an 8-ft-wide trench beside the wall.

Figure 3.10 - Secant Pile Wall, Tiebacks, and Struts (After Bryson, 2002).

Figure 3.11 - Excavation Site (View from Roof of adjacent School) (After Bryson, 2002).

3.3.2 Site Specifications

The excavation along State Street was approximately 40-m-long and 24-m-wide and was advanced to an average final depth of 12.2 m. The excavation along Chicago Avenue was approximately 24-m-long and 7-m-wide and was advanced to a depth of 8.2 m.

3.3.2.1 Subsurface Conditions

Figure 3.12 shows the subsurface conditions, index properties, and undrained shear strengths obtained from both field and laboratory tests for the Chicago and State project site. It can be seen that the subsurface conditions consist of a fill deposit overlying a sequence of glacial clay deposits. The fill is mostly medium dense sand, but also contains construction debris. Four strata lie beneath the fill: (i) Blodgett, (ii) Deerfield, (iii) Park Ridge and (iv) Tinley. They are ice margin layers deposited underwater, and are distinguished by water content and undrained shear strength (Chung and Finno, 1992). The elevations in Figure 3.12 are given in terms of Chicago City Datum (CCD) where an elevation of 0 m CCD corresponds to the mean average level of Lake Michigan.

56

Bryson (2002) described the soils at the Chicago and State project site as primarily lightly overconsolidated glacial clays. The Blodgett stratum consists of a desiccated crust and underlying soft clays with undrained shear strengths that increase with depth. This stratum is characterized by a relatively wide range of water contents and liquid limits. The Deerfield stratum consists of medium stiff clay and is characterized by uniform water contents. The Park Ridge stratum is a stiff to very stiff clay with water contents lower than those recorded in the Deerfield stratum. The Tinley stratum underlies the ice margin deposits and consists of very stiff to hard clays and silts. The hard soils encountered below elevation -18.3 m are known locally as "hardpan."
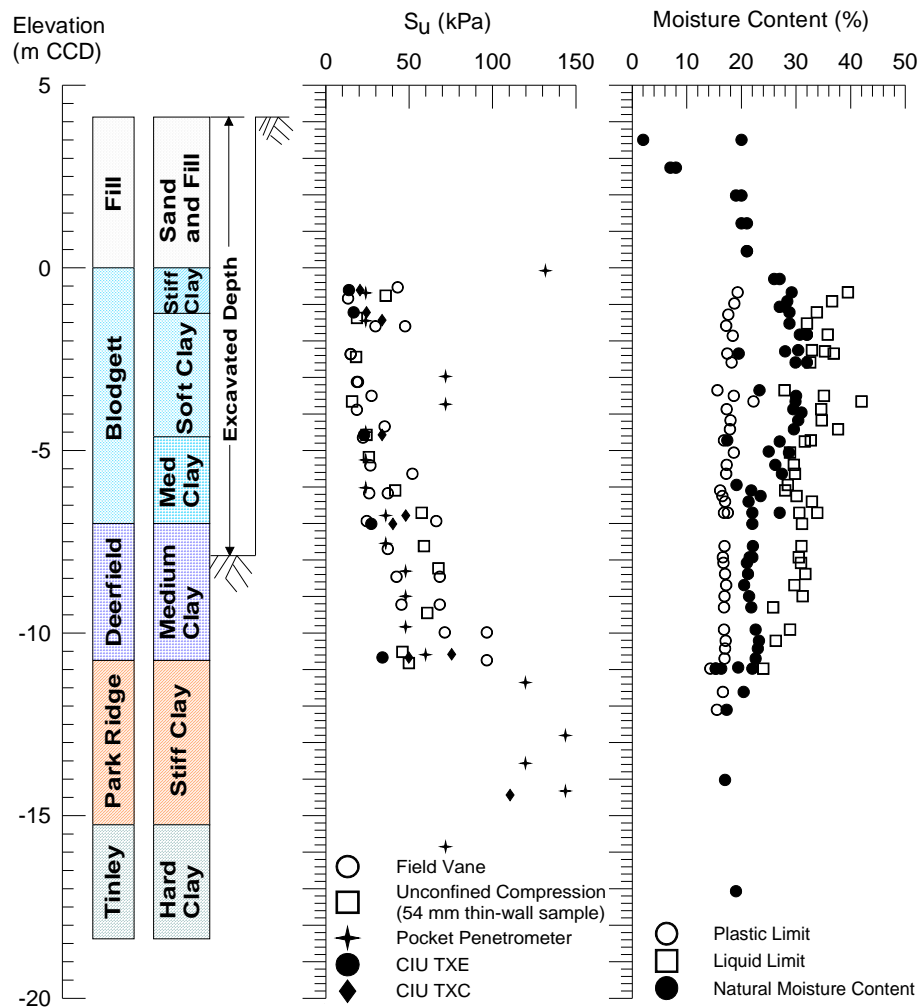
Figure 3.12 - Subsurface Profile (After Bryson, 2002).

3.3.2.2 Adjacent Structures

Two structures were directly related with the excavation, the Frances Xavier Warde School located approximately 2 m away from the excavation, and the Chicago and State Street subway tunnel-station located underground at a depth of -2.6 m CCD approximately. The effects of the Holy Name Cathedral, located approximately 15 m southeast of the excavation, were neglected because the recorded measurements throughout the project indicated that the excavation-related deformations at the cathedral were insignificant. See Bryson (2002) for a complete description of the adjacent structures.

The school is a 3-story reinforced concrete frame structure with a basement. The floor system at each level consists of a reinforced concrete pan-joist system supported by reinforced concrete beams. The beams are supported by concrete columns at interior locations and by masonry bearing walls around the perimeter. The bearing walls rest on a reinforced concrete foundation wall, which is supported by a 1.2-m-wide continuous footing at a depth of 4 m below ground surface. The interior columns are supported on spread footings. The continuous wall footings were located at 1.2 m from the excavation along State Street.

The subway station and tunnel were constructed between 1939 and 1941. Excavation was performed using the liner-plate tunneling method. The tunnel consists of twin subway tubes and passenger platforms and is symmetrical about its centerline. The tunnel travels in the north and south directions. Each tube is approximately 5-m-wide and 6-m-tall in the interior and each passenger platform is 2-m-wide and 5-m-tall in the interior. The bottom elevation of the tunnel is located at 9 m CCD. It was reported by Finno et al. (2002) that the existing subway tunnel increased the overall stability of the excavation because of its mass and stiffness.

58

3.3.2.3   Excavation Support System

Figure 3.13 shows an east-west cross-section of the excavation support system. The excavation support system consisted of a secant pile wall with three combined levels of support. The combined support was required because the 3-m-deep basement of the Warde School precluded using tiebacks for the first level and the presence of the tunnel did not permit the use of cross-lot supports for the second and third levels.
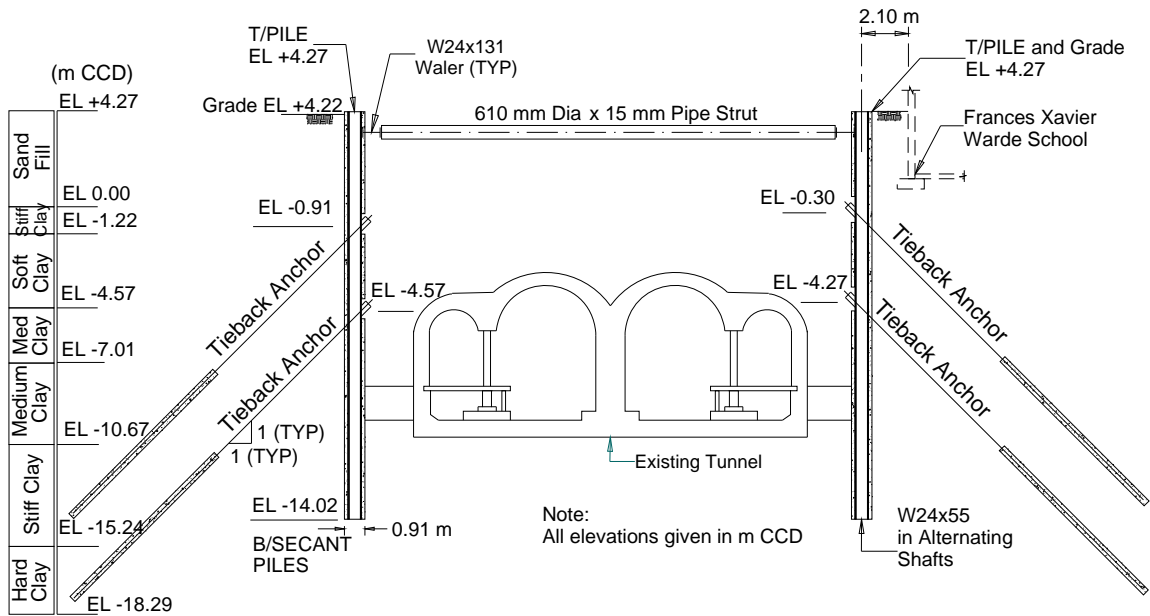
Figure 3.13 - Section View of Excavation Support System (After Bryson, 2002).

The retaining wall was constructed with overlapping 915-mm-diameter drilled shafts filled with concrete grout with a design unconfined compressive strength of 7 MPa. Each shaft overlapped adjacent shafts by 150 mm. W24×55 sections were placed in alternating shafts. The first level of support consisted of 610-mm-diameter steel pipe struts with a nominal wall thickness of 17 mm. The pipe struts were installed without preload at a depth of 0.6 m below ground surface and at a 6.1 m center-to-center horizontal spacing. Regroutable tieback anchors were used for the second and third levels of support. The 150-

mm-diameter tieback anchors were installed at 1.5 m center-to-center spacing and at 45°
angle with the bonded zone (9.1-10.7 m) located within the stiff and hard clays. Unbonded
lengths were at least 9.1 m. The regroutable tiebacks consisted of a bundle of four or five, 15
mm, 1860 MPa strands stressed to at least 1.3 times its design load, and subsequently
unloaded to 80% of its design load.

3.3.3   Finite Element Simulation

The problem was simulated using a complete three-dimensional model of the Francis
Xavier Warde School, the Chicago and State Street Subway Tunnel-Station, and the secant
pile wall. The finite element software PLAXIS 3D FOUNDATION was used to compute
the response of the soil around the secant pile wall. Figure 3.14 shows a schematic of the
PLAXIS input model. Details about the definition of the finite element problem, the
calculation phases, and the model parameters used in the simulation described herein can be
found in Appendix A.

The soil stratigraphy was assumed to be uniform across the site (see Figure 3.12). Seven
uniform soil layers were considered in the analysis: (1) a sand fill layer, (2) a clay crust, (3) a
soft clay layer named Upper Blodgett, (4) a medium clay layer named Lower Blodgett, (5) a
medium clay layer named Deerfield, (6) a stiff silty clay stratum known as Park Ridge, and (7)
a hard clay stratum. The Hardening Soil Model (Schanz et al., 1999) was used to represent
the elasto-plastic response of the clay soil layers while the sand fill and the clay crust layer
were modeled using the classical Mohr-Coulomb soil model. A complete description of the
Hardening Soil Model can be found in Appendix B.
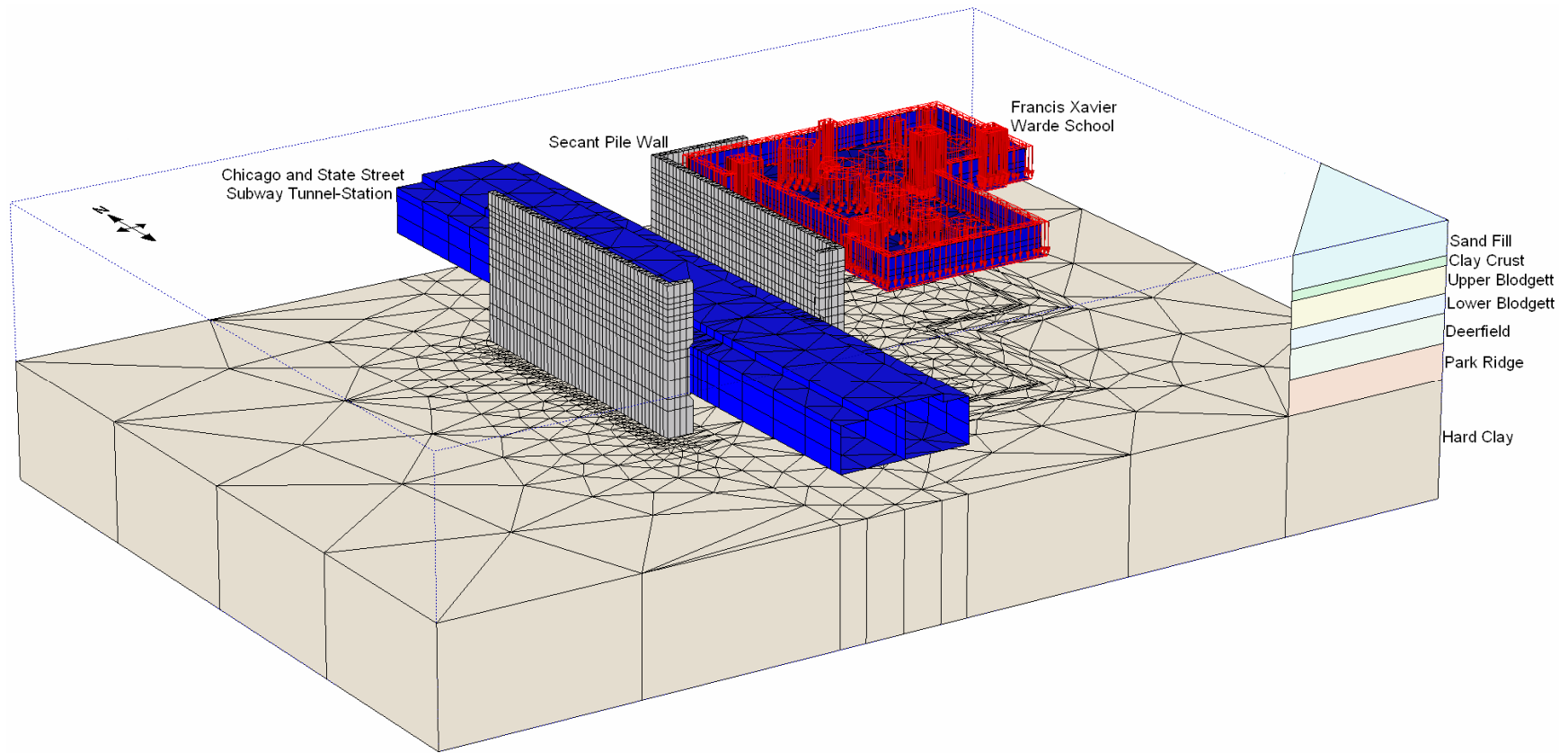
Figure 3.14 - Schematic of PLAXIS 3D FOUNDATION Input.

Francis Xavier
Warde School

Secant Pile Wall

Chicago and State Street
Subway Tunnel-Station

Sand Fill
Clay Crust
Upper Blodgett
Lower Blodgett
Deerfield
Park Ridge
Hard Clay

The model presented in Figure 3.14 was extended beyond the settlement zone of influence induced by the excavation (Hsien and Ou ,1998). The boundary conditions in the finite element model are set automatically by PLAXIS 3D FOUNDATION as: (i) vertical model boundaries with their normal in x-direction (i.e. parallel to the y-z-plane) are fixed in x-direction ($u_x = 0$) and free in y- and z-direction; (ii) vertical model boundaries with their normal in z-direction (i.e. parallel to the x-y- plane) are fixed in z-direction ($u_z = 0$) and free in x- and y-direction; (iii) vertical model boundaries with their normal neither in x- nor in z-direction (skew boundary lines in a work plane) are fixed in x- and z-direction ($u_x = u_z = 0$) and free in y-direction; (iv) the model bottom boundary is fixed in all directions ($u_x = u_y = u_z = 0$); and (v) the ground surface of the model is free in all directions.

3.3.3.1   Tunnel and School Construction Simulation

Calvello (2002), using a plane strain finite element analysis of the Chicago and State Street excavation, showed the importance of including the subway tunnel tubes and school basement adjacent to the excavation in the finite element model. For the present work, both structures were explicitly included in the three-dimensional finite element simulation of the problem to take into account their construction effects on the stress history of the surrounding soil.

Table 3.1 shows the PLAXIS calculation phases used for the simulation of the Chicago and State Street Subway Tunnel-Station and the Francis Xavier Warde School. In the table, the first column indicates the element that is being modeled, the second column shows the calculation phase number, the third column explains the purpose of the calculation phase, the fourth column indicates the calculation type, and the last column specifies the load input condition.

Table 3.1 - PLAXIS Calculation Phases (Tunnel and School).

Element	Phase	Identification	Calculation	Load Input
Initial stress field	0	Initial phase	K_0 procedure	Staged construction
Tunnel construction (late '30s)	1	Dry excavation and installation of temporary ribs	Plastic	Staged construction
	2	Installation of permanent liner	Plastic	Staged construction
	3	Plastic nil-step stage	Plastic	Staged construction
	4	Dewatering of the site	Plastic	Staged construction
	5	Consolidation for 19 years	Consolidation	Ultimate time
School construction (late '50s)	6	Reset displacements to zero (Plastic nil-step stage)	Plastic	Staged construction
	7	Stepped excavation for school and excavation of footings.	Plastic	Staged construction
	8	Place basement wall and footings Backfill surrounding soil	Plastic	Staged construction
	9	Activate school loads	Plastic	Staged construction
	10	Plastic nil-step stage	Plastic	Staged construction
	11	Consolidation for 40 years	Consolidation	Ultimate time

The initial phase calculates the initial situation of the project, i.e. the initial geometry configuration and the corresponding initial stress field. The initial stress state is calculated by means of the simplified procedure (K_0 procedure). The initial phase is the starting point for further calculations. However, deformations calculated in this phase are not considered to be relevant and are, by default, reset to zero at the beginning of the next calculation phase.

Plastic calculations are used to carry out elastic-plastic deformation analyses according to the small deformation theory. The stiffness matrix in a plastic calculation is based on the original undeformed geometry. For the simulation described herein, plastic calculations are always associated with staged construction loading conditions, which indicate changes in the geometric configuration of the finite element model. As expressed by Brinkgreve and Broere (2006), this type of calculation is appropriate in most practical geotechnical applications.

Plastic nil-step stages are calculation phases in which no additional loading is applied. They are required to solve large out-of-balance forces and to restore equilibrium. Such a

63

situation can occur after a calculation phase in which large loadings are activated. During these stages, neither geometry configuration nor water conditions are changed.

Consolidation calculations are used to analyze the development and dissipation of excess pore pressures in the saturated soil layers as a function of time. PLAXIS 3D FOUNDATION defines by default all the external model boundaries except for the ground surface, as closed (impermeable). As a result of this setting, excess pore pressures can only dissipate through the ground surface. Note that an "ultimate time" (load input condition) is specified to terminate a consolidation calculation. More details about calculation types and load input conditions can be found in the PLAXIS manual (Brinkgreve and Broere, 2006).

3.3.3.2   Secant Pile Wall Construction Simulation

The secant pile wall was constructed in two stages (see Figure 3.15.a). In the first stage, primary shafts were drilled to a deep of 18.3 m below ground surface (-14 m CCD). Then, a W24×55 section was placed and concrete grout was poured into the holes for completing the primary shafts. In the second stage, secondary shafts were drilled overlapping primary shafts by 150 mm on each side. Then, the holes were filled with concrete grout. It was reported by Bryson (2002) that excavation and posterior concrete grout filling for four shafts took approximately 24 hours.

The aforementioned wall installation procedure was simulated in two different ways. First, it was approximated as an excavated trench (Figure 3.15.b), where different dimensions and several excavation techniques such as: excavation under slurry head, excavation under hydrostatic pressure, and unsupported excavation were modeled (Figure 3.16). In the second way, the secant pile wall was modeled as adjacent rectangular slots (Figure 3.15.c) which closely resemble the actual sequence construction for the overlapping drilled shafts.

64
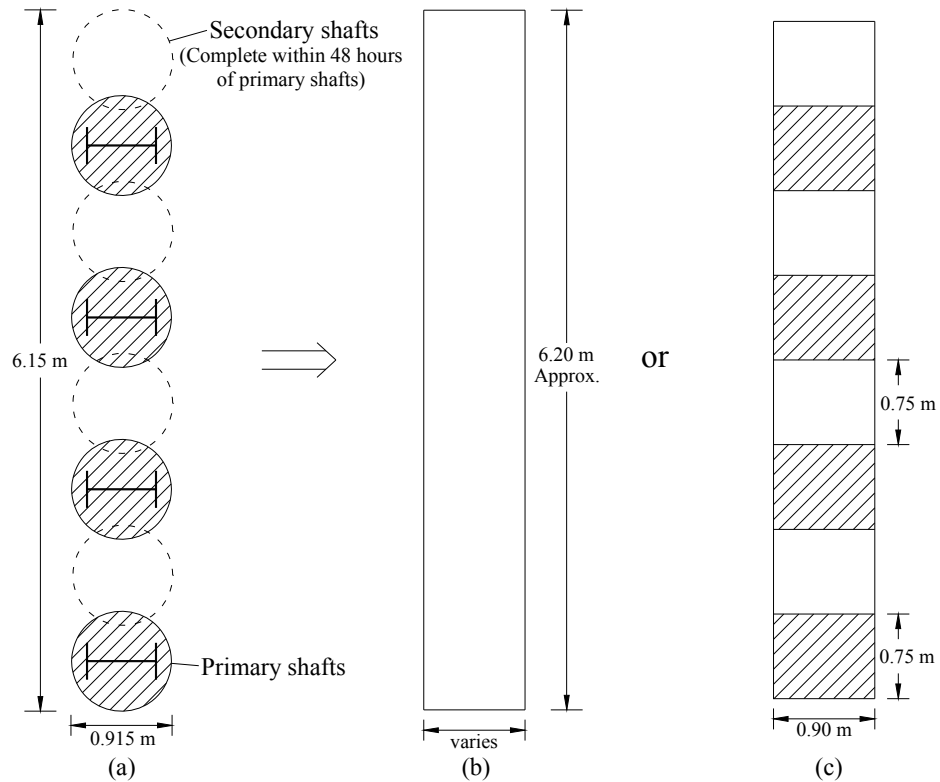
Figure 3.15 - Secant Pile Wall: (a) As Constructed; (b) Modeled as a Trench; and (c) Modeled as Adjacent Rectangular Slots.
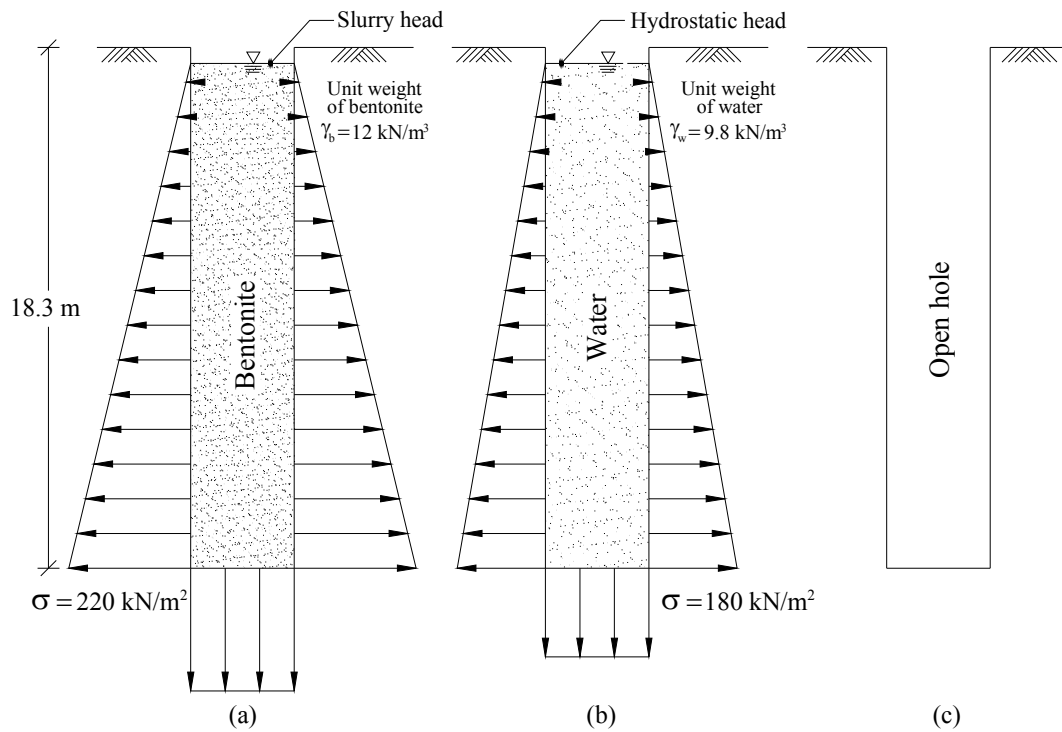
Figure 3.16 - Excavation Techniques: (a) Under Slurry Head; (b) Under Hydrostatic Pressure; and (c) Unsupported.

Tables 3.2 and 3.3 list the PLAXIS calculation phases used to simulate the wall installation using the trench and adjacent rectangular slot models, respectively. The simulation procedure for the trench model consisted principally of two steps. First, the excavation of the trench under slurry head or hydrostatic pressure is modeled by removing the soil inside the corresponding section and activating the loads that simulate the action of the fluid inside the trench (see Figure 3.16). Second, in the next calculation phase, the loads are deactivated and the corresponding trench sections filled with concrete grout. For the trench model using the unsupported excavation technique and for the adjacent rectangular slot model, the simulation procedure was quite similar to the previously described. However, for theses cases no loads were applied. It yielded to a simplify procedure that consisted of excavating and then filling with concrete grout.

In all of the phases listed in Tables 3.2 and 3.3, plastic calculations and staged construction load input types were used. No consolidation phases were included in the wall construction simulation because the wall installation speed reported by Bryson (2002) was relatively quick. The secant pile wall was installed along the entire east side and west side of the Warde School within 30 and 37 days, respectively; and the wall portion to the north of the Warde School was completed in 9 days. The inclusion of consolidation calculation phases during the wall construction simulation would have considerably increased the calculation time.

Figure 3.17 illustrates and numbers the wall sections employed to describe the construction sequence of the complete wall at the Chicago and State Street excavation. Figure 3.17.a shows a plan view of the secant pile wall as constructed while Figures 3.17.b and 3.17.c show the sections employed in the trench and adjacent rectangular slot models, respectively.

66

Table 3.2 - PLAXIS Calculation Phases for Wall Installation (Trench Model).

Phase	Excavation under slurry head and hydrostatic pressure		Unsupported excavation	
	Excavate to -14 m CCD and activate loads	Fill with concrete and deactivate loads	Excavate to -14 m CCD	Fill with concrete
12	Reset displacements to zero (Plastic nil-step stage)			
13	Section 1		Section 1	
14	Section 2	Section 1	Section 2	Section 1
15	Section 3	Section 2	Section 3	Section 2
16	Section 4	Section 3	Section 4	Section 3
17	Section 5	Section 4	Section 5	Section 4
18	Section 6	Section 5	Section 6	Section 5
19	Section 7	Section 6	Section 7	Section 6
20	Section 8	Section 7	Section 8	Section 7
21	Section 9	Section 8	Section 9	Section 8
22	Section 10	Section 9	Section 10	Section 9
23	Section 11	Section 10	Section 11	Section 10
24	Section 12	Section 11	Section 12	Section 11
25	Section 13	Section 12	Section 13	Section 12
26	Section 14	Section 13	Section 14	Section 13
27	Section 15	Section 14	Section 15	Section 14
28	Section 16	Section 15	Section 16	Section 15
29		Section 16		Section 16

Table 3.3 - PLAXIS Calculation Phases for Wall Installation (Adjacent Rectangular Slot Model).

Wall Portion	Phase	Excavate to -14 m CCD	Fill with concrete
	12	Reset displacements to zero (Plastic nil-step stage)	
East	13	Sections 2, 4, 6, and 8	
	14	Sections 10, 12, 14, and 16	Sections 2, 4, 6, and 8
	15	Sections 18, 20, 22, and 24	Sections 10, 12, 14, and 16
	16	Sections 26, 28, 30, and 32	Sections 18, 20, 22, and 24
	17	Sections 34, 36, 38, and 40	Sections 26, 28, 30, and 32
	18	Sections 42, 44, 46, and 48	Sections 34, 36, 38, and 40
	19	Sections 50, 52, and 54	Sections 42, 44, 46, and 48
	20	Sections 1, 3, 5, and 7	Sections 50, 52, and 54
	21	Sections 9, 11, 13, and 15	Sections 1, 3, 5, and 7
	22	Sections 17, 19, 21, and 23	Sections 9, 11, 13, and 15
	23	Sections 25, 27, 29, and 31	Sections 17, 19, 21, and 23
	24	Sections 33, 35, 37, and 39	Sections 25, 27, 29, and 31
	25	Sections 41, 43, 45, and 47	Sections 33, 35, 37, and 39
	26	Sections 49, 51, 53, and 55	Sections 41, 43, 45, and 47
West	27	Sections 57, 59, 61, and 63	Sections 49, 51, 53, and 55
	28	Sections 65, 67, 69, and 71	Sections 57, 59, 61, and 63
	29	Sections 73, 75, 77, and 79	Sections 65, 67, 69, and 71
	30	Sections 81, 83, 85, and 87	Sections 73, 75, 77, and 79
	31	Sections 89, 91, 93, and 95	Sections 81, 83, 85, and 87
	32	Sections 97, 99, 101, and 103	Sections 89, 91, 93, and 95
	33	Sections 105, 107, and 109	Sections 97, 99, 101, and 103
	34	Sections 56, 58, 60, and 62	Sections 105, 107, and 109
	35	Sections 64, 66, 68, and 70	Sections 56, 58, 60, and 62
	36	Sections 72, 74, 76, and 78	Sections 64, 66, 68, and 70
	37	Sections 80, 82, 84, and 86	Sections 72, 74, 76, and 78
	38	Sections 88, 90, 92, and 94	Sections 80, 82, 84, and 86
	39	Sections 96, 98, 100, and 102	Sections 88, 90, 92, and 94
	40	Sections 104, 106, and 108	Sections 96, 98, 100, and 102
North	41	Sections 110, 112, 114, and 116	Sections 104, 106, and 108
	42	Sections 118, 120, 122, and 124	Sections 110, 112, 114, and 116
	43	Sections 111, 113, 115, and 117	Sections 118, 120, 122, and 124
	44	Sections 119, 121, 123, and 125	Sections 111, 113, 115, and 117
	45		Sections 119, 121, 123, and 125

Chicago Avenue

Chicago Avenue

Chicago Avenue

State Street

State Street

State Street

(a)

(b)

(c)
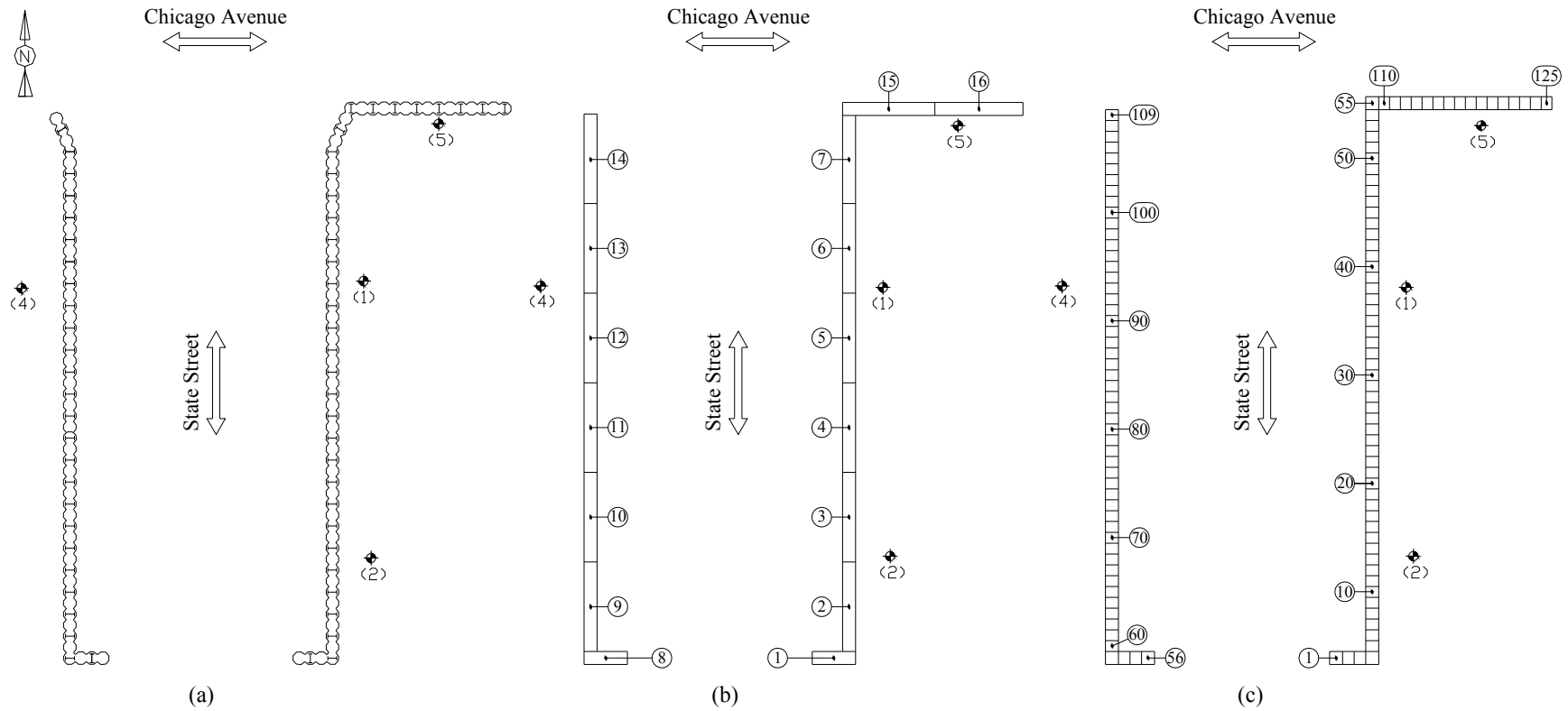
Figure 3.17 - Secant Pile Wall Sections: (a) As Constructed; (b) in Trench Model; and (c) in Adjacent Rectangular Slot Model.

3.3.4 Effects of Construction Techniques

In order to investigate the effects of excavation techniques employed in the construction of supporting walls on the lateral movements, three different construction techniques were analyzed: (i) excavation under slurry head, (ii) excavation under hydrostatic pressure, and (iii) unsupported excavation. The lateral pressures employed in the modeling of each case are presented in Figure 3.16. Unit weights of 12 and 9.8 kN/m^3 were assumed for the bentonite and water, respectively. The secant pile wall was modeled as a 0.9-m-wide, 18.3-m-deep, and approximately 6.2-m-long trench.

Figure 3.18 presents the results of the finite element analyses for the Chicago and State wall installation using the aforementioned excavation techniques. Lateral deformations at the end of wall installation are shown for inclinometer locations 1, 2, 4, and 5 (see Figure 3.9). For comparison, the inclinometer readings reported by Bryson (2002) are also included. Bryson (2002) reported that Inclinometer 5 was damaged during the installation of the wall. Consequently, the upper 4 m of the data reflects movements caused by impacts against the inclinometer casing and not lateral deformations of the soil resulting from wall installation. In Figure 3.18, positive lateral displacements represent movement toward the trench while negative values correspond to displacements in the direction of the soil mass.

As expected, the maximum lateral movement was obtained for the unsupported excavation case. It is because no lateral pressures were applied to the exposed trench faces during the calculation phases. Where lateral pressures were used (e.g., excavation under slurry head and hydrostatic pressure), negative values between approximately 0 and 10 m of depth were observed. Also, note that the maximum lateral deformation towards the trench decreases with increasing the unit weight of the supporting fluid.

70
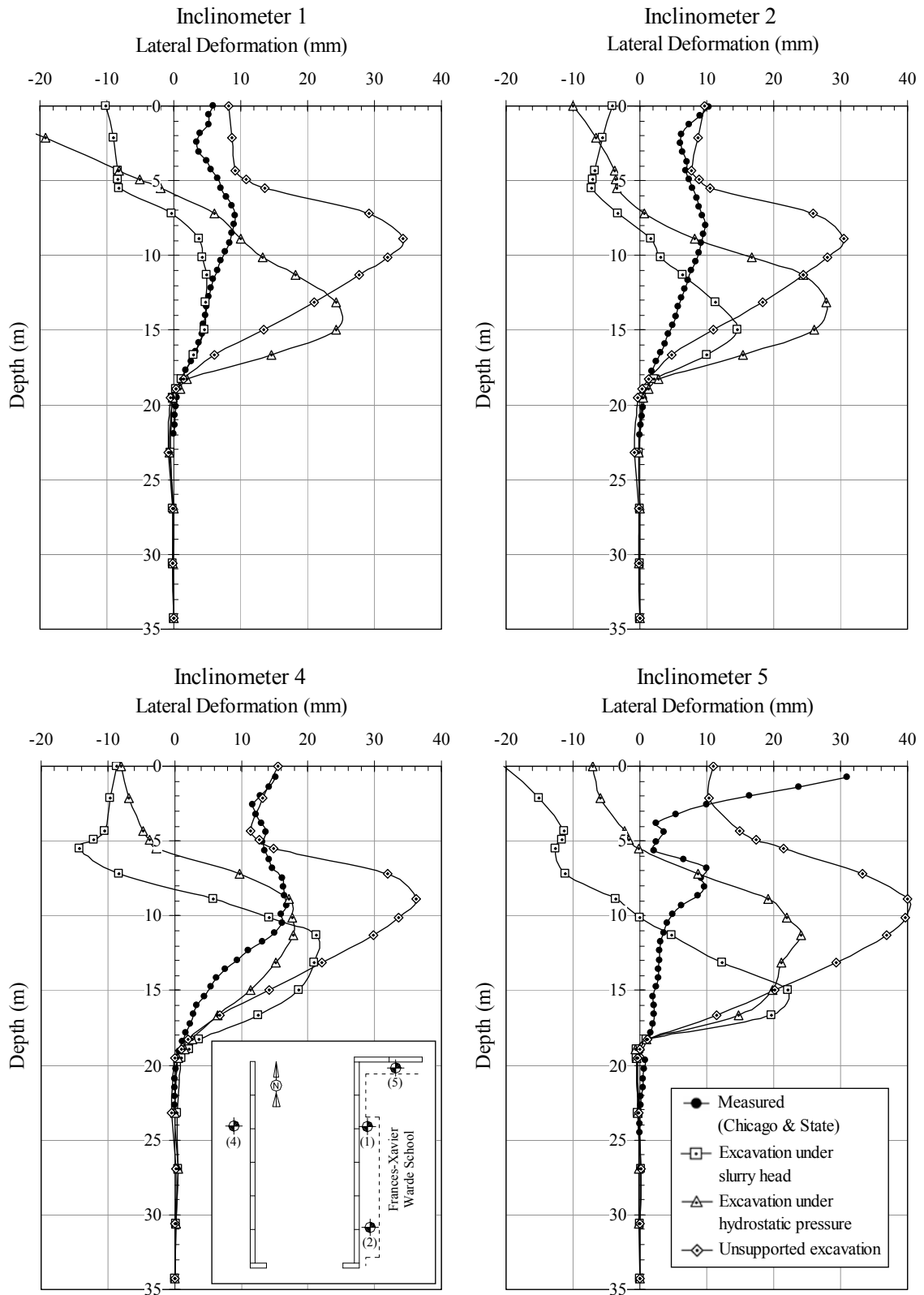
Figure 3.18 - Effects of Construction Techniques (0.9-m-wide, 18.3-m-deep, and approximately 6.2-m-long Trench Installation Sequence).

71

It can be seen in Figure 3.18 that the measured and unsupported excavation curves have the location of the maximum lateral movement very close (between 7.5 m and 9 m of depth). In addition, their curves are fairly similar for the upper 5 m of data in Inclinometers 1, 2, and 4. No comparisons can be made for the upper 4 m of Inclinometer 5 readings because, as explained earlier, it was damaged.

It is important to mention that for the Chicago and State wall installation and for the trench model both the wall configuration and construction method are quite different (see Figure 3.15). Consequently, only a rough comparison can be made between them.

3.3.5   Effects of Trench Dimensions

Figures 3.19 and 3.20 present the results of the finite element simulations intended for investigating the effects of trench dimensions on the lateral movements due to wall installation. Figure 3.19 shows the results of varying the trench width while Figure 3.20 illustrates the effects of varying the trench length. It can be seen in the figures that by reducing the width of the trench the lateral deformations are slightly decreased, but when the length of the trench is reduced, a remarkable diminution in the lateral deformations is observed. Note in Figure 3.20 that by reducing the trench length by 50 and 75 percent (3.0-m and 1.5-m-long trench, respectively) the lateral soil deformations are approximately reduced in 50 and 78 percent, respectively.

Although the sequence and wall configuration modeled for this case differ significantly from the actual ones, it is observed that the 1.5-m-long unsupported trench predicts quite closely the measured data for Inclinometers 1, 2, and 5. For Inclinometer 4, which is a free field inclinometer (i.e., not affected by the Warde School), the 3.0-m-long unsupported trench provides better results.

72

Inclinometer 1
Lateral Deformation (mm)

Inclinometer 2
Lateral Deformation (mm)

Inclinometer 4
Lateral Deformation (mm)

Inclinometer 5
Lateral Deformation (mm)

Measured (Chicago & State)

0.6-m-wide unsupported trech

0.75-m-wide unsupported trech

0.9-m-wide unsupported trech
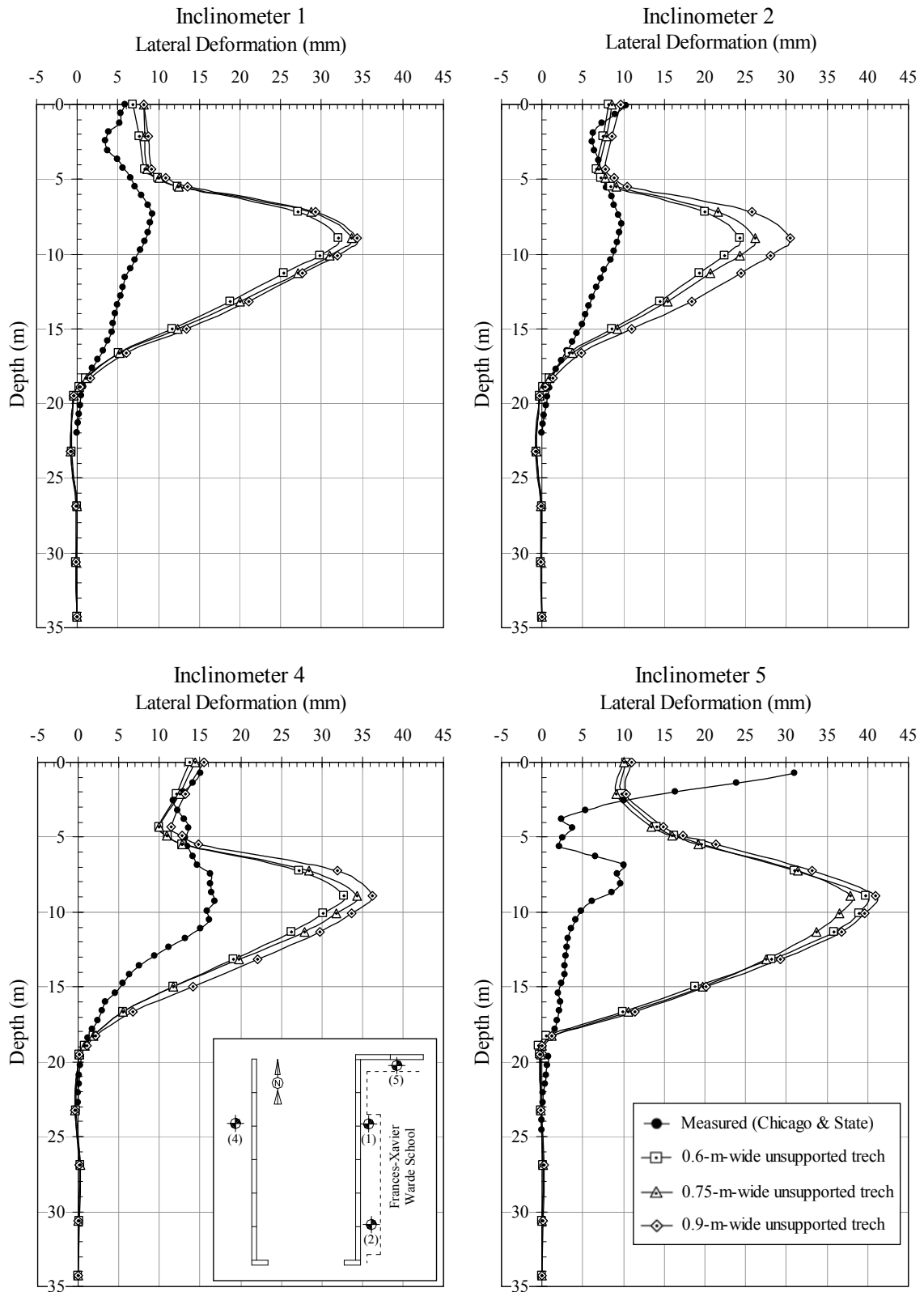
Figure 3.19 - Effects of Trench Dimensions (Variation of Width for an approximately 6.2-m-Long Trench Installation Sequence).

73
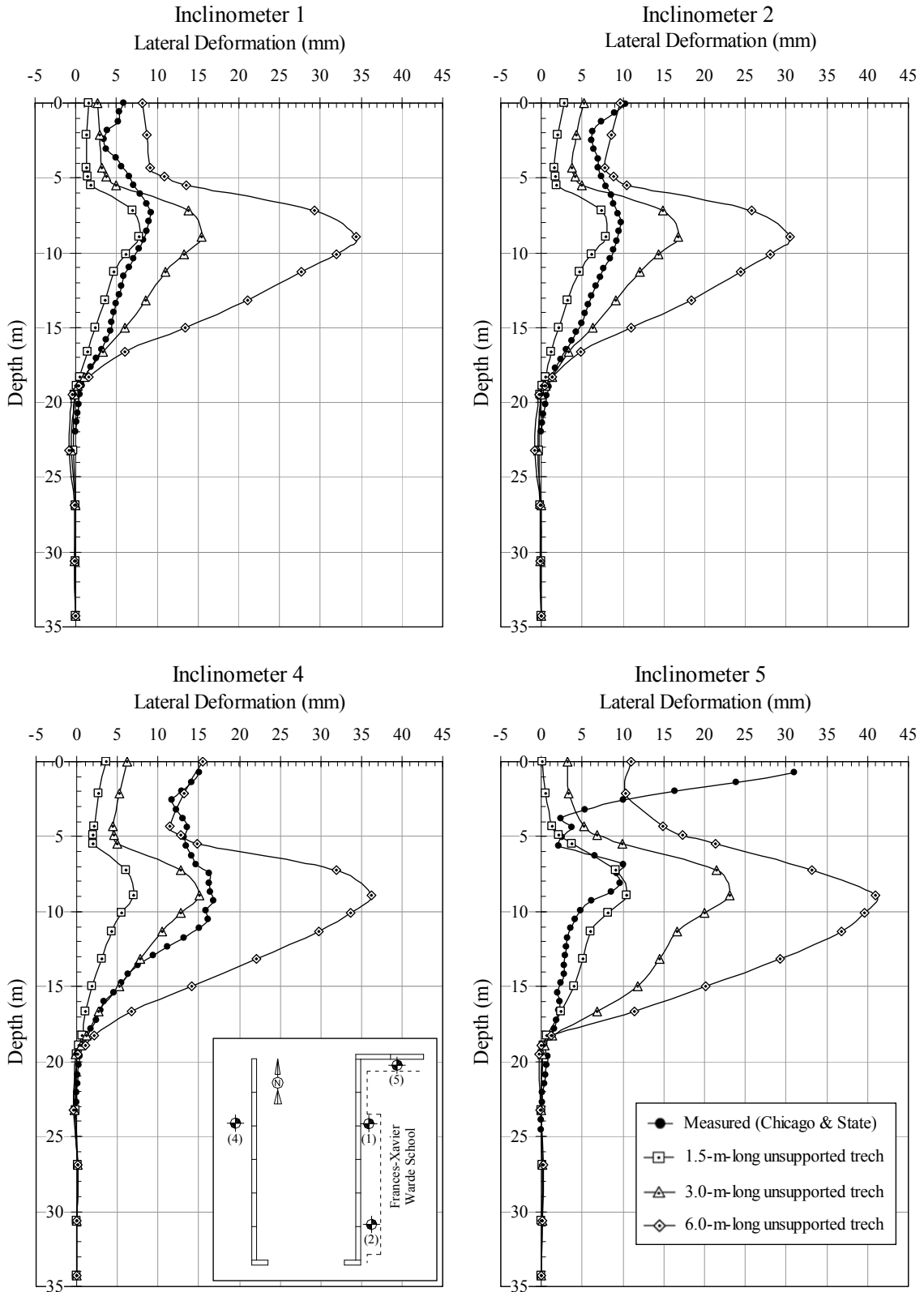
Figure 3.20 - Effects of Trench Dimensions (Variation of Length for a 0.9-m-Wide Trench Installation Sequence).

www.manaraa.com

3.3.6   Effects of Construction Sequencing

In order to investigate the effects of construction sequencing on the lateral deformations caused by the wall installation, the adjacent rectangular slot model (see Figure 3.15.c) was used. As presented earlier, it closely models the actual sequence construction and wall configuration of the Chicago and State Street secant pile wall. Three different sequences were modeled: (i) 4 slots per phase, (ii) half wall per phase, and (iii) whole wall per phase. The 4 slots per phase model was previously described in Table 3.3, the other two models are illustrated in Tables 3.4 and 3.5.

Table 3.4 - PLAXIS Calculation Phases for Half Wall per Phase Model.

Wall Portion	Phase	Excavate to -14 m CCD	Fill with concrete
	12	Reset displacements to zero (Plastic nil-step stage)	
East	13	Sections 2, 4, 6, to 28	
	14	Sections 30, 32, 34, to 54	Sections 2, 4, 6, to 28
	15	Sections 1, 3, 5, to 27	Sections 30, 32, 34, to 54
	16	Sections 29, 31, 33, to 55	Sections 1, 3, 5, to 27
West	17	Sections 57, 59, 61, to 83	Sections 29, 31, 33, to 55
	18	Sections 85, 87, 89, to 109	Sections 57, 59, 61, to 83
	19	Sections 56, 58, 60, to 82	Sections 85, 87, 89, to 109
	20	Sections 84, 86, 88, to 108	Sections 56, 58, 60, to 82
North	21	Sections 110, 112, 114, to 124	Sections 84, 86, 88, to 108
	22	Sections 111, 113, 115, to 125	Sections 110, 112, 114, to 124
	23		Sections 111, 113, 115, to 125

Table 3.5 - PLAXIS Calculation Phases for Whole Wall per Phase Model.

Wall Portion	Phase	Excavate to -14 m CCD	Fill with concrete
	12	Reset displacements to zero (Plastic nil-step stage)	
East	13	Sections 2, 4, 6, to 54	
	14	Sections 1, 3, 5, to 55	Sections 2, 4, 6, to 28
West	15	Sections 56, 58, 60, to 108	Sections 1, 3, 5, to 55
	16	Sections 57, 59, 61, to 109	Sections 56, 58, 60, to 108
North	17	Sections 110, 112, 114, to 124	Sections 57, 59, 61, to 109
	18	Sections 111, 113, 115, to 125	Sections 110, 112, 114, to 124
	19		Sections 111, 113, 115, to 125

75

Note in Tables 3.4 and 3.5 that the calculation phases used for modeling the north portion of the wall installation along the Chicago Avenue are the same for the half and whole wall per phase models. It is because the number of piles in the north wall is small compared with the number of piles for the east and west walls. Consequently, in order to keep the same construction rate along the wall installation process, the north wall was installed in only three calculation phases for the half and whole wall per phase sequences. This fact can be seen in the lateral deformations presented in Figure 3.21 for Inclinometer 5 where the lateral deformations for both sequences are basically the same.

Figure 3.21 shows the lateral deformations for the three aforementioned sequences. It was observed that for Inclinometer locations 1, 2, and 4, the whole wall per phase sequence gives lateral movements similar to the 6.0-m-long unsupported trench model presented in Figure 3.20. Note that for Inclinometer 5, the half and whole wall per phase sequences compares well with the 3.0-m-long unsupported trench.

As expected, the lateral deformations decreases as the excavate number of piles per phase is reduced. Note that for Inclinometers 1, 2, and 4, when the excavated number of piles is reduce to the half and 4 slots per phase, the maximum lateral deformations decrease by 10 to 20 percent, and by 65 to 75 percent, respectively. It was also expected that the 4 slots per phase model gave results in agreement with the measured data because it closely models the actual sequence construction, wall configuration, and installation velocity. However, for Inclinometer 4 it is not the case. Note that the lateral deformations given by the 4 slots per phase model are approximately 50 percent of the measured deformations. This is attributable to the fact that neither the tunnel nor the school were modeled in this case. Furthermore, as will be discussed in the next section, the soil model employed for the sand fill and clay crust layers has a significant effect on the final deformations.
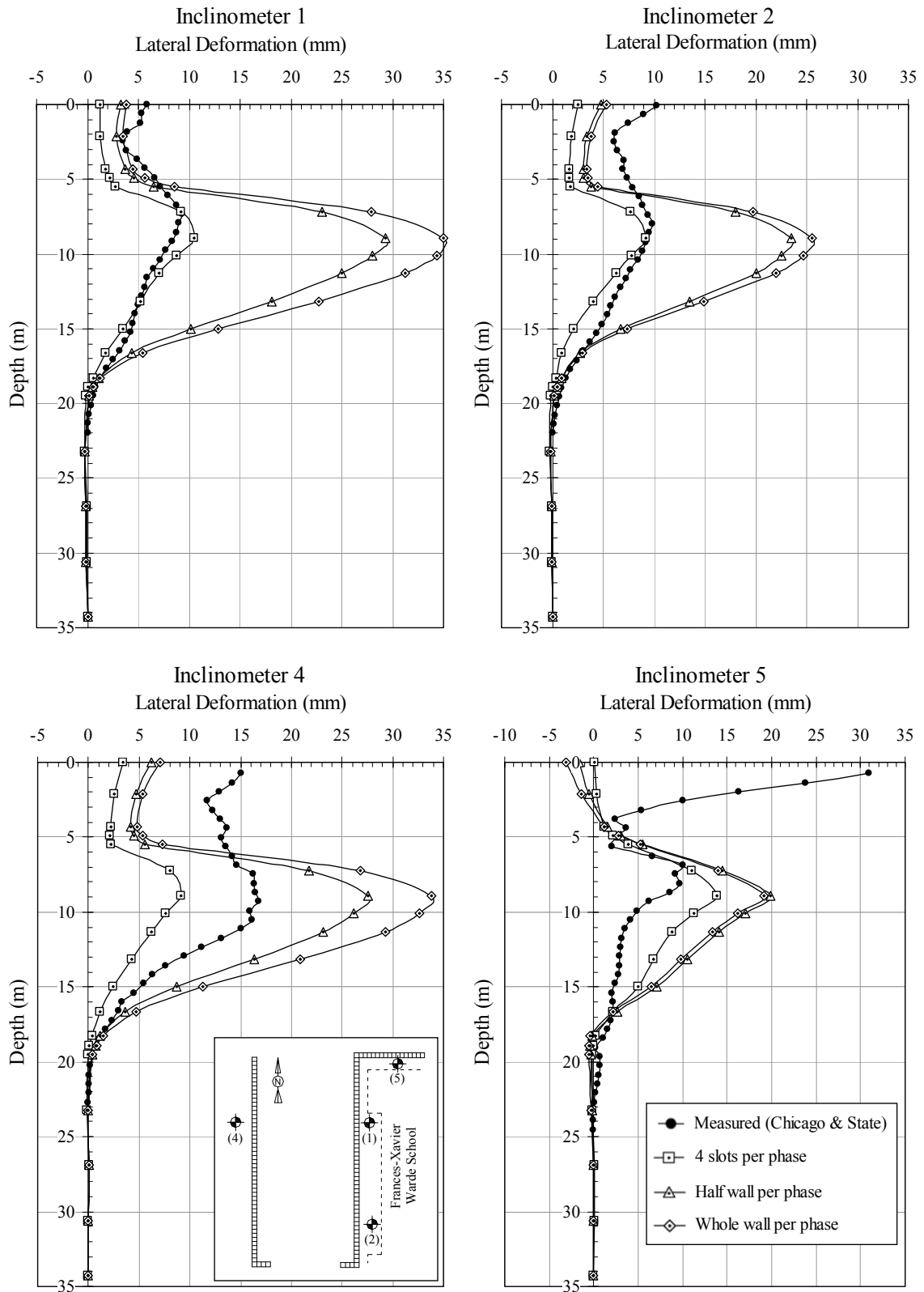
Figure 3.21 - Effects of Construction Sequencing (Adjacent Rectangular Slot Model).

3.3.7 Effects of Adjacent Structures and Soil Model

Figure 3.22 presents the results of the finite element simulations performed to investigate the effects of modeling adjacent structures and the effects of the employed soil model on the lateral deformation due to wall installation. For such purposes, three models were used: (i) a model that simulates the wall installation on free field conditions (i.e., no tunnel and school modeled); (ii) a complete model including the tunnel, school, and wall installation sequence using the Mohr-Coulomb soil model for the sand fill and clay crust layers; and (iii) a complete model using the Hardening Soil model for all of the layers. Table 3.6 list the Hardening Soil parameters employed in the third model for the sand fill and clay crust layers. These parameters were found by Blackburn (2005) using inverse modeling techniques at a different site in Chicago city. The other employed soil parameters can be found in Appendix A.

The effects of modeling the adjacent structures (tunnel and school) can be seen clearly in Inclinometers 1, 2, and 5. Note that the location of the maximum lateral movement moves up agreeing with the measured data. Furthermore, it is observed that within the clay layers, where the most reliable soil data was obtained, the predicted lateral deformations for Inclinometer 2, 4, and 5 are in better agreement when the tunnel and school structures are included in the model.

Note in Figure 3.22 that the model using the hardening soil parameters performed better in the west side of the excavation (Inclinometer 4) than in the east side (Inclinometer 1, 2, and 5). This is because the Hardening Soil parameters for the sand fill and clay crust layers were determined using inverse modeling techniques based on a site where free field conditions were predominant.

78
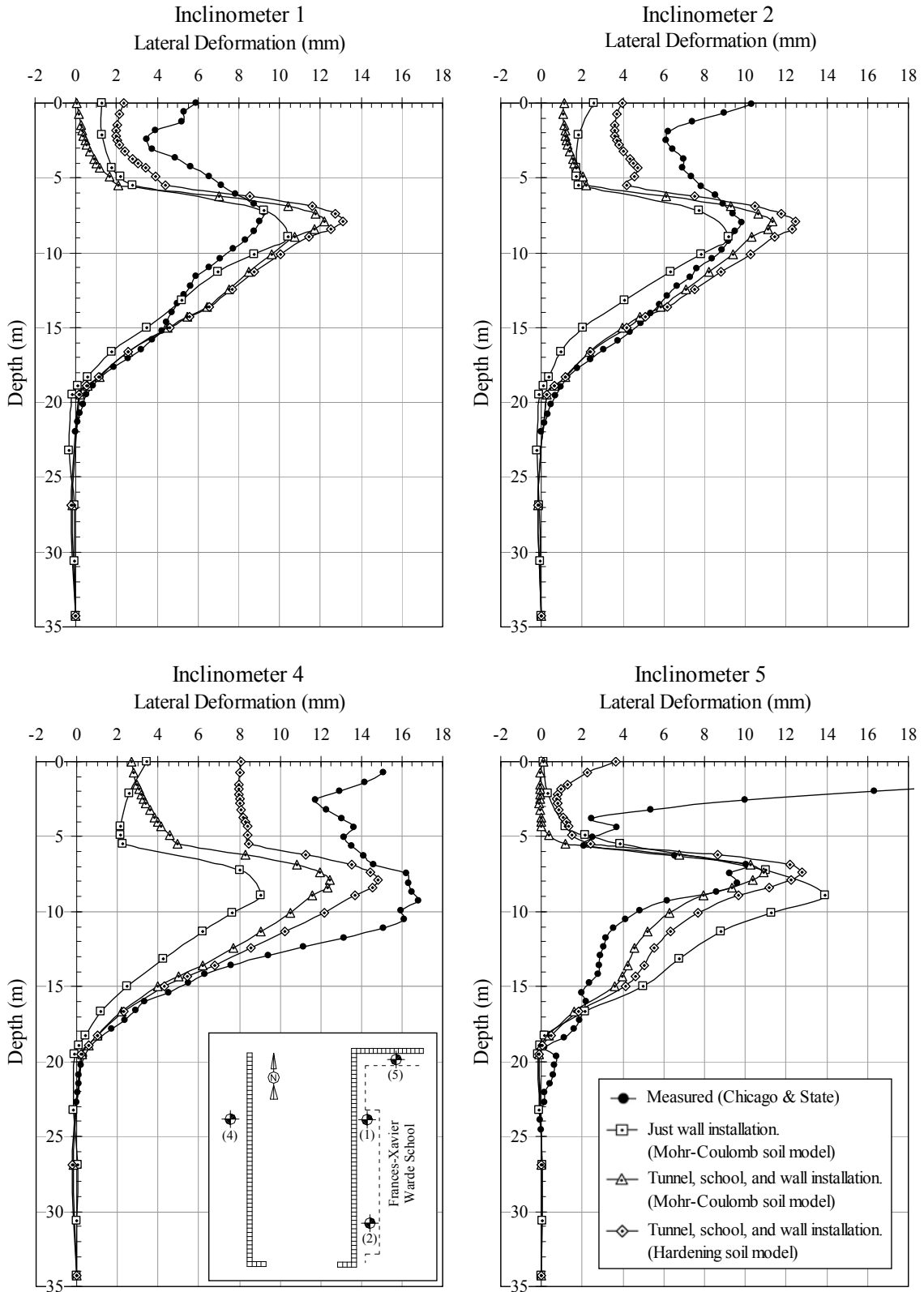
Figure 3.22 - Effects of Adjacent Structures and Soil Model (Adjacent Rectangular Slot Model).

79

Table 3.6 - Hardening Soil Parameters for Sand Fill and Clay Crust Layers (From Blackburn, 2005).

Hardening Soil Model		Sand Fill	Clay Crust
Type	[-]	Drained	Drained
γ_{unsat}	[kN/m³]	18.85	18.8
γ_{sat}	[kN/m³]	18.85	18.8
$k_x = k_z$	m/day	9.1	9.1
k_y	m/day	9.1	9.1
E_{50}^{ref}	[kN/m²]	7,185	14,370
E_{oed}^{ref}	[kN/m²]	7,185	14,370
E_{ur}^{ref}	[kN/m²]	21,555	43,110
c_{ref}	[kN/m²]	1	1
φ (phi)	[°]	37	40
ψ (psi)	[°]	5	15
υ_{ur}	[-]	0.2	0.2
p^{ref}	[kN/m²]	100	100
power (m)	[-]	0.5	0.5
K_0^{NC}	[-]	0.398	0.357
$c_{increment}$	[kN/m³]	0	0
y_{ref}	[m]	0	0
c_k	[-]	1.00E+15	1.00E+15
e_{init}	[-]	0.5	0.5
e_{min}	[-]	0	0
e_{max}	[-]	999	999
R_f	[-]	0.9	0.9
T-Strength	[kN/m²]	0	0
R_{interf}	[-]	1	1
$\delta - inter$	[m]	0	0

CHAPTER 4

4 THREE-DIMENSIONAL INFLUENCES OF SYSTEM STIFFNESS

4.1 Introduction

This chapter presents the three-dimensional effects that the support system stiffness has on the behavior and performance of deep excavations. First, the traditional methods presented in Section 2.4, which relate system stiffness with ground deformations, are compared with extensive excavation case history data available in the literature and with a new expanded database presented in Appendix C. In the second part of this chapter, the description and results of an extensive parametric study, carried out to overcome the deficiencies of the actual methods, are presented and a new design chart that includes the inherent three-dimensional nature of the excavation is proposed.

4.2 Evaluation of Traditional Methods

Currently, the most used design chart for predicting lateral movements in deep excavations is the proposed by Clough et al. (1989) (Figure 2.9). As presented in Section 2.4, the Clough et al. (1989) design chart allows the estimation of lateral movements in terms of effective system stiffness and the factor of safety against basal heave [Equation (2-26)]. In this section, this chart is compared with existing databases presented by Long (2001), Moormann (2004), and with an expanded database which includes complete data from soil, supporting system, and ground movements.

4.2.1 Existing Databases

The system stiffness is represented principally by three factors: (i) the bending stiffness of the retaining wall and supports; (ii) the configuration, location and distance of the struts;

and (iii) the embedment length of the retaining wall. Long (2001) and Moormann (2004) studied some of these parameters using databases of more than 296 and 530 case histories, respectively. They analyzed deep excavations mostly on cohesive soils and focused their empirical analyses in identifying relationships between the ground movements recorded, the support system employed, and the excavation method used.

In order to assess the validity and applicability of the Clough et al. (1989) design chart, Long (2001) and Moormann (2004), using the data from their respective databases, plotted maximum lateral deformation, normalized with respect to the excavation height, versus system stiffness and compared the result with the curves proposed by Clough et al. (1989) for different factors of safety against basal heave. Long (2001) differentiated the data by low and high factor of safety (see Figures 4.1 and 4.2, respectively), and Moormann (2004) differentiated it by soft and stiff ground (see Figures 4.3 and 4.4, respectively).

Long (2001), based on the information contained in Figures 4.1 and 4.2, concluded that the lateral deformations in stiff clays are largely independent of the system stiffness of the wall and supports as well as the kind of support employed. He noted that the system stiffness has a significant influence on the observed lateral deformations only for deep excavations in soft clays with a low factor of safety against basal heave, whereas for excavations in soft clays with an adequate factor of safety the dependency on the system stiffness becomes less relevant.

82
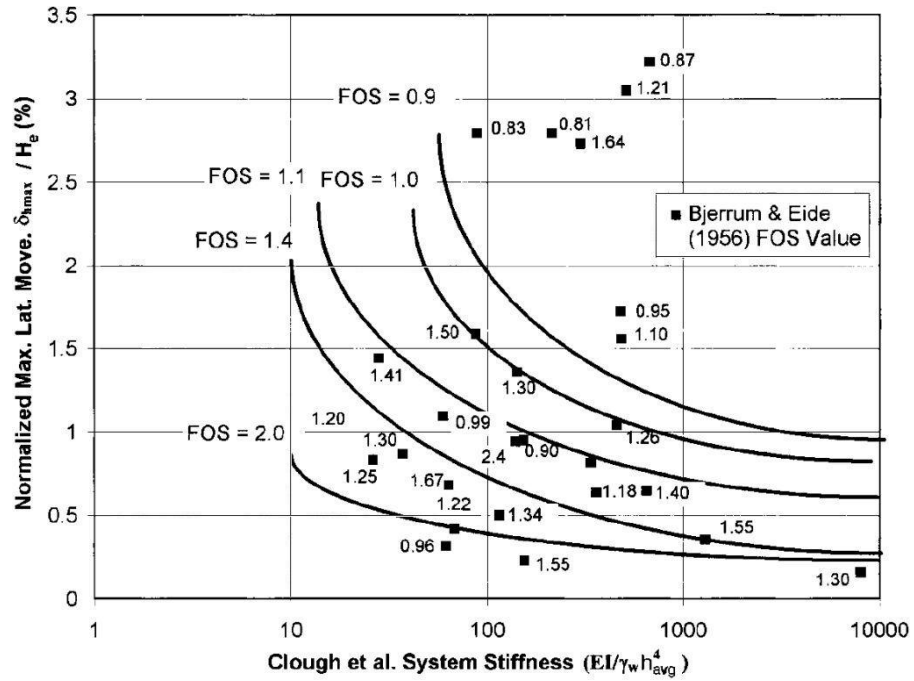
Figure 4.1 - Normalized Maximum Lateral Movement vs. System Stiffness for Propped Walls with Low FOS against Basal Heave (After Long, 2001).
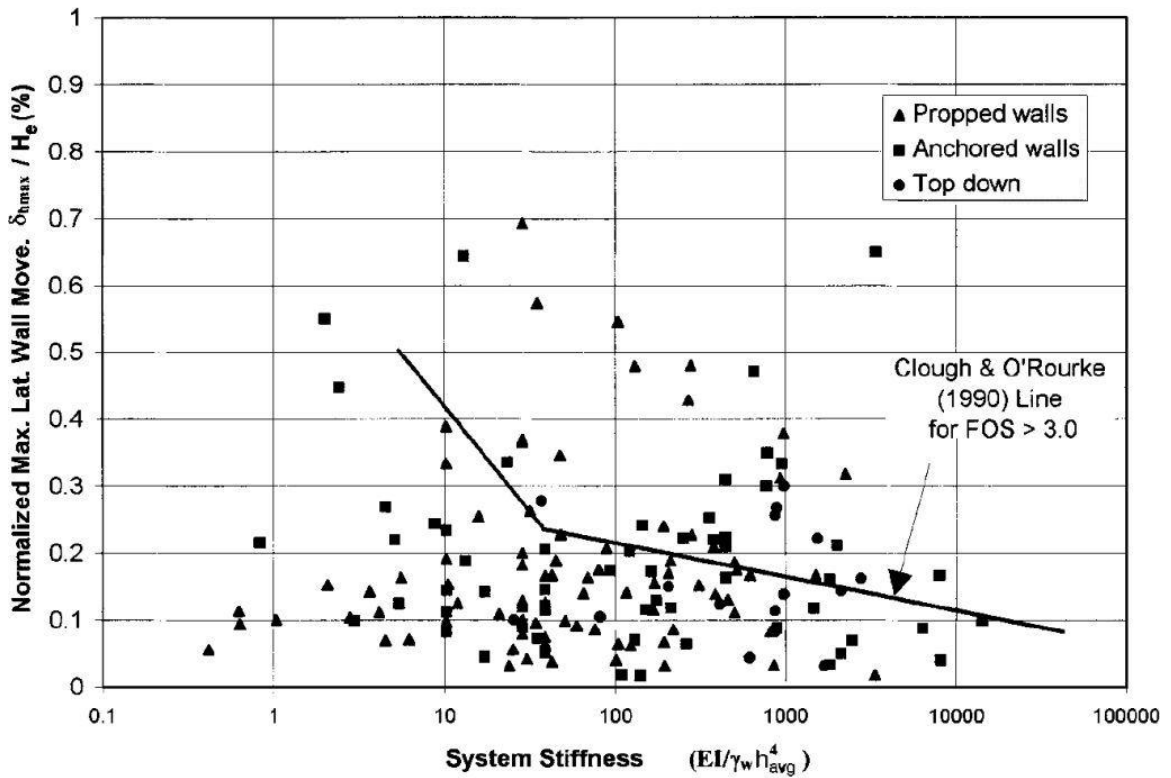
Figure 4.2 - Normalized Maximum Lateral Movement vs. System Stiffness for Walls with High FOS against Basal Heave (After Long, 2001).
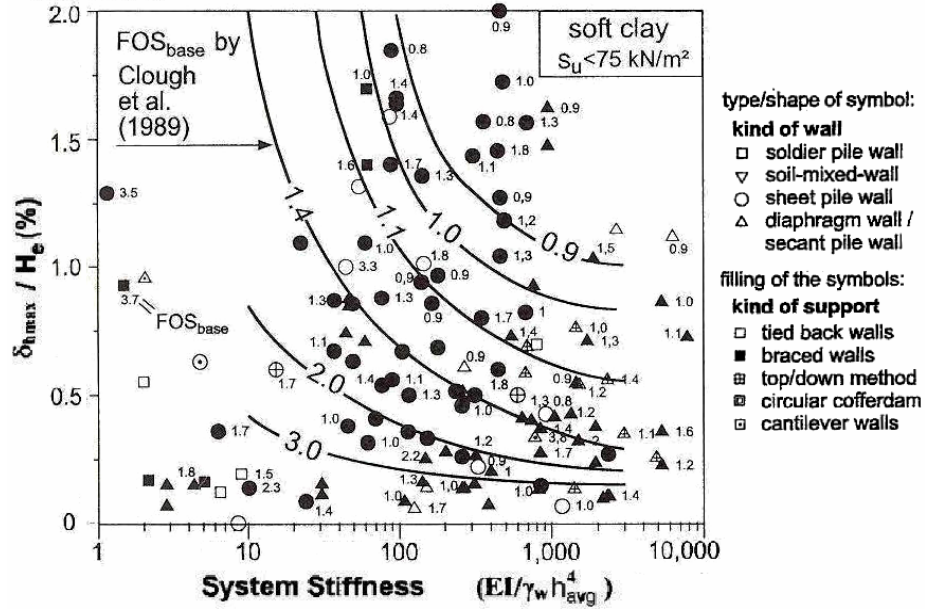
Figure 4.3 - Deep Excavations in Soft Ground: Maximum Horizontal Wall Displacement vs. System Stiffness (Adapted from Moormann, 2004).
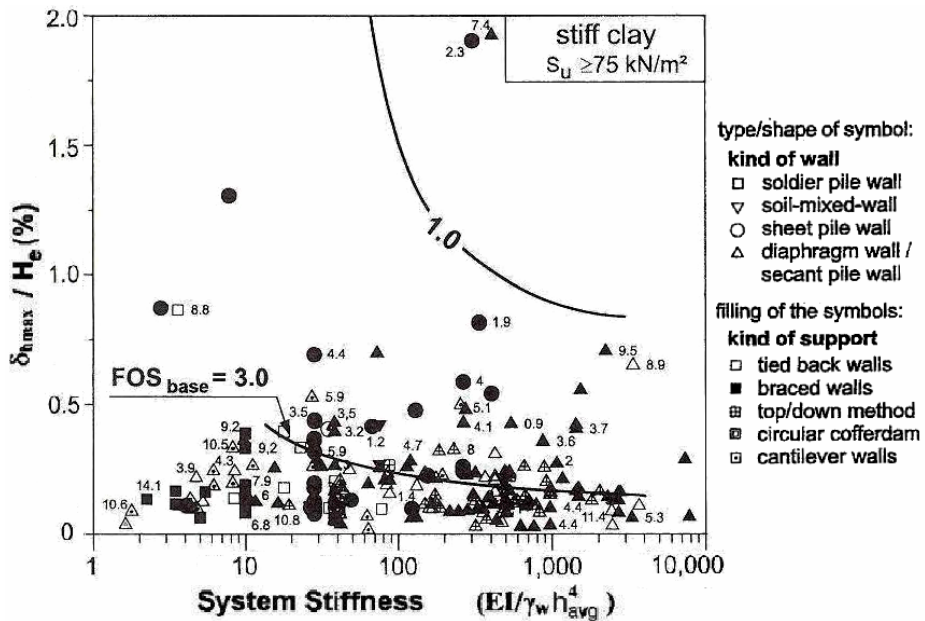
Figure 4.4 - Deep Excavations in Stiff Ground: Maximum Horizontal Wall Displacement vs. System Stiffness (Adapted from Moormann, 2004).

Moormann (2004), based on the results of his empirical study, concluded that the data for deep excavations in soft clays (Figure 4.3) scatter in a wide range. It is seen that there is not a clear dependency of the system stiffness factor proposed by Clough et al. (1989) on the

84

lateral wall displacements. For stiff clays (Figure 4.4), the results are similar to the ones presented by Long (2001) where the displacements are not influenced by the factor of safety against basal heave and their dependency on the system stiffness is not observed. Note that the limits of undrained shear strength, s_u, used by Moormann (2004) in Figures 4.3 and 4.4 for defining the soft and stiff clays (soft: $s_u < 75 \ kN / m^2$ and stiff: $s_u \geq 75 \ kN / m^2$) are different from the ones used in this work (see Section 4.2.2).

Figures 4.1 to 4.4 confirmed the Clough et al. (1989) design chart as an approach to roughly estimate the horizontal wall displacements in soft to medium cohesive soils where the factor of safety against basal heave is an important issue.

Moormann (2004) regarded the lack of dependency of lateral movements on system stiffness to factors like: (i) soil conditions at the embedment portion of the wall; (ii) ground water conditions; (iii) surrounding buildings or geometrically irregularities; (iv) workmanship; (v) unforeseen events and excavation sequence; (vi) pre-stressing of struts and anchors; and (vii) time-dependent effects. However, a quantification of all these factors is difficult because they are not reported and documented in detail in most cases. For this reason and because of the lack of information in the case histories presented by Long (2001) and Moormann (2004), an expanded database is needed for investigating the aforementioned factors that might influence the lateral movements in deep excavations.

4.2.2 Expanded Database

Table 4.1 presents the case histories that form the basics of the proposed database. The cases are distinguished by soil type based on the undrained shear strength (Stiff Clay, $s_u > 50 \ kPa$; Medium Clay, $25 \ kPa \leq s_u \leq 50 \ kPa$; and Soft Clay, $s_u < 25 \ kPa$) found at the dredge level of the excavation.

Table 4.1 - Case Histories for Own Database.

Soil	Case	Location	Reference
Stiff Clay	St1	Lion Yard Development, Cambridge	Ng (1992)
	St2	New Palace Yard Park Project, London	Burland and Hancock (1977)
	St3	Far-East Enterprise Center Project, Taipei	Hsieh and Ou (1998)
	St4	Oxley Rise Development, Singapore	Poh et al. (1997)
	St5	Central Insurance Building, Taipei	Ou and Shiau (1998)
	St6	Post Office Square Garage, Boston	Whittle et al. (1993)
	St7	National Taiwan University Hospital, Taiwan	Liao and Hsieh (2002)
	St8	Taipei County Administration Center, Taiwan	Liao and Hsieh (2002)
	St9	75 State Street, Boston	Becker and Haley (1990)
	St10	Smith Tower, Houston	Ulrich (1989)
Medium Clay	M1	Taipei National Enterprise Center (TNEC), Taiwan	Ou et al. (1998)
	M2	Robert H. Lurie Medical Building, Chicago (East Wall)	Finno and Roboski (2005)
	M3	Robert H. Lurie Medical Building, Chicago (West Wall)	Finno and Roboski (2005)
	M4	Taiwan Formosa, Taipei	Hsieh and Ou (1998)
	M5	Tokyo Subway Excavation Project, Japan	Miyoshi (1977)
	M6	HDR - 4 Project for the Chicago Subway	Finno et al. (1989)
	M7	Oslo Subway Excavation Project	NGI (1962)
	M8	Embarcadero BART Zone 1, San Francisco	Clough and Buchignani (1981)
	M9	Metro Station South Xizan Road, Shanghai	Wang et al. (2005)
	M10	Open Cut in Oslo	Peck (1969)
Soft Clay	So1	Chicago and State Street Excavation, Chicago	Finno et al. (2002)
	So2	Mass Rapid Transit Line, Singapore	Goh et al. (2003)
	So3	Deep Excavation adjacent to the Shanghai Metro Tunnels	Hu et al. (2003)
	So4	Excavation in Downtown Chicago	Gill and Lukas (1990)
	So5	Peninsula Hotel Project, Bangkok	Teparaksa (1993)
	So6	AT&T Corporate Center, Chicago	Baker et al. (1989)
	So7	Museum of Science and Industry Parking Garage, Chicago	Konstantakos (2000)
	So8	One Market Plaza Building, San Francisco	Clough and Buchignani (1981)
	So9	Sheet Pile Wall Field Test, Rotterdam	Kort (2002)
	So10	MUNI Metro Turnback Project, San Francisco	Koutsoftas et al. (2000)

Note that 10 case histories are presented for each soil type, giving a total of 30 case histories. For further information about subsurface soil conditions, geometry characteristics, excavation support system details, raw inclinometer data, and maximum ground movements for each of the case histories, see Appendix C.

Tables 4.2, 4.3 and 4.4 summarize the geometric (H, H_e, and B), soil (γ_s and s_u), and support system (t, S_V, S_H and, EI) parameters for the case histories on stiff, medium and soft clay, respectively. In addition, the maximum horizontal wall movement and the maximum vertical ground settlement recorded at the end of excavation are presented. The last two columns of Tables 4.2 to 4.4 show the factors of safety against basal heave calculated using Equations (2-26) and (2-27) (i.e., with and without wall embedment depth included, respectively). It can be seen that for excavations in soft to medium clays, the inclusion of the wall embedment depth generally increases the factor of safety against basal heave. In contrast, for excavations in stiff clays, the wall embedment depth has no significant contribution to the stability of the excavation system.

Figure 4.5 compares the Clough et al. (1989) design chart with the aforementioned excavation case histories. In Figure 4.5.a, the case histories are grouped by soil type (stiff, medium, and soft clay). It is fairly similar to the way that Long (2001) and Moormann (2004) presented their data. However, it is noted in Tables 4.2 to 4.4 that the ranges of factor of safety for each soil type are quite large (stiff, $1.0 \leq FS \leq 7.5$; medium, $0.6 \leq FS \leq 1.2$; and soft, $0.2 \leq FS \leq 1.3$), and consequently no direct comparisons can be made based on Figure 4.5.a. Conversely, Figure 4.5.b, presents the data distinguishing by factor of safety against basal heave ($FS < 1.0$, $1.0 \leq FS < 1.4$, $1.4 \leq FS < 3.0$, and $FS \geq 3.0$). Note that the data is much easier to visualize and therefore more accurate conclusions can be drawn.

It can be seen in Figure 4.5 that for excavations with factors of safety less than 1.0 and between 1.0 and 1.4 the Clough et al. (1989) design chart shows a considerable discrepancy between the predicted and the measured values of maximum lateral deformation. Note that for excavations in soft to medium clay it generally overpredicts the horizontal wall movements. For excavations in stiff clay with a factor of safety between 1.4 and 3.0, the

chart gives better results. However, the data still scatter. It is for the case of excavations in stiff clay with a factor of safety greater than 3.0, where as explained by Clough and O'Rourke (1990) the wall stiffness and support spacing have a small influence on the predicted movements, that the measured and predicted lateral wall movements agree the best.
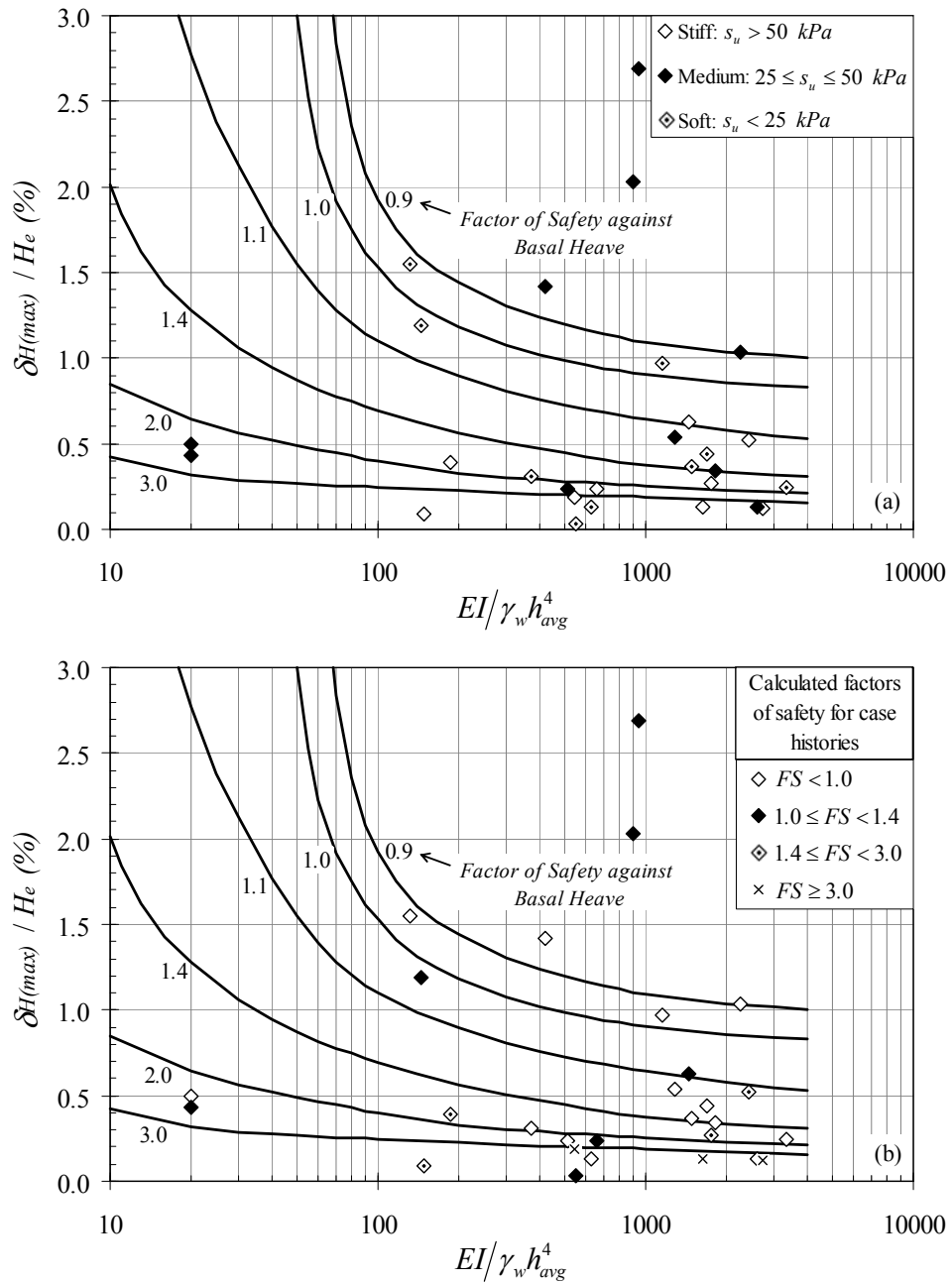
Figure 4.5 - Comparison of Database Case Histories with Clough et al. (1989) Design Chart.

As presented in Section 2.4, the ground movement behavior in deep excavations is highly dependent of the three-dimensional nature of the excavation, the effects of the wall construction, the effects of different support types, the influences of the excavation geometry and sequencing, and the wall embedment depth below the base of excavation. Note that none of these factors were included in the analyses performed by Clough et al. (1989) and as a result the values given by their design chart do not agree with the measured lateral wall movements of the case histories. In conclusion, the Clough et al. (1989) design chart, where the system stiffness ($EI/\gamma_w h_{avg}^4$) and the factor of safety against basal heave given by Equation (2-26) are the only control parameters, must be used just as an approach to roughly estimate the horizontal wall displacements in soft to medium cohesive soils at the early stages of the design and not as a design tool to calculate the final movements in deep excavations where sensitive structures are nearby.

89

Table 4.2 - Case Histories in Stiff Clay.

Case	Wall Type	t (m)	H (m)	H_e (m)	B (m)	S_V (m)	S_H (m)	γ_s (kN/m³)	s_u (kPa)	EI (kN-m²/m)	$\delta_{H(max)}$ (mm)	$\delta_{V(max)}$ (mm)	$\delta_{H(max)}/H$ (%)	$\delta_{H(max)}/H_e$ (%)	$EI/(\gamma_w h^4_{avg})$	FS Eq. (2-26)	FS Eq. (2-27)
St1	Diaph.	0.6	16.3	9.6	45	3.2	1.5	20	120	558000	17.66	10.13	0.108	0.185	543.01	4.40	3.73
St2	Diaph.	0.9	30.0	18.5	18.5*	3.2	3.2*	20	170	1676700	24.06	19.53	0.080	0.130	1631.66	7.48	3.99
St3	Diaph.	0.9	33.0	20.0	63.8	3.3	3.3*	19	76.5	1676700	124.76	77.76	0.378	0.624	1442.69	1.26	1.26
St4	Diaph.	0.6	14.0	11.1	33	4.3	6	20.75	80*	500000	10.02	NA	0.072	0.090	149.23	2.37	2.05
St5	Diaph.	0.6	23.0	11.4	33.7	3.3	3.3*	19.7	50	216000	44.53	NA	0.194	0.391	185.85	1.42	1.51
St6	Diaph.	0.9	25.6	20.2	61	3	3*	20.24	91	1397250	53.61	45.00	0.209	0.265	1760.20	1.42	1.32
St7	Diaph.	0.8	27.0	15.7	140	2.65	1.92	20	77.5	1177600	81.37	NA	0.301	0.518	2436.62	1.46	1.38
St8	Diaph.	1.2	38.0	20.0	93	2.33	1.85	20	65	3974400	54.30	NA	0.143	0.272	13760.11	0.97	0.99
St9	Diaph.	0.75	26.0	20.0	45.7	3.35	3*	18	70	815625	47.26	101.60	0.182	0.236	660.82	1.26	1.21
St10	Secant	0.75	20.0	12.2	36.6	2.45	2.45*	20.1	140	970313	14.75	NA	0.074	0.121	2748.03	4.45	3.62

Diaph. means diaphragm.

* assumed values. B was assumed equal to H_e and S_H was assumed equal to S_V.

Table 4.3 - Case Histories in Medium Clay.

Case	Wall Type	t (m)	H (m)	H_e (m)	B (m)	S_V (m)	S_H (m)	γ_s (kN/m³)	s_u (kPa)	EI (kN-m²/m)	$\delta_{H(max)}$ (mm)	$\delta_{V(max)}$ (mm)	$\delta_{H(max)}/H$ (%)	$\delta_{H(max)}/H_e$ (%)	$EI/(\gamma_w h^4_{avg})$	FS Eq. (2-26)	FS Eq. (2-27)
M1	Diaph.	0.9	35.0	19.7	40	3.4	slab	18.9	50	1676700	106.51	77.18	0.304	0.541	1280.31	0.84	0.96
M2	Sheet	NA	16.5	10.0	68	4	2.29	19	36	50400	43.23	NA	0.262	0.432	20.09	1.12	1.08
M3	Sheet	NA	19.0	12.8	68	4	2.29	20	36	50400	63.48	74.00	0.334	0.496	20.09	0.83	0.80
M4	Diaph.	0.8	31.0	18.4	35	2.85	2.85*	19	47.5	1177600	62.61	43.16	0.202	0.340	1821.35	0.86	0.97
M5	S-C.	0.8*	32.0	17.0	30	2.7	2.7*	19	42	1177600	176.56	152.42	0.552	1.039	2261.08	0.83	0.99
M6	Sheet	NA	19.2	12.2	12.2	2.5	2.5*	19	30	161000	172.64	255.70	0.899	1.415	420.57	0.90	1.10
M7	Sheet	NA	16.0	11.0	11	1.7	1.7*	19	30	73800	223.58	200.00	1.397	2.033	901.64	1.03	1.16
M8	Diaph.	1	30.5	21.3	21.3*	3	3*	17	44	2083333	28.25	NA	0.093	0.133	2624.51	0.84	0.98
M9	Diaph.	0.8	38.0	20.6	22.8	4	3	18	35	1280000	48.12	30.90	0.127	0.234	510.20	0.61	0.85
M10	Sheet	NA	14.0	8.5	11	1.68	1.68*	19	27.5	73800*	228.87	210.00	1.635	2.693	945.35	1.19	1.35

S-C means Steel Concrete Wall.

Table 4.4 - Case Histories in Soft Clay.

Case	Wall Type	t (m)	H (m)	H_e (m)	B (m)	S_V (m)	S_H (m)	γ_s (kN/m^3)	s_u (kPa)	EI (kN-m^2/m)	$\delta_{H(max)}$ (mm)	$\delta_{V(max)}$ (mm)	$\delta_{H(max)}/H$ (%)	$\delta_{H(max)}/H_e$ (%)	$EI/(\gamma_w h^4_{avg})$	FS Eq. (2-26)	FS Eq. (2-27)
So1	Secant	0.9	18.3	12.2	22	3.8	6.1	19.1	20	768488	38.13	27.43	0.208	0.313	376.08	0.52	0.59
So2	Diaph.	0.8	31.0	16.0	20	2.5	9	17.6	10	1280000	38.55	NA	0.124	0.241	3343.67	0.21	0.31
So3	Diaph.	0.8	21.0	11.5	28.5	3.5	9	18	22	925867	15.39	7.00	0.073	0.134	629.58	0.64	0.73
So4	Sheet	NA	16.8	7.0	7.0*	2.5	2.5*	19	22.7	55250	83.27	NA	0.496	1.190	144.33	1.28	1.93
So5	Sheet	NA	18.0	8.0	65	2.5	2.5*	16	13.5	50400	123.65	NA	0.687	1.546	131.66	0.61	0.62
So6	Diaph.	0.76	18.3	8.5	25	2.75	2.75*	19	21.5	951115	37.39	37.00	0.204	0.440	1696.98	0.81	0.93
So7	Diaph.	0.76	13.7	10.3	85	3.65	3.65*	19	45	951115	3.63	NA	0.026	0.035	546.81	1.36	1.25
So8	Soldier	0.75	30.5	11.0	11.0*	3	3*	17	25	914063	107.06	NA	0.351	0.973	1151.50	0.94	1.69
So9	Sheet	NA	19.0	8.0	12.2	7.75	7.2	14	20	41370	385.38	NA	2.028	4.817	1.17	1.22	1.63
So10	Soldier	0.91	41.0	13.1	16	3.3	6	16.5	25	1733213	48.10	30.20	0.117	0.367	1491.32	0.76	1.42

4.3   Parametric Studies

A sequence of parametric studies was conducted to investigate the effects of the system stiffness on the three-dimensional ground movements caused by excavation in clay soils. Full three-dimensional finite element models were used to account for the real three-dimensional nature of the excavation and an advance soil model (Hardening Soil Model) was employed in order to include the elasto-plastic response of the soil (see Appendix B). In this section, features and modeling assumptions made in the finite element simulations are presented and the obtained results are discussed.

4.3.1   Finite Element Models

A total of 48 finite element simulations, performed in the three-dimensional software package PLAXIS 3D FOUNDATION, are the basis of the parametric study conducted to overcome the deficiencies of the actual methods used to predict maximum wall movements for deep excavations in cohesive soils. Figure 4.6 shows a PLAXIS 3D FOUNDATION schematic of one of the finite element models used in the analyses. Note that only half of the excavation was modeled because symmetry conditions applied to both the geometry and excavation sequence.

In the simulations, soil elements were modeled with 15-node wedge elements that are generated from the projection of two-dimensional 6-node triangular elements between work planes. The 15-node wedge element is composed of 6-node triangles in the horizontal direction and 8-node quadrilaterals in the vertical direction. As expressed by Brinkgreve and Broere (2006), the accuracy of the 15-node wedge element and the compatible structural elements is comparable with the 6-node triangular element and compatible structural elements in a 2D PLAXIS analysis.

92
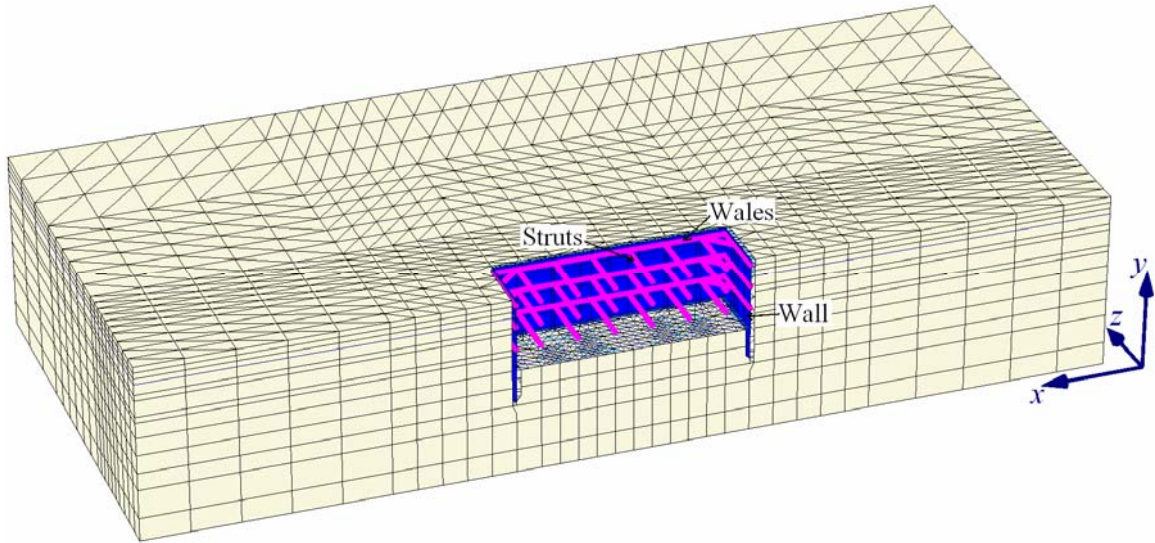
Figure 4.6 - Schematic of Finite Element Model Input for Parametric Studies.

Struts and wales were modeled with horizontal beams elements, which are composed of 3-node line elements with six degrees of freedom per node: three translational degrees of freedom (u_x, u_y and u_z) and three rotational degrees of freedom (φ_x, φ_y and φ_z). The beam element allows for beam deflections due to shear force, bending moment, and axial load. However, beam elements can not sustain torsional forces.

The supporting walls were "wished into place," which means that the installation of the wall caused no stress changes or displacements in the surrounding soil. The walls were modeled with 8-node quadrilateral plate elements (see Section A.6.2 for a further description of plate elements).

Soil-structure interaction was simulated by the inclusion of 16-node interface elements. These elements consist of eight pairs of nodes, compatible with the 8-noded quadrilateral side of a soil element. When degenerated soil elements are presented, interface elements are composed of 6 node pairs, compatible with the triangular side of the degenerated soil elements. In some output plots (e.g., Figure 4.6), interface elements are shown to have a finite thickness, but in the finite element formulation the coordinates of each node pair are

93

identical, which means that the element has zero thickness. For further reference about soil and structural elements employed by PLAXIS 3D FOUNDATION see Brinkgreve and Broere (2006).

The boundaries of the finite element models were extended beyond the settlement zone of influence induced by the excavation (Hsieh and Ou, 1998) and were automatically set by PLAXIS 3D FOUNDATION. The side boundaries of the mesh are constrained by "roller" fixities to prevent displacement in the perpendicular direction to the boundary, the bottom boundary prevents displacements in all directions, and the top boundary (the ground surface of the model) is free to move in all directions (see Section 3.3.3 for a more specified description about boundary conditions in PLAXIS).

Excavations in three different soil types (stiff, medium, and soft clay) were considered in this parametric study. The employed clays are real soils whose properties have been extensively reported in the technical literature. For the models in stiff soil, the Gault Clay at Lion Yard, Cambridge reported by Ng (1992) was employed; for the models in medium clay, the Taipei Silty Clay found at the TNEC project which is reported by Ou et al. (1998) was used; and for excavations in soft soil, the Upper Blodgett soft clay found at Chicago downtown was utilized.

Table 4.5 presents the Hardening Soil model parameters used in the analyses for each type of soil. Note that the soil parameters for the soft clay (Upper Blodgett) are the same parameters used in the finite element analysis of the wall installation for the Chicago and State Street excavation in Appendix A. Those parameters were defined by Roboski (2001). The Hardening Soil parameters for the Gault Clay and Taipei Silty Clay were extracted from Ou et al. (2000) and Ng (1992), respectively.

Table 4.5 - Hardening Soil Parameters for Parametric Study.

Hardening Soil Model		Stiff Clay	Medium Clay	Soft Clay
Name	[-]	Gault Clay	Taipei Silty Clay	Upper Blodgett
Type	[-]	Undrained	Undrained	Undrained
γ_{unsat}	[kN/m³]	20	18.1	18.1
γ_{sat}	[kN/m³]	20	18.1	18.1
$k_x = k_z$	m/day	0.00015	0.00015	0.00015
k_y	m/day	0.00009	0.00009	0.00009
E_{50}^{ref}	[kN/m²]	14847	6550	2350
E_{oed}^{ref}	[kN/m²]	4267	2380	1600
E_{ur}^{ref}	[kN/m²]	44540	19650	10000
c_{ref}	[kN/m²]	0.05	0.05	0.05
φ (phi)	[°]	33	29	24.1
ψ (psi)	[°]	0	0	0
υ_{ur}	[-]	0.2	0.2	0.2
p^{ref}	[kN/m²]	100	100	100
power (m)	[-]	1.0	1.0	1.0
K_0^{NC}	[-]	1.5	0.55	0.59
$c_{increment}$	[kN/m³]	0	0	0
y_{ref}	[m]	0	0	0
c_k	[-]	1.00E+15	1.00E+15	1.00E+15
e_{init}	[-]	1	1	1
e_{min}	[-]	0	0	0
e_{max}	[-]	999	999	999
R_f	[-]	0.96	0.95	0.7
T-Strength	[kN/m²]	0	0	0
R_{interf}	[-]	1	1	1
$\delta - inter$	[m]	0	0	0

The excavation geometry employed in the parametric study is a simplification of the Chicago and State Street excavation. The subway tunnel and the Warde School were not included and the two tieback supporting levels were replaced by strut levels in the simulations. Sixteen different finite element models were run for each type of soil presented in Table 4.5. Figure 4.7 shows the plan and section views for Model 1.
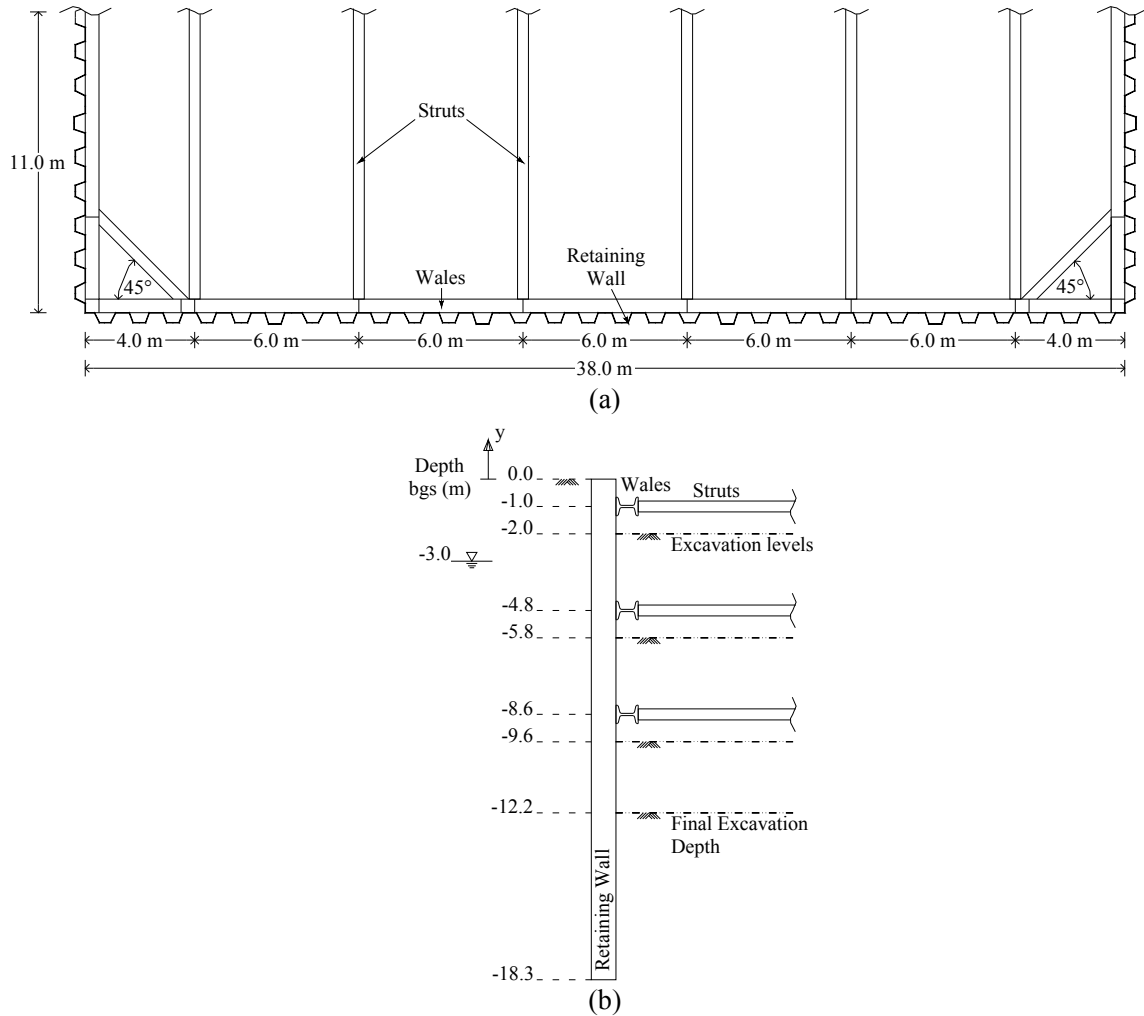
Figure 4.7 - Model 1: (a) Plan View; and (b) Section View.

In Models 2 and 3, the effects of varying the horizontal support spacing on the ground movement behavior of deep excavations are studied. Figures 4.8.a and 4.8.b show the plan views for Models 2 and 3, respectively. In Model 2, the horizontal support spacing was reduced approximately by 35 percent of that in Model 1, while in Model 3, the horizontal support spacing was increased approximately by 25 percent. It has to be mentioned that the only parameter that varied in Models 2 and 3 was the horizontal support spacing; all the other parameters, including the vertical support spacing, were kept unchanged from those in Model 1.
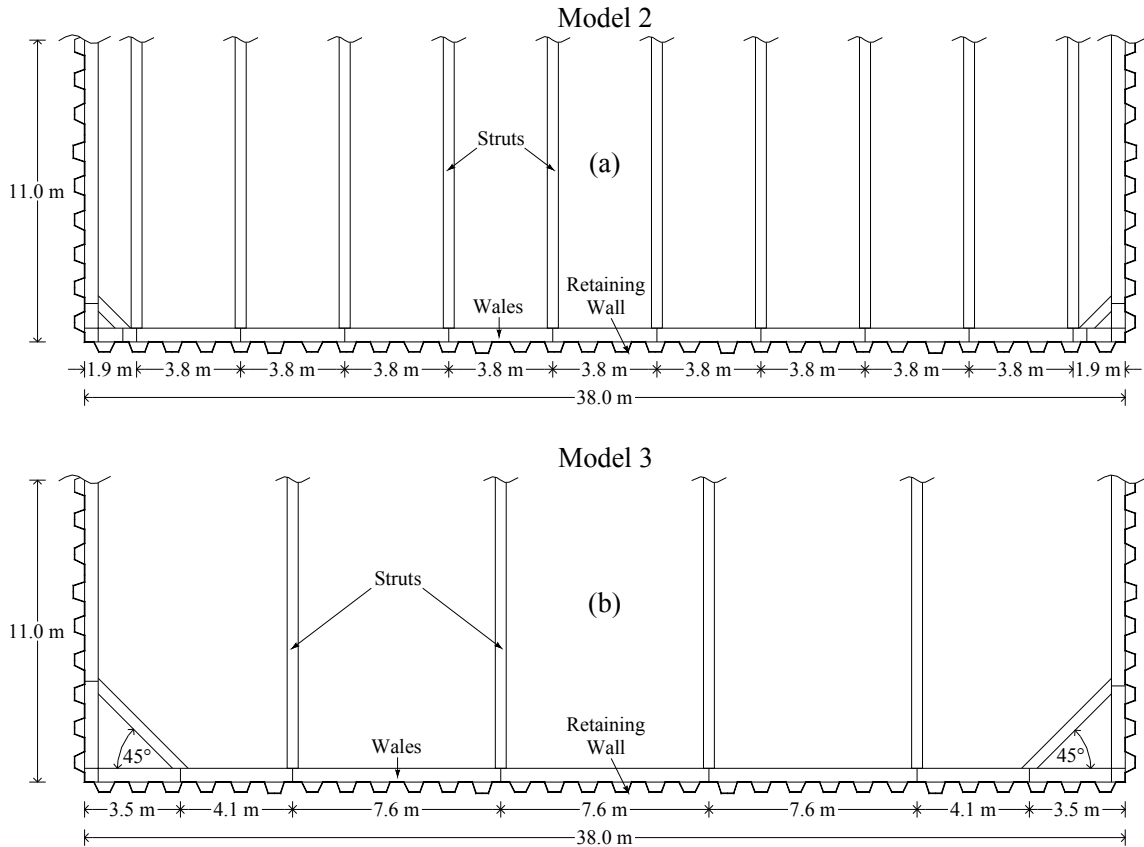
Figure 4.8 - Plan View: (a) Model 2; and (b) Model 3.

The effects of varying the vertical support spacing on the performance and final ground movements of excavation support systems are investigated in Models 4 to 7. For these models, just the vertical support spacing was varied while all the other parameters were kept unchanged from those in Model 1. Figure 4.9 shows the section views for Models 4 to 7.

In Models 8 to 16, the wall stiffness is the variable parameter. For these models the support configuration of Model 1 was used. Table 4.6 shows the wall stiffness specified for each model. Models 8, 9, and 10 represent very flexible walls such as sheet pile walls; Models 11, 12, 13, and 1 to 7 represent medium stiff walls such as secant and tangent pile walls and diaphragm walls with low to moderate steel reinforcement; and Models 14, 15, and 16 represent very stiff walls such as secant pile and diaphragm walls with inserted steel sections or with a high reinforcement quantity.

97
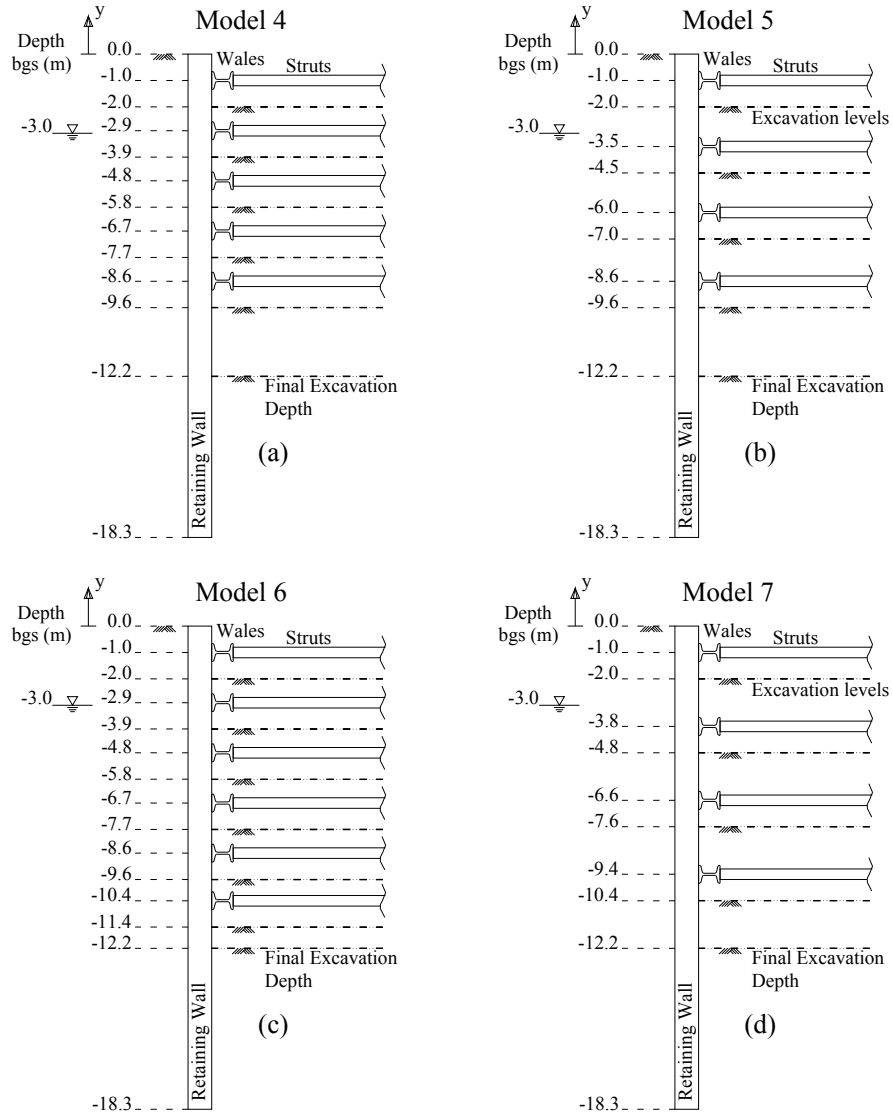
Figure 4.9 - Section Views: (a) Model 4; (b) Model 5; (c) Model 6; and (d) Model 7.

Table 4.6 - Wall Stiffness for Finite Element Models.

Model	α	$\alpha \times EI*$ (kN-m²/m)
1 - 7	1	540,675
8	0.05	27,033.75
9	0.1	54,067.5
10	0.25	135,168.75
11	0.5	270,337.5
12	5	2,703,375
13	10	5,406,750
14	25	13,516,875
15	100	54,067,500
16	250	135,168,750

*EI = 540,675 kN-m²/m

98

For all the simulations performed in the parametric study, the water table level was assumed to be at -3.0 m below ground surface and a simplified excavation sequence consisting of excavating uniformly the soil 1 m below each support level prior to adding the supports was employed (see Figures 4.7.b and 4.9).

4.3.2   Influence of Support Spacing

Figures 4.10 and 4.11 show the influences of the horizontal and vertical support spacing on the lateral wall movements for deep excavations, respectively. In both figures, the lateral wall deformations are normalized with respect to the height of the wall and the spacing axis is normalized with respect to the spacing specified for Model 1 (see Figure 4.7). As expected, the more space between supports the more lateral deformations in the retaining wall. However, as can be seen in the Figures 4.10 and 4.11, the variation in the horizontal and vertical support spacing does not have a significant effect in the lateral wall deformations of excavation support systems.

The system stiffness factor ($EI/\gamma_w S_V^4$) proposed by Clough et al. (1989) was calculated for each model and their corresponding values included in Figures 4.10 and 4.11. As expected, the variation of horizontal support spacing does not influence the system stiffness factor and its value stays constant. On the other hand, it was observed that the vertical support spacing parameter, which is elevated to four in the Clough et al. (1989) system stiffness factor, is a very sensitive parameter that increases or decreases significantly the value of the system stiffness. Note that by reducing the vertical support spacing by 50 percent, the system stiffness parameter is increased by 1610 percent! However, this increase in the system stiffness is not reflected in the final lateral wall deformations which stay essentially unchanged.

99
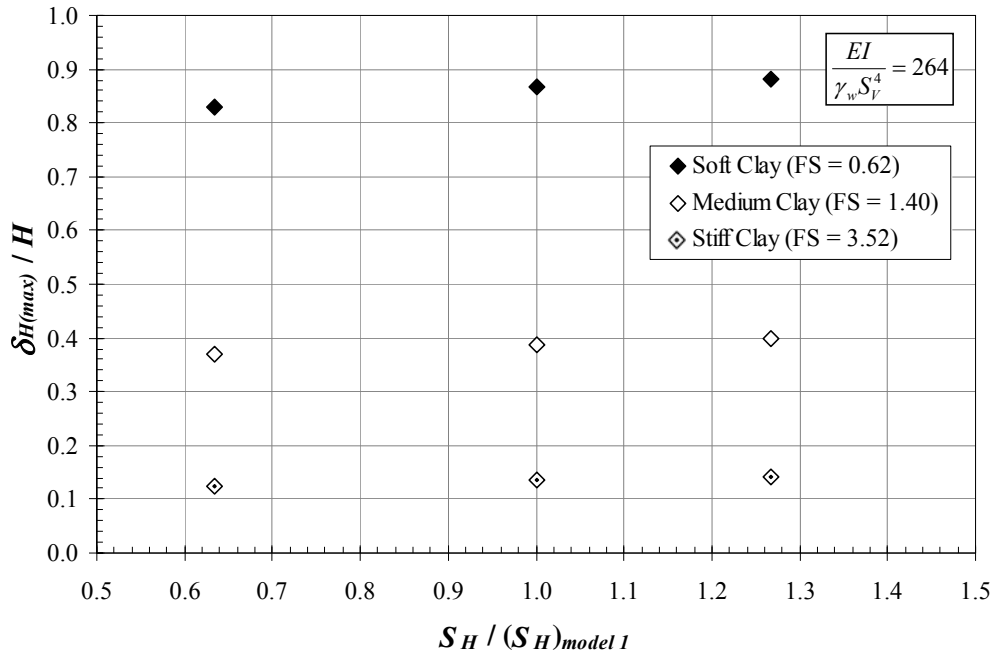
Figure 4.10 - Normalized Maximum Lateral Deformation vs. Horizontal Spacing.
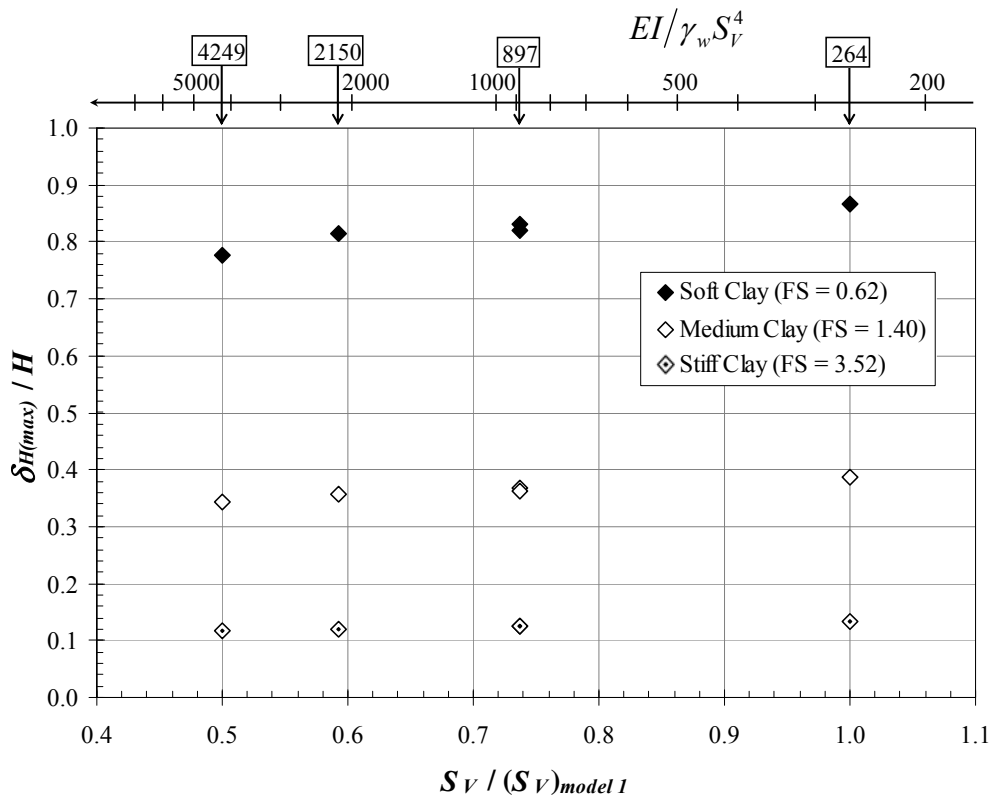
Figure 4.11 - Normalized Maximum Lateral Deformation vs. Vertical Spacing.

100

4.3.3   Influence of Wall Stiffness

Figure 4.12 illustrates the effects that the variation in wall stiffness has on the lateral wall movements for deep excavations in clays. As expected, the stiffer the wall is the smaller the movements are. Note that for excavations in stiff clays, the wall stiffness does not have a significant effect on the final lateral movements. Consequently, flexible retaining walls can be used for deep excavation on these soils without expecting excessive ground movements. This result agrees with the findings previously presented by Clough and O'Rourke (1990), who stated that for stiff clays where basal stability is not an issue, wall stiffness and support spacing have a small influence on the lateral wall movements.

On the contrary, it is evident that in soft to medium clays the wall stiffness plays an important role in the excavation performance. It is one of the key parameters that the designer has to control ground movements in deep excavations. However, for values of $EI > 10,000$ MN-m^2/m the ground movement variation is so small that can be neglected and therefore, the use of stiffer walls is worthless.
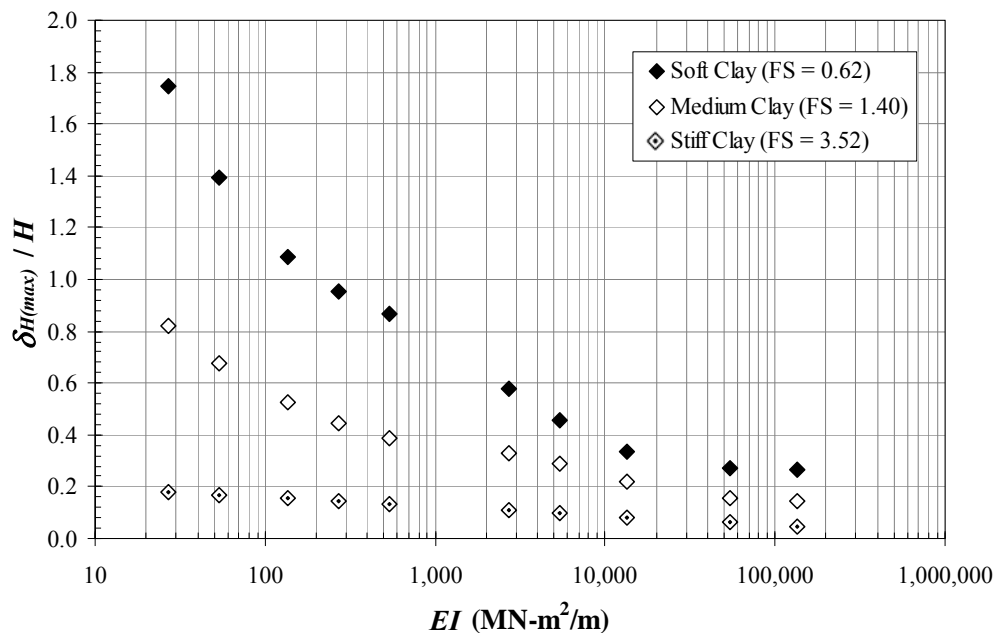
Figure 4.12 - Influence of Wall Stiffness on Lateral Wall Deformations.

101

4.4 Data Synthesis

Figure 4.13 presents the result of the parametric study compared with the Clough et al. (1989) design chart. The data was differentiated by type of soil (i.e., factor of safety against basal heave) and by parameters that were varied or maintained constant during the finite element simulations (wall stiffness, EI, and support spacing, S_H and S_V).
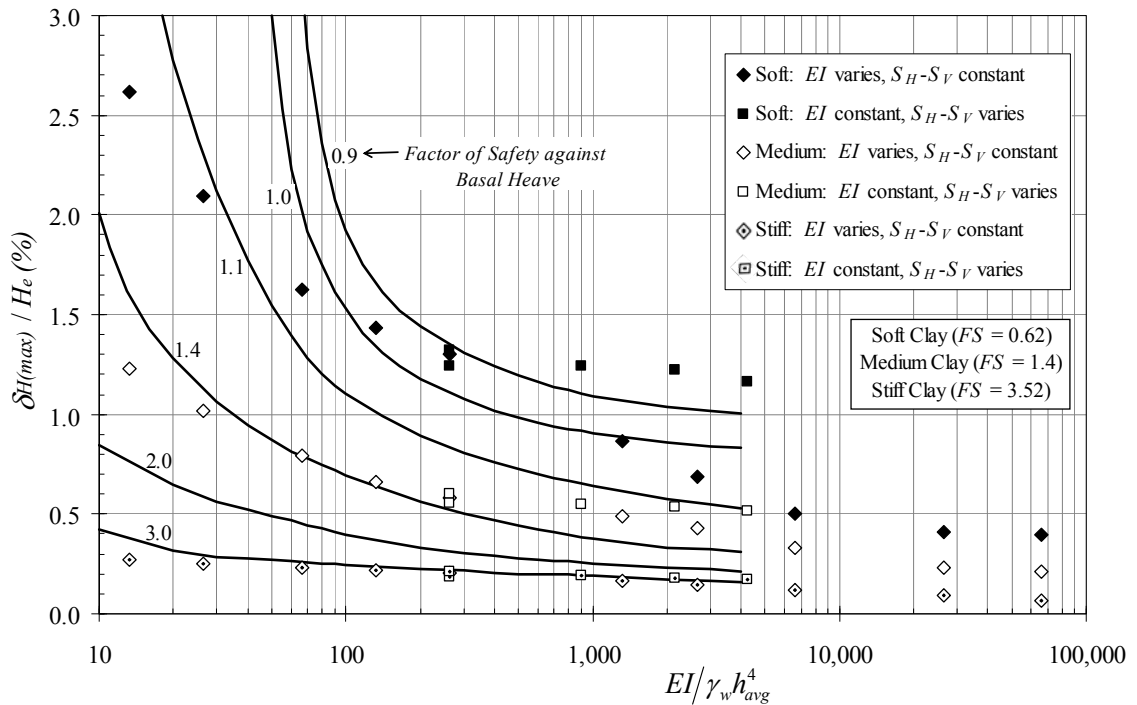
Figure 4.13 - Comparison of Parametric Studies with Clough et al. (1989) Design Chart.

It can be seen in Figure 4.13 that for stiff clays, the Clough et al. (1989) design chart and the results from the parametric studies agree well. It is because for excavations in stiff soils with high factors of safety against basal heave, the system stiffness parameter has no significant effects on the lateral wall displacements (see Section 2.4). It is for excavations in soft to medium clays where the stiffening effects of the excavation corners and the beneficial effect of the wall embedment depth on the factor of safety are evident.

102

It is also noted in Figure 4.13 that for soft and medium clays the system stiffness factor ($EI/\gamma_w S_V^4$) presented by Clough et al. (1989) does not group the data from the parametric study. In other words, there is not a clear correlation between the system stiffness factor and the lateral wall movements. It is because the Clough et al. (1989) system stiffness factor does not include the three-dimensional nature of the excavation. Additionally, as presented in Section 4.3.2, the vertical support spacing parameter when elevated to four becomes a very sensitive parameter that does not represent the correlation between the real system stiffness and lateral wall movements.

The above analyses yield the conclusion that the Clough et al. (1989) system stiffness parameter ($EI/\gamma_w S_V^4$) does not represent the real nature of deep excavations and must be rewritten.

4.4.1 Proposed System Stiffness Chart

In this section, a new relative stiffness ratio, R, which relates the stiffness of the soil with the stiffness of the supporting system, is proposed to overcome the deficiencies of the system stiffness parameter presented by Clough et al (1989). The relative stiffness ratio, R, is defined as:

$$R = \frac{E_s}{E} \cdot \frac{S_H S_V H}{I} \cdot \frac{\gamma_s H_e}{s_u} \tag{4-1}$$

where:

$R =$ relative stiffness ratio,

$E_s =$ reference secant Young's modulus at the 50% of the stress level, E_{50}^{ref} in Appendix C,

$E =$ Young's modulus of the wall,

$I =$ moment of inertia per unit length of the wall,

S_H = average horizontal support spacing,

S_V = average vertical support spacing,

H = height of the wall,

H_e = excavation depth,

γ_s = average unit weight of the soil, and

s_u = undrained shear strength.

In Equation (4-1), the terms E_s/E, $S_H S_V H/I$, and $\gamma_s H_e/s_u$ represent the relative stiffness resistance, the relative bending resistance, and the excavation stability number, respectively. Note that all the variables included in Equation (4-1) are basic soil and geometry parameters that the designer can easily determine from standard soil tests and excavation specifications. Also, note that the used relative stiffness ratio, R, does not have sensitive variables like the vertical support spacing, S_V^4, in the Clough et al. (1989) system stiffness parameter.

Tables 4.7, 4.8, and 4.9 list the necessary parameters to calculate the relative stiffness ratio, R, for the finite element models in stiff, medium, and soft clay, respectively. In addition, the maximum vertical ground settlement, $\delta_{V(max)}$, and the maximum lateral wall displacement, $\delta_{H(max)}$, obtained at the center line of the excavation are presented in the last two columns of the tables. It can be seen by observing the calculated values of R and the specified stiffness for the walls that contrary to the Clough et al. (1989) system stiffness factor ($EI/\gamma_w S_V^4$), low values of R represents rigid walls such as secant and diaphragm walls, and high values of R represent flexible retaining walls such as sheet pile walls.

104

Table 4.7 - Relative Stiffness Ratio and Maximum Ground Movements for Finite Element Models in Stiff Clay.

Model	EI (kN-m²/m)	S_V (m)	S_H (m)	H (m)	H_e (m)	E_s (kPa)	γ_s (kN/m³)	s_u (kPa)	$EI / (\gamma_w h^4_{avg})$	R	$\delta_{V(max)}$ (mm)	$\delta_{H(max)}$ (mm)
1	540,675	3.8	6	18.3	12.2	14847	20	125	264	22.36	6.41	24.64
2	540,675	3.8	3.8	18.3	12.2	14847	20	125	264	14.16	5.80	22.69
3	540,675	3.8	7.6	18.3	12.2	14847	20	125	264	28.33	6.81	26.09
4	540,675	2.25	6	18.3	12.2	14847	20	125	2,150	13.24	5.37	22.07
5	540,675	2.8	6	18.3	12.2	14847	20	125	897	16.48	5.74	23.01
6	540,675	1.9	6	18.3	12.2	14847	20	125	4,229	11.18	5.26	21.29
7	540,675	2.8	6	18.3	12.2	14847	20	125	897	16.48	5.83	23.07
8	27,034	3.8	6	18.3	12.2	14847	20	125	13	447.30	9.21	32.67
9	54,068	3.8	6	18.3	12.2	14847	20	125	26	223.65	8.23	30.93
10	135,169	3.8	6	18.3	12.2	14847	20	125	66	89.46	7.39	28.52
11	270,338	3.8	6	18.3	12.2	14847	20	125	132	44.73	6.87	26.56
12	2,703,375	3.8	6	18.3	12.2	14847	20	125	1,322	4.47	5.27	20.06
13	5,406,750	3.8	6	18.3	12.2	14847	20	125	2,643	2.24	4.76	17.83
14	13,516,875	3.8	6	18.3	12.2	14847	20	125	6,608	0.89	4.07	14.79
15	54,067,500	3.8	6	18.3	12.2	14847	20	125	26,432	0.22	2.99	11.16
16	135,168,750	3.8	6	18.3	12.2	14847	20	125	66,080	0.09	2.22	8.07

Table 4.8 - Relative Stiffness Ratio and Maximum Ground Movements for Finite Element Models in Medium Clay.

Model	EI (kN-m²/m)	S_V (m)	S_H (m)	H (m)	H_e (m)	E_s (kPa)	γ_s (kN/m³)	s_u (kPa)	$EI / (\gamma_w h^4_{avg})$	R	$\delta_{V(max)}$ (mm)	$\delta_{H(max)}$ (mm)
1	540,675	3.8	6	18.3	12.2	6550	18.1	45	264	24.80	32.29	70.77
2	540,675	3.8	3.8	18.3	12.2	6550	18.1	45	264	15.71	31.00	67.56
3	540,675	3.8	7.6	18.3	12.2	6550	18.1	45	264	31.42	33.55	72.98
4	540,675	2.25	6	18.3	12.2	6550	18.1	45	2,150	14.69	28.68	65.52
5	540,675	2.8	6	18.3	12.2	6550	18.1	45	897	18.28	29.86	67.19
6	540,675	1.9	6	18.3	12.2	6550	18.1	45	4,229	12.40	27.77	62.91
7	540,675	2.8	6	18.3	12.2	6550	18.1	45	897	18.28	29.82	66.41
8	27,034	3.8	6	18.3	12.2	6550	18.1	45	13	496.07	80.21	150.3
9	54,068	3.8	6	18.3	12.2	6550	18.1	45	26	248.04	62.96	123.8
10	135,169	3.8	6	18.3	12.2	6550	18.1	45	66	99.21	46.90	96.36
11	270,338	3.8	6	18.3	12.2	6550	18.1	45	132	49.61	38.52	80.97
12	2,703,375	3.8	6	18.3	12.2	6550	18.1	45	1,322	4.96	22.02	59.79
13	5,406,750	3.8	6	18.3	12.2	6550	18.1	45	2,643	2.48	18.39	52.58
14	13,516,875	3.8	6	18.3	12.2	6550	18.1	45	6,608	0.99	13.80	39.94
15	54,067,500	3.8	6	18.3	12.2	6550	18.1	45	26,432	0.25	8.49	28.07
16	135,168,750	3.8	6	18.3	12.2	6550	18.1	45	66,080	0.10	6.13	25.95

105

Table 4.9 - Relative Stiffness Ratio and Maximum Ground Movements for Finite Element Models in Soft Clay.

Model	EI (kN-m²/m)	S_V (m)	S_H (m)	H (m)	H_e (m)	E_s (kPa)	γ_s (kN/m³)	s_u (kPa)	$EI / (\gamma_w h^4_{avg})$	R	$\delta_{V(max)}$ (mm)	$\delta_{H(max)}$ (mm)
1	540,675	3.8	6	18.3	12.2	2350	18.1	20	264	20.02	71.40	158.6
2	540,675	3.8	3.8	18.3	12.2	2350	18.1	20	264	12.68	67.92	151.7
3	540,675	3.8	7.6	18.3	12.2	2350	18.1	20	264	25.36	73.54	161.5
4	540,675	2.25	6	18.3	12.2	2350	18.1	20	2,150	11.86	63.69	149.2
5	540,675	2.8	6	18.3	12.2	2350	18.1	20	897	14.75	65.97	151.9
6	540,675	1.9	6	18.3	12.2	2350	18.1	20	4,229	10.01	61.20	142.2
7	540,675	2.8	6	18.3	12.2	2350	18.1	20	897	14.75	65.95	150.2
8	27,034	3.8	6	18.3	12.2	2350	18.1	20	13	400.46	190.20	319.6
9	54,068	3.8	6	18.3	12.2	2350	18.1	20	26	200.23	147.90	255.2
10	135,169	3.8	6	18.3	12.2	2350	18.1	20	66	80.09	109.60	198.4
11	270,338	3.8	6	18.3	12.2	2350	18.1	20	132	40.05	87.67	174.6
12	2,703,375	3.8	6	18.3	12.2	2350	18.1	20	1,322	4.00	41.41	105.4
13	5,406,750	3.8	6	18.3	12.2	2350	18.1	20	2,643	2.00	32.64	83.66
14	13,516,875	3.8	6	18.3	12.2	2350	18.1	20	6,608	0.80	23.19	61.54
15	54,067,500	3.8	6	18.3	12.2	2350	18.1	20	26,432	0.20	13.74	50.11
16	135,168,750	3.8	6	18.3	12.2	2350	18.1	20	66,080	0.08	10.65	48.61

Figure 4.14 presents maximum lateral wall displacements recorded at the end of excavation versus the relative stiffness ratio, R, for different factors of safety against basal heave. In the figure, the lateral movements are normalized with respect to the height of the wall, and the factors of safety are calculated using Equation (2-27) which includes the effects of the wall embedment depth below the base of excavation. In addition, the finite element data calculated for the three different soil types (FS = 0.62, 1.40, and 3.52) is presented in the figure. Note that the proposed relative stiffness ratio, R, correlates very well with all the finite element data obtained from the parametric study.

Figure 4.14 becomes a new design chart that allows the designer to predict maximum lateral wall movements for deep excavations in cohesive soils based on simple soil data and excavation geometry including the inherent three-dimensional nature of the excavation and the wall embedment depth below the excavation base.
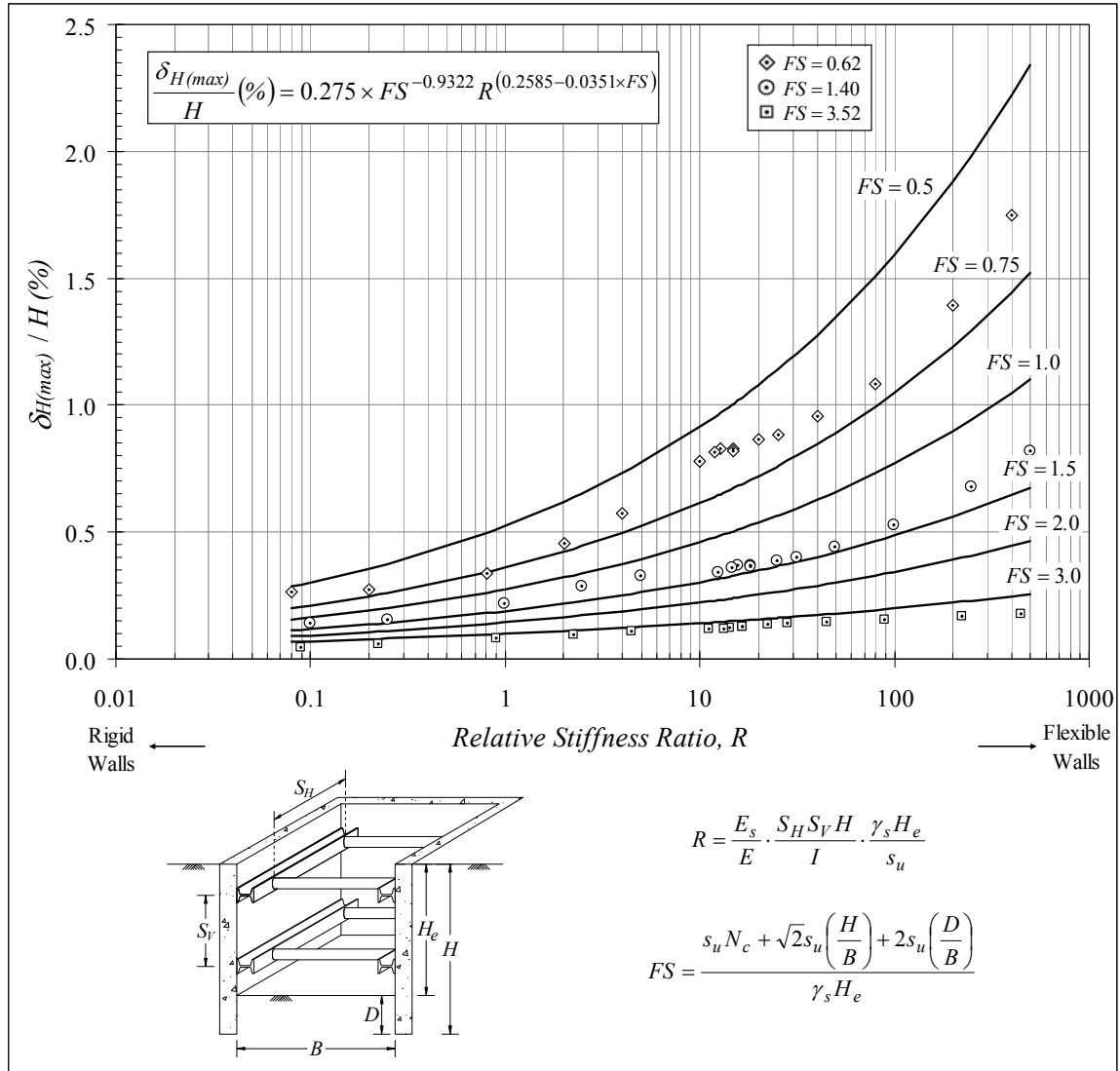
Figure 4.14 - Normalized Lateral Wall Movements vs. Relative Stiffness Ratio, _R_, for Deep Excavations in Cohesive Soils.

It is well-known that design charts are broadly used in the current engineering practice, but most of them require the designer to extract the data from the charts by pure visualization, making the design process a tedious labor of data inferring. For this reason, a close form equation, which can be easily programmed in a pocket calculator, was fitted to the finite element data. The close form equation that describes the tendency for the curves presented in Figure 4.14 is:

$$\frac{\delta_{H(max)}}{H}(\%) = 0.275 \times FS^{-0.9322} R^{(0.2585 - 0.0351 \times FS)} \tag{4-2}$$

The fitting process employed to find Equation (4-2) is described as follows:

1. The data from the finite element simulations was plotted as presented in Figure 4.15. Then, functions having the form of Equation (4-3) were fitted to the data using the software LAB Fit (Silva et al., 2006) which is a software for Windows developed for treatment and analysis of experimental data.

$$\frac{\delta_{H(max)}}{H}(\%) = A \times R^B \tag{4-3}$$
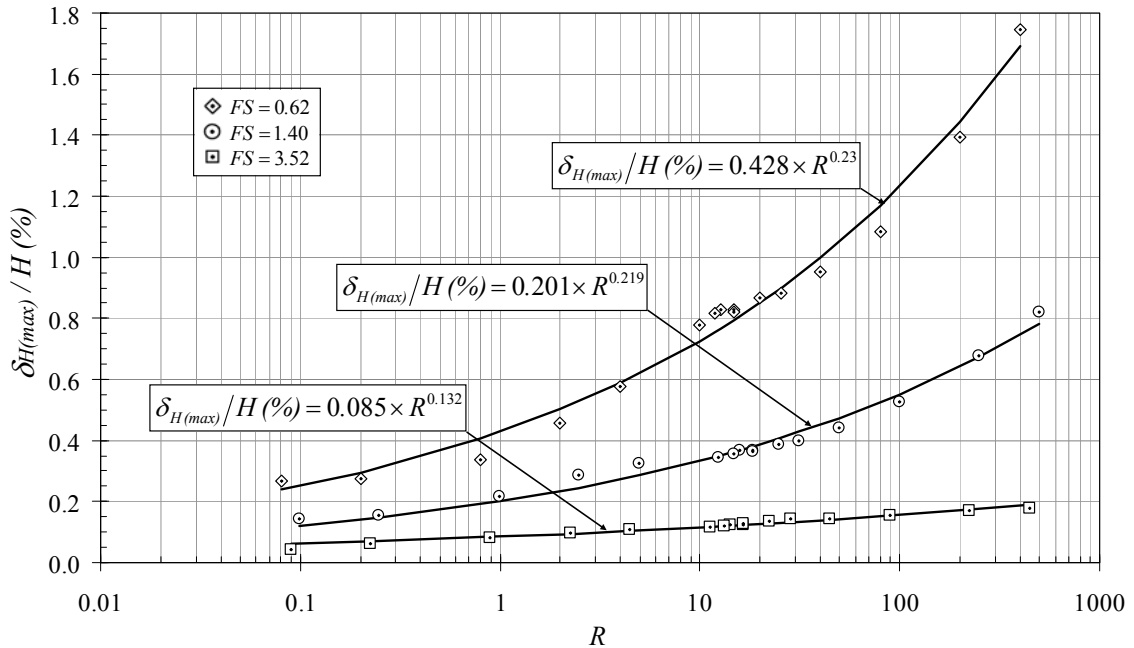
Figure 4.15 - Fitting Functions for the Finite Element Data.

2. The fitting function parameters (A and B), found in Step 1 for Equation (4-3), were plotted versus the factor of safety against basal heave and the best functions were fitted to the curves using the software LAB Fit (see Figure 4.16). Note that the only difference between the curves showed in Figure 4.15 is the factor of safety against basal heave and the fitting function parameters (*A* and *B*).

3. Finally, the expressions for *A* and *B*, found in Step 2, are substituted in Equation (4-3) to obtain Equation (4-2).
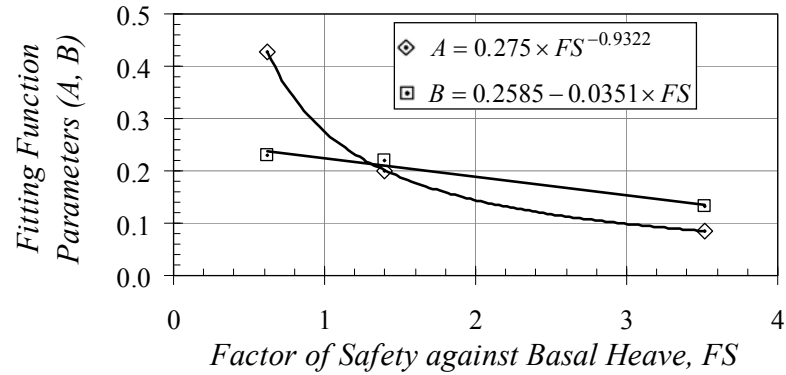
Figure 4.16 - Fitting Function Parameters *A* and *B* vs. Factor of Safety.

4.4.2 Proposed Lateral Wall Deformation Profiles

Found $\delta_{H(max)}$ from the proposed design chart (Figure 4.14) or from Equation (4-2) presented in the previous section, one can use this value to get lateral wall deformation distributions for excavation support systems.

Figure 4.17 shows lateral wall deformations versus depth for the case histories on stiff, medium and soft clay presented in Section 4.2.2. In the Figure, lateral deformations are normalized with respect to the maximum horizontal movement recorded at the end of excavation, and the depth axis is normalized with respect to the height of the wall. Note that a three-linear plot was included for each soil type in order to show the lateral deformation profile tendency of the case history data. These empirical three-linear plots allow the designer, having the maximum lateral wall displacement and the height of the wall, to predict the shape of lateral wall deformations for deep excavations based on soil type (i.e., based on the undrained shear strength parameter). Figure 4.18 shows a summary of the empirical lateral deformation profiles proposed for each soil type.
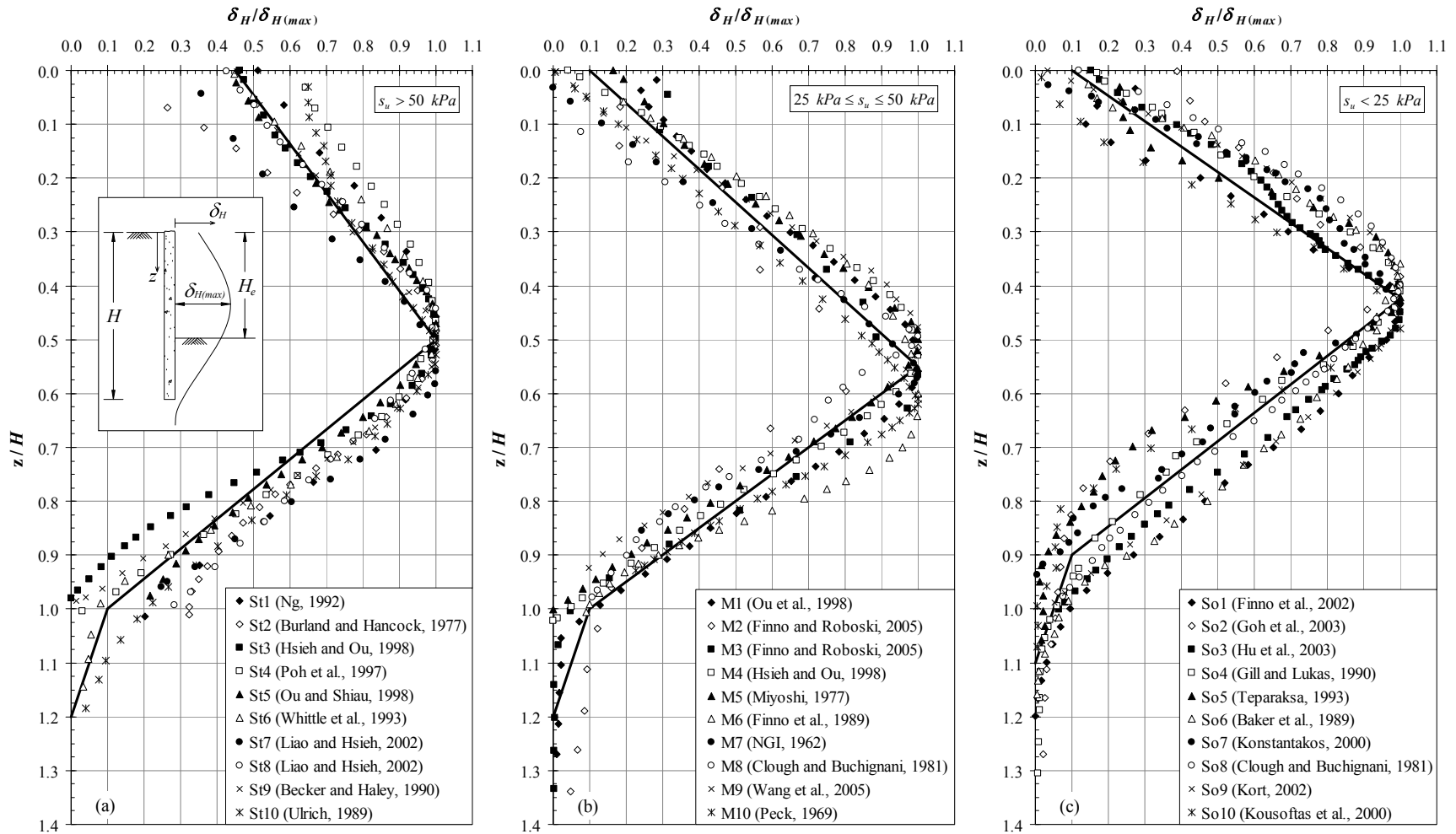
Figure 4.17 - Normalized Lateral Deformations for Case Histories: (a) Stiff Clay; (b) Medium Clay; and (c) Soft Clay.
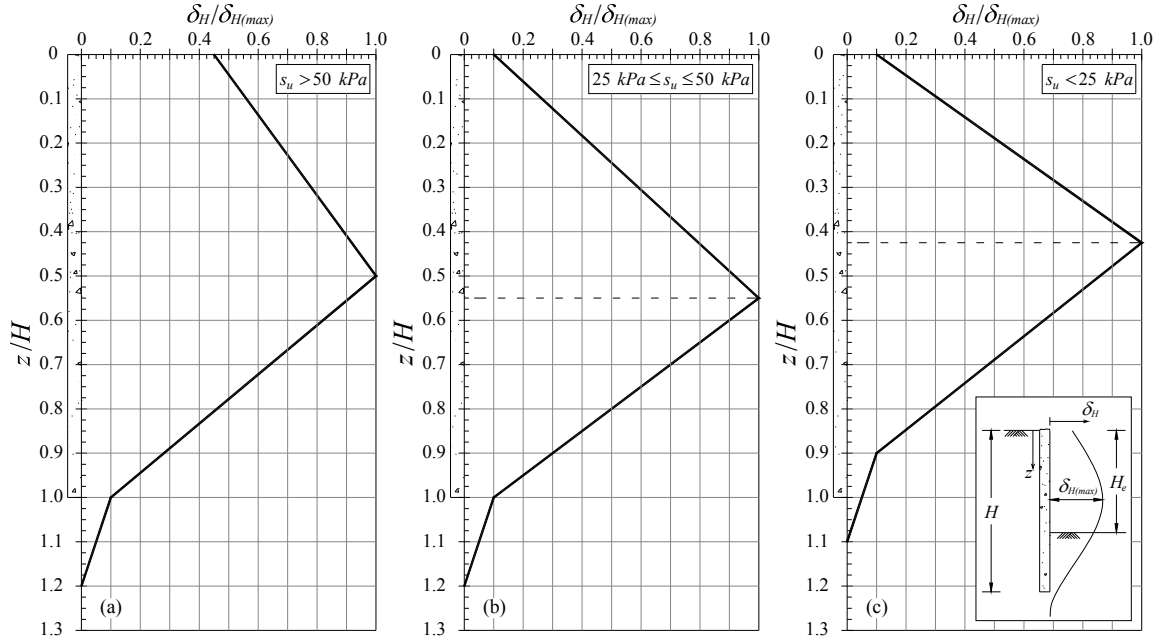
Figure 4.18 - Proposed Lateral Deformation Profiles: (a) Stiff Clay; (b) Medium Clay; and (c) Soft Clay.

4.4.3 Proposed Relationship between $\delta_{H(max)}$ and $\delta_{V(max)}$

The procedure for finding the relationship between the maximum vertical ground settlement, $\delta_{V(max)}$, and the maximum lateral wall displacement, $\delta_{H(max)}$, is basically similar to the one used in Section 4.4.1 for finding Equation (4-2). This procedure is described as follows:

1. The maximum settlements and lateral wall movements obtained from the finite element simulations were plotted as shown in Figure 4.19 where the x and y-axes are $\left(\delta_{H(max)}/H\right)\times R \times FS$ and $\delta_{V(max)}/H\left(\%\right)$, respectively.

2. Functions having the form of Equation (4-4) were fitted to the data using the software LAB Fit. These functions and their respective fitting parameters, C and D, are shown in the Figure 4.19 for each soil type. Note again that the only difference between the curves is the factor of safety against basal heave and the fitting function parameters (C and D).

111

$$\frac{\delta_{V(max)}}{H}(\%) = C\left[\frac{\delta_{H(max)}}{H} \times R \times FS\right]^{D} \qquad (4\text{-}4)$$
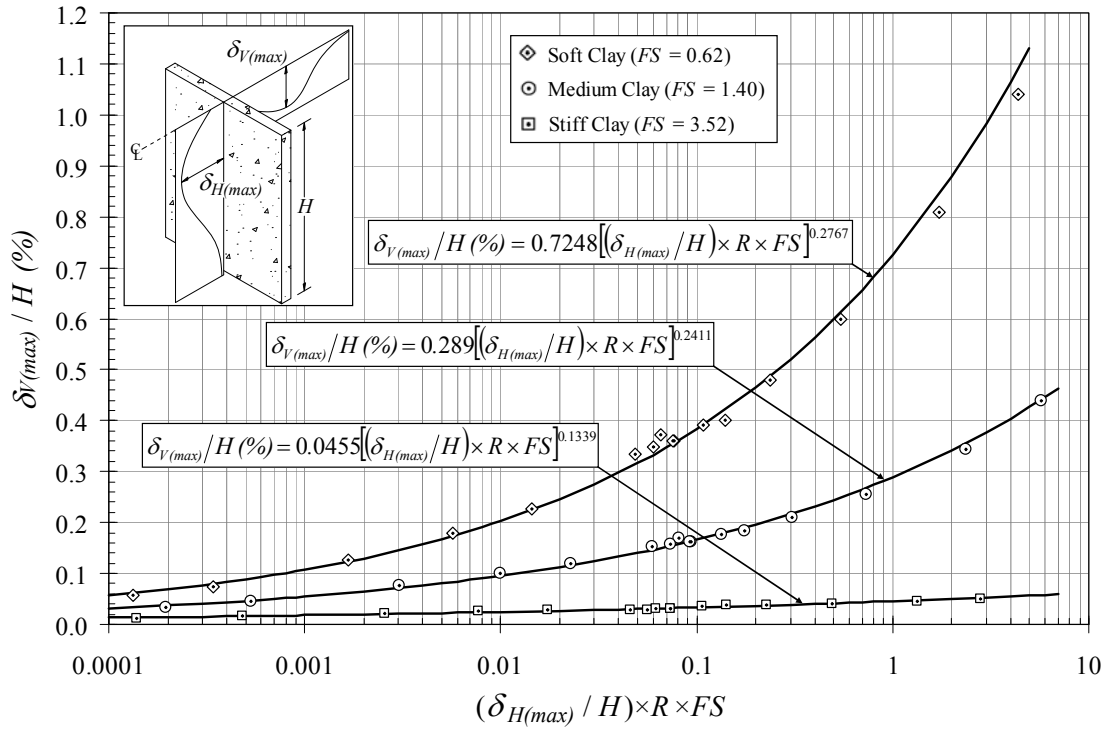
Figure 4.19 - Determination of $\delta_{V(max)}$ - $\delta_{H(max)}$ Relationship.

3. The fitting function parameters (*C* and *D*), found in Step 2, were plotted versus the factor of safety against basal heave and the best functions were fitted to the curves using the software LAB Fit (see Figure 4.20).
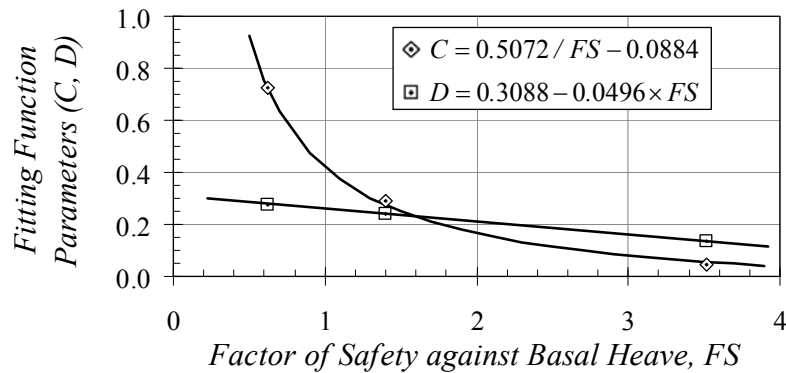
Figure 4.20 - Fitting Function Parameters *C* and *D* vs. Factor of Safety.

112

4. Finally, the expressions for *C* and *D*, found in Step 3, are substituted in Equation (4-4) to obtain:

$$\frac{\delta_{V(max)}}{H}(\%) = \left(\frac{0.5072}{FS} - 0.0884\right)\left[\frac{\delta_{H(max)}}{H} \times R \times FS\right]^{(0.3088 - 0.0496 \times FS)} \tag{4-5}$$

Equation (4-4) relates the maximum vertical ground settlement, $\delta_{V(max)}$, and the maximum lateral wall displacement, $\delta_{H(max)}$, at the center line of deep excavations in cohesive soils. Note that Equation (4-5) overcomes the limitations of Equation (2-30) (see Section 2.5.3) by including the effects of the factor of safety against basal heave and system stiffness.

4.4.4   Proposed Perpendicular Settlement Profiles

Figure 4.21 shows the obtained settlement distributions normalized with respect to the maximum vertical movement for the finite element Models 1, 8, 10, 12, 14, 15, and 16. Only settlement distributions for these models are presented because of visualization purposes. It was observed that excavations with similar relative stiffness ratio, *R*, have similar settlement distributions (see Figures 4.22, 4.23, and 4.24). Note in tables 4.7, 4.8, and 4.9 that the values of *R* for Models 1, 8, 10, 12, 14, 15, and 16 cover uniformly the proposed range of *R* presented in Figure 4.14 for excavation support systems.

Figures 4.22, 4.23, and 4.24 present the proposed perpendicular settlement profiles at the center line of the excavation for stiff, medium, and soft clays, respectively. In the figures, the settlement and distance axes are normalized with respect to the maximum settlement value and height of the wall, respectively. These figures were obtained by fitting three-linear curves to the settlement distributions presented in Figure 4.21. Note that the coordinates that define the settlement profiles are dependent of the stiffness of the system represented by *R*.

113
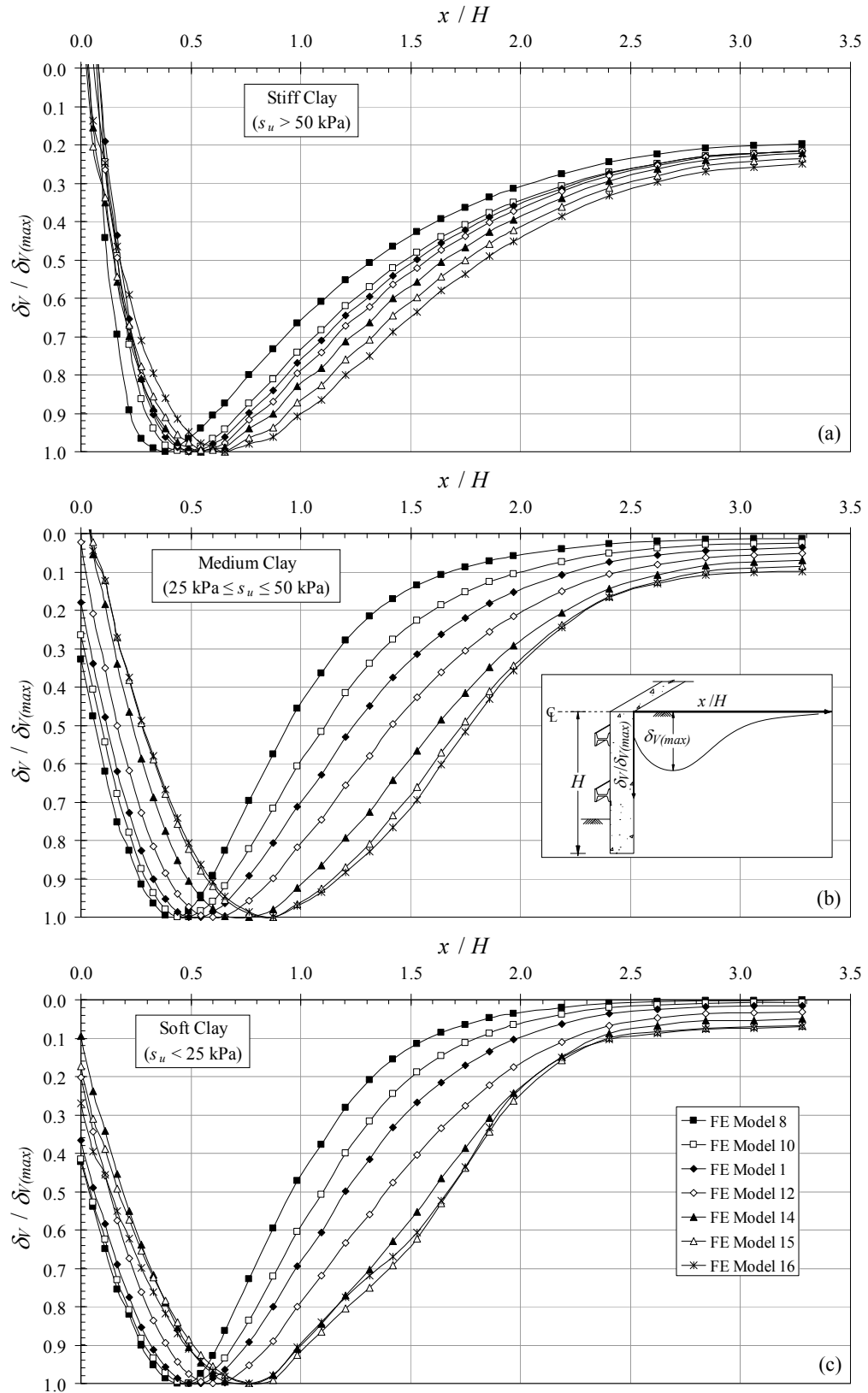
Figure 4.21 - Normalized Settlement vs. Distance from the Wall for the Finite Element Data: (a) Stiff Clay; (b) Medium Clay; and (c) Soft Clay.

114
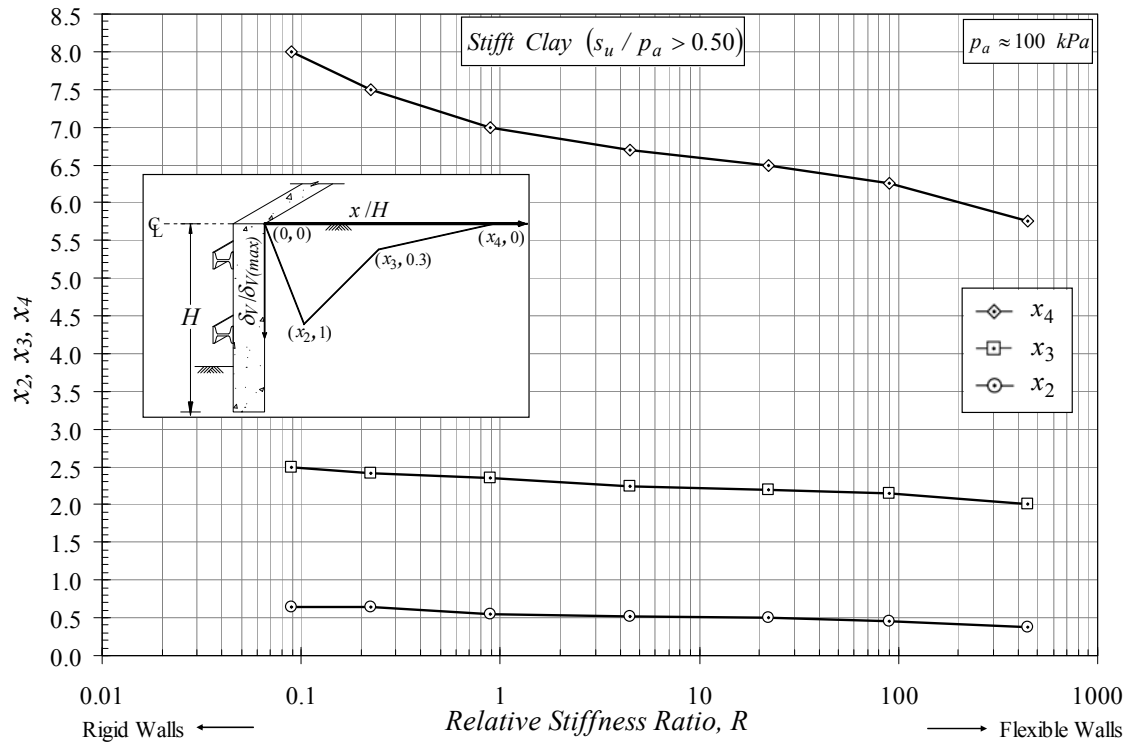
Figure 4.22 - Proposed Perpendicular Settlement Profile for Stiff Clay.
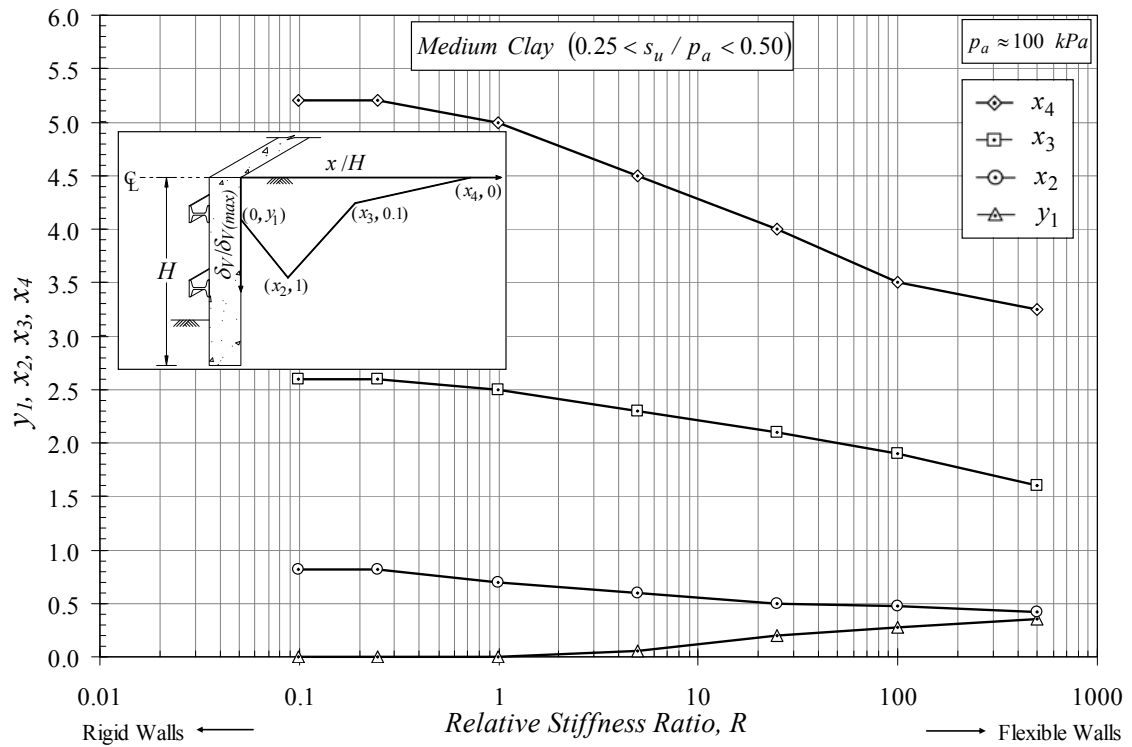
Figure 4.23 - Proposed Perpendicular Settlement Profile for Medium Clay.

115
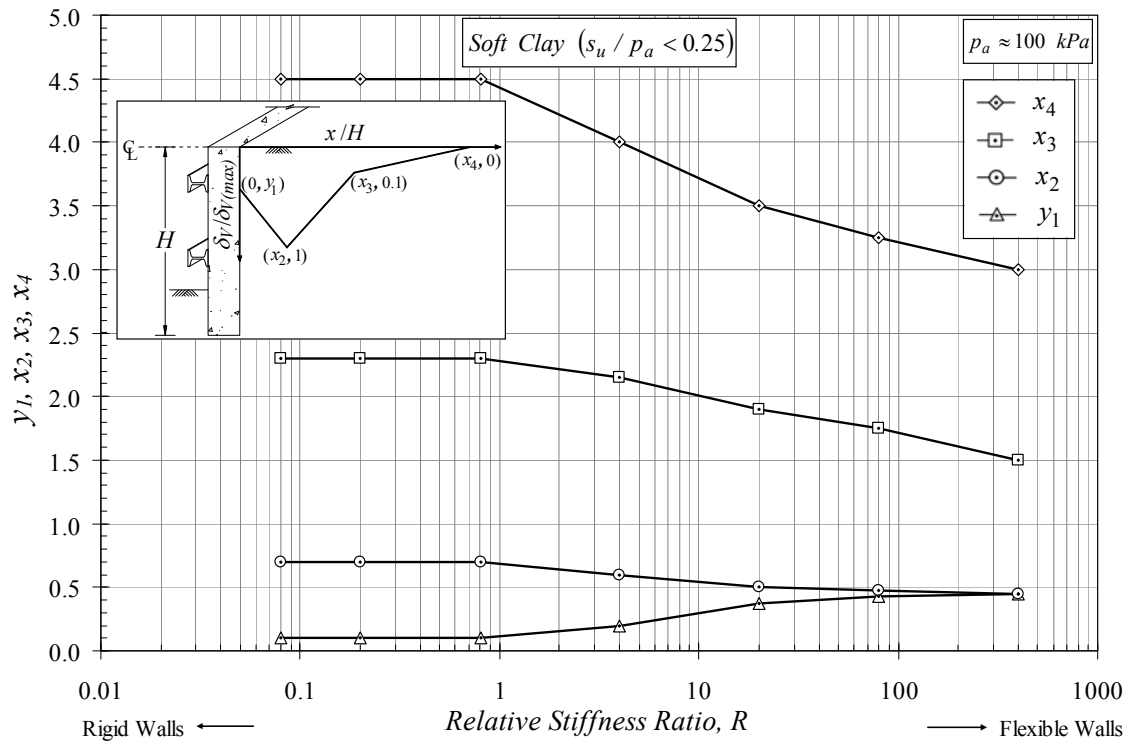
Figure 4.24 - Proposed Perpendicular Settlement Profile for Soft Clay.

116

CHAPTER 5

5   DEFORMATION-BASED DESIGN APPROACH FOR EXCAVATION SUPPORT
     SYSTEMS

5.1   Introduction

Empirical design approaches are commonly used to evaluate the behavior and performance of deep excavations and their corresponding support systems. It is well-known that these methods have many weaknesses and limitations due to the huge number of factors that influence the behavior of any excavation project, which make the design process a multi-dimensional task. Moreover, each excavation is influenced by parameters and construction incidents such as workmanship or deviations from design that generally are not mentioned or presented in the excavation reports. Additionally, many of these factors are impossible to quantify and may well be relevant to the measured ground deformations.

The enormous advance in computational technology during past years has allowed the application of numerical techniques like the finite element method to excavation problems. These techniques have been broadly used because they allow the variation of a single parameter while keeping all the others constant. In this way, some of the limitations that the empirical observation approaches present can be overcome.

In this chapter, empirical approaches and numerical techniques are combined to create a semi-empirical method for designing excavation support systems based on deformation control. The method is illustrated by two flow charts that allow the designer to predict final ground movements (horizontal and vertical), given data about soil and support system or size all the elements of the excavation support system, given the allowable soil distortion of infrastructure adjacent to the excavation.

117

5.2   Iterative Method for Predicting Ground Movements in Deep Excavations

A proposed method that allows the designer to predict final horizontal wall displacements and vertical ground settlements, given data about soil and support system is presented in this section. The necessary steps for the design of the excavation support system and the determination of the ground movements are numbered as follows:

1. *Define soil properties and excavation geometry*: for each layer of soil determine unit weight, γ_s; undrained shear strength, s_u; effective friction angle, ϕ'; and reference secant modulus, E_s. For multiple layers, make a weighted average to find the soil design parameters for the excavation. Also, define the plan dimensions of the excavation (i.e., width, B, and length, L) and the final excavation depth, H_e.

2. *Define support system parameters*: based on the plan dimensions and the required construction equipment to use in the excavation, define the average vertical and horizontal support spacing (S_V and S_H, respectively) to allow for enough space for accommodation. Generally the vertical support spacing is between 3.0 m and 4.5 m and the horizontal is between $0.5S_V$ and $2.0S_V$. It has to be mentioned that the more struts the more connections; consequently the construction is much more expensive. In addition, define the wall Young's modulus and an initial guess value for the wall moment of inertia per unit length. For sheet pile walls, both parameters are listed by the manufacturer. When a reinforced concrete walls is used, a Young's modulus for the concrete equal to 27.6 GPa is advisable to use in the design. The moment of inertia per unit length for a reinforced concrete wall can be calculated as:

$$I = \frac{1}{12}(1.0 \cdot m)(t^3) \qquad \text{per meter of wall} \tag{5-1}$$

118

where t is the thickness of the retaining wall.

3. *Determined the apparent earth pressure envelope*: from Figure 2.1, determine the shape of the apparent earth pressure diagram. For a layered soil profile, determine which layer of soil is the dominant within the deep of the excavation and use those properties for design, or apply Peck's (1943) equivalent undrained shear strength, $s_{u,av}$, and unit weight, γ_{av}, parameters given by Equations (2-2) and (2-3) or (2-4) and (2-5). As presented in Section 2.1.1, the apparent earth pressures diagrams proposed by Peck (1969) must only be used to size the struts and wales.

4. *Define strut levels*: based on the average vertical support spacing defined in Step 2, define the number of support levels and their respective locations as presented in Figure 5.1.a. It is advisable to have the first support level installed at a depth below the ground surface less than the depth of the tensile crack given by Equation (2-25).

5. *Calculate strut loads*: the two most commonly used methods for calculating the loads in the struts are the internal hinge and the tributary area methods. The internal hinge method assumes a pivot generally located at the midpoint of the excavation depth in order to obtain a statically determinate structure. If it is necessary, more pivot locations can be assumed in order to satisfy statically determinate conditions. The strut load equations obtained after applying equilibrium to the three strut excavation system illustrated in Figure 5.1.a are presented in Figure 5.1.b. The tributary area method is a much more simplified approach where no equilibrium conditions are satisfied. Figure 5.1.c illustrates its procedure and presents the necessary equations for calculating the strut loads using this approach.

119
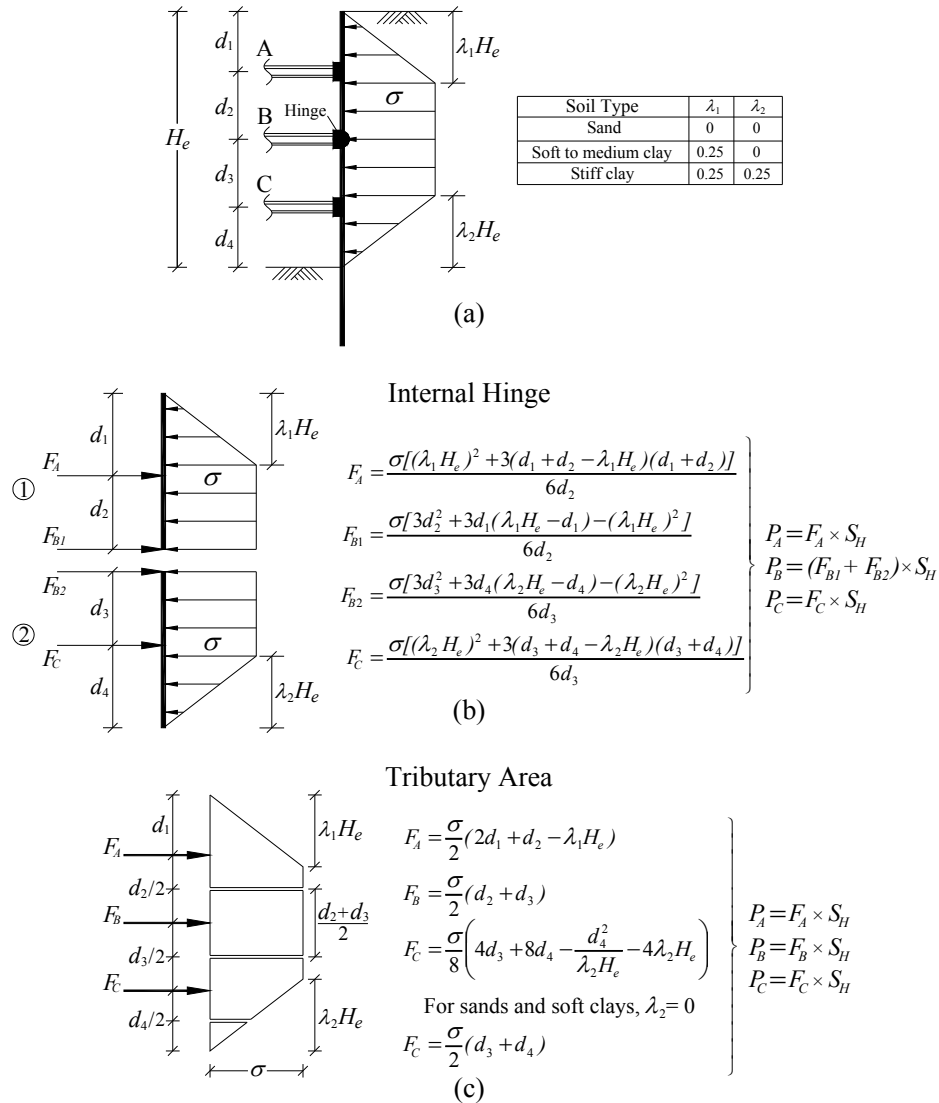
Figure 5.1 - Determination of Strut Loads: (a) Excavation Schematic; (b) Internal Hinge Method; and (c) Tributary Area Method.

6. *Select proper struts sections*: commonly, circular steel pipes are used as horizontal supports in deep excavations because of their symmetry cross section and simplified design. In this step, the struts are sized based on the load and resistance factor design specification for steel hollow structural sections (HSS) presented by the Manual of Steel Construction (AISC, 2001).

First, calculate the required cross section area as:

$$A_{required} = P_u / F_y \tag{5-2}$$

120

where P_u is the required axial strength calculated in Step 5 and F_y is the specified minimum yield strength of the HSS material.

Second, try a round HSS steel section with $A \geq A_{required}$.

Third, assume the value of the effective length factor, K, equal to 1. This value is recommended for horizontal struts in deep excavations by authors like Ou (2006) and Fang (1991).

Fourth, calculate the design compressive strength of the member from AISC (2001) Table 4-7 or as follows:

$$Design\ Compressive\ Strength = \phi_c P_n \tag{5-3}$$

where ϕ_c is a resistance factor taken equal to 0.85 and P_n is the nominal axial strength of the HSS element calculate as:

$$P_n = F_{cr} A_g \tag{5-4}$$

In Equation (5-4), A_g is the gross area of the HSS cross-section and F_{cr} is the critical stress for column buckling computed from:

$$F_{cr} = Q\left(0.658^{Q\lambda_c^2}\right)F_y \qquad \text{for} \qquad \lambda_c\sqrt{Q} \leq 1.5 \tag{5-5}$$

$$F_{cr} = \left[\frac{0.877}{\lambda_c^2}\right]F_y \qquad \text{for} \qquad \lambda_c\sqrt{Q} > 1.5 \tag{5-6}$$

where the column slenderness, λ_c, is:

$$\lambda_c = \frac{Kl}{r\pi}\sqrt{\frac{F_y}{E}} \tag{5-7}$$

and the effective area factor, Q, is:

$$Q = 1 \qquad \text{for} \qquad \lambda \leq 0.114\,E/F_y \tag{5-8}$$

$$Q = \frac{0.0379E}{F_y \left(D_{pipe} / t_{pipe} \right)} + \frac{2}{3} \quad \text{for} \quad 0.114 \, E/F_y < \lambda < 0.448 \, E/F_y \quad\quad (5\text{-}9)$$

In Equations (5-7) to (5-9), λ $(= D_{pipe} / t_{pipe})$ is the wall slenderness ratio, D_{pipe} is the outside diameter of the cross-section, t_{pipe} is the wall thickness of the cross-section, l is the unsupported length of the member, E is the elasticity modulus of the material, and r is the radius of gyration.

Finally, check that $\phi_c P_n \geq P_u$.

7. *Calculate the maximum moment in the wales*: the wales may be treated as a continuous horizontal member if they are spliced properly. They may also be treated as though they are pinned at the struts, but this is a very conservative approach. Even though, the load distribution in the wales is not uniform (Fang, 1991), it can be approximated as a uniform load with magnitude F_i as shown in Figure 5.2. Fang (1991) suggests that the maximum bending moment for the wales be calculated as:

$$M_{max} = \frac{F_i \times S_H^2}{10} \quad\quad \text{(For 3 or less spans)} \quad\quad (5\text{-}10)$$

$$M_{max} = \frac{F_i \times S_H^2}{12} \qu\quad\quad \text{(For more than 3 spans)} \qu\quad\quad (5\text{-}11)$$

where S_H is the horizontal support spacing and F_i is the load per unit length at the wale level *ith* which was previously calculated in Step 5.

Equation (5-10) assumes partially fixed connections and Equation (5-11) assumes that the wales are supported as a continuous beam.
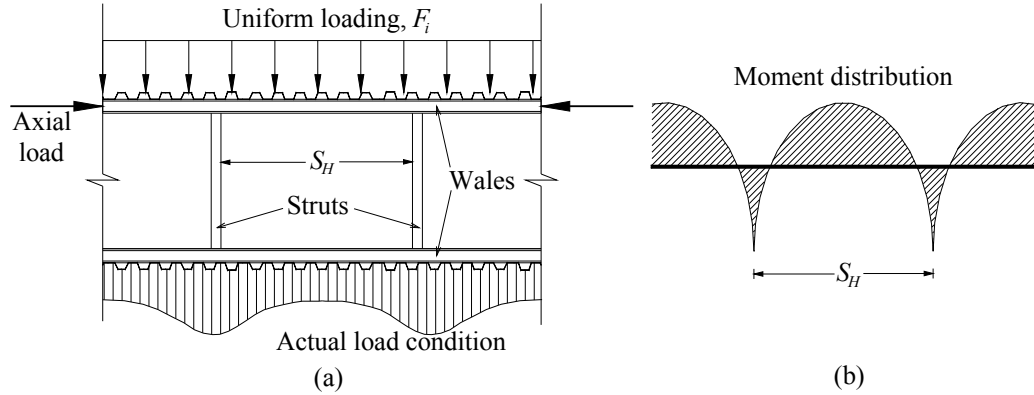
Figure 5.2 - Determination of Wale Bending Moments: (a) Excavation Plan View; and (b) Bending Moment at the Wales (Adapted from Fang, 1991).

8. *Calculate the required wale section modulus*: the required section modulus of the wales is calculated as:

$$S_{req} = \frac{M_{max}}{\sigma_{all}} \qquad (5\text{-}12)$$

where M_{max} is the maximum bending moment at the wale (calculated in Step 7) and σ_{all} is the allowable flexural stress of the wale material.

9. *Size the wales*: to size the wales, just choose a W steel section such as $S_{wale} \geq S_{req}$.

10. *Determine the wall design earth pressure*: (see Section 2.1.4).

11. *Calculate the required wall embedment depth*: once the strut loads and the wall design earth pressure are determined from Steps 5 and 10, respectively, find the required wall embedment, D, by solving Equation (5-13). This equation is found by applying moment equilibrium at the wall toe of the system shown in Figure 5.3.

$$a_1 D^3 + a_2 D^2 + a_3 D + a_4 = 0 \qquad (5\text{-}13)$$

Where:

$$a_1 = \gamma_s \left(K_p - K_a \right) \qquad (5\text{-}14)$$

$$a_2 = 2c \left(K_{ac} + 3K_{pc} \right) - 3\gamma_w \left(H_e - d_w \right) - 3\gamma_s H_e K_a \qquad (5\text{-}15)$$

123

$$a_3 = 6(F_A + F_B + F_C) + 4cH_eK_{ac} - 3\gamma_s H_e^2 K_a - 3\gamma_w(d_w - H_e)^2 \qquad (5\text{-}16)$$

$$a_4 = 6[F_A(H_e - d_1) + F_B(d_3 + d_4) + F_C d_4] + H_e^2(2cK_{ac} - \gamma_s H_e K_a) \\ + \gamma_w(d_w - H_e)^3 \qquad (5\text{-}17)$$

$$\sigma_p = \sigma_v K_p + 2cK_{pc} \qquad\qquad \sigma_a = \sigma_v K_a - 2cK_{ac}$$

Figure 5.3 - Determination of Wall Embedment Depth.

12. *Calculate the maximum wall bending moment*: Once D is determined, find the maximum bending moment in the wall, M_{max}, by applying static equilibrium to the system shown in Figure 5.3.

13. *Calculate the required wall section modulus*: the required section modulus of the wall is calculated in the same form as for the wales:

$$S_{req} = \frac{M_{max}}{\sigma_{all}} \qquad (5\text{-}18)$$

where M_{max} is the maximum bending moment at the wall (calculated in Step 12) and σ_{all} is the allowable flexural stress of the wall material.

14. *Size the wall*: from the sheet pile wall section properties tables provided by the fabricant, choose a sheet pile wall such as $S_{wall} \geq S_{req}$. If the required wall section modulus is so

124

big to be satisfied by commercial sheet pile walls, a reinforced concrete wall is needed. To size this type of wall, first, assume the thickness, t, of the wall. Typical diaphragm walls have thicknesses between 0.6 m and 1.0 m. Second, calculate the nominal bending moment capacity, M_n, of the section based on reinforced concrete theory. Finally, check that $0.9 \times M_n \geq M_{max}$.

15. *Calculate the factor of safety against basal heave*: use Equation (2-27) which includes the wall embedment depth below the excavation level.

16. *Check the factor of safety value*: it is advisable to have a factor of safety against basal heave, FS, higher than 1.5. If the computed FS is less than 1.5, go back to Step 11 and increase the wall embedment depth below the excavation level until an adequate factor of safety is obtained.

17. *Calculate relative stiffness ratio, R*: use Equation (4-1) to calculate *R*.

18. *Predict the maximum horizontal wall deformation, $\delta_{H(max)}$*: use Figure 4.14 to calculate $\delta_{H(max)}$.

19. *Predict the maximum vertical settlement, $\delta_{V(max)}$*: use Equation (4-5) to calculate $\delta_{V(max)}$.

20. *Compute perpendicular ground movement profiles*: for the horizontal wall deformation profiles, use the empirical three-linear plots presented in Figure 4.18. For the vertical settlement profiles, use the proposed profiles presented in Figures 4.22, 4.23 and 4.24 for stiff, medium, and soft clay, respectively. Alternatively, the empirical settlement profiles presented by Ou et al (1993) and Hsieh and Ou (1998) (Figures 2.10 and 2.11, respectively) can be used.

21. *Compute parallel ground movement profiles*: (see section 2.5.2).

22. *Check if the ground movements are acceptable*: based on the allowable soil movements of adjacent infrastructure, define if the obtained ground movements are admissible. If they

are not, go back to Step 2 and redefine the support system parameters. If vertical and horizontal support spacing can not be changed due to space limitation for construction equipment, increase the stiffness of the retaining wall.

The above 22 design steps are summarized in Figure 5.4. It becomes the new iterative methodology for designing excavation support systems based on deformation control.
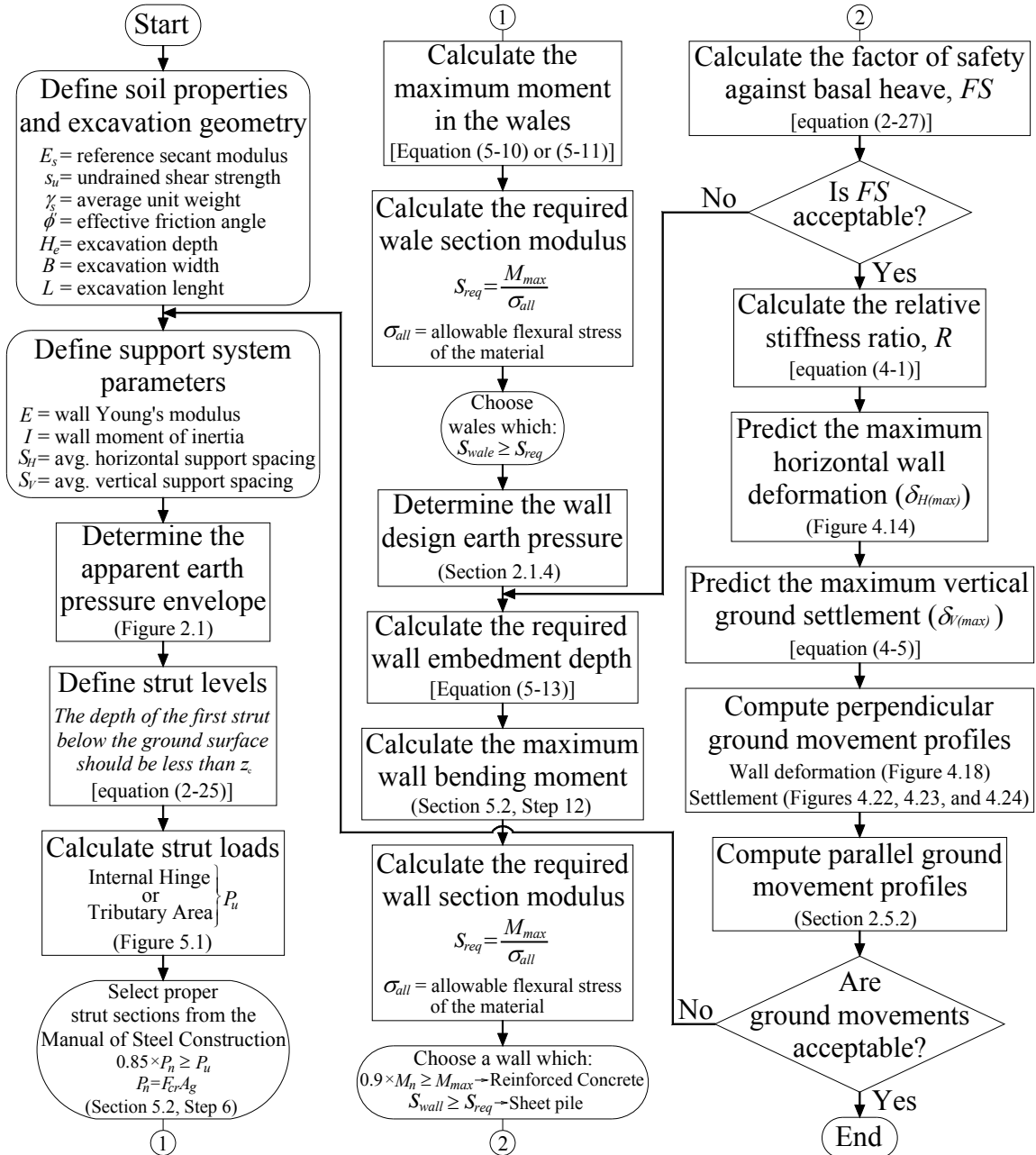

Figure 5.4 - Iterative Method for Designing Excavation Support Systems (Flow Chart).

126

5.3 Direct Method for Designing Excavation Support Systems

This section presents a procedure for designing excavation support systems starting from maximum ground movements defined from the allowable soil distortion of adjacent infrastructure. The retaining wall is sized based on the design chart proposed in Section 4.4.1 and designed to resist the maximum bending moment calculated based on the specified deformation.

5.3.1 Maximum Bending Moment in Retaining Walls

The bending moment in the wall is derived from the fundamental relations of mechanics of materials and the classical theory of beams. It is expressed as:

$$M = -\kappa EI \tag{5-19}$$

where M is the bending moment, κ is the curvature, E is the elasticity modulus of the material, and I is the moment of inertia of the cross-section. From calculus, the curvature of a beam expressed in terms of its displacements is given by the relation:

$$\kappa = \frac{1}{\rho} = \frac{\dfrac{d^2\delta_H}{dz^2}}{\left[1+\left(\dfrac{d\delta_H}{dz}\right)^2\right]^{3/2}} \tag{5-20}$$

where δ_H is the displacement and z is the abscissa along the element.

Assuming that all transverse deflections, rotations, and strains along the member are small so that the principle of superposition is applicable, the term $(d\delta_H/dz)^2$ can be approximated to zero yielding Equation (5-20) to:

$$\kappa = \frac{1}{\rho} \approx \frac{d^2\delta_H}{dz^2} \tag{5-21}$$

127

Substituting Equation (5-21) into (5-19), the following expression is obtained:

$$M = -EI \frac{d^2 \delta_H}{dz^2} \tag{5-22}$$

which is the classical equation that relates the internal bending moment and the components of translation of the member.

Introducing the following non-dimensional terms: $\overline{\delta}_H = \delta_H / \delta_{H(max)}$ and $\overline{z} = z / H$, Equation (5-22) becomes:

$$\overline{M} = \frac{M \times H^2}{EI \times \delta_{H(max)}} = -\frac{d^2 \overline{\delta}_H}{d\overline{z}^2} \tag{5-23}$$

Equation (5-23) is the non-dimensional bending moment expression to be used in this analysis to design the retaining walls of excavation support systems.

In order to determine the bending moment in the retaining wall, an expression for lateral deformation along the member is needed. For this purpose, the empirical lateral wall deformation profiles presented in Section 4.4.2 are used. A six-order polynomial function having the form of Equation (5-24) was fitted to each soil type.

$$\overline{\delta}_H(\overline{z}) = A_1(\overline{z})^6 + A_2(\overline{z})^5 + A_3(\overline{z})^4 + A_4(\overline{z})^3 + A_5(\overline{z})^2 + A_6(\overline{z}) + A_7 \tag{5-24}$$

To find the constants A_1 to A_7, seven different conditions are needed. Based on the shape of the three-linear plots presented in Figure 4.18 and assuming that the bending moment at the top of the wall is equal to zero, the following conditions were applied.

For stiff clay:

$$\overline{\delta}_H(0) = 0.45 \qquad \text{at} \qquad \overline{z} = 0 \tag{5-25}$$

$$\overline{\delta}_H(0.5) = 1 \qquad \text{at} \qquad \overline{z} = 0.5 \tag{5-26}$$

$$\overline{\delta}_H(1) = 0.1 \qquad \text{at} \qquad \overline{z} = 1 \tag{5-27}$$

128

$$\overline{\delta}_H(1.2) = 0 \qquad \text{at} \qquad \overline{z} = 1.2 \tag{5-28}$$

$$\frac{d\overline{\delta}_H(0.5)}{d\overline{z}} = 0 \qquad \text{at} \qquad \overline{z} = 0.5 \tag{5-29}$$

$$\frac{d\overline{\delta}_H(1.2)}{d\overline{z}} = 0 \qquad \text{at} \qquad \overline{z} = 1.2 \tag{5-30}$$

$$\frac{d^2\overline{\delta}_H(0)}{d\overline{z}^2} = 0 \qquad \text{at} \qquad \overline{z} = 0 \tag{5-31}$$

For Medium clay:

$$\overline{\delta}_H(0) = 0.1 \qquad \text{at} \qquad \overline{z} = 0 \tag{5-32}$$

$$\overline{\delta}_H(0.55) = 1 \qquad \text{at} \qquad \overline{z} = 0.55 \tag{5-33}$$

$$\overline{\delta}_H(1) = 0.1 \qquad \text{at} \qquad \overline{z} = 1 \tag{5-34}$$

$$\overline{\delta}_H(1.2) = 0 \qquad \text{at} \qquad \overline{z} = 1.2 \tag{5-35}$$

$$\frac{d\overline{\delta}_H(0.55)}{d\overline{z}} = 0 \qquad \text{at} \qquad \overline{z} = 0.55 \tag{5-36}$$

$$\frac{d\overline{\delta}_H(1.2)}{d\overline{z}} = 0 \qquad \text{at} \qquad \overline{z} = 1.2 \tag{5-37}$$

$$\frac{d^2\overline{\delta}_H(0)}{d\overline{z}^2} = 0 \qquad \text{at} \qquad \overline{z} = 0 \tag{5-38}$$

For soft clay:

$$\overline{\delta}_H(0) = 0.1 \qquad \text{at} \qquad \overline{z} = 0 \tag{5-39}$$

$$\overline{\delta}_H(0.425) = 1 \qquad \text{at} \qquad \overline{z} = 0.425 \tag{5-40}$$

$$\overline{\delta}_H(0.9) = 0.1 \qquad \text{at} \qquad \overline{z} = 0.9 \tag{5-41}$$

$$\overline{\delta}_H(1.1) = 0 \qquad \text{at} \qquad \overline{z} = 1.1 \tag{5-42}$$

$$\frac{d\overline{\delta}_H(0.425)}{d\overline{z}} = 0 \quad \text{at} \qquad \overline{z} = 0.425 \tag{5-43}$$

129

$$\frac{d\bar{\delta}_H(1.1)}{d\bar{z}} = 0 \quad \text{at} \quad \bar{z} = 1.1 \tag{5-44}$$

$$\frac{d^2\bar{\delta}_H(0)}{d\bar{z}^2} = 0 \quad \text{at} \quad \bar{z} = 0 \tag{5-45}$$

Substituting Equation (5-24) and its respective derivatives in Equations (5-25) to (5-31), which are the conditions applied for stiff clay, and organizing in matrix form, we get:

$$[B]\{X\} = \{b\} \tag{5-46}$$

where:

$$[B] = \begin{bmatrix} 0 & 0 & 0 & 0 & 0 & 0 & 1 \\ 0.0156 & 0.0313 & 0.0625 & 0.125 & 0.25 & 0.5 & 1 \\ 1 & 1 & 1 & 1 & 1 & 1 & 1 \\ 2.986 & 2.4883 & 2.0736 & 1.728 & 1.44 & 1.2 & 1 \\ 0.1875 & 0.3125 & 0.5 & 0.75 & 1 & 1 & 0 \\ 14.9299 & 10.368 & 6.912 & 4.32 & 2.4 & 1 & 0 \\ 0 & 0 & 0 & 0 & 2 & 0 & 0 \end{bmatrix} ; \{X\} = \begin{Bmatrix} A_1 \\ A_2 \\ A_3 \\ A_4 \\ A_5 \\ A_6 \\ A_7 \end{Bmatrix} ; \text{ and } \{b\} = \begin{Bmatrix} 0.45 \\ 1 \\ 0.1 \\ 0 \\ 0 \\ 0 \\ 0 \end{Bmatrix}.$$

Solving Equation (5-46) as $\{X\} = [B]^{-1}\{b\}$, the constants A_1 to A_7 are obtained.

$$\{X\} = \begin{Bmatrix} A_1 \\ A_2 \\ A_3 \\ A_4 \\ A_5 \\ A_6 \\ A_7 \end{Bmatrix} = \begin{Bmatrix} -14.2845 \\ 48.2784 \\ -52.6924 \\ 17.6440 \\ 0 \\ 0.7045 \\ 0.45 \end{Bmatrix} \tag{5-47}$$

Finally, substituting A_1 to A_7 into Equation (5-24), the expression for computing the normalized lateral wall movements in stiff clays is obtained:

$$\bar{\delta}_H(\bar{z}) = -14.2845(\bar{z})^6 + 48.2784(\bar{z})^5 - 52.6924(\bar{z})^4 + 17.644(\bar{z})^3 + 0.7045(\bar{z}) + 0.45 \tag{5-48}$$

130

Applying a similar procedure to the one used above for the stiff clay case, Equations (5-49) and (5-50) are obtained for the medium and soft clay cases, respectively.

$$\bar{\delta}_H(\bar{z}) = -20.688(\bar{z})^6 + 70.7792(\bar{z})^5 - 79.5526(\bar{z})^4 + 28.7096(\bar{z})^3 \\ + 0.7517(\bar{z}) + 0.1 \tag{5-49}$$

$$\bar{\delta}_H(\bar{z}) = -14.7492(\bar{z})^6 + 40.5417(\bar{z})^5 - 30.9317(\bar{z})^4 + 2.0419(\bar{z})^3 \\ + 3.0051(\bar{z}) + 0.1 \tag{5-50}$$

Figure 5.5 shows the six-order polynomial function curves fitted for each soil case and compared them with the case history data. The three-linear plots previously defined in Section 4.4.2 are also included. Note that the fitted six-order polynomial functions describe very well the tendency showed by the empirical data.

The non-dimensional bending moment expressions for stiff, medium, and soft clay are found by differentiating twice Equations (5-48), (5-49), and (5-50), respectively, and substituting in Equation (5-23). The obtained expressions are:

For Stiff Clay:

$$\overline{M} = 428.535(\bar{z})^4 - 965.568(\bar{z})^3 + 632.309(\bar{z})^2 - 105.864(\bar{z}) \tag{5-51}$$

For Medium Clay:

$$\overline{M} = 620.64(\bar{z})^4 - 1415.58(\bar{z})^3 + 954.631(\bar{z})^2 - 172.258(\bar{z}) \tag{5-52}$$

For Soft Clay:

$$\overline{M} = 442.476(\bar{z})^4 - 810.834(\bar{z})^3 + 371.18(\bar{z})^2 - 12.2514(\bar{z}) \tag{5-53}$$

The shape for the above non-dimensional moment expressions is presented in Figure 5.6. Note that the locations of the maximum positive moment and maximum displacement are very close. As expected, the moment is zero at the upper end of the wall, and some negative moment is obtained at the embedment portion of the wall.
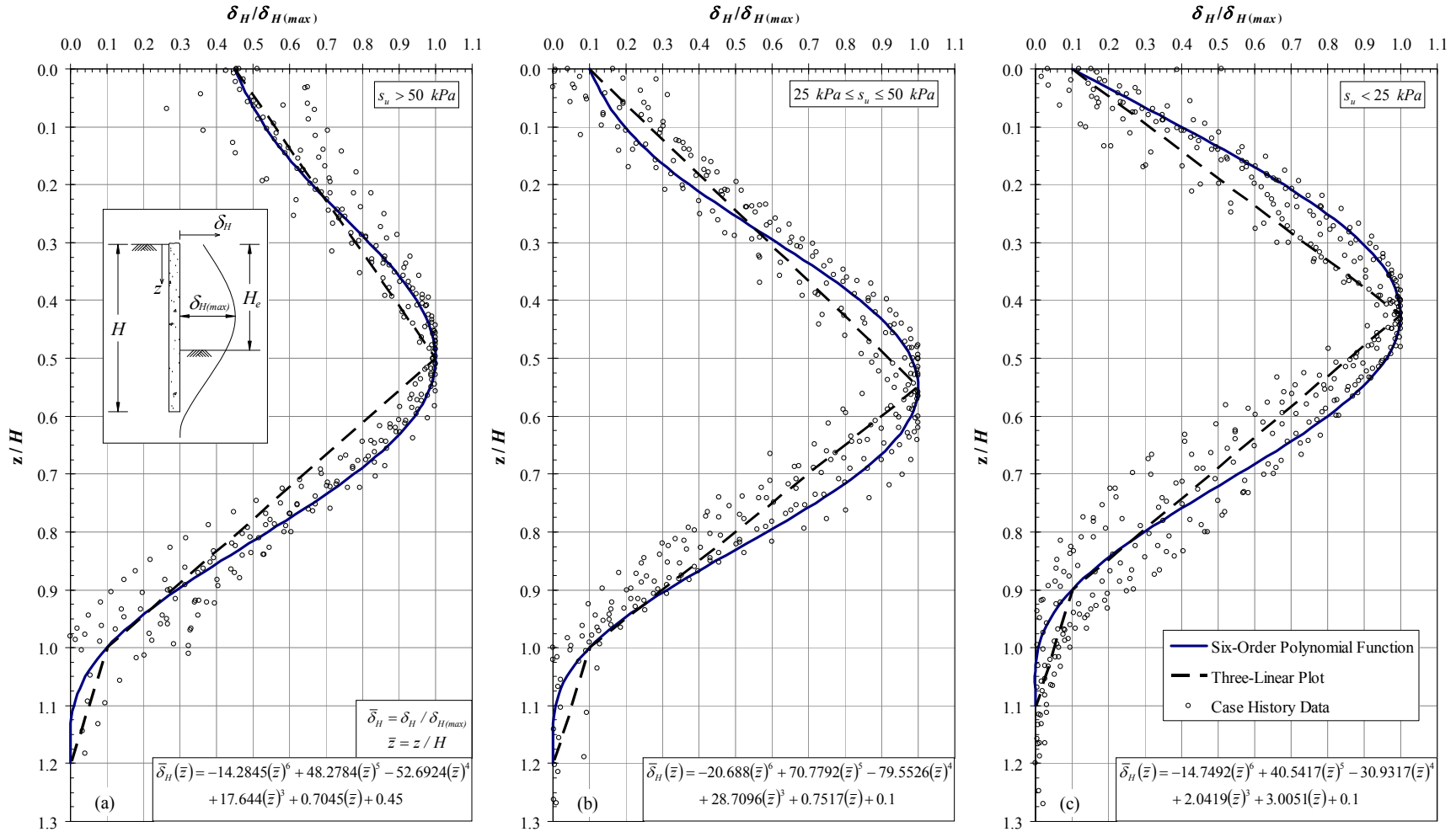
131

Figure 5.5 - Six-Order Polynomial Functions: (a) Stiff Clay; (b) Medium Clay; and (c) Soft Clay.

(a) $s_u > 50 \ kPa$

$$\overline{\delta}_H = \delta_H / \delta_{H(max)}$$
$$\overline{z} = z / H$$

$$\overline{\delta}_H(\overline{z}) = -14.2845(\overline{z})^6 + 48.2784(\overline{z})^5 - 52.6924(\overline{z})^4 + 17.644(\overline{z})^3 + 0.7045(\overline{z}) + 0.45$$

(b) $25 \ kPa \leq s_u \leq 50 \ kPa$

$$\overline{\delta}_H(\overline{z}) = -20.688(\overline{z})^6 + 70.7792(\overline{z})^5 - 79.5526(\overline{z})^4 + 28.7096(\overline{z})^3 + 0.7517(\overline{z}) + 0.1$$

(c) $s_u < 25 \ kPa$

Six-Order Polynomial Function
Three-Linear Plot
Case History Data

$$\overline{\delta}_H(\overline{z}) = -14.7492(\overline{z})^6 + 40.5417(\overline{z})^5 - 30.9317(\overline{z})^4 + 2.0419(\overline{z})^3 + 3.0051(\overline{z}) + 0.1$$

$$\overline{M} = \frac{M \times H^2}{EI \times \delta_{H(max)}}$$
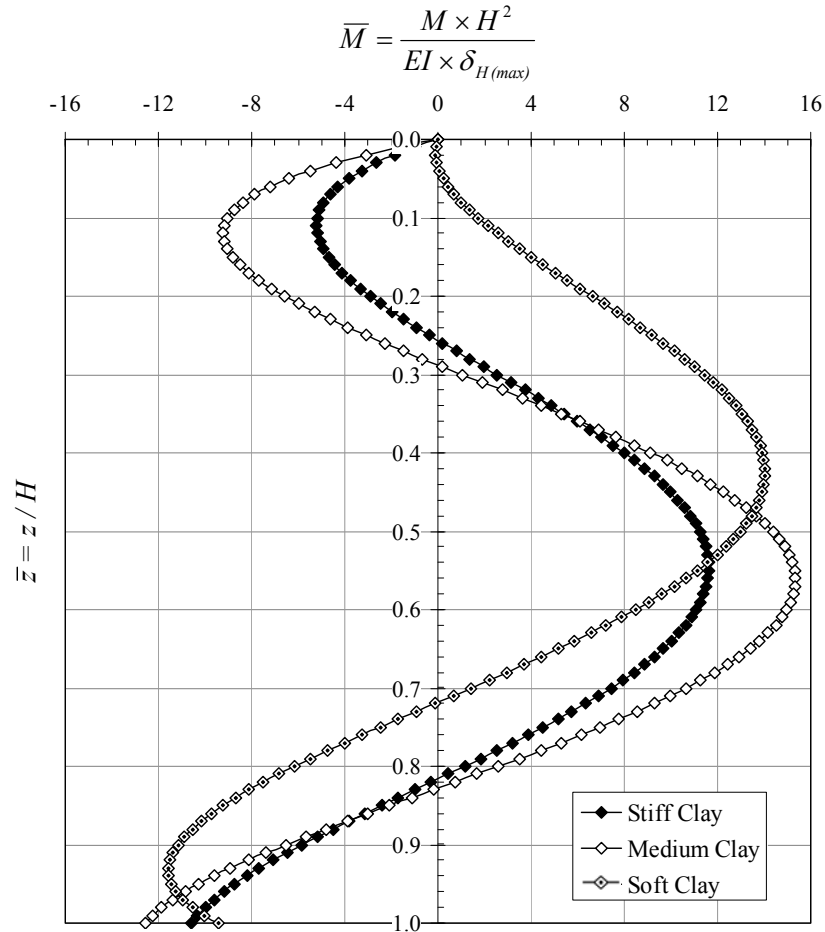

Figure 5.6 - Non-dimensional Bending Moment vs. Normalized Depth.

5.3.2 Design Procedure

The necessary steps for designing an excavation support system based on anticipated ground movements are listed as follows:

1. *Define soil properties and excavation geometry*: (see Section 5.2, Step 1).

2. *Define maximum admissible ground movements*: based on the allowable soil distortion of adjacent infrastructure, define the admissible ground movements $\delta_{V(max)}$ and $\delta_{H(max)}$.

3. *Determine the wall design earth pressure*: (see Section 2.1.4).

4. *Calculate the required wall embedment depth*: (see Section 5.2, Step 11).

5. *Calculate the factor of safety against basal heave*: (see Section 5.2, Step 15).

6. *Check the factor of safety value*: (see Section 5.2, Step 16).

7. *Obtain the required Relative Stiffness Ratio, R*: from Figure 4.14 using the maximum admissible lateral wall deformation, $\delta_{H(max)}$, defined in Step 2, obtain the Relative Stiffness Ratio, *R*.

8. *Calculate the required wall stiffness and support spacing*: first, define the average vertical and horizontal support spacing following the recommendations given in Section 5.2, Step 2. Then, find the required wall stiffness, EI_{req}, from Equation (4-1) as:

$$EI_{req} = \frac{S_H S_V H}{R} \cdot \frac{\gamma_s H_e E_s}{s_u} \tag{5-54}$$

9. *Size the wall*: first, set the value of the elasticity modulus of the wall to 200 GPa for steel or 26.7 GPa for reinforced concrete. Then, find a wall with a moment of inertia such as $EI_{wall} \geq EI_{req}$. It is recommended to try initially with sheet pile walls, which moment of inertia per unit length is specified by the manufacturer. If no commercial sheet pile section meets the stiffness requirement, use a reinforced concrete diaphragm wall. The thickness of the reinforced concrete wall can be found as:

$$t = \sqrt{\frac{12 \times I_{req} \times (m \ of \ wall)}{1 \ m}} \tag{5-55}$$

Where I_{req} must be in units of $m^4/(m \ of \ wall)$.

10. *Maximum Bending Moment*: based on the type of soil use Equation (5-51), (5-52), or (5-53) to calculate the maximum bending moment in the wall for stiff, medium, or soft clays, respectively. It is advisable to check the value of the bending moment with the one calculated using the method proposed and Section 5.2 Step 12.

11. *Check the design wall section*: for reinforced concrete walls, calculate the nominal bending moment capacity, M_n, of the section based on reinforced concrete theory and check that $0.9 \times M_n \geq M_{max}$. For sheet pile walls, calculate the required wall section modulus, S_{req} $(= M_{max}/\sigma_{all})$, and check that $S_{wall} \geq S_{req}$.

12. *Determined the apparent earth pressure envelope*: (see Section 5.2, Step 3).

13. *Design the struts*: (see Section 5.2, Steps 4-6).

14. *Design the wales*: (see Section 5.2, Steps 7-9).

Figure 5.7 summarizes the proposed semi-empirical method for designing excavation support systems based on deformation control. It is a straightforward approach that has as an advantage the time calculation saving by eliminating the iterative process in the design.
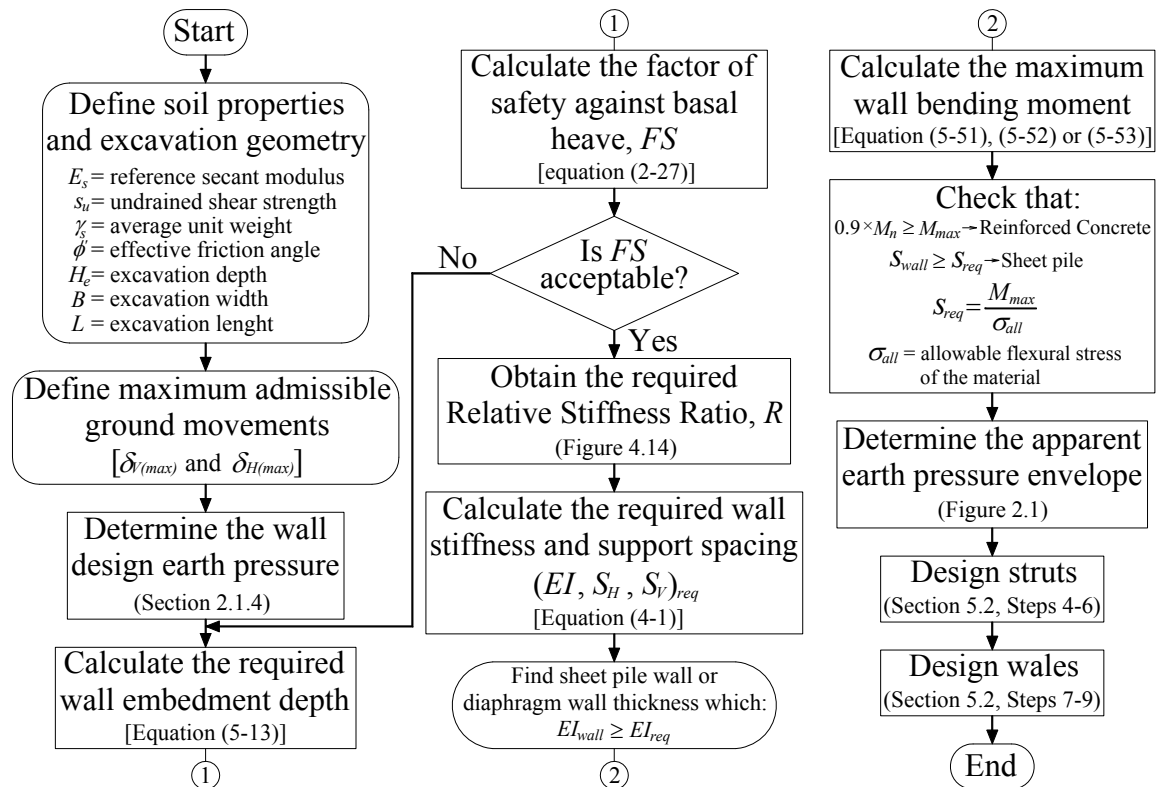

Figure 5.7 - Direct Method for Designing Excavation Support Systems (Flow Chart).

6   SUMMARY AND CONCLUSIONS

6.1   Summary

Excessive excavation-induced movements are a major concern for most underground construction projects in urban areas because these can cause damage or possible collapse in adjacent structures. Consequently, accurate predictions of lateral wall deflections and surface settlements are important design criteria in the analysis and design of excavation support systems. Direct and quantitative predictions of ground movements are not easy tasks. This is not only because of the complexity of the system itself, but also because of the difficulty in modeling the wall installation and excavation processes. Three-dimensional (3D) finite element models are required for a realistic analysis of the interaction between the soil and the excavation support system.

Conventionally, excavation support systems are designed based on structural limit equilibrium preventing structural failure of the support wall. However, these generally result in excessive wall deformations and ground movements. Furthermore, current design methods, which relate ground movements to excavation support system stiffness and basal stability, are based on plane strain analyses that do not represent the real nature of deep excavations.

This research proposed a new deformation-based design methodology based on both observation of real case histories reported worldwide and fully three-dimensional finite element analyses that realistically model the excavation support system and the excavation activities. This semi-empirical approach allows for the design of excavation support systems based on deformation criteria including the influences of the inherent three-dimensional

136

behavior of the excavation support system and the associated excavation. It is expected that the proposed deformation-based methodology will save millions of dollars typically expended in repairs and mitigation of excavation-induced damage to adjacent infrastructure.

Chapter 2 presented a detail literature review concerning the analysis and design of excavation support systems. The available methods for determining earth pressures and calculating factors of safety against basal heave were discussed and the methods for predicting perpendicular and parallel excavation-related ground movements were reviewed. It also provided a review and discussion of the available deformation based design methods and three-dimensional finite element analyses of excavations.

Chapter 3 focused on wall installation effects. First, a complete literature evaluation that includes field observations of ground deformations (lateral and vertical), pore water pressure changes, and lateral earth pressures resulting from wall installation was presented. It also reported on several efforts to include wall installation effects in various numerical models placing particular emphasis on techniques used to simulate the construction methods. In addition, the influences of: (i) the analysis type, (ii) the soil and wall constitutive models employed in the simulation, and (iii) the drainage conditions assumed in the analysis, on the performance of the numerical models were evaluated. Second, the finite element analysis of the wall installation for the Chicago and State excavation case history was presented. Subsurface conditions, adjacent structures, and excavation support system were described in detail. This section also presented features and assumptions made in the finite element model and discussed several attempts to simulate the installation and behavior of the retaining wall.

Chapter 4 showed the three-dimensional effects that the support system stiffness has on the excavation-related ground movements. The deficiencies of the existing methods and

137

charts were shown by comparing with extensive excavation case history data available in the literature and with a new expanded database presented in Appendix C. In the second part of this chapter, the description and results of an extensive parametric study based on fully three-dimensional finite element analyses, carried out to overcome the deficiencies of the actual methods, were presented. At the conclusion of this chapter, a new system stiffness index and design chart that include the inherent three-dimensional nature of the excavation were proposed. In addition, guidelines for determining the magnitude and distribution of final ground movement were given.

Chapter 5 combined empirical and numerical approaches to create a semi-empirical method for designing excavation support systems based on deformation control. The method was illustrated by two flow charts which embrace in an organized means the information contained in chapters 2 to 4. The flow charts allow the designer to predict final ground movements (horizontal and vertical), given data about soil and support system or size all the elements of the excavation support system, given the allowable soil distortion of infrastructure adjacent to the excavation.

6.2   Conclusions

Based on the technical background presented in Chapter 2, the following conclusions can be drawn:

- Excavation support systems are conventionally designed based on anticipated earth pressures calculated from the apparent pressure diagrams developed by Peck (1969). These apparent earth pressure diagrams must only be used to calculate the strut loads and it is incorrect to use them for calculating the stress or bending moments in the retaining wall.

- To design the retaining walls in excavation support systems, the Rankine's earth pressure distribution must be used with some modifications to include the detrimental effects of the tension cracks in cohesive soils and the friction between the retaining wall and the soil that for cast-in place retaining walls is very significant.

- When calculating the factor of safety against basal heave for deep excavations, Equation (2-27) must be used in order to include the beneficial effect of the wall embedment depth below the excavation base.

- Available methods to predict ground movements in excavations, which use system stiffness and basal stability as control parameters, are only based on plane strain analyses and were developed using a limited number of wall types and configurations. In addition, they do not include considerations for soil types, excavation support types and materials, excavation geometry, wall installation effects, construction techniques, and construction sequencing.

- It was noted that the available ground deformation profiles, currently used to calculate perpendicular and parallel ground movement distributions in excavations, are based on empirical observation of case histories with similar soil conditions and do not include the effects of the support system stiffness and factor of safety of the excavation. Consequently, they are only applicable to excavations with similar conditions to the ones use to deduce the profiles.

- It was found that "wish the walls into place" and model them using beam elements is a common design and analysis practice. This is because the implementation of a finite element model that explicitly considers the wall construction is a very difficult task. In addition, based on the several finite element analyses of insitu retaining wall installation that have been reported in the literature, it is difficult to draw any general conclusions

because all the analyses generally differ in ground conditions and wall geometries. Furthermore, their results are presented in different ways making very difficult to correlated them.

- Fully three-dimensional finite element analyses of deep excavations are rarely performed by the engineer during the design process because of their complexity and time-cost constraints. In addition, it was found that no one has presented in the technical literature a design methodology for excavation support systems that relates system stiffness to excavation-related ground movements incorporating the three-dimensional nature of the excavation.

Based on the analyses for quantifying wall installation effects and the three-dimensional finite element simulation of the Chicago and State excavation case history presented in Chapter 3, the following conclusions can be made regarding the wall installation for excavation support systems:

- Deformations associated with wall installation can comprise 25 to 30 percent of the total excavation-induced movements observed, depending on wall type, wall dimensions, soil type, and construction techniques. In addition, these parameters also significantly affect the pre-excavation insitu effective stresses.

- The "true" 3D analyses, which is the only one capable of modeling the downward load transfer and the horizontal arching mechanisms, match the field data more closely than the plane strain or pseudo 3D analyses.

- The results of the evaluation presented in Chapter 3 confirm that it is essential to include the wall installation effects in any performance prediction model, especially at sites where sensitive structures are nearby. In addition, further work is needed in the development of

prediction tools for estimating horizontal movements and stresses due to the wall installation processes.

Based on the results presented in Chapter 4, the following conclusion can be drawn regarding the three-dimensional influences of system stiffness:

- Lateral deformations in stiff clays and in soft to medium clays with an adequate factor of safety against basal heave are largely independent of the system stiffness of the wall. Consequently, flexible retaining walls, which are generally cheaper, can be used for deep excavation on these soils without expecting excessive ground movements.

- For excavations in soft to medium clays with low factors of safety against basal heave, the stiffening effects of the excavation corners and the beneficial effect of the wall embedment depth on the factor of safety play an important role in the excavation performance. For these soils, the wall stiffness is one of the key parameters that the designer has to control ground movements.

- For excavations in soft to medium clays, the inclusion of the wall embedment depth generally increases the factor of safety against basal heave. In contrast, for excavations in stiff clays, the wall embedment depth has no significant contribution to the stability of the excavation system.

- The variation in the horizontal and vertical support spacing does not have a significant effect in the lateral wall deformations of excavation support systems. It was found that wall stiffness is a much more predominant factor for controlling ground movements.

- It was shown that in the Clough et al. (1989) system stiffness factor ($EI/\gamma_w h_{avg}^4$), the vertical support spacing is a very sensitive parameter that can increase significantly the value of the system stiffness. However, this increase in the system stiffness is not reflected in the final lateral wall deformations which stay almost unchanged. It was also

141

shown that the Clough et al. (1989) system stiffness factor does not represent the real nature of deep excavations and must be rewritten.

- The Clough et al. (1989) design chart, where the system stiffness ($EI/\gamma_w h_{avg}^4$) and the factor of safety given by Equation (2-26) are the only control parameters, must be used just as an approach to roughly estimate the horizontal wall displacements in soft to medium cohesive soils at the early stages of the design and not as a design tool to calculate the final movements in deep excavations where sensitive structures are nearby.

- The proposed design chart (Figure 4.14), which includes the inherent three-dimensional nature of the excavation and the wall embedment depth below the excavation base, allows the designer to predict maximum lateral wall movements for deep excavations in clays based on the proposed relative stiffness ratio, R, and the factor of safety, FS, given by Equation (2-27). These two parameters can be easily defined using simple soil data and excavation geometry.

- The empirical three-linear plots proposed in Figure 4.18 allow the designer to predict the shape of the lateral wall deformations by knowing the maximum horizontal wall displacement and the height of the wall. These empirical profiles are suitable for deep excavations in stiff, medium, and soft clays.

- Equation (4-5) overcomes the limitations of Equation (2-30) by including the factor of safety against basal heave, FS, and the relative stiffness ratio, R, in the relationship between the maximum vertical ground settlement, $\delta_{V(max)}$, and the maximum lateral wall displacement, $\delta_{H(max)}$, for deep excavations in clays.

The semi-empirical method for designing excavation support systems based on deformation control proposed in Chapter 5 is the first method capable to assist the engineer

142

in all the necessary design steps. It allows the designer to predict final ground movements, given data about soil and support system or size all the elements of the excavation support system, given the allowable soil distortion of adjacent structures including the inherent three-dimensional nature of the excavation. It is important to mention that the new design procedures proposed in this investigation must be verified and validated with real case history data.

A   THREE-DIMENSIONAL (3D) FINITE ELEMENT ANALYSIS OF THE WALL

INSTALLATION AT THE CHICAGO AND STATE STREET EXCAVATION

A.1 Introduction

A complete three-dimensional (3D) finite element analysis of the wall installation at the Chicago and State Street excavation, reported by Bryson (2002), Finno and Bryson (2002), and Finno et al. (2002), is presented herein. The finite element software PLAXIS 3D FOUNDATION version 2.0 was used to model the Francis Xavier Warde School, the Chicago and State Street Subway Tunnel-Station, and the construction sequence of the secant pile wall.

This appendix presents features and modeling assumptions made for the four different components (soil, tunnel, school, and wall) included in the finite element model. Furthermore, the calculation phases employed for each component, the material properties assumed for the elements, and the generation of the finite element mesh used are fully described and presented.

A.2 Modeling the Tunnel

Terzaghi (1943b) described the construction methods and procedures for the original Chicago subway project. The construction began on December 17, 1938 and concluded when it was opened to the public on October 17, 1943. The tunneling method used at the Chicago and State Street excavation site was the liner-plate method. According to Figure A.1.a, excavation started at the crown and ended with the excavation of the invert section. The ribs consisted of I-beams (6 in × 17.25 lb/ft steel sections spaced 2 to 2.5 ft on centers) and were installed in sections starting at the crown. Figure A.1.b shows section view of the concrete permanent liner system. Note that the liner thicknesses at the crown, mid-height, and bottom are 2, 2.5, and 2.66 ft, respectively.
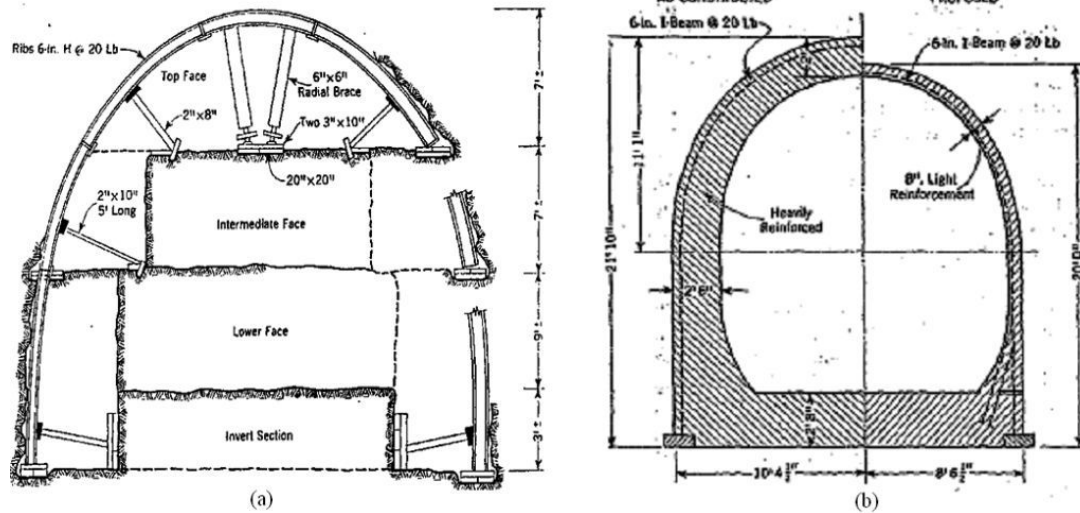
145

Figure A.1 - (a) Characteristics of Tunneling Operations; and (b) Permanent Liner (After Terzaghi, 1943b).

A.2.1   Temporary Support System

Figure A.2 shows a representation of the temporary support system used for the construction of the Chicago subway and the equivalent system employed in the analysis. Also included in the figure are the section properties of the steel sections used as ribs.
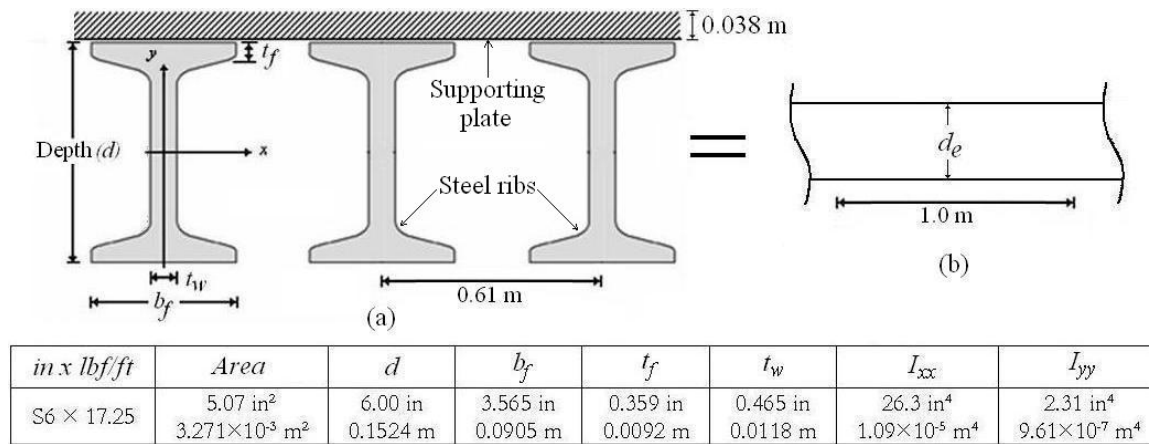

in x lbf/ft	Area	d	b_f	t_f	t_w	I_{xx}	I_{yy}
S6 × 17.25	5.07 in² 3.271×10⁻³ m²	6.00 in 0.1524 m	3.565 in 0.0905 m	0.359 in 0.0092 m	0.465 in 0.0118 m	26.3 in⁴ 1.09×10⁻⁵ m⁴	2.31 in⁴ 9.61×10⁻⁷ m⁴

Figure A.2 - Schematic of Temporary Support System: (a) actual; and (b) Equivalent.

The temporary rib support system presented in Figure A.2.a was modeled using floor and wall elements in PLAXIS 3D FOUNDATION. The equivalent thickness (see Figure A.2.b) for the model elements was found as follows:

First, the actual stiffness for the temporary support system configuration presented in Figure A.2.a is calculated as:

$$(EI)_{actual} = E_s I_{actual} \qquad (A-1)$$

where E_s is the elastic modulus of steel and I_{actual} is the moment of inertia per unit length of the temporary support system which is approximated as:

$$I_{actual} = 1.09 \times 10^{-5} \ m^4 / 0.61 \ m \qquad \Rightarrow \qquad I_{actual} = 1.79 \times 10^{-5} \ m^4 / m$$

Second, the stiffness for the equivalent floor element presented in Figure A.2.b, assuming that the element is made of the same material, is calculated as:

$$(EI)_{eq} = E_s I_{eq} \qquad (A-2)$$

where I_{eq} is the moment of inertia per unit length of the equivalent temporary support system which can be approximated as:

$$I_{eq} = \frac{1}{12}(1 \ m)(d_e^3)/m$$

Finally, assuming that the elastic modulus of steel, $E_s = 2 \times 10^8 \ kPa$, and making $(EI)_{actual} = (EI)_{eq}$, it is found that $d_e = 60 \ mm$. However, note that the supporting plate shown in Figure A.2.a was no included in the stiffness of the temporary support system. Then, to account for it, the equivalent thickness, d_e, is adjusted as:

$$d_e = 60 \ mm + 38 \ mm \qquad \Rightarrow \qquad d_e = 98 \ mm$$

A.2.2   Permanent Support System

The shape of the subway concrete liner at the Chicago and State excavation site can be seen in Figure 3.13, which shows a section view of the excavation support system. For modeling purposes, the shape of the tunnel was approximate to straight elements as shown

in Figure A.3. Note that just horizontal and vertical members were used because PLAXIS 3D FOUNDATION does not allow the input of inclined planes. Vertical members were modeled as wall elements and horizontal members as floor elements assuming an elastic modulus of concrete, $E_c = 21 \times 10^6 \ kPa$.
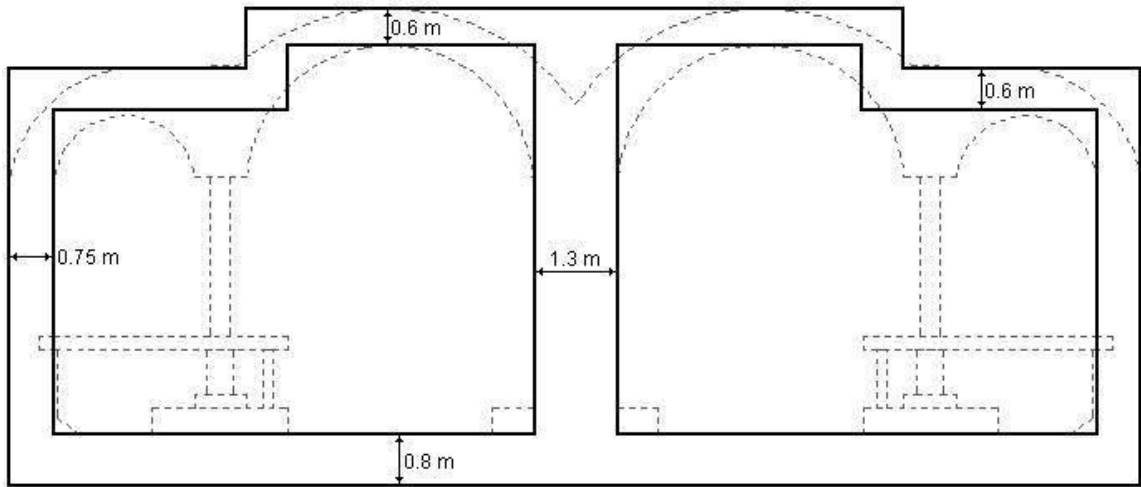
Figure A.3 - Permanent Support Liner.

A.3   Modeling the School

As presented in Section 3.3.2.2, the Warde School is a 3-story concrete frame building supported on shallow foundations. The floor slabs are supported by columns at interior locations and masonry bearing walls around the perimeter. The interior columns rest on reinforced concrete spread footings, which are 0.76-m-thick and vary in size from 3 by 3 m to 4.5 by 4.5 m. The bearing walls rest on a 2.75-m-tall reinforced concrete basement wall, which is supported by a 0.2-m-thick and 1.2-m-wide continuous footing. The average depth of the foundations was found to be at 3.7 m below ground surface (i.e. +0.6 m CCD). Figure A.4 shows a plan view of the school's foundation and indicates the input footing loads used in the PLAXIS 3D FOUNDATION simulation. The footing loads were reported by Bryson (2002) who presented a complete three-dimensional SAP2000 model of the school structure.

148

Floor and wall elements were used to model the footings and reinforced concrete basement wall, respectively. In addition, a floor slab resting on the ground at an elevation of +1.5 m CCD was included in the analysis to model the final basement floor and avoid basal heave of the soil. An elastic modulus of concrete, $E_c = 25 \times 10^6 \ kPa$, was assumed for all the elements of the school.
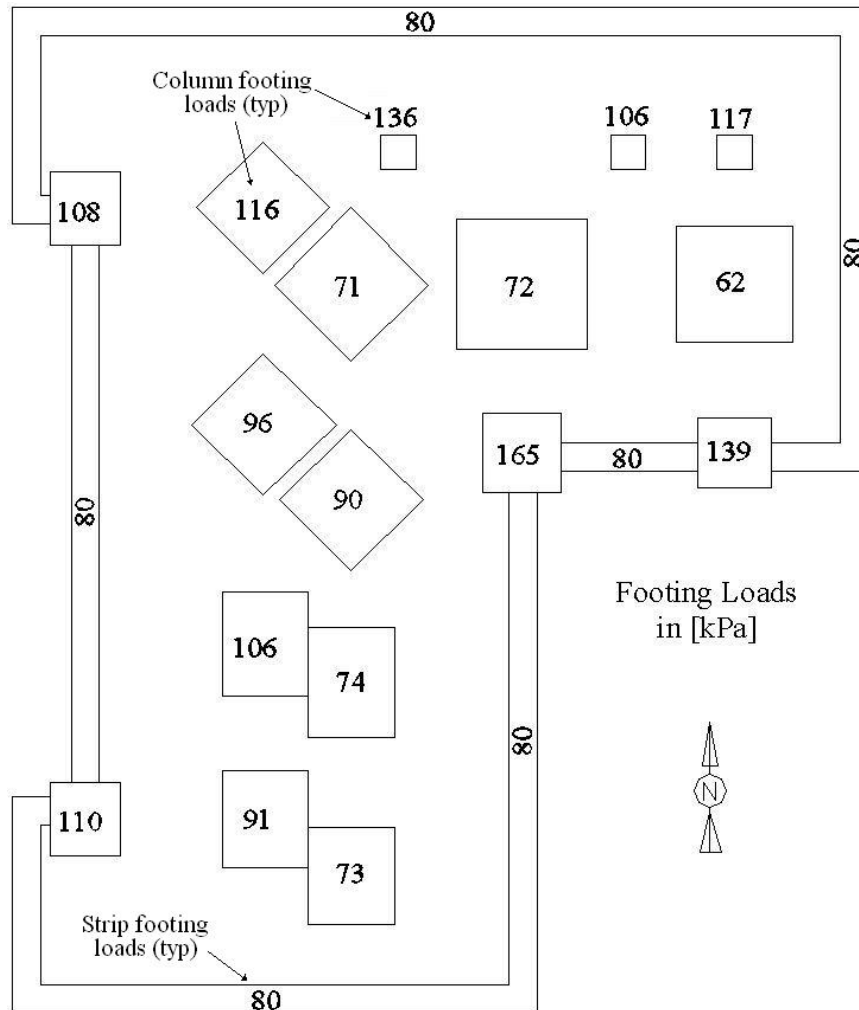

Figure A.4 - Frances-Xavier Warde School Foundation Plan and Applied Loads.

A.4   Modeling the Wall Installation

The secant pile wall was constructed with overlapping 915-mm-diameter, 18.3-m-long drilled shafts filled with 7-MPa-strength concrete. Each shaft overlapped adjacent shafts by

149

150 mm. W24×55 steel sections were placed in alternating shafts to provide additional stiffness to the wall. Figure A.5.a shows a scheme of the constructed secant pile wall. Because of the high number of elements required to model circular slots and the consequent increase in calculation time and modeling effort, a simplified geometry model was used to model the secant pile wall (see Figure A.5.b).
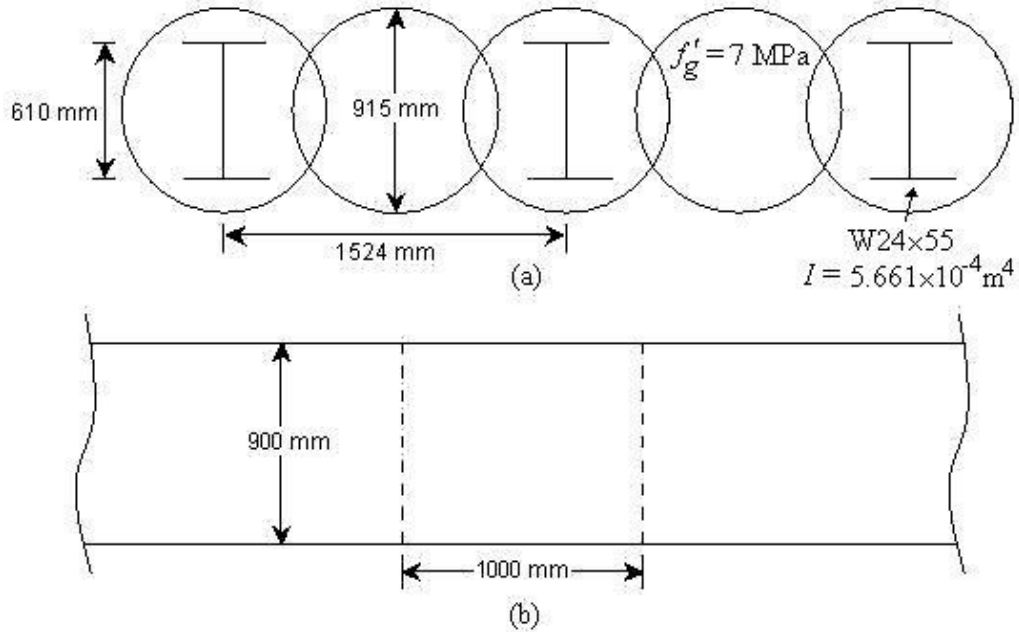
Figure A.5 - Secant Pile Wall: (a) as Constructed; (b) as Modeled in PLAXIS.

The wall was modeled as a 0.9-m-wide trench with the length varying as presented in Section 3.3.3.2 and an equivalent elastic stiffness modulus calculated as:

$$E_{eq} = \frac{E_s I_s + E_g I_g}{I_{eq}} , \qquad\qquad (A-3)$$

where I_s, I_g, and I_{eq} are the moments of inertia per unit length of wall of the steel section, concrete grout, and equivalent section, respectively; $E_s = 2 \times 10^8 \ kPa$ is the elastic modulus of steel and E_g is the elastic modulus of the concrete grout calculated from the following expression:

$$E_g = 4{,}780\sqrt{f'_g} \ \text{(MPa)} \qquad \text{[ACI 318-02 section 8.5]} \qquad\qquad \text{(A-4)}$$

Then, from Figure A.5, the properties of a W24×55 steel section ($I = 5.661 \times 10^{-4}\,m^4$), and for a $f'_g = 7\ MPa = 1000\ psi$, the following parameter can be found:

$$E_g = 4{,}780\sqrt{7} \qquad\qquad\qquad \Rightarrow \qquad E_g = 12.65 \times 10^6\,kPa$$

$$I_s = \frac{5.661 \times 10^{-4}\,m^4}{1.524\ m} \qquad\qquad \Rightarrow \qquad I_s = 3.715 \times 10^{-4}\,m^4/m$$

$$I_g = \frac{\pi}{4}\left(\frac{0.915\ m}{2}\right)^4 \times \frac{1}{0.915\ m} \qquad \Rightarrow \qquad I_g = 3.76 \times 10^{-2}\,m^4/m$$

$$I_{eq} = \frac{1}{12}(1\ m) \times (0.9\ m)^3 \times \frac{1}{1\ m} \qquad \Rightarrow \qquad I_{eq} = 0.0607\ m^4/m$$

Finally, from Equation (A-3) the elastic stiffness modulus of the equivalent material is calculated as: $E_{eq} = 8.9 \times 10^6\ kPa$.

The installation of a single segment of the wall was simulated in PLAXIS 3D FOUNDATION using two staged construction calculations. In the first calculation stage, the soil within the trench was removed and loads per unit area were applied to the expose faces of the trench. These loads modeled the hydrostatic pressure of a fluid (water or bentonite) acting on the faces of the excavated trench (see Figure 2.14). This pressure assures the stability of the excavated trench. In addition, some models were run without applied hydrostatic loads in order to model an unsupported hole, which was the case during the wall installation at the Chicago and State Street excavation. In the second calculation stage, the applied loads were deactivated, if the case, and the trench clusters filled with a linear elastic material with Young's modulus, $E_{eq} = 8.9 \times 10^6\ kPa$, and Poisson's ratio, $\nu = 0.2$.

151

www.manaraa.com

A.5   Calculation Phases

A.5.1   Tunnel Construction

Figure A.6 shows the sequence of phases used to model the construction of the Chicago Subway Tunnel-Station in PLAXIS 3D FOUNDATION. Phase 1 models the dry excavation of the tunnels (e.g., removal of soil and water) and the installation of the temporary supports (steel ribs). Phase 2 models the installation of the permanent concrete liner. Phase 3 represents a plastic nil-step stage where no additional loads or elements are included. It is used to eliminate possible out-of-balance forces that may have been generated during the previous phases. In phase 4, the water table at the tunnel location is lowered to the bottom tunnel elevation. It is presumed that the tunnel tubes act as drains. Finally, phase 5 simulates the consolidation of the clay layers between the end of the tunnel construction (late 30's) and the construction of the school (late 50's). An ultimate time load input condition of 19 years (6940 days) was specified to terminate the consolidation calculation.

A.5.2   School Construction

Six phases were used to simulate the construction of the Francis Xavier Warde School (see Figure A.7). In phase 6, the displacements are reset to zero during a plastic nil-step stage. Phase 7 models the stepped excavation for the school basement and its footings. In phase 8, the structural elements of the school (basement wall, floor, and footings) are placed and the soil around the school is backfilled. In phase 9, the footing loads, which represent the weight of the school, are activated. Phase 10 is a plastic nil-step stage. Lastly, Phase 11 simulates the consolidation of the clay layers between the end of the school construction and the beginning of the wall installation. An ultimate time load input condition of 40 years (14610 days) was specified to terminate the consolidation calculation.
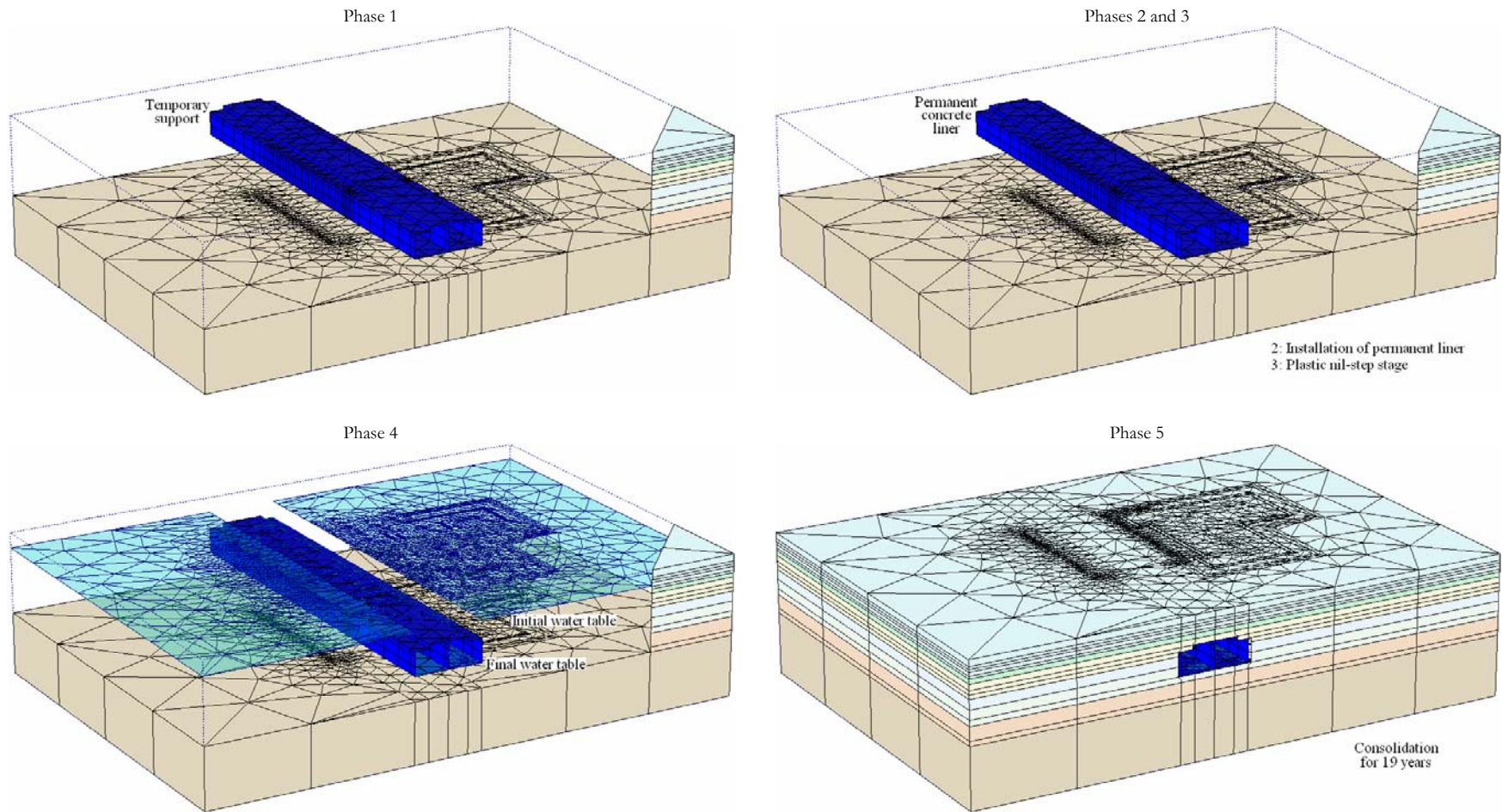
152

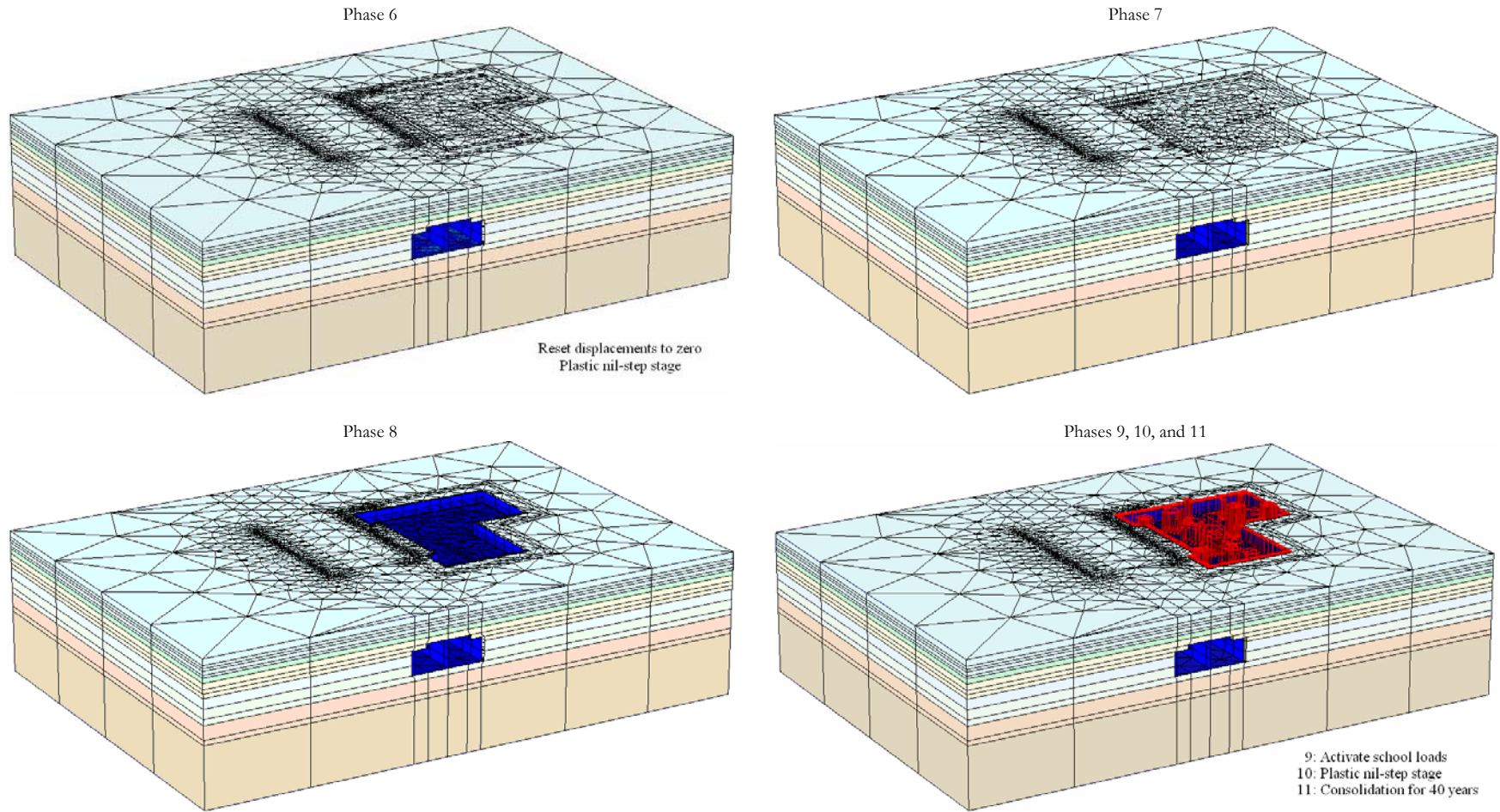**Figure A.6 - Modeling the Tunnel Construction in PLAXIS 3D FOUNDATION.**

Phase 1

Temporary support

Phases 2 and 3

Permanent concrete liner

2: Installation of permanent liner
3: Plastic nil-step stage

Phase 4

Initial water table
Final water table

Phase 5

Consolidation for 19 years

Phase 6

Phase 7

Reset displacements to zero
Plastic nil-step stage

Phase 8

Phases 9, 10, and 11

9: Activate school loads
10: Plastic nil-step stage
11: Consolidation for 40 years

Figure A.7 - Modeling the School Construction in PLAXIS 3D FOUNDATION.

A.5.3   Wall Installation

Figure A.8 shows the complete sequence of the wall installation modeling in PLAXIS 3D FOUNDATION. The sand fill layer, the school elements, and the footing loads are hidden for visualization purposes. Only the sand fill clusters that correspond to the location of the wall elements are shown.

The modeling procedure used for the construction of the secant pile wall consisted principally of two steps. First, the soil of four (4) alternate slots is excavated to a deep of 18.3 m below ground surface (-14 m CCD). The slots were kept unsupported during the calculation stage in order to resemble the construction procedure at the Chicago and State Street excavation (Bryson, 2002). In the next calculation stage, the excavated slots are filled with an elastic grout material and the next four (4) alternate slots are excavated. The properties of the elastic grout material are described in Section A.3. The excavation phases are advanced in 4-slot intervals because that is the approximate number of piles completed in one day for the Chicago and State Street wall installation (Bryson, 2002).

Following the aforementioned modeling procedure, a total of thirty-four calculation phases were necessary to model the installation of the secant pile wall. In phase 12, the displacements are reset to zero during a plastic nil-step stage. Phases 13 to 27 model the construction of the East portion of the wall along State Street. In Phases 27 to 41, the West section of the secant pile wall along State Street is installed. Phases 41 to 45 model the construction of the North wall along the Chicago Avenue.
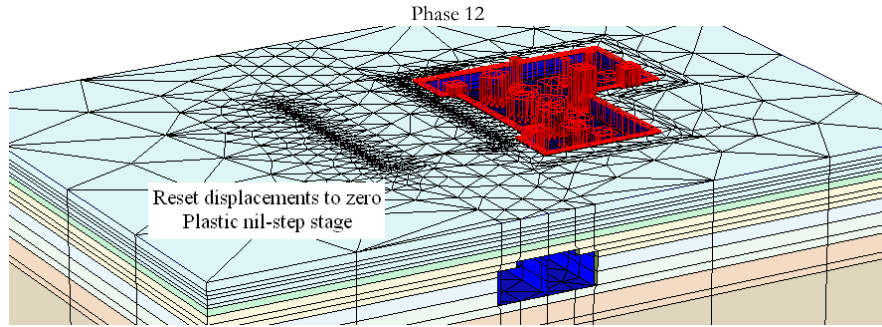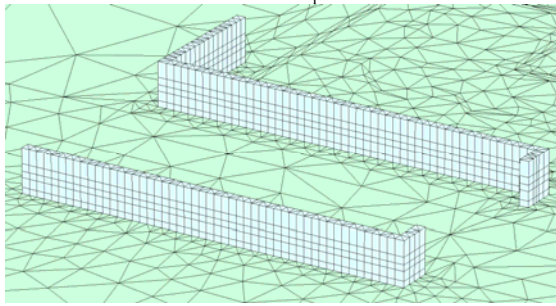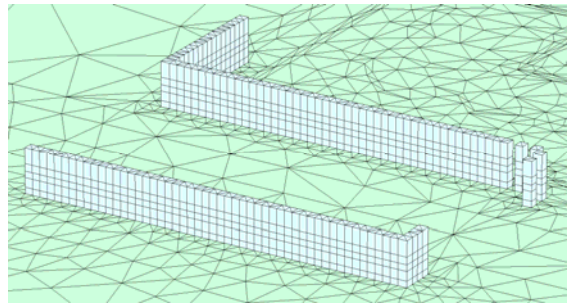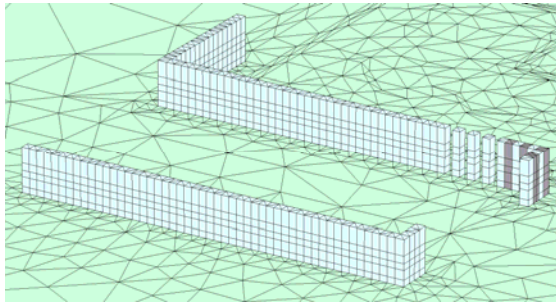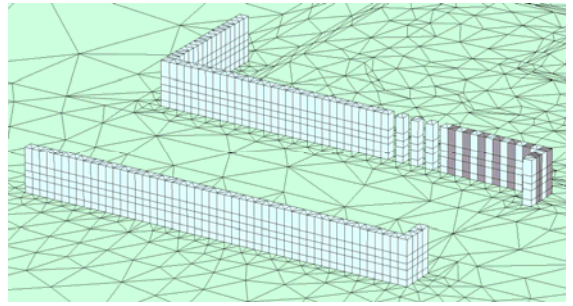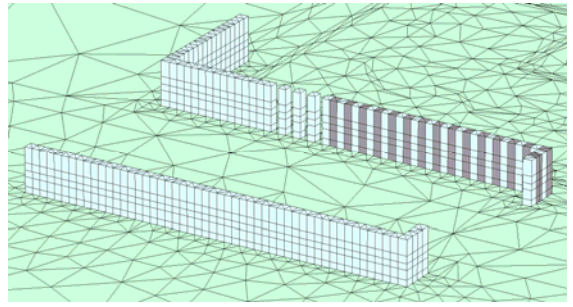
Figure A.8 - Modeling the Wall Installation in PLAXIS 3D FOUNDATION.

Figure A.8 - (Continued) Modeling the Wall Installation in PLAXIS 3D FOUNDATION.
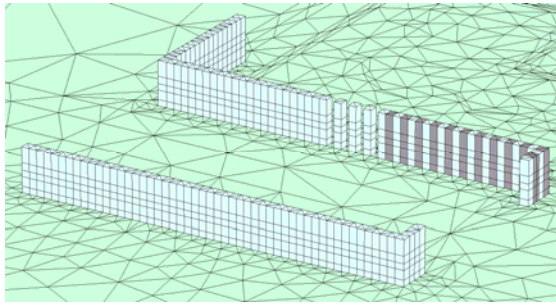
Phase 30

Phase 31

Phase 32

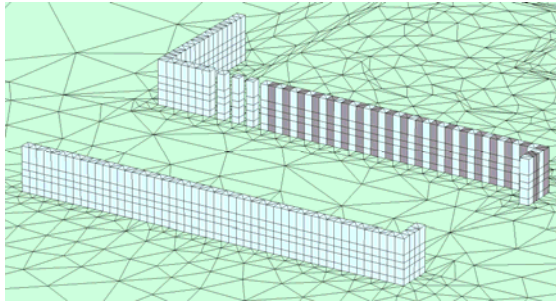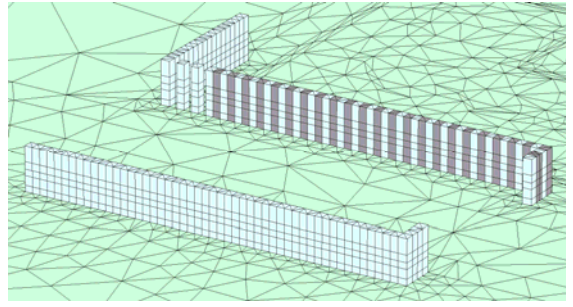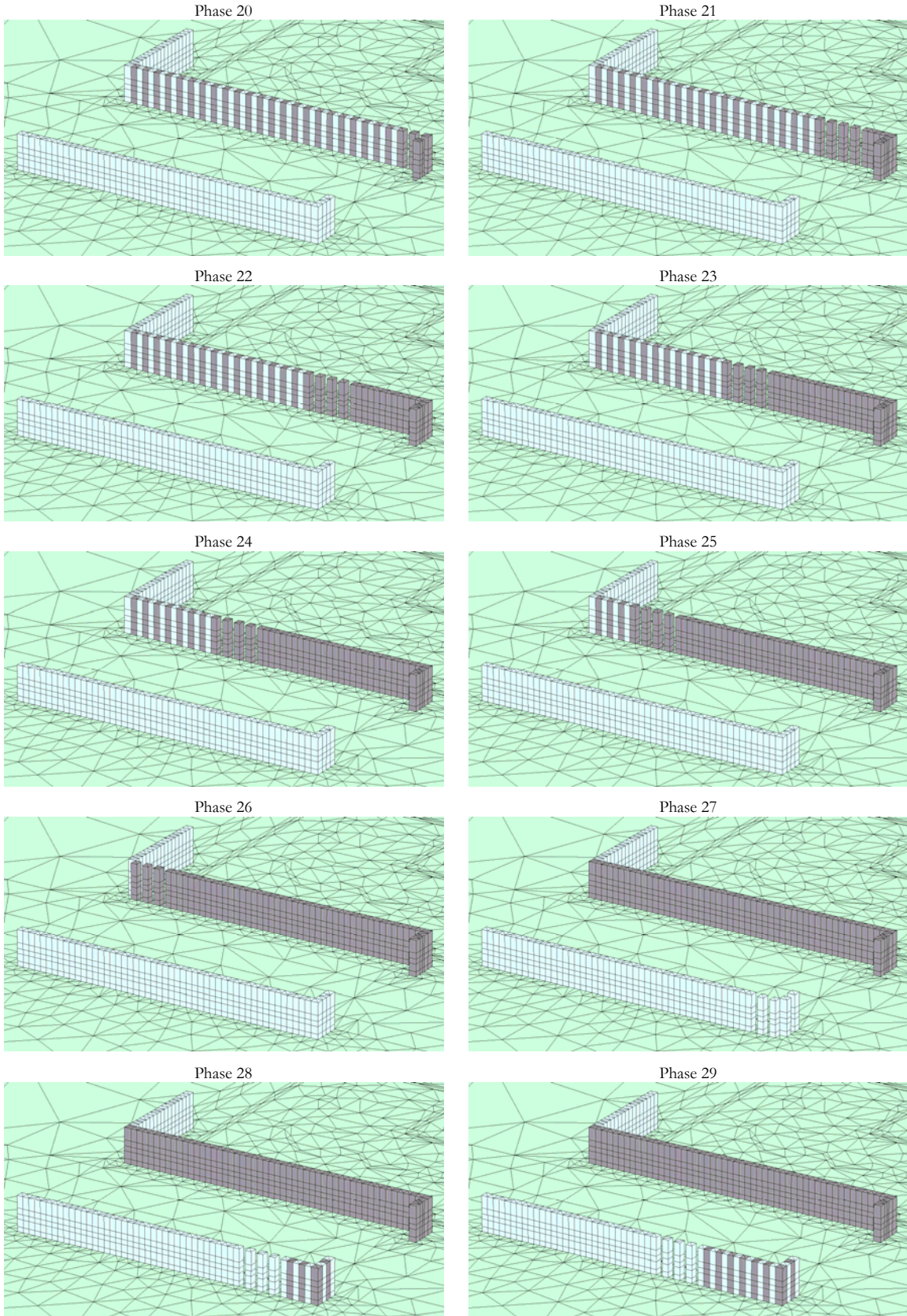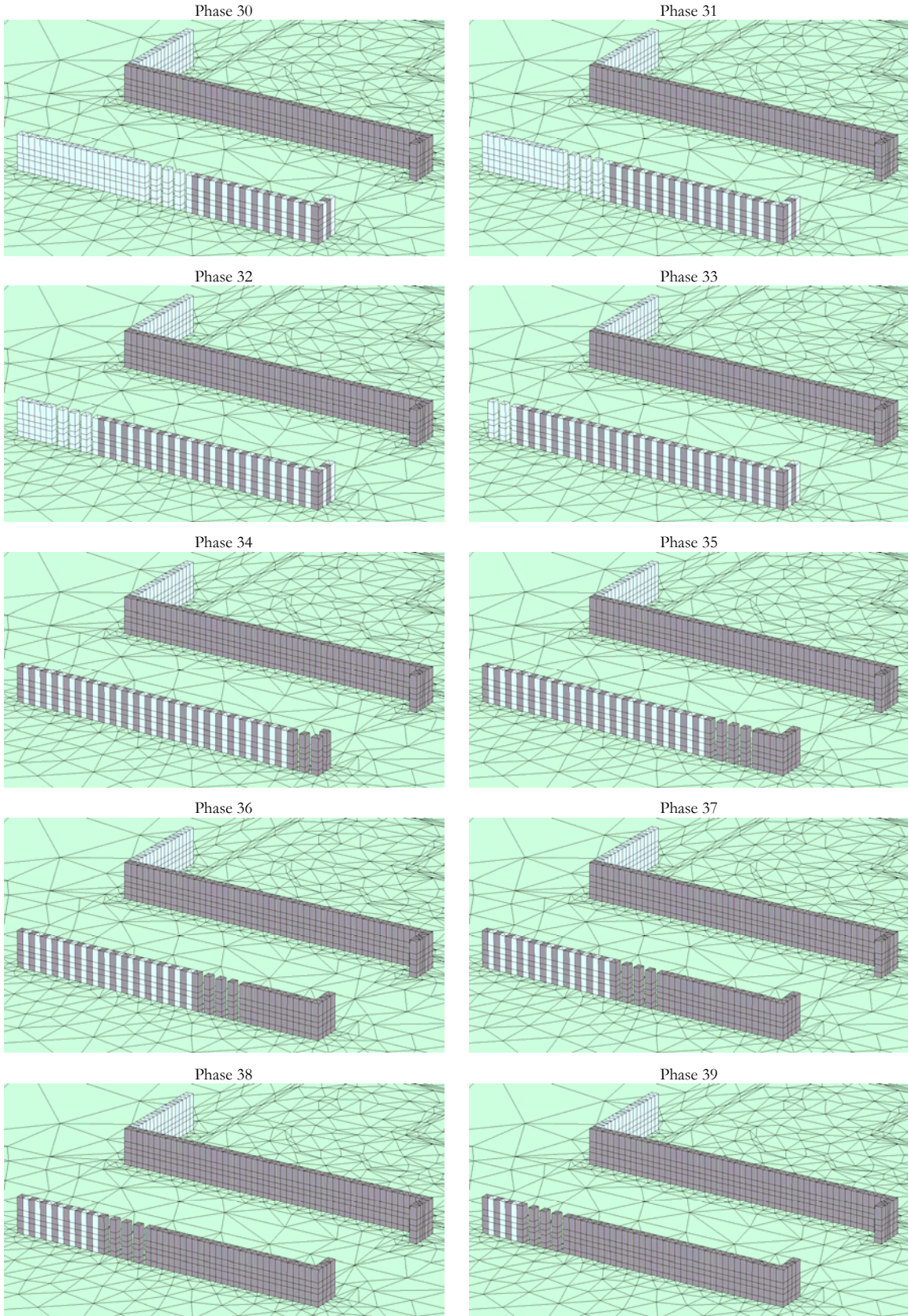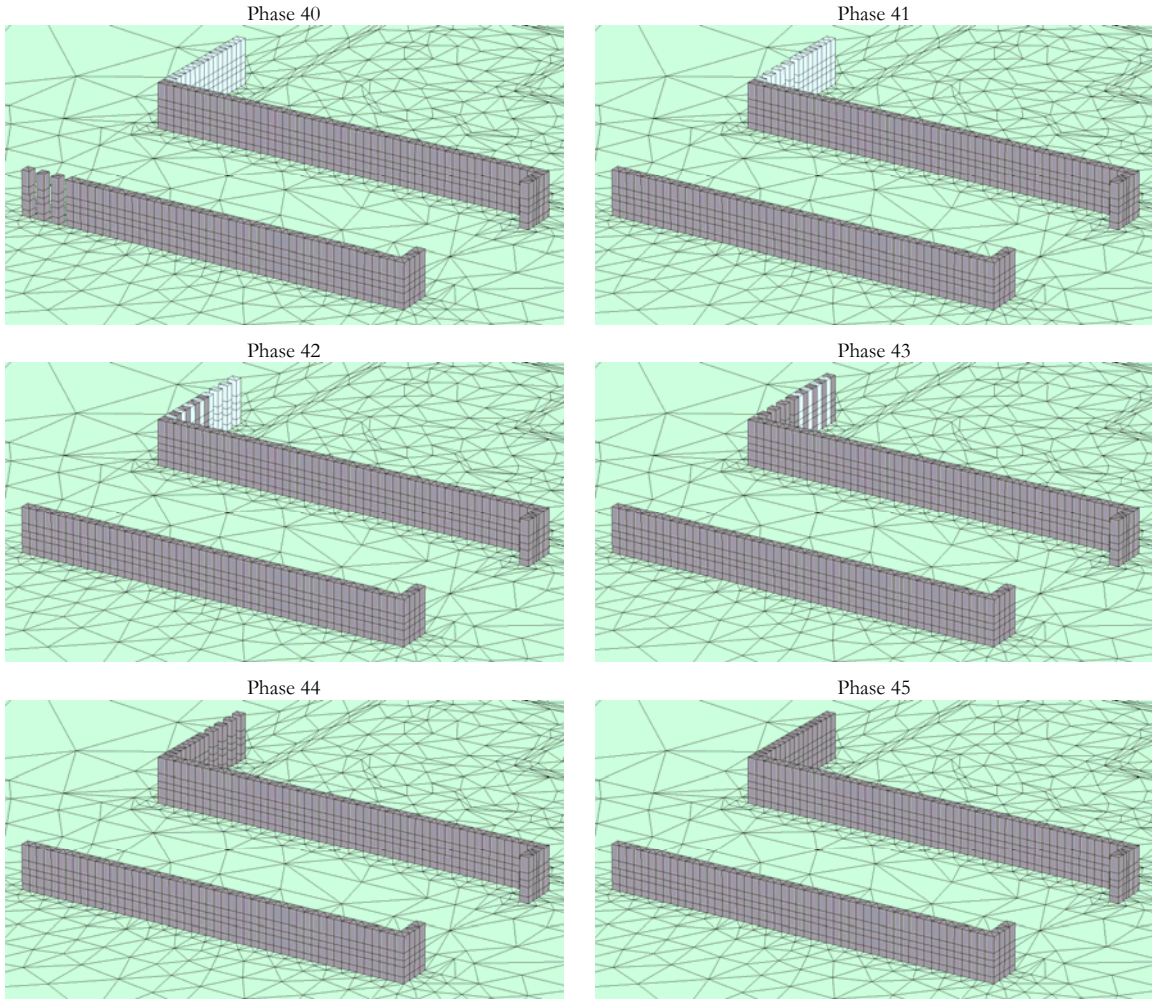Phase 33

Phase 34

Phase 35

Phase 36

Phase 37

Phase 38

Phase 39

Figure A.8 - (Continued) Modeling the Wall Installation in PLAXIS 3D FOUNDATION.

Phase 40   Phase 41

Phase 42   Phase 43

Phase 44   Phase 45

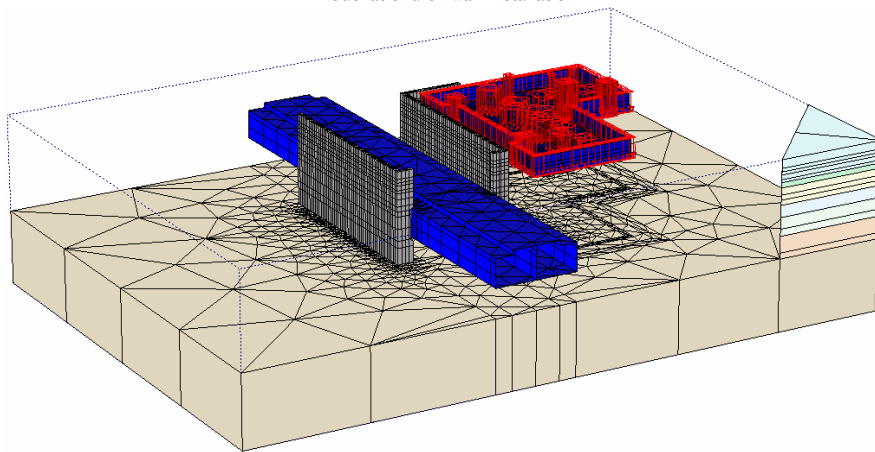Model at end of wall installation

Figure A.8 - (Continued) Modeling the Wall Installation in PLAXIS 3D FOUNDATION.

www.manaraa.com

A.6   Material Properties

A.6.1   Soil and Interfaces

Tables A.1 and A.2 list the parameters for the different soil layers used in the PLAXIS model. The sand fill and the clay crust layers were modeled using the classical Mohr-Coulomb soil model while the Hardening Soil Model (Schanz et al., 1999) was used for the Upper Blodgett, Lower Blodgett, Deerfield, Park Ridge, and Hard Clay. The Hardening Soil parameters for the clay layers were determined based on extensive triaxial lab testing of samples taken from Chicago soils (See Roboski, 2001).

Table A.1 - Sand Fill and Clay Crust Parameters (From Calvello, 2002).

Mohr-Coulomb		Sand	Clay Crust
Type	[-]	Drained	Undrained
γ_{unsat}	[kN/m³]	18.85	19.64
γ_{sat}	[kN/m³]	18.85	19.64
$k_x = k_z$	m/day	15.24	0.00015
k_y	m/day	15.24	0.00009
E_{ref}	[kN/m²]	17620	25051
c_{ref}	[kN/m²]	19.1	0.05
φ (phi)	[°]	35	32.8
ψ (psi)	[°]	5	0
υ_{ur}	[-]	0.33	0.2
$E_{increment}$	[kN/m³]	4713	0
$c_{increment}$	[kN/m³]	0	0
y_{ref}	[m]	2.74	0
c_k	[-]	1.00E+15	1.00E+15
e_{init}	[-]	1	1
e_{min}	[-]	0	0
e_{max}	[-]	999	999
T-Strength	[kN/m²]	0	0
$R_{inter f}$	[-]	0.67	0.5
$\delta - int\,er$	[m]	0	0

160

Table A.2 - Clay Layer Parameters (From Roboski, 2001).

Hardening Soil Model		Upper Blodgett	Lower Blodgett	Deerfield	Park Ridge	Hard Clay
Type	[-]	Undrained	Undrained	Undrained	Undrained	Undrained
γ_{unsat}	[kN/m³]	18.1	18.1	18.85	19.63	20.42
γ_{sat}	[kN/m³]	18.1	18.1	18.85	19.63	20.42
$k_x = k_z$	m/day	0.00015	0.00015	0.00015	0.00015	0.00015
k_y	m/day	0.00009	0.00009	0.00009	0.00009	0.00009
E_{50}^{ref}	[kN/m²]	2350	3700	4000	11700	24658
E_{oed}^{ref}	[kN/m²]	1600	2300	2440	4090	17261
E_{ur}^{ref}	[kN/m²]	10000	29100	30500	35000	73975
c_{ref}	[kN/m²]	0.05	0.05	0.05	0.05	0.05
φ (phi)	[°]	24.1	27	28.9	31.4	35
ψ (psi)	[°]	0	0	0	0	0
υ_{ur}	[-]	0.2	0.2	0.2	0.2	0.2
p^{ref}	[kN/m²]	100	100	100	100	100
power (m)	[-]	1.0	0.91	1.0	0.94	0.6
K_0^{NC}	[-]	0.59	0.55	0.52	0.48	0.426
$c_{increment}$	[kN/m³]	0	0	0	0	0
y_{ref}	[m]	0	0	0	0	0
c_k	[-]	1.00E+15	1.00E+15	1.00E+15	1.00E+15	1.00E+15
e_{init}	[-]	1	1	1	1	1
e_{min}	[-]	0	0	0	0	0
e_{max}	[-]	999	999	999	999	999
R_f	[-]	0.7	0.77	0.71	0.83	0.9
T-Strength	[kN/m²]	0	0	0	0	0
$R_{int\,erf}$	[-]	1	1	1	0.5	0.5
$\delta - int\,er$	[m]	0	0	0	0	0

As presented in Section A.3, the secant pile wall was modeled with a linear-elastic material with and stiffness equivalent to the one of the composite section (steel section and concrete grout). The parameters used for modeling the wall material are presented in Table A.3.

Table A.3 - Wall Material Parameters.

Linear-Elastic		Wall
Type	[-]	Non-porous
γ_{unsat}	[kN/m³]	24
γ_{sat}	[kN/m³]	24
$k_x = k_z$	m/day	0
k_y	m/day	0
E_{ref}	[kN/m²]	8.9×10^6
υ	[-]	0.2
$R_{int\,erf}$	[-]	1
$\delta - int\,er$	[m]	0

A.6.2   Floors

In PLAXIS 3D FOUNDATION, floors are structural objects used to model thin horizontal structures in the ground with a significant flexural rigidity (bending stiffness). Floors elements are composed of 6-node triangular plate elements with six degrees of freedom per node: three translational degrees of freedom (u_x, u_y and u_z) and three rotational degrees of freedom (φ_x, φ_y and φ_z). The floor element allows for plate deflections due to shearing as well as bending. In addition, the element can change length when an axial force is applied (For further reference see Brinkgreve and Broere, 2006).

Tables A.4 and A.5 present the floor material parameters assigned to the structural elements of the tunnel and school, respectively.

Table A.4 - Floor Material Parameters for Tunnel.

Linear (Isotropic)		Temporary Liner	Permanent Liner (Bottom)	Permanent Liner (Top)
d	[m]	0.1	0.8	0.6
γ	[kN/m³]	76.8	23.6	23.6
$E_1 = E_2$	[kN/m²]	2×10^8	21×10^6	21×10^6
υ	[-]	0.3	0.2	0.2

Table A.5 - Floor Material Parameters for School.

162

Linear (Isotropic)		Internal Footings	Wall Footings	Basement Floor
d	[m]	0.76	0.2	0.4
γ	[kN/m³]	23.6	23.6	23.6
$E_1 = E_2$	[kN/m²]	25×10^6	25×10^6	25×10^6
υ	[-]	0.2	0.2	0.2

A.6.3   Walls

Walls are structural objects used to model thin vertical structures in the ground with a significant flexural rigidity. Walls are composed of 8-node quadrilateral plate elements and have the same six degrees of freedom per node described for the floor element. When creating walls, corresponding interfaces are automatically generated at both sides of the wall to allow for proper soil-structure interaction. As for floor elements, the wall element allows for plate deflections due to shearing as well as bending. It can also change length when an axial force is applied. Tables A.6 and A.7 present the wall material parameters assigned to the structural elements of the tunnel and school, respectively.

Table A.6 - Wall Material Parameters for Tunnel.

Linear (Isotropic)		Temporary Liner	Permanent Liner (Sides)	Permanent Liner (Middle)	Permanent Liner (Top)
d	[m]	0.1	0.75	1.3	0.6
γ	[kN/m³]	76.8	23.6	23.6	23.6
$E_1 = E_2$	[kN/m²]	2×10^8	21×10^6	21×10^6	21×10^6
υ	[-]	0.3	0.2	0.2	0.2

Table A.7 - Wall Material Parameters for School.

Linear (Isotropic)		Basement Wall
d	[m]	0.4
γ	[kN/m³]	23.6
$E_1 = E_2$	[kN/m²]	25×10^6
υ	[-]	0.2

A.7   Finite Element Mesh

The PLAXIS 3D FOUNDATION program allows for a fully automatic generation of finite element meshes. The mesh generation consists of two steps. First, all the plane geometry information (points, lines and clusters) which is contained in the work planes is combined with additional lines automatically generated by the program and included in the two-dimensional (2D) mesh generation. Second, when the 2D mesh is satisfactory, the three-dimensional (3D) mesh generation process will take into account the information from the work planes at different levels as well the soil stratigraphy from the boreholes.

The generation of the 2D mesh is based on a robust triangulation procedure, which results in "unstructured" meshes. These meshes may look disorderly, but the numerical performance of such meshes is usually better than for regular "structured" meshes (Brinkgreve and Broere, 2006).

The 3D mesh is based on a system of horizontal and pseudo-horizontal planes in which the 2D mesh is used. These planes are formed by the work planes and the soil layer boundaries as defined by the boreholes. If the local distance between two successive planes is significantly larger than the target vertical element size, additional planes are introduced. This is done in such a way that the element size in vertical direction is approximately equal to the target vertical element size, which reduces the possibility that badly shaped elements occur (For further reference see Brinkgreve and Broere, 2006).

Figure A.9 shows the complete 3D finite element mesh for the Chicago and State Street model. Figure A.10 shows a detail view of the generated finite elements mesh of the structural elements for the tunnel and school.
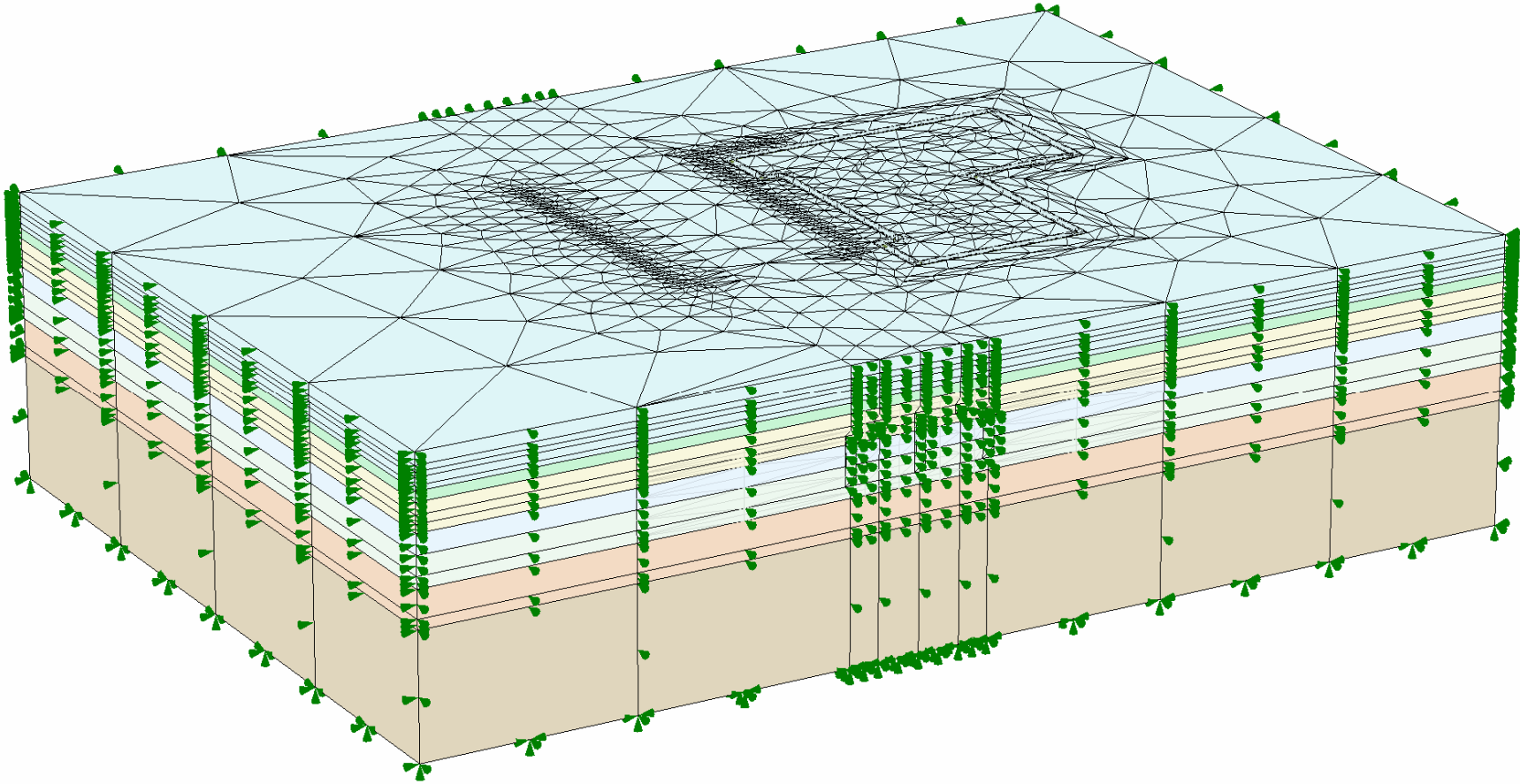
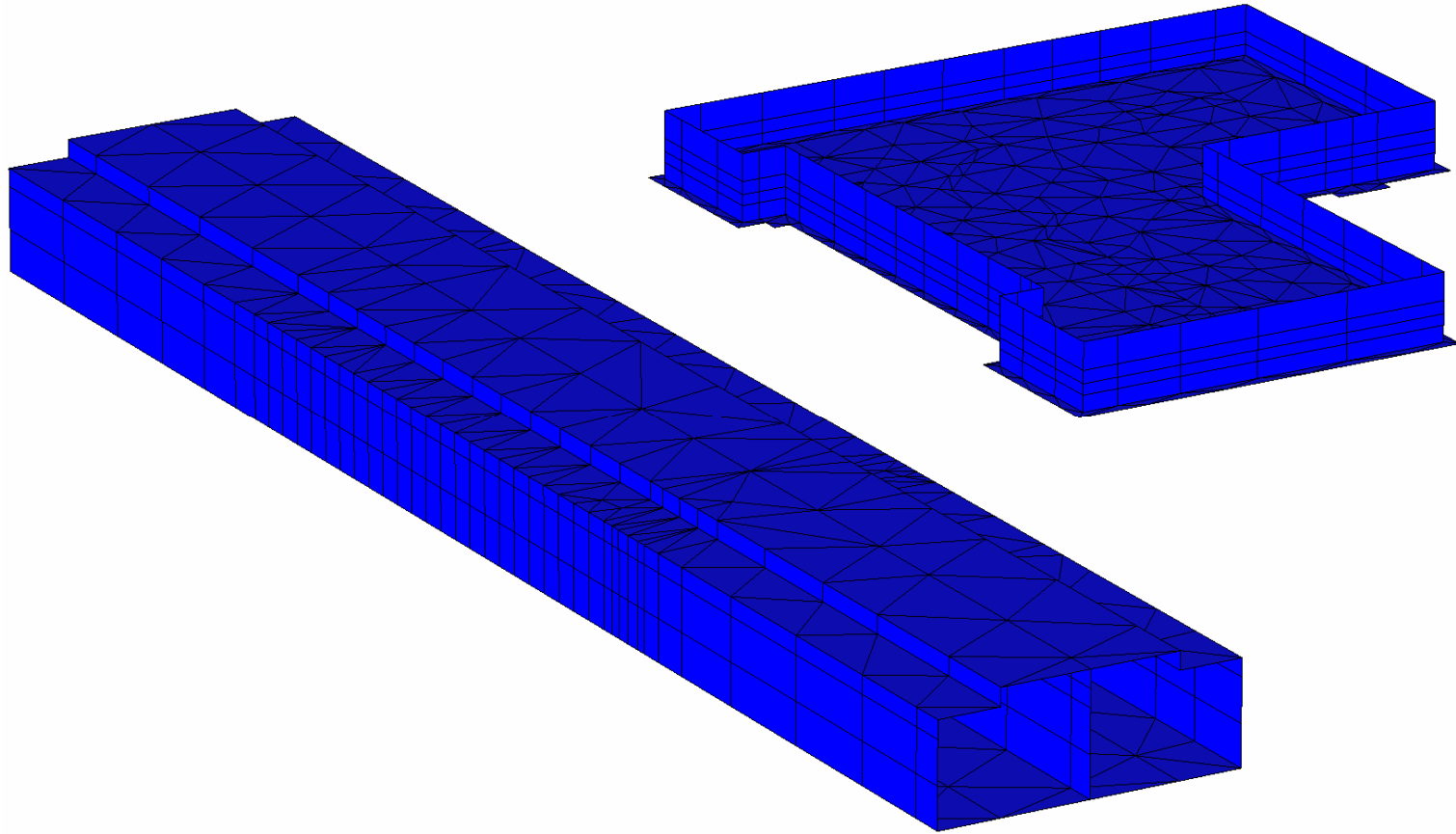**Figure A.9 - Generated 3D Finite Element Mesh in PLAXIS 3D FOUNDATION.**

Figure A.10 - Generated 3D Finite Element Mesh for Structural Elements in PLAXIS 3D FOUNDATION.

B HARDENING SOIL MODEL (HSM)

B.1   Introduction

The Hardening-Soil Model (Schanz et al., 1999) has been developed to simulate the elasto-plastic response of both stiff and soft soils. It is an elasto-plastic multi-yield surface model formulated in the framework of classical theory of plasticity. When subjected to primary deviatoric loading, soil shows a decreasing stiffness and simultaneously irreversible plastic strains develop. Failure is defined by the Mohr-Coulomb failure criteria. Two families of yield surfaces are considered to account for both volumetric and shear plastic strains. A yield cap surface controls the volumetric plastic strains. On this cap, the flow rule is associative. On the shearing yield surfaces, increments of plastic strain are non-associative and the plastic potential is defined to assure a hyperbolic stress-strain response for triaxial compression load conditions. The Hardening-Soil model surpasses the hyperbolic model by (i) using the theory of plasticity rather than the theory of elasticity; (ii) including soil dilatancy; and (iii) introducing a yield cap.

B.2   Parameters of the Hardening-Soil Model

The HSM requires the input of 13 parameters. Between them are the classical Mohr-Coulomb failure parameters and some others used for defining the stiffness of the soil. The 13 input parameters necessary for defining the HSM are listed as follows:

Failure parameters (as in the Mohr-Coulomb model):

$c =$ (effective) cohesion,

$\varphi =$ (effective) angle of internal friction,

$\psi =$ angle of dilatancy.

Basic parameters for soil stiffness:

168

E_{50}^{ref} = secant stiffness at 50% stress level in standard drained triaxial test,

E_{oed}^{ref} = tangent stiffness for primary oedometer loading,

m = power for stress-level dependency of stiffness.

Advanced parameters:

E_{ur}^{ref} = unloading/ reloading stiffness (default $E_{ur}^{ref} = 3E_{50}^{ref}$),

ν_{ur} = Poisson's ratio for unloading-reloading (default $\nu_{ur} = 0.2$),

p^{ref} = reference stress for stiffnesses (default $p^{ref} = 100$ stress units),

K_0^{NC} = K_0 -value for normal consolidation (default $K_0^{NC} = 1 - sin\,\varphi$),

R_f = failure ratio $q_f\,/\,q_a$ (default $R_f = 0.9$),

$\sigma_{tension}$ = tensile strength (default $\sigma_{tension} = 0$ stress units), and

$c_{increment}$ = increase of cohesion per unit of depth (default $c_{increment} = 0$)

B.2.1   Basic Parameters to Define Soil Stiffness

The soil stiffness parameters can be divided on two categories: (i) the parameters needed for defining the primary deviatoric loading behavior; and (ii) those required for determining the one-dimensional compression stiffness.

B.2.1.1   Stiffness for Primary Deviatoric Loading

The HSM is based on a hyperbolic stress-strain curve (Figure B.1) to represent the response of the soil to monotonic loading (see Section B.3).

As can be seen in Figure B.1, E_{50} is a secant modulus determined from a triaxial stress-strain curve at 50% of the ultimate shear strength q_f. This is the reference modulus used in the HSM for primary loading. The E_{50} value is dependent on the effective confining stress,

169

$-\sigma'_3$, in an isotropically consolidated triaxial test. To account for the stress-level dependency of the modulus, the secant modulus E_{50} is defined for a reference minor principal stress, $-\sigma_3 = p^{ref}$, as:

$$E_{50} = E_{50}^{ref}\left(\frac{c\cot\varphi - \sigma'_3\sin\varphi}{c\cos\varphi + p^{ref}\sin\theta}\right)^m \tag{B-1}$$

where E_{50}^{ref} is the secant modulus at the reference stress, the power m defines the amount of stress dependency, and c and φ are the Mohr-Coulomb strength parameters of cohesion and friction angle, respectively. For a logarithmic stress dependency, as commonly observed for soft clays, m is taken as 1.0. For other soils, the m value varies between 0.5 to 1.0.
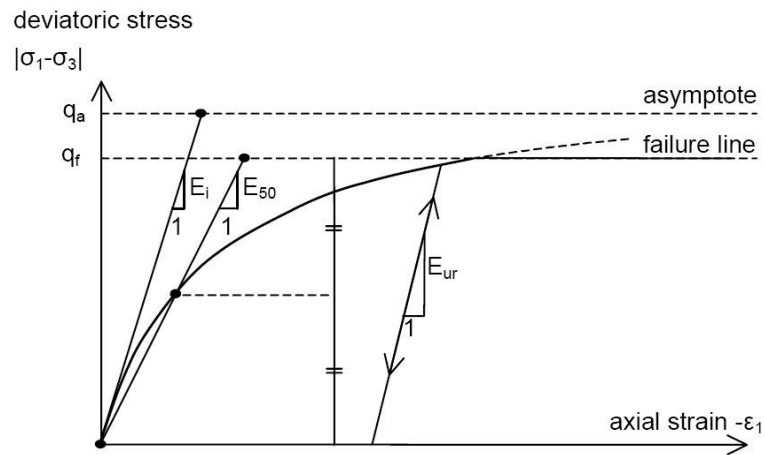

Figure B.1 - Hyperbolic Stress-Strain Relation in Primary Loading for a Standard Drained Triaxial Test (after Schanz et al., 1999).

B.2.1.2   Stiffness for One-Dimensional Compression

The HSM uses an oedometer reference modulus for defining the stiffness for one-dimensional compression. The oedometer stiffness modulus at the reference stress value, p^{ref}, is defined as:

$$E_{oed} = E_{oed}^{ref}\left(\frac{c\cot\varphi - \sigma'_1\sin\varphi}{c\cos\varphi + p^{ref}\sin\varphi}\right)^m \tag{B-2}$$

170

where E_{oed} is the tangent stiffness modulus for primary loading in constrained compression (i.e., compression with zero lateral strain) and E_{oed}^{ref} is a tangent stiffness at a vertical stress of $-\sigma_3 = p^{ref}$ as indicated in Figure B.2.

It must be noted that σ'_1 is used rather than σ'_3 and that primary loading is considered. In contrast to elasticity based models, the HSM does not involve a fixed relationship between the (drained) triaxial stiffness E_{50} and the oedometer stiffness E_{oed} for one-dimensional compression. Instead, these stiffnesses can be inputted independently.
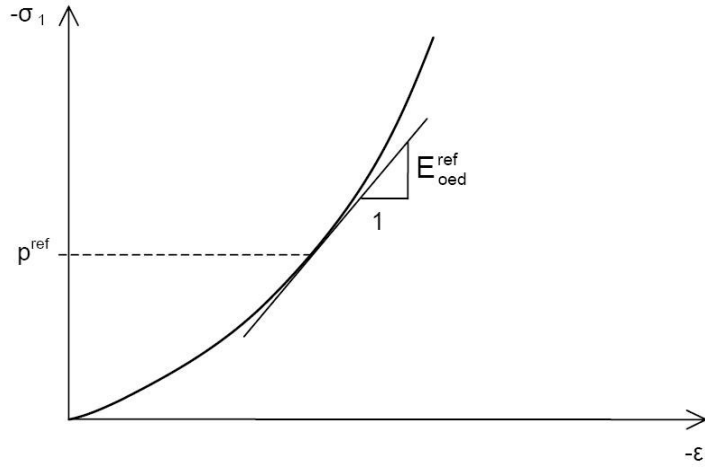

Figure B.2 - Definition of E_{oed}^{ref} in Oedometer Test Results (after PLAXIS, 2006).

B.2.2   Advanced Parameters

B.2.2.1   Stiffness for Unloading and Reloading

For unloading and reloading stress paths, the elastic Young's modulus, E_{ur} is used (see Figure B.1). This modulus is also dependent on the effective confining stress and thus, a reference modulus, E_{ur}^{ref}, corresponding to a reference pressure, p^{ref}, is defined:

$$E_{ur} = E_{ur}^{ref} \left(\frac{c \cos\varphi - \sigma'_3 \sin\varphi}{c \cos\varphi + p^{ref} \sin\varphi} \right)^m \tag{B-3}$$

171

In many practical cases, E_{ur}^{ref} is taken equal to $3E_{50}^{ref}$. This is the default value for the HSM implemented in PLAXIS. However, it can be set as any value in the code.

B.2.2.2   Other Advanced Parameters

In most cases, Poisson's ratio, ν_{ur}, varies between 0.1 and 0.2, depending on the strain level. A value of 0.2 is used as the default value for the HSM. The coefficient of lateral earth pressures for normally consolidated soils, K_0^{NC}, is not a function of the Poisson's ratio, as is dictated by elastic theory. The correlation most commonly used that gives realistic values is:

$$K_0^{NC} = 1 - sin\,\varphi \qquad\qquad (B\text{-}4)$$

It is suggested to maintain this value since the correlation is quite realistic. However, other values can be input to PLAXIS within a certain range, which depends on the other parameters. All possible different input values for K_0^{NC} cannot be accommodated for. Depending on other parameters, such as E_{50}^{ref}, E_{oed}^{ref}, E_{ur}^{ref}, and ν_{ur}, there happens to be a certain range of valid K_0^{NC}-values. K_0^{NC} values outside this range are rejected by PLAXIS. On inputting values, the program shows the nearest possible value that will be used in the computations.

B.3   Constitutive Equations for Standard Drained Triaxial Tests

The hyperbolic relationship between vertical strain, ε_1, and deviatoric stress, $q = \sigma_1 - \sigma_3$, in primary triaxial loading forms the basis of the HSM. Soil under primary deviatoric loading shows a reduction of stiffness with axial strain developing irreversible plastic strains. Standard drained triaxial tests yield curves that demonstrate such behavior, (see Figure B.1). These curves can be described by:

172

$$- \varepsilon_1 = \frac{1}{E_i} \frac{q}{\left(1 - q/q_a\right)} \qquad \text{for: } q < q_f \qquad (B\text{-}5)$$

where q_f is the ultimate deviatoric stress, q_a is the asymptotic value of shear strength, and E_i is the initial stiffness. E_i is related to E_{50} by:

$$E_i = \frac{2E_{50}}{2 - R_f} \qquad (B\text{-}6)$$

The deviatoric stresses in Equation B-5 are defined by the following equations:

$$q_f = \left(c \cot \varphi - \sigma'_3\right) \frac{2 \sin \varphi}{1 - \sin \varphi} \qquad (B\text{-}7)$$

$$q_a = \frac{q_f}{R_f} \qquad (B\text{-}8)$$

where R_f is the failure ratio, given by the ratio between q_f and q_a. The value of q_a is found as the inverse of the slope of a plot of $\varepsilon_1/(\sigma_1 - \sigma_3)$ versus ε_1. This number should be smaller than 1.0. In PLAXIS, $q_a = 0.9$ is used as the default value.

The relationship for q_f is based on the Mohr-Coulomb failure criterion, previously defined. Note that when $q = q_f$, the failure criterion is satisfied and there is perfectly plastic yielding as defined by the Mohr-Coulomb model.

B.4   Yield Surfaces

B.4.1   Shear Yield Surface, Shear Hardening

The Hardening-Soil model gives virtually the hyperbolic stress-strain curve of Equation B-5 when considering stress paths of standard drained triaxial tests. The HSM uses a shear hardening yield function defined as follows:

173

$$f = \bar{f} - \gamma^p \tag{B-9}$$

where $\bar{f}$ is function of the stress and γ^p is function of plastic shear strains:

$$\bar{f} = \frac{2}{E_i} \frac{q}{1 - q/q_a} - \frac{2q}{E_{ur}} \tag{B-10}$$

$$\gamma^p = -\left(2\varepsilon_1^p - \varepsilon_v^p\right) \approx -2\varepsilon_1^p \tag{B-11}$$

Although plastic volumetric strain, ε_v^p, is never precisely equal to zero, this approximation is made because for hard soils, plastic volume changes tend to be very small compared to the axial strains.

Plastic shear strain is used as a parameter for frictional hardening. For given constant values of this parameter, yield loci can be used to visualize the yield condition $f = 0$ in the $p' - q$ plane. To plot the yield loci, one must use the yield function (Equation B-9), as well as the equations for the two moduli E_{50} and E_{ur} (Equations B-1 and B-3, respectively). Note that the shape of the loci depends on the exponent m. When $m = 1.0$, straight lines are formed, but when the exponent has a lower value, slightly curved lines are created. Figure B.3 shows the shape of yield loci for $m = 0.5$, a typical value for hard soils.
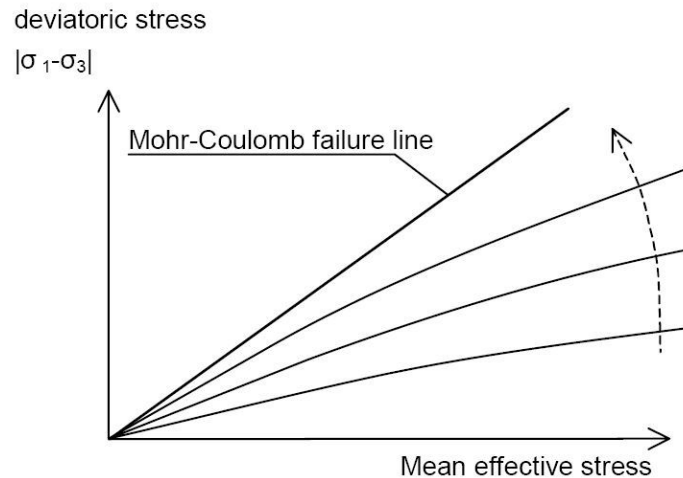

Figure B.3 - Yield Loci for Various Constant Values of Plastic Shear Strain (after Schanz et al., 1999).

174

Note that as the shear stress level increases, the yield surfaces approach the linear failure condition described by Equation B-7.

B.4.2   Cap Yield Surface, Compression Hardening

The shear yield surfaces discussed in the previous section do not explain the plastic volume strain observed in isotropic compression. Another yield surface must be used to close the elastic region in the direction of the hydrostatic axis. Such a cap yield surface allows the use of the independent input of both E_{50}^{ref} and E_{oed}^{ref}. The triaxial secant modulus E_{50}^{ref} largely controls the shear yield surface, by controlling the magnitude of the plastic strains associated with that surface. Similarly, the oedometer modulus E_{oed}^{ref} controls the cap yield surface, controlling the magnitude of plastic strains that originate from the yield cap. The HSM defines an elliptical cap yield surface as:

$$f^c = \frac{\tilde{q}^2}{\alpha^2} + p^2 - p_p^2 \tag{B-12}$$

where f^c is the cap yield surface and α is a parameter which relates to K_0^{NC}. Also:

$$p = (\sigma_1 + \sigma_2 + \sigma_3)/3 \tag{B-13}$$

$$\tilde{q} = \sigma_1 + (\delta - 1)\sigma_2 - \delta\sigma_3 \tag{B-14}$$

with

$$\delta = \frac{3 + \sin\varphi}{3 - \sin\varphi} \tag{B-15}$$

$\tilde{q}$ is a special stress measure for deviatoric stresses. In triaxial compression, where $-\sigma_1 > -\sigma_2 = -\sigma_3$, $\tilde{q}$ becomes $-(\sigma_1 - \sigma_3)$. In triaxial extension, where $-\sigma_1 = -\sigma_2 > -\sigma_3$, $\tilde{q}$ reduces to $-\delta(\sigma_1 - \sigma_3)$.

175

The isotropic preconsolidation stress, p_p, determines the magnitude of the yield cap. For isotropic compression, this stress can be derived from relations with the plastic volumetric strain rate. The following hardening law results:

$$\varepsilon_v^{pc} = \frac{\beta}{1-m}\left(\frac{p_p}{p^{ref}}\right)^{1-m} \tag{B-16}$$

where ε_v^{pc} is the volumetric cap strain, β is a hardening modulus which relates to E_{oed}^{ref}, and m is the power for stress-level dependency, as defined earlier. Although both α and β are cap parameters, their values are not direct inputs, but derived from K_0^{NC} and E_{oed}^{ref}, respectively.

The yield cap has the shape of an ellipse in p - $\widetilde{q}$ space, as shown in Figure B.4. It has the length p_p on the p -axis, and αp_p on the $\widetilde{q}$ -axis. Thus, preconsolidation stress, p_p, determines the ellipse's magnitude, while α determines its aspect ratio. High α values give steep caps under the Mohr-Coulomb line, while lower values show caps more pointed about the p -axis.
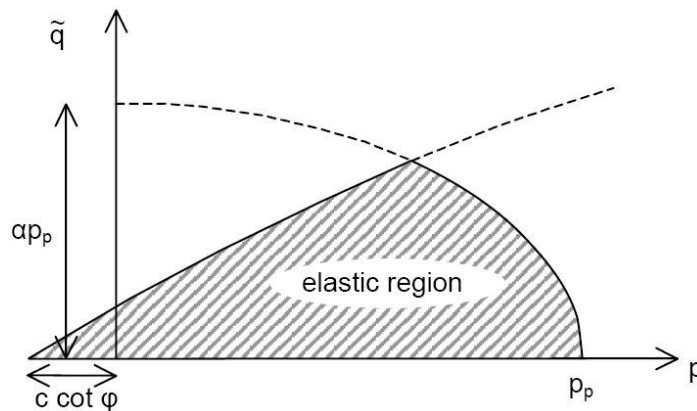

Figure B.4 - Yield Cap Surface of HSM in p - $\widetilde{q}$ -Plane (after PLAXIS, 2006).

While Figure B.4 shows simple yield lines, Figure B.5 depicts yield surfaces in principal stress space. The hexagonal shape of the Mohr-Coulomb failure criterion can be seen in

176

both the shear loci and the yield cap. The shear yield loci can expand up to the ultimate Mohr-Coulomb failure surface. The yield cap expands as a function of the preconsolidation stress, p_p.
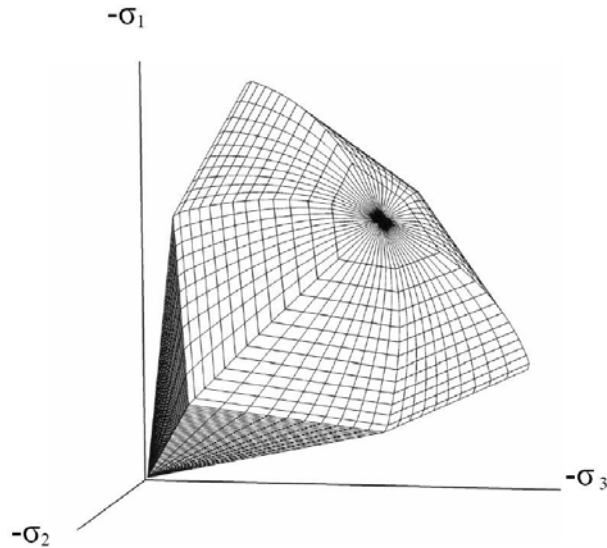
Figure B.5 - Representation of Total Yield Contour of the HSM in Principal Stress Space for Cohesionless Soil (after Schanz et al., 1999).

B.5   Plastic Volumetric Strains

The HSM makes use of a linear relationship between the rates of plastic shear strain, $\dot{\gamma}^p$, and plastic volumetric strain, $\dot{\varepsilon}_v^p$. This shear hardening flow rule has the form:

$$\dot{\varepsilon}_v^p = sin\,\psi_m \dot{\gamma}^p \tag{B-17}$$

where ψ_m is the mobilized dilatancy angle. This angle is defined for this model as:

For $sin\,\varphi_m < 3/4\,sin\,\varphi$ $\psi_m = 0$ (B-18)

For $sin\,\varphi_m \geq 3/4\,sin\,\varphi$ and $\psi > 0$ $sin\,\psi_m = max\left(\dfrac{sin\,\varphi_m - sin\,\varphi_{cv}}{1 - sin\,\varphi_m\,sin\,\varphi_{cv}}, 0 \right)$ (B-19)

For $sin\,\varphi_m \geq 3/4\,sin\,\varphi$ and $\psi \leq 0$ $\psi_m = \psi$ (B-20)

If $\varphi = 0$ $\psi_m = 0$ (B-21)

Where φ_{cv} is the critical state friction angle, and φ_m is the mobilized friction angle. The critical state friction angle is a material constant independent of density and strain conditions (Shanz & Vermeer, 1996). The mobilized friction angle is defined as:

$$sin\,\varphi_m = \frac{\sigma'_1 - \sigma'_3}{\sigma'_1 + \sigma'_3 - 2c\,cot\,\varphi} \tag{B-22}$$

The above equations are used in the stress-dilatancy theory (Rowe, 1962). The stress-dilatancy theory suggests that soil contracts for small stress ratios $\varphi_m < \varphi_{cv}$, and dilates for high stress ratios $\varphi_m > \varphi_{cv}$. In other words, loose soil will contract under relatively high consolidation stresses, and dense soil will expand under relatively low consolidation stresses. At failure, the mobilized friction angle, φ_m, equals the failure angle, φ, giving the following relationship valid at failure:

$$sin\,\varphi_{cv} = \frac{sin\,\varphi - sin\,\psi}{1 - sin\,\varphi\,sin\,\psi} \tag{B-23}$$

The critical state angle can thus be computed from the friction angle, φ, and dilatancy angle, ψ. This is equivalent to plastic potential functions, which can be manipulated by the Koiter-rule for yielding to give the flow rule Equation B.17 (Shanz et al. 1999).

B.6   Dilatancy Cut-Off

Dilatancy stops when, after extensive shearing, the soil reaches a state of critical density, as indicated in Figure B.6. This behavior is accounted for in the HSM by defining a dilatancy cut-off point. To specify this behavior, both an initial void ratio, e_{init}, and the maximum void ratio, e_{max}, are entered as general parameters. A conditional definition for the mobilized dilatancy angle, ψ_m, imposes this behavior:

178

for $e < e_{max}$ $sin\,\psi_m = \dfrac{sin\,\varphi_m - sin\,\varphi_{cv}}{1 - sin\,\varphi_m\,sin\,\varphi_{cv}}$ (B-24)

for $e \geq e_{max}$ $\psi_{mob} = 0$ (B-25)

The void ratio is related to volumetric strain ε_v by:

$$-\left(\varepsilon_v - \varepsilon_v^{init}\right) = ln\left(\frac{1+e}{1+e_{init}}\right)$$ (B-26)

where an increment of ε_v is negative for dilatancy. The initial void ratio, e_{init}, is the insitu

void ratio of the soil body. The maximum void ratio is the void ratio of the material in a

state of critical void (critical state). As soon as the maximum void ratio is reached, the

dilatancy angle is set to zero. The minimum void ratio, e_{min}, of a soil can also be inputted,

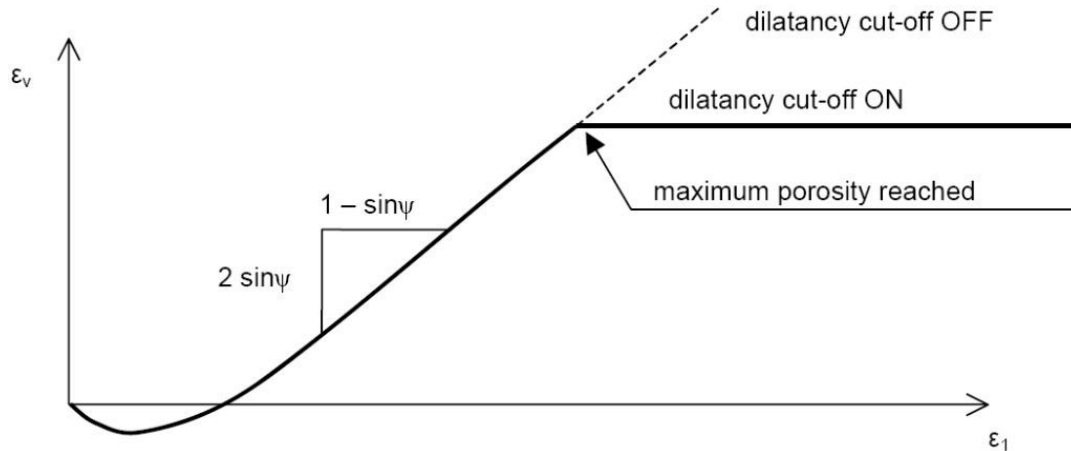but this general soil parameter is not used within the context of the Hardening-Soil model.

Figure B.6 - Resulting Strain Curve for a Standard Drained Triaxial Test When Including Dilatancy Cut-Off (after Schanz et al., 1999).

B.7   Limitations of the Model

Although the HSM can be regarded as an advanced soil model, there are a number of

features of real soil behaviour the model does not include. It is a hardening model that does

not account for softening due to soil dilatancy and debonding effects. In fact, it is an

179

isotropic hardening model so that it models neither hysteretic and cyclic loading nor cyclic mobility. Moreover, the model does not distinguish between large stiffness at small strains and reduced stiffness at engineering strain levels. The user has to select the stiffness parameters in accordance with the dominant strain levels in the application. Last but not least, the use of the HSM generally results in longer calculation times, since the material stiffness matrix is formed and decomposed in each calculation step.

APPENDIX C

C   DATABASE

C.1　Case Histories in Stiff Clay

St1: Lion Yard Development in Cambridge, UK (Ng, 1992)

Wall Type =	Diaphragm
Thickness (m) =	0.6
H (m) =	16.3
H_e (m) =	9.6
B (m) =	45
I (m⁴/m) =	0.018
E (GPa) =	31
S_V (m) =	3.2
S_H (m) =	1.5
$\delta_{H(max)}$ ($\delta_{V(max)}$) (mm) =	17.66 (10.13)
$EI/\gamma_w S_V^4$ =	543.01
$\gamma_{s,avg}$ (kN/m³) =	20
s_u (kPa) =	120
FS (Eq. 2-26 and 2-27) =	4.40 and 3.73
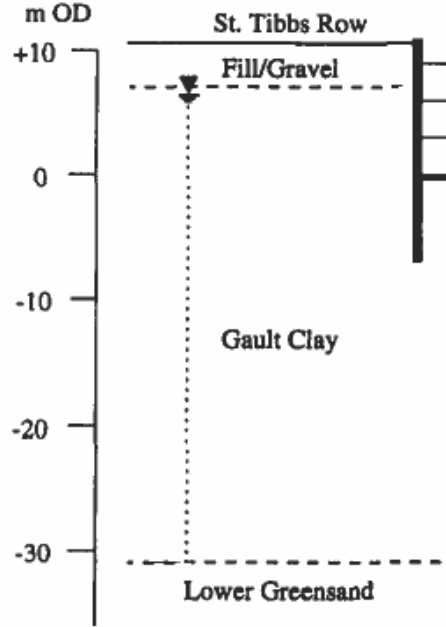
| Depth (m)	δ_H (mm)
0.00	9.04
1.04	10.30
2.50	12.04
3.50	13.73
4.48	15.01
5.50	16.26
6.48	17.02
7.47	17.67
8.47	17.64
10.01	16.18
11.51	14.76
12.49	11.73
13.51	9.62
15.03	6.24
16.57	3.57

Lateral Deformation (mm)

182
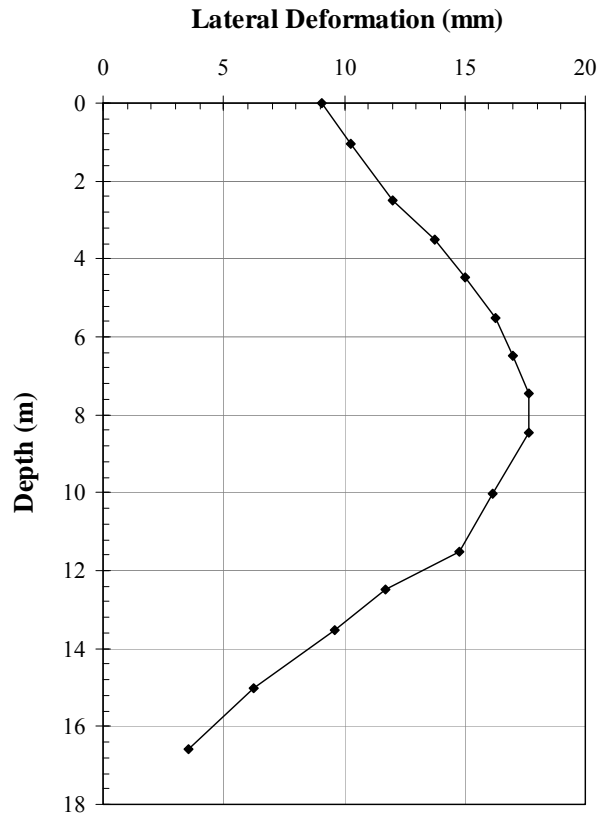
St2: New Palace Yard Park project in London, UK (Burland and Hancock, 1977)

Wall Type = Diaphragm
Thickness (m) = 0.9 (assumed)
H (m) = 30
H_e (m) = 18.5
B (m) = ?
I (m⁴/m) = 0.0607
E (GPa) = 27.6 (assumed)
S_V (m) = 3.2
S_H (m) = ?
$\delta_{H(max)}$ $(\delta_{V(max)})$ (mm) = 24.06 (19.53)
$EI/\gamma_w S_V^4$ = 1631.66
$\gamma_{s,avg}$ (kN/m³) = 20
S_u (kPa) = 170
FS (Eq. 2-26 and 2-27) = 7.78 and 3.99
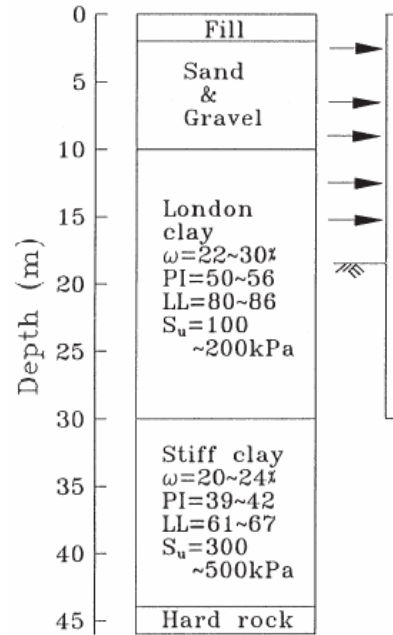
Depth (m)	δ_H (mm)
2.05	6.36
3.20	8.78
4.37	10.90
5.72	12.97
6.82	14.92
8.03	17.31
8.90	19.00
10.09	20.65
11.05	21.73
12.25	22.86
13.23	23.62
14.53	24.06
15.32	24.06
16.10	23.81
17.20	23.15
18.25	22.12
19.33	20.79
20.27	19.45
21.40	17.57
22.14	16.15
24.31	12.44
25.94	10.61
26.81	9.74
27.63	8.98
28.33	8.44
29.89	7.81

Lateral Deformation (mm)

183
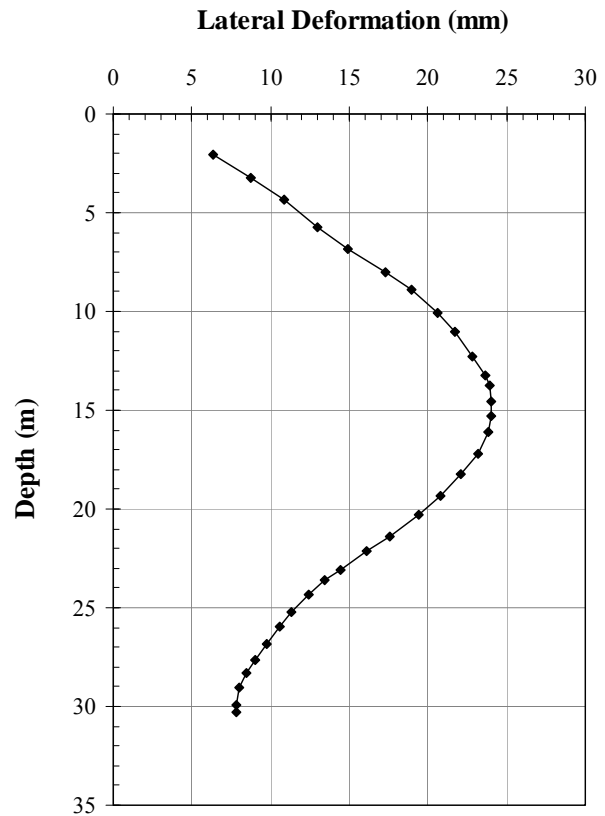
St3: Far-East Enterprise Center project in Taipei (Hsieh and Ou, 1998)

Wall Type =	Diaphragm
Thickness (m) =	0.9 (assumed)
H (m) =	33
H_e (m) =	20
B =	63.8
I (m⁴/m) =	0.0607
E (GPa) =	27.6
S_V (m) =	3.3
S_H (m) =	?
$\delta_{H(max)}$ $(\delta_{V(max)})$ (mm) =	124.76 (77.76)
$EI/\gamma_w S_V^4$ =	1442.69
$\gamma_{s,avg}$ (kN/m³) =	19
s_u (kPa) =	76.5
FS (Eq. 2-26 and 2-27) =	1.26 and 1.26
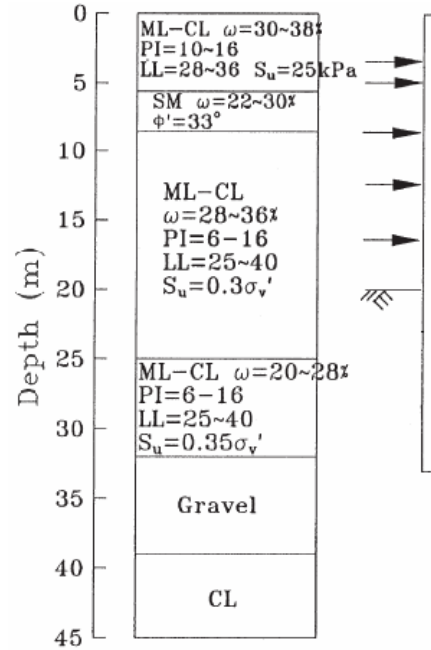
Depth (m)	δ_H (mm)
0.00	57.71
2.79	65.91
3.99	69.94
5.70	77.61
6.53	82.04
7.45	87.54
8.44	94.00
9.55	100.97
10.68	107.43
12.55	117.06
13.36	120.39
14.00	122.33
15.57	124.76
16.40	124.76
17.47	123.39
18.60	120.09
20.45	109.40
21.18	102.63
22.04	94.20
22.83	85.60
23.43	78.41
24.62	63.71
26.03	47.08
28.63	22.16
30.43	10.33
32.35	0.00

Lateral Deformation (mm)

184
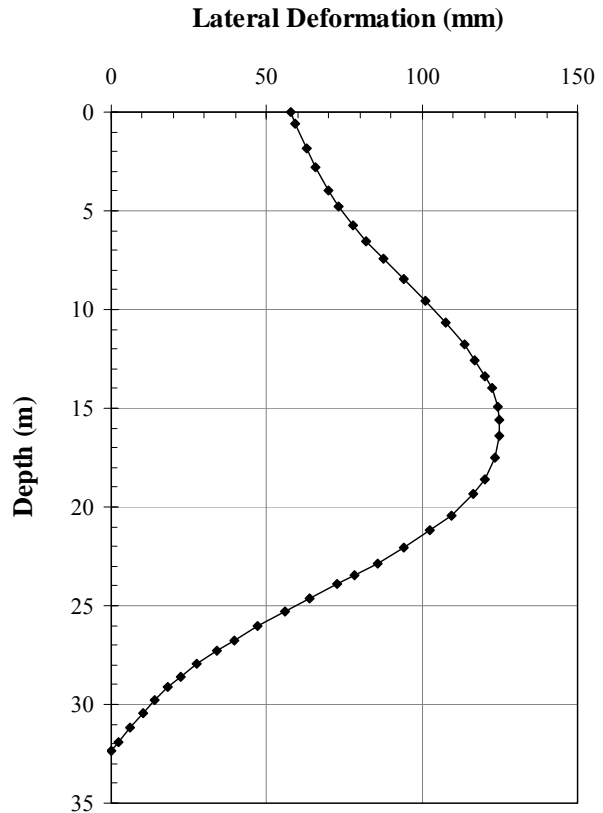
## St4: Oxley Rise Development in Singapore (Poh et al., 1997)

Wall Type = Diaphragm
Thickness (m) = 0.6
H (m) = 14
H_e (m) = 11.1
B (m) = 33
I (m⁴/m) = 0.018
EI (kN-m²/m) = 500,000
S_V (m) = 4.3
S_H (m) = 6
$\delta_{H(\max)}$ ($\delta_{V(max)}$) (mm) = 10.02 (NA)
$EI / \gamma_w S_V^4$ = 149.23
$\gamma_{s,avg}$ (kN/m³) = 20.75
E_s / s_u = 600-900
FS (Eq. 2-26 and 2-27) = 2.37 and 2.05
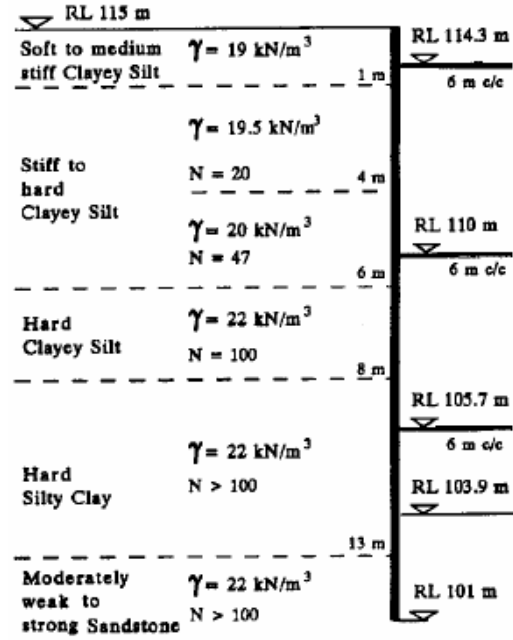
| Depth (m)	δ_H (mm)
0.46	6.44
1.00	6.70
2.00	7.45
2.51	7.86
3.01	8.25
3.50	8.60
4.02	8.97
4.53	9.33
5.01	9.57
5.52	9.83
6.00	9.93
6.50	10.02
7.00	9.95
7.50	9.62
7.99	9.32
8.49	9.01
9.00	8.55
9.48	7.89
10.00	7.05
10.55	6.23
11.04	5.38
12.08	3.64
12.59	2.74
13.07	1.93
13.56	1.23
14.06	0.32

Lateral Deformation (mm)

185
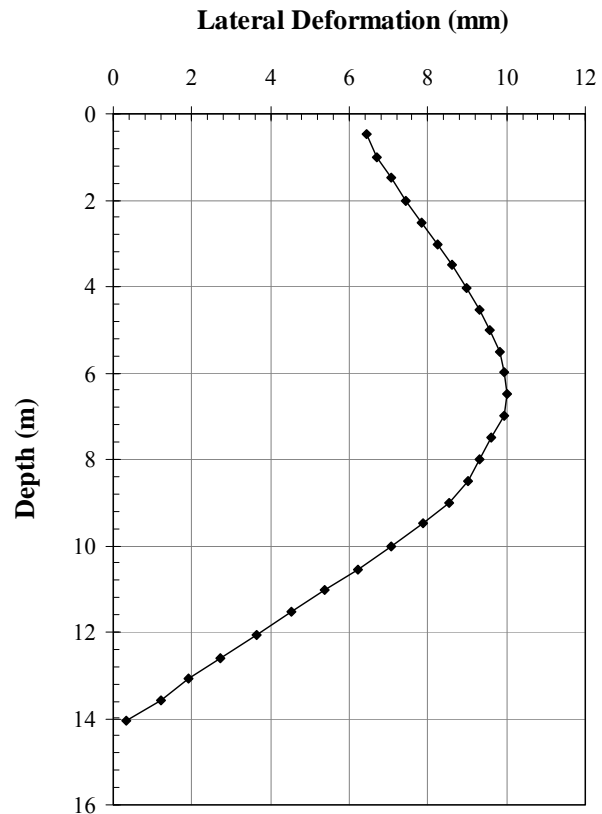
St5: Central Insurance Building in Taipei (Ou and Shiau, 1998)

Wall Type = Diaphragm
Thickness (m) = 0.6
H (m) = 23
H_e (m) = 11.4
B = 33.7
I (m⁴/m) = 0.018
E (GPa) = 12
S_V (m) = 3.3
S_H (m) = ?
$\delta_{H(\max)}$ $(\delta_{V(max)})$ (mm) = 44.53 (NA)
$EI/\gamma_w S_V^4$ = 185.85
$\gamma_{s,avg}$ (kN/m³) = 19.7
s_u (kPa) = 50
FS (Eq. 2-26 and 2-27) = 1.42 and 1.51
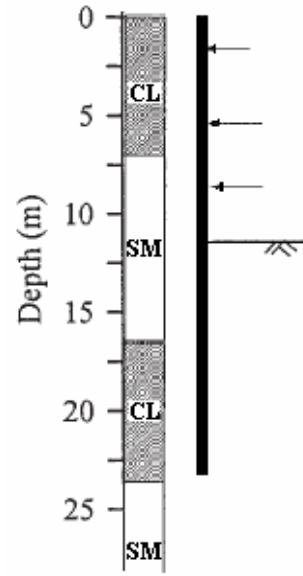
| Depth (m)	δ_H (mm)
0.006	20.251
0.523	20.126
1.304	21.590
2.007	22.906
3.133	26.635
4.802	29.902
5.612	31.534
6.713	36.064
7.813	38.882
8.078	39.538
9.438	43.336
9.973	44.084
10.410	44.382
11.880	43.488
12.548	42.144
13.447	40.210
14.796	35.658
15.465	32.991
16.093	30.645
16.614	28.201
17.685	23.876
18.236	21.622
19.445	17.487
20.012	15.607
21.069	12.789
22.431	9.689

Lateral Deformation (mm)

186
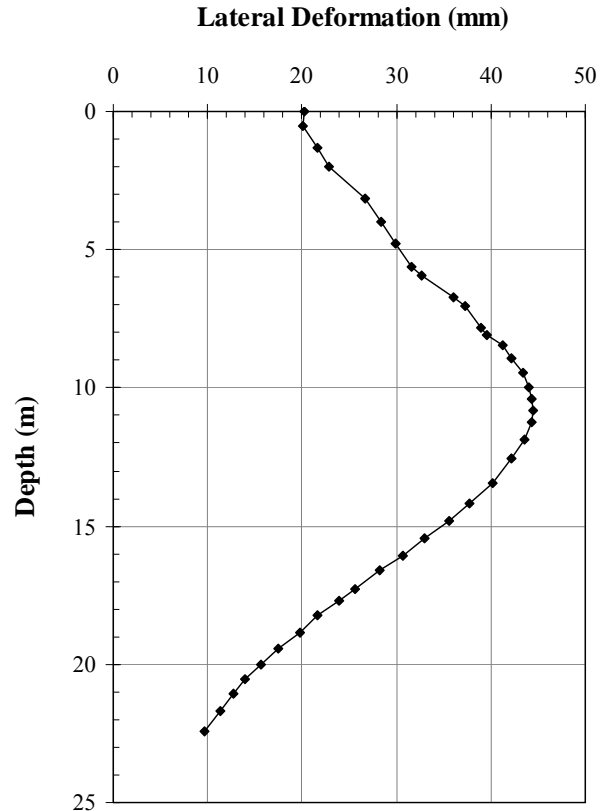
St6: Post Office Square Garage in Boston (Whittle et al., 1993)

Wall Type = Diaphragm
Thickness (m) = 0.9
H (m) = 25.6
H_e (m) = 20.2
B = 61
I (m⁴/m) = 0.0607
E (GPa) = 23
S_V (m) = 3
S_H (m) = Floor Slab
$\delta_{H(max)}$ ($\delta_{V(max)}$) (mm) = 53.61 (45)
$EI/\gamma_w S_V^4$ = 1760.20
$\gamma_{s,avg}$ (kN/m³) = 20.24
s_u (kPa) = 91
FS (Eq. 2-26 and 2-27) = 1.42 and 1.32
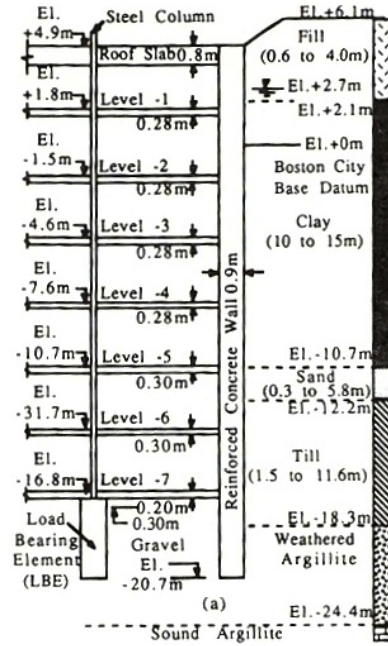
| Depth (m)	δ_H (mm)
0.18	24.04
1.22	26.71
2.42	29.92
3.60	33.80
4.83	38.10
6.12	42.63
7.48	46.45
8.80	48.96
10.00	51.68
11.23	53.10
12.20	53.61
13.48	52.94
14.63	50.99
15.87	47.75
17.14	43.83
18.36	39.01
19.69	32.35
20.70	26.48
21.82	20.56
23.05	14.33
24.26	7.92
25.34	4.29
26.83	2.97
27.97	2.58
29.29	1.81

Lateral Deformation (mm)

187
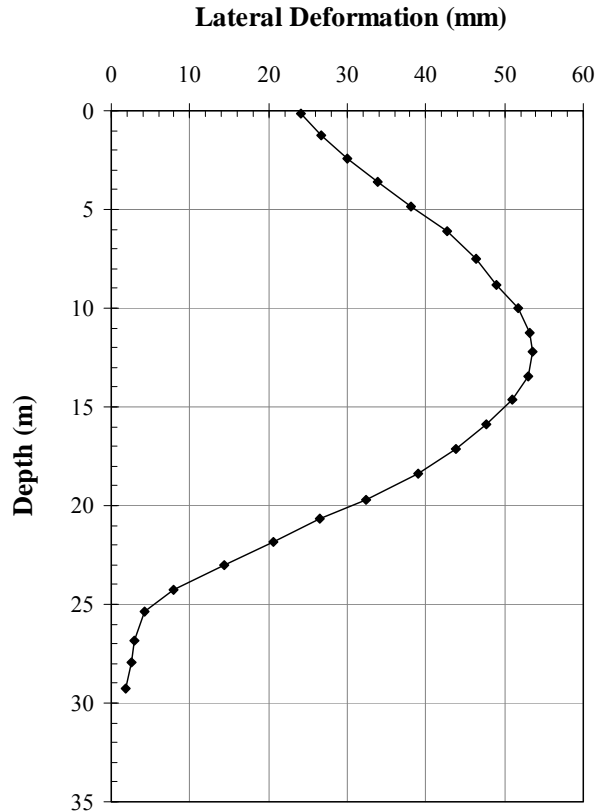
St7: National Taiwan University Hospital in Taiwan (Liao and Hsieh, 2002)

Wall Type = Diaphragm
Thickness (m) = 0.8
H (m) = 27
H_e (m) = 15.7
B = 140
I (m⁴/m) = 0.0426
E (GPa) = 27.6
S_V (m) = 2.65
S_H (m) = 1.92
$\delta_{H(\max)}$ $(\delta_{V(max)})$ (mm) = 81.3 (NA)
$EI/\gamma_w S_V^4$ = 2432.82
$\gamma_{s,avg}$ (kN/m³) = 20 (assumed)
s_u (kPa) = 70-85
FS (Eq. 2-26 and 2-27) = 1.46 and 1.38
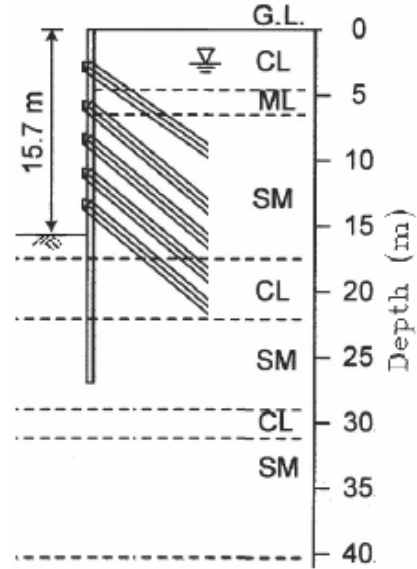
| Depth (m)	δ_H (mm)
1.19	29.09
3.45	36.26
5.21	42.79
6.85	49.71
8.49	58.37
9.51	64.53
10.58	70.06
11.61	74.33
12.77	77.85
13.99	80.36
15.06	81.37
15.75	81.12
16.30	79.61
17.24	76.38
18.50	70.11
19.52	64.45
20.49	57.88
21.62	49.29
22.65	43.02
23.52	36.65
24.91	27.61
25.65	21.52
25.89	20.12

Lateral Deformation (mm)

188
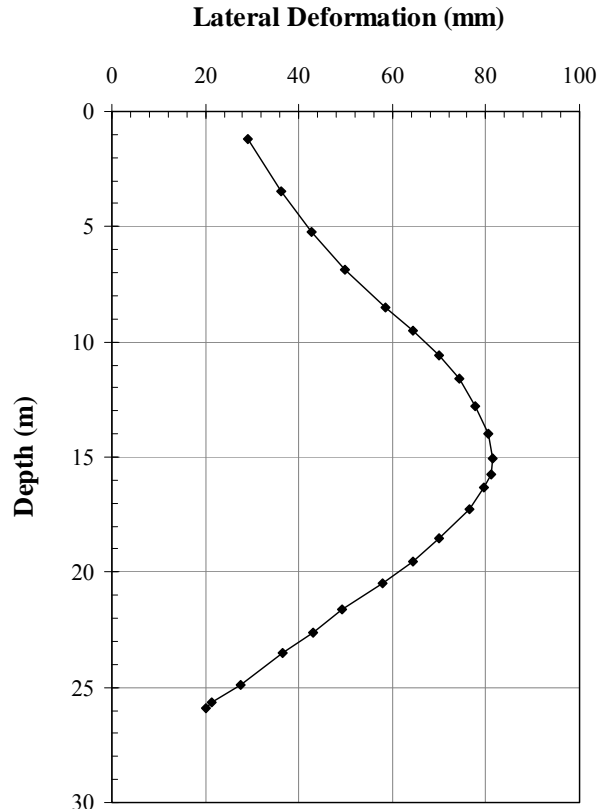
St8: Taipei County Administration Center in Taiwan (Liao and Hsieh, 2002)

Wall Type = Diaphragm
Thickness (m) = 1.2
H (m) = 38
H_e (m) = 20
B = 93
I (m⁴/m) = 0.144
E (GPa) = 27.6
S_V (m) = 2.33
S_H (m) = 1.85
$\delta_{H(max)}$ ($\delta_{V(max)}$) (mm) = 54.30 (NA)
$EI/\gamma_w S_V^4$ = 13760.11
$\gamma_{s,avg}$ (kN/m³) = 20 (assumed)
s_u (kPa) = 52-78
FS (Eq. 2-26 and 2-27) = 0.97 and 0.99
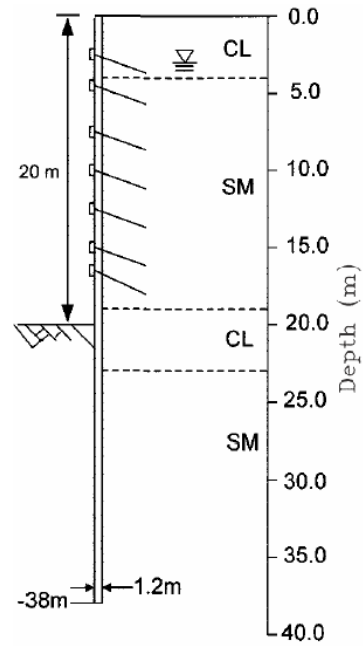
| Depth (m)	δ_H (mm)
0.09	23.12
1.38	25.20
2.48	27.27
3.94	29.21
5.07	31.14
6.67	34.47
8.07	37.37
9.27	40.41
10.87	43.32
12.51	46.63
14.30	50.42
15.51	52.97
16.81	54.30
18.14	53.83
19.71	52.72
21.38	50.79
23.31	47.64
24.56	45.21
27.46	38.67
28.91	35.46
30.41	31.81
31.88	28.82
33.41	25.28
35.05	21.40
36.83	17.86
37.76	15.42

Lateral Deformation (mm)

189
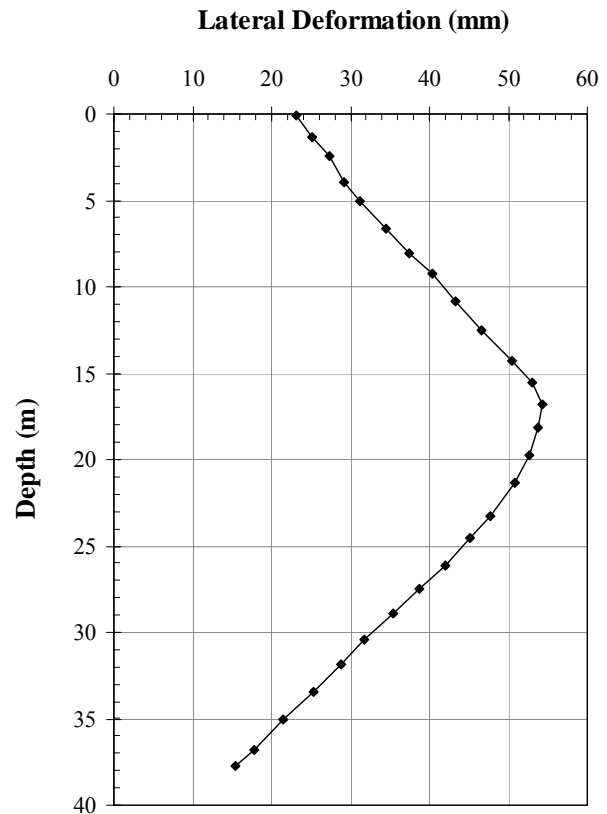
St9: 75 State Street in Boston (Becker and Haley, 1990)

Wall Type = Diaphragm
Thickness (m) = 0.75
H (m) = 26
H_e (m) = 20
B = 45.7
I (m⁴/m) = 0.035
E (GPa) = 23.2
S_V (m) = 3.35
S_H (m) = Floor Slab
$\delta_{H(\max)}$ $(\delta_{V(max)})$ (mm) = 47.26 (101.6)
$EI/\gamma_w S_V^4$ = 660.71
$\gamma_{s,avg}$ (kN/m³) = 18
s_u (kPa) = 45-95
FS (Eq. 2-26 and 2-27) = 1.26 and 1.21
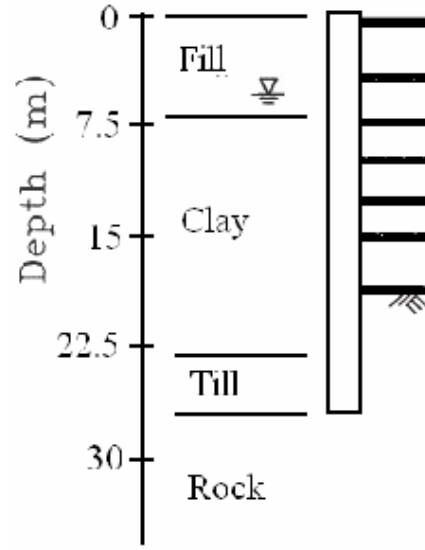
| Depth (m)	δ_H (mm)
0.05	21.45
1.66	24.41
2.88	26.68
5.03	31.74
6.61	34.88
7.81	36.45
8.68	39.07
10.67	43.77
11.57	45.87
12.55	47.26
13.17	47.26
14.26	46.74
15.27	44.99
16.25	42.20
17.17	39.37
17.89	36.56
18.68	33.23
19.50	29.37
20.81	22.26
21.58	18.61
22.33	14.83
22.90	12.30
24.19	6.69
24.95	4.03
25.35	1.92
25.55	0.65

Lateral Deformation (mm)

190
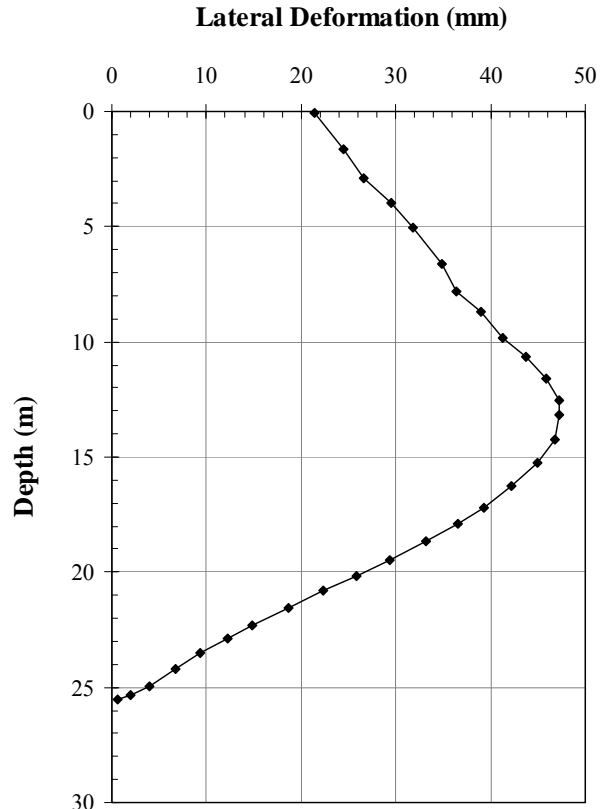
St10: Smith Tower in Houston, Texas (Ulrich, 1989)

Wall Type = Secant Pile
Thickness (m) = 0.75
H (m) = 20
H_e (m) = 12.2
B = 36.6
I (m⁴/m) = 0.035
E (GPa) = 27.6
S_V (m) = 2.45
S_H (m) = ?
$\delta_{H(max)}$ $(\delta_{V(max)})$ (mm) = 14.75 (NA)
$EI/\gamma_w S_V^4$ = 2748.03
$\gamma_{s,avg}$ (kN/m³) = 20.1
s_u (kPa) = 140
FS (Eq. 2-26 and 2-27) = 4.45 and 3.62
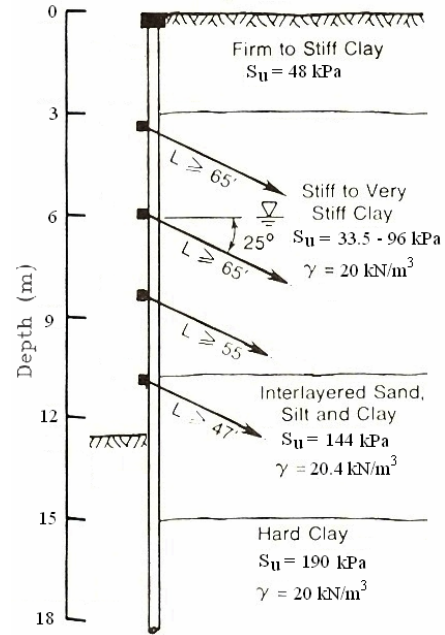
Depth (m)	δ_H (mm)
0.62	9.59
1.74	9.63
2.28	9.91
3.86	10.51
4.26	10.51
5.63	11.34
6.53	12.18
7.16	12.63
8.33	13.40
9.19	14.20
9.95	14.65
10.46	14.75
11.20	14.43
11.82	13.96
12.43	13.32
13.02	12.77
14.33	11.21
15.65	8.71
16.56	7.31
17.51	5.92
18.20	5.04
19.01	3.94
20.18	2.67
21.72	1.41
22.44	1.11
23.47	0.59

Lateral Deformation (mm)

191
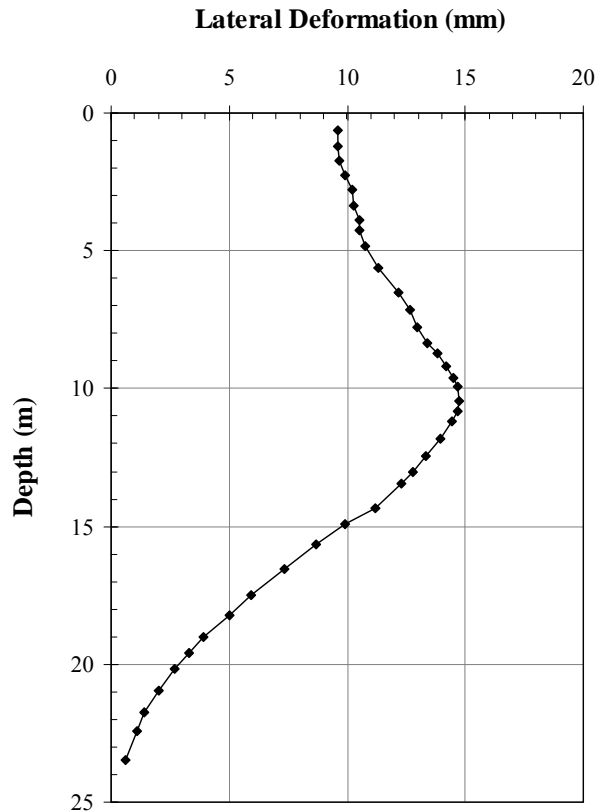
C.2 Case Histories in Medium Clay

M1: Taipei National Enterprise Center (TNEC) in Taiwan (Ou et al., 1998)

Wall Type = Diaphragm

Thickness (m) = 0.9

H (m) = 35

H_e (m) = 19.7

B (m) = 40

I (m⁴/m) = 0.0607

E (GPa) = 27.6

S_V (m) = 3.4

S_H (m) = Floor Slab

$\delta_{H(\max)}$ ($\delta_{V(max)}$) (mm) = 106.51 (77.18)

$EI/\gamma_w S_V^4$ = 1280.31

$\gamma_{s,avg}$ (kN/m³) = 18.9
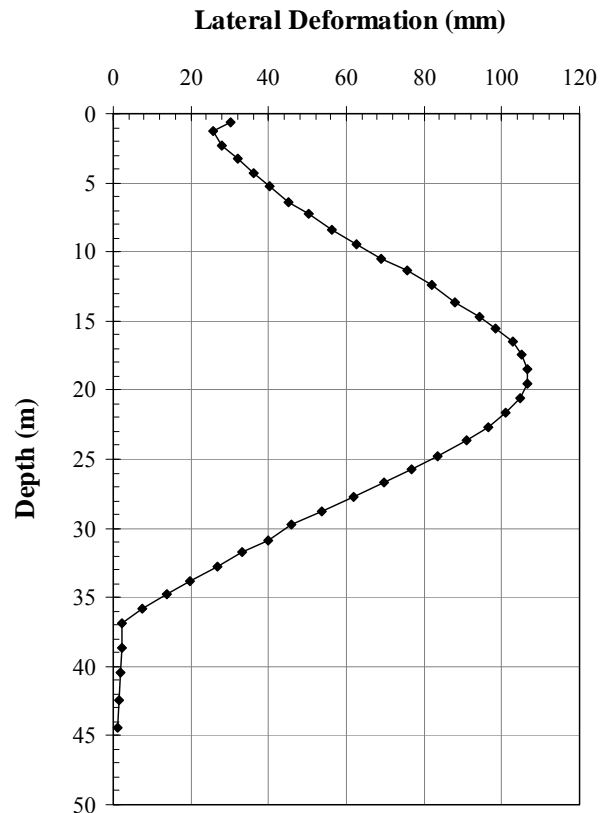
S_u (kPa) = 50

FS (Eq. 2-26 and 2-27) = 0.84 and 0.96
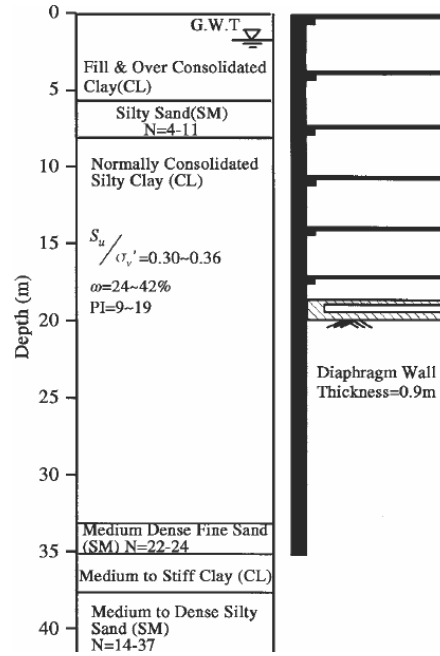
Depth (m)	δ_H (mm)
0.64	30.30
1.29	25.56
3.22	32.19
4.29	35.98
6.44	44.97
8.37	56.33
10.52	69.11
12.45	81.89
14.70	94.20
15.56	98.46
17.49	105.09
18.45	106.51
19.53	106.51
20.60	104.62
22.64	96.57
25.75	76.69
27.68	62.01
29.72	45.92
30.90	39.76
33.80	19.88
35.84	7.57
36.91	2.37
40.45	1.89
44.42	0.95

Lateral Deformation (mm)

192

M2: Robert H. Lurie Medical Research Building in Chicago (East Wall) (Finno and Roboski, 2005)

Wall Type = Sheet Pile
Ref. = PZ-27
H (m) = 16.5
H_e (m) = 10
B (m) = 68
I (m⁴/m) = 0.000252
E (GPa) = 200
S_V (m) = 4
S_H (m) = 2.74 – 1.83
$\delta_{H(max)}$ $(\delta_{V(max)})$ (mm) = 43.22 (NA)
$EI/\gamma_w S_V^4$ = 20.09
$\gamma_{s,avg}$ (kN/m³) = 19
s_u (kPa) = 29-43
FS (Eq. 2-26 and 2-27) = 1.12 and 1.08
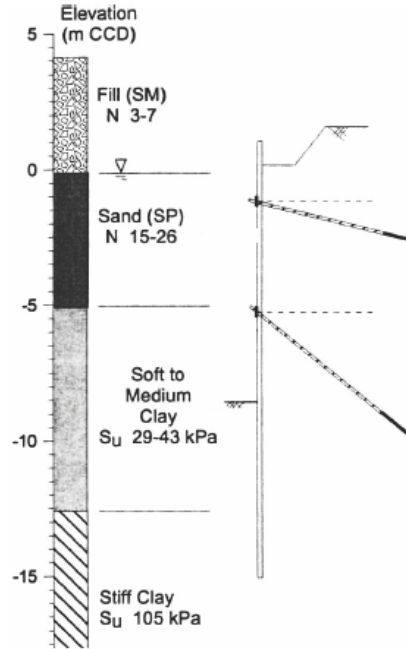
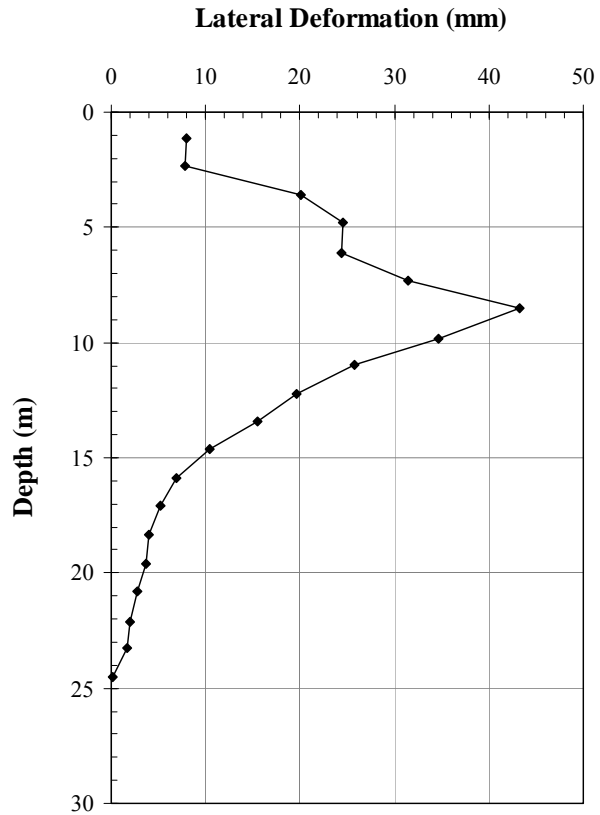| Depth (m)	δ_H (mm)
1.12	7.91
2.32	7.81
3.58	20.06
4.81	24.54
6.09	24.45
7.29	31.51
8.50	43.23
9.82	34.64
10.96	25.70
12.21	19.62
13.44	15.51
14.64	10.45
15.86	6.94
17.09	5.24
18.35	4.04
19.61	3.73
20.81	2.84
22.09	2.04
23.28	1.63
24.51	0.10

Lateral Deformation (mm)

193

M3: Robert H. Lurie Medical Research Building in Chicago (West Wall) (Finno and Roboski, 2005)

Wall Type = Sheet Pile
Ref. = PZ-27
H (m) = 19
H_e (m) = 12.8
B (m) = 68
I (m⁴/m) = 0.000252
E (GPa) = 200
S_V (m) = 4
S_H (m) = 2.74 – 1.83
$\delta_{H(max)}$ ($\delta_{V(max)}$) (mm) = 63.48 (74)
$EI/\gamma_w S_V^4$ = 20.09
$\gamma_{s,avg}$ (kN/m³) = 19
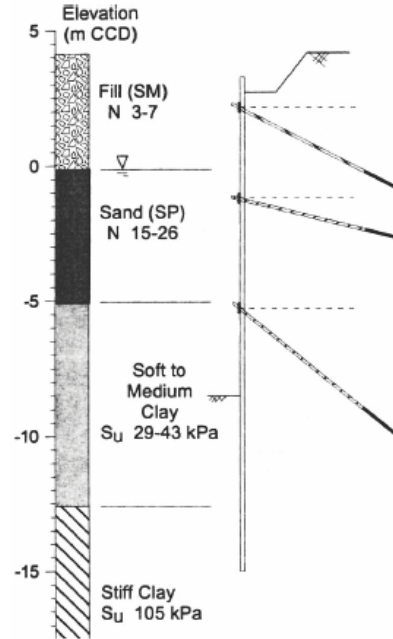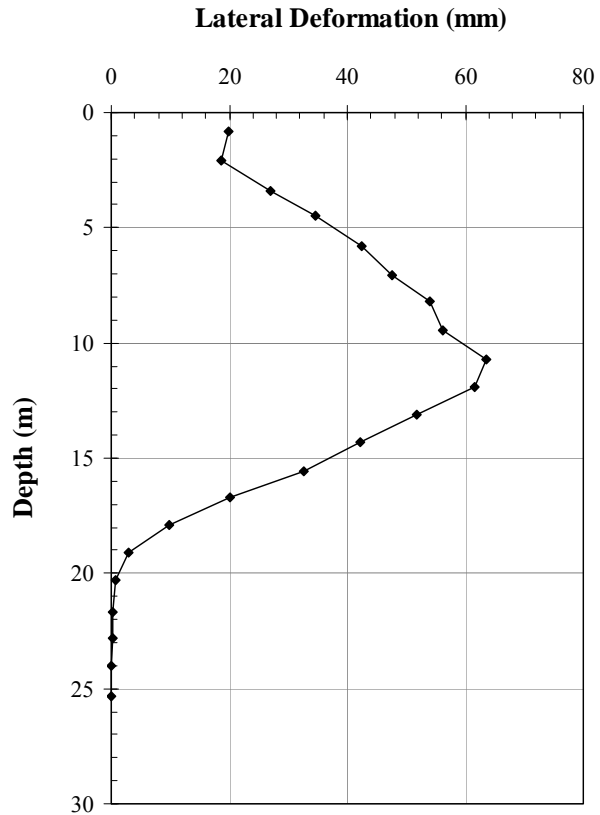S_u (kPa) = 29-43
FS (Eq. 2-26 and 2-27) = 0.83 and 0.80

Depth (m)	δ_H (mm)
0.84	19.96
2.10	18.60
3.38	27.11
4.51	34.61
5.81	42.44
7.04	47.66
8.20	54.02
9.42	56.26
10.73	63.48
11.94	61.65
13.12	51.67
14.33	42.31
15.54	32.54
16.72	20.22
17.92	9.84
19.08	2.99
20.28	0.83
21.67	0.19
22.84	0.31
24.00	0.12
25.34	0.08

Lateral Deformation (mm)

M4: Taiwan Formosa in Taipei basin (Ou et al., 1993; Hsieh and Ou, 1998)

Wall Type = Diaphragm

Thickness (m) = 0.8

H (m) = 31

H_e (m) = 18.4

B (m) = 35

I (m⁴/m) = 0.04267

E (GPa) = 27.6

S_V (m) = 2.85

S_H (m) = ?

$\delta_{H(max)}(\delta_{V(max)})$ (mm) = 62.61 (43.16)

$EI/\gamma_w S_V^4 =$ 1821.35

$\gamma_{s,avg}$ (kN/m³)= 19

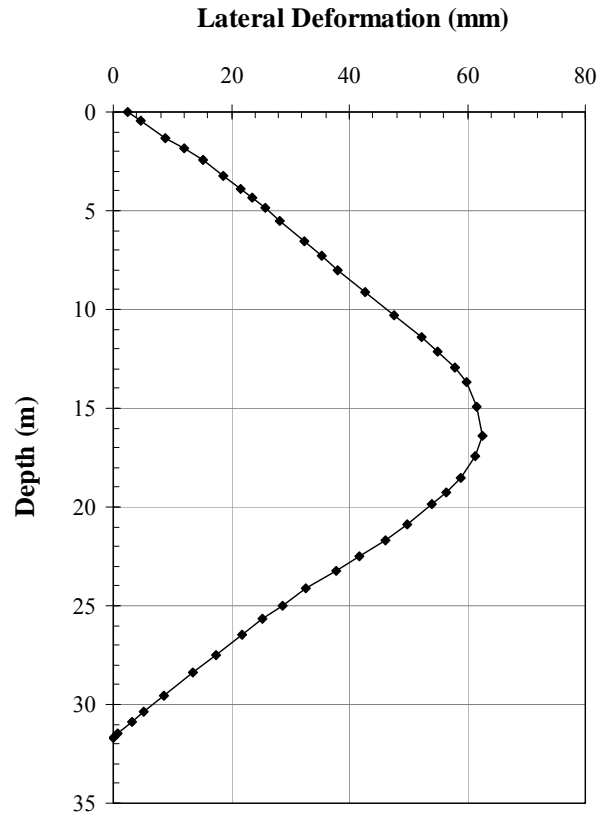s_u (kPa) = 25-70

FS (Eq. 2-26 and 2-27) = 0.86 and 0.97
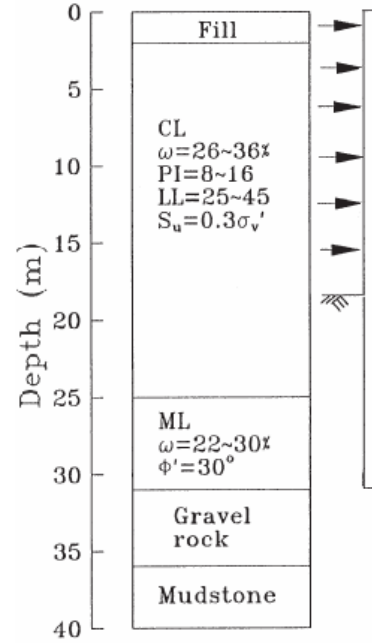
Depth (m)	δ_H (mm)
0.00	2.56
1.30	8.90
3.26	18.53
4.33	23.47
6.53	32.40
7.29	35.41
7.99	38.15
9.14	42.81
10.28	47.50
12.12	55.05
13.65	59.78
14.95	61.61
16.41	62.61
17.44	61.46
18.51	58.90
19.26	56.35
20.86	49.88
21.66	46.03
22.47	41.76
23.23	37.88
24.12	32.73
26.47	21.75
27.47	17.42
29.53	8.66
30.39	5.08
31.67	0.00

Lateral Deformation (mm)

195

M5: Tokyo Subway Excavation project in Japan (Miyoshi, 1977)

Wall Type =	Steel Concrete
Thickness (m) =	0.8 (assumed)
H (m) =	32
H_e (m) =	17
B (m) =	30
I (m⁴/m) =	0.04267
E (GPa) =	27.6
S_V (m) =	2.7
S_H (m) =	?
$\delta_{H(\max)}$ ($\delta_{V(max)}$) (mm) =	176.56 (152.42)
$EI/\gamma_w S_V^4$ =	2261.08
$\gamma_{s,avg}$ (kN/m³) =	19 (assumed)
s_u (kPa) =	42
FS (Eq. 2-26 and 2-27) =	0.83 and 0.99
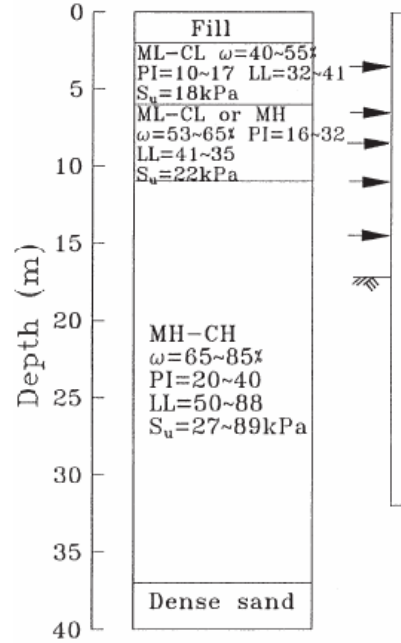
Depth (m)	δ_H (mm)
0.00	28.86
1.85	44.15
3.15	53.37
5.57	73.06
6.73	84.64
7.91	97.94
8.92	109.29
10.92	131.11
11.76	140.47
12.85	152.47
14.11	165.30
15.98	176.56
16.64	176.00
17.49	172.02
18.81	161.83
19.71	153.95
20.60	144.45
21.25	136.48
22.05	126.25
23.71	103.27
25.71	76.03
26.58	64.72
27.28	55.32
28.07	45.49
30.21	20.52
32.01	0.00

Lateral Deformation (mm)
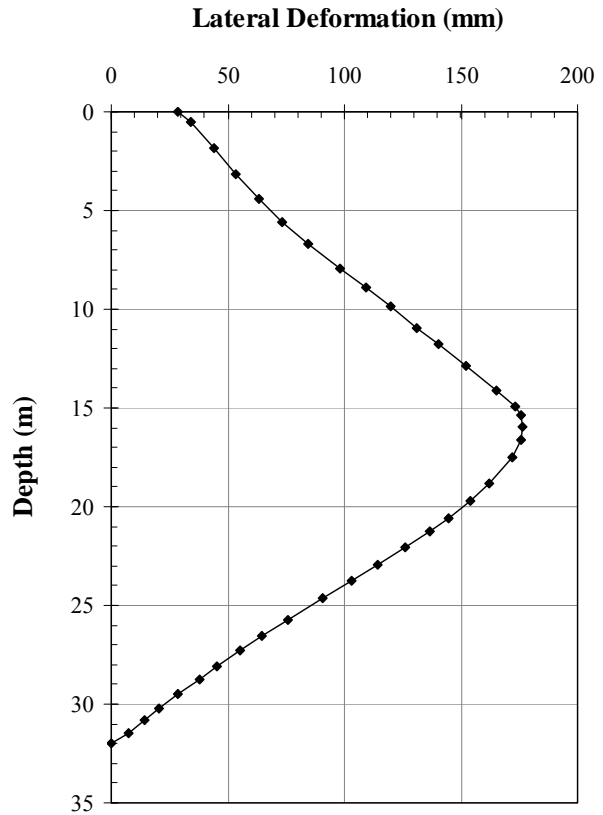
M6: HDR - 4 Project for the Chicago Subway (Finno et al., 1989)

Wall Type =	Sheet Pile
Ref. =	NA
H (m) =	19.2
H_e (m) =	12.2
B (m) =	12.2
EI (kN-m²/m) =	161,000
E (GPa) =	200
S_V (m) =	2.5
S_H (m) =	?
$\delta_{H(max)}$ ($\delta_{V(max)}$) (mm) =	172.64 (255.7)
$EI/\gamma_w S_V^4$ =	420.57
$\gamma_{s,avg}$ (kN/m³)=	19
s_u (kPa) =	30
FS (Eq. 2-26 and 2-27) =	0.90 and 1.10
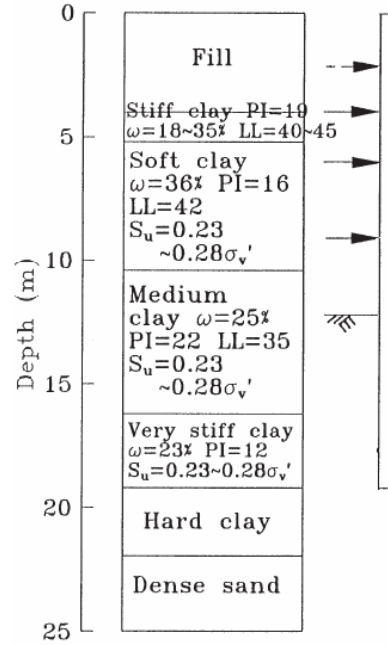
Depth (m)	δ_H (mm)
1.10	33.34
2.45	61.83
3.09	74.81
4.49	100.54
5.15	111.76
6.90	138.84
7.62	149.39
8.76	160.56
9.59	166.38
10.12	169.31
11.52	172.64
12.32	172.24
12.97	169.53
13.45	165.08
14.25	149.56
14.94	129.65
15.26	118.93
16.06	90.27
16.36	78.36
16.93	59.58
17.27	49.70
17.89	33.62
18.28	26.91
18.65	21.83
19.02	17.43
19.30	15.63

Lateral Deformation (mm)

197
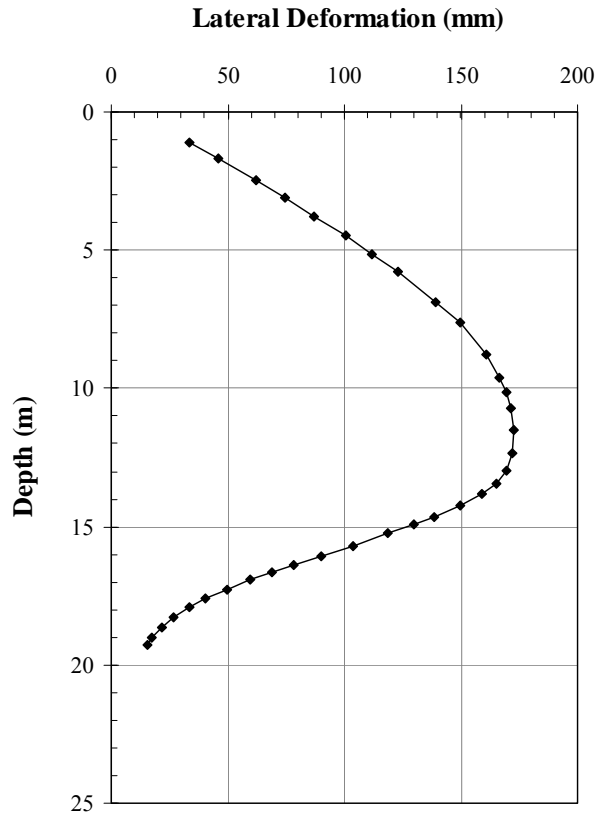
M7: Oslo Subway Excavation Project (Norwegian Geotechnical Institute, 1962)

Wall Type =	Sheet Pile
Ref. =	NA
H (m) =	16
H_e (m) =	11
B (m) =	11
EI (kN-m²/m) =	73,800
E (GPa) =	200
S_V (m) =	1.7
S_H (m) =	?
$\delta_{H(max)}$ ($\delta_{V(max)}$) (mm) =	223.58 (200)
$EI/\gamma_w S_V^4$ =	901.64
$\gamma_{s,avg}$ (kN/m³) =	19 (assumed)
s_u (kPa) =	30
FS (Eq. 2-26 and 2-27) =	1.03 and 1.16
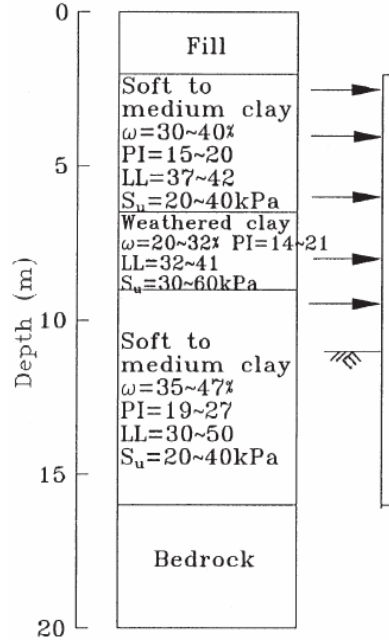
8epth (m)	δ_H (mm)
0.51	0.00
0.92	10.85
1.57	29.68
2.23	48.86
3.31	79.88
3.93	97.71
4.72	121.64
5.36	139.47
6.19	160.88
6.83	178.06
7.54	193.55
8.15	208.04
8.70	220.94
8.89	223.23
9.05	223.58
9.13	223.23
9.28	221.58
9.62	212.02
10.32	187.92
10.81	170.15
11.34	149.03
11.87	125.92
12.40	101.47
12.76	86.69
13.19	70.56
13.67	54.43

Lateral Deformation (mm)

198
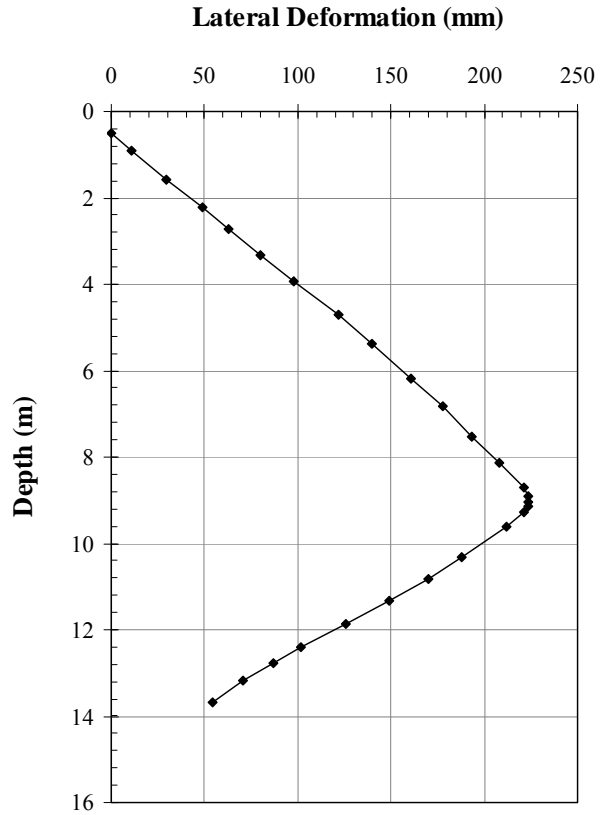
M8: Embarcadero BART Zone 1 in San Francisco (Clough and Buchignani, 1981)

$$\text{Wall Type} = \text{Diaphragm}$$
$$\text{Thickness (m)} = 1.0$$
$$H \text{ (m)} = 30.5$$
$$H_e \text{ (m)} = 21.3$$
$$B \text{ (m)} = ?$$
$$I \text{ (m}^4\text{/m)} = 0.0833$$
$$E \text{ (GPa)} = 25$$
$$S_V \text{ (m)} = 3$$
$$S_H \text{ (m)} = ?$$
$$\delta_{H(max)} (\delta_{V(max)}) \text{ (mm)} = 28.3 \text{ (NA)}$$
$$EI/\gamma_w S_V^4 = 2624.51$$
$$\gamma_{s,avg} \text{ (kN/m}^3\text{)} = 17$$
$$s_u \text{ (kPa)} = 28\text{-}60$$
$$FS \text{ (Eq. 2-26 and 2-27)} = 0.84 \text{ and } 0.98$$
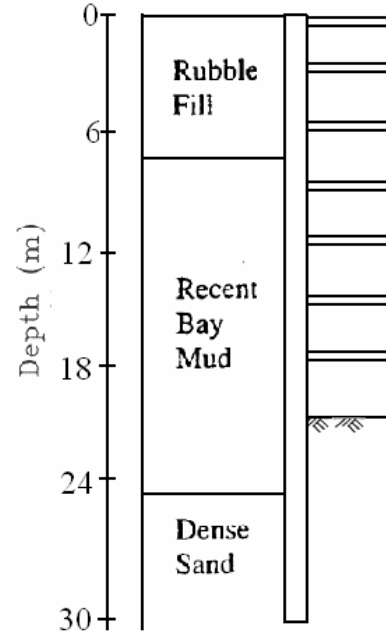
Depth (m)	δ_H (mm)
3.49	2.14
5.19	5.86
6.35	8.66
7.66	11.39
8.67	13.29
9.86	15.94
11.27	19.12
12.66	22.35
13.39	24.16
14.68	27.58
15.07	28.25
15.60	27.78
16.15	26.54
17.11	23.97
18.70	21.31
19.80	20.26
20.92	19.02
22.07	16.17
23.04	13.63
24.76	9.50
25.59	8.27
26.60	6.44
27.47	5.75
28.47	4.53
29.43	3.45
29.85	2.99

Lateral Deformation (mm)

199
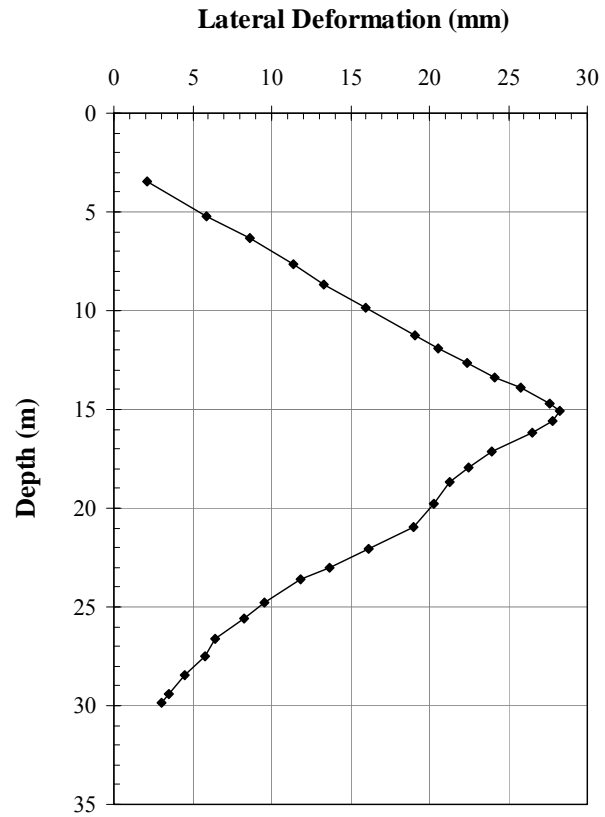
M9: Metro Station South Xizan Road in Shanghai (Wang et al., 2005)

Wall Type =	Diaphragm
Thickness (m) =	0.8
H (m) =	38
H_e (m) =	20.6
B (m) =	22.8
I (m⁴/m) =	0.0426
EI (kN-m²/m) =	1,280,000
S_V (m) =	4
S_H (m) =	3
$\delta_{H(\max)}$ ($\delta_{V(max)}$) (mm) =	48.12 (30.9)
$EI/\gamma_w S_V^4$ =	510.2
$\gamma_{s,avg}$ (kN/m³)=	18
s_u (kPa) =	20-50
FS (Eq. 2-26 and 2-27) =	0.61 and 0.85
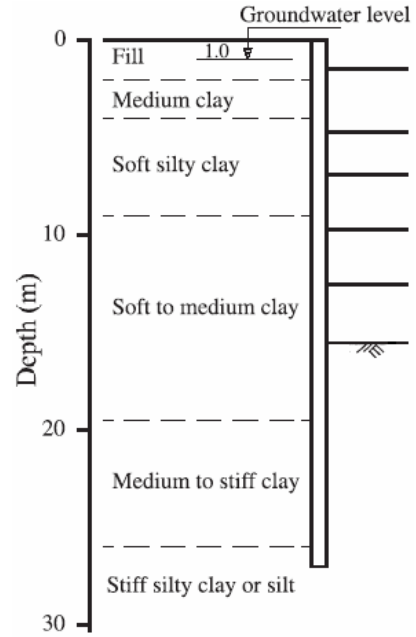
Depth (m)	δ_H (mm)
0.06	0.33
2.01	4.42
3.05	6.60
4.97	12.23
7.01	18.86
8.03	22.21
9.09	25.59
11.08	31.56
12.06	34.71
13.16	38.21
15.09	43.95
16.15	45.30
17.11	47.11
18.13	48.12
19.05	48.12
20.09	47.67
21.10	46.54
23.10	42.50
24.11	39.34
25.09	36.06
27.05	28.62
28.08	24.96
29.08	20.41
31.16	14.48
33.09	8.71
35.11	4.65

Lateral Deformation (mm)

200
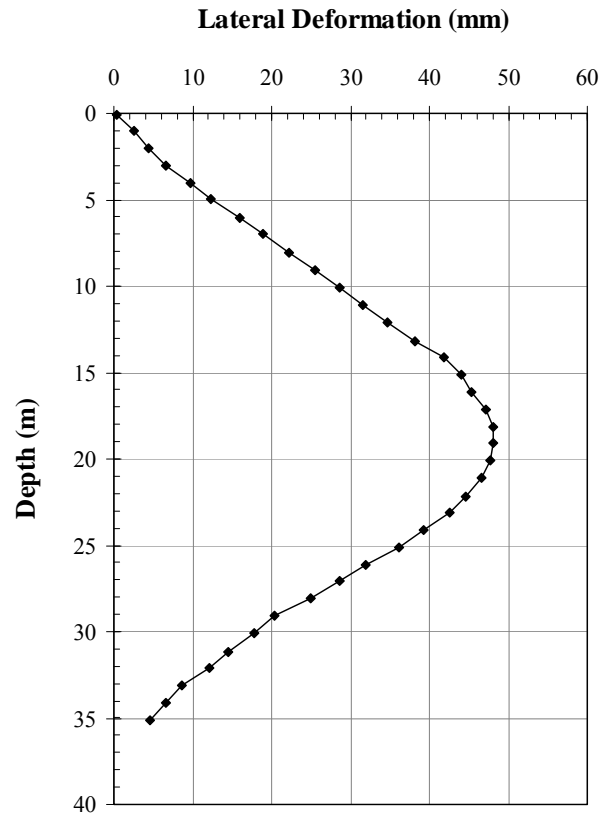
M10: Open Cut in Oslo (Peck, 1969)

Wall Type = Sheet Pile
Ref = Belval Z IV N-50
H (m) = 14
H_e (m) = 8.5
B (m) = 11
EI (kN-m²/m) = 73,800 (assumed)
E (GPa) = 200
S_V (m) = 1.68
S_H (m) = ?
$\delta_{H(max)}$ $(\delta_{V(max)})$ (mm) = 228.88 (210)
$EI/\gamma_w S_V^4$ = 945.35
$\gamma_{s,avg}$ (kN/m³) = 19 (assumed)
s_u (kPa) = 20-35
FS (Eq. 2-26 and 2-27) = 1.19 and 1.35
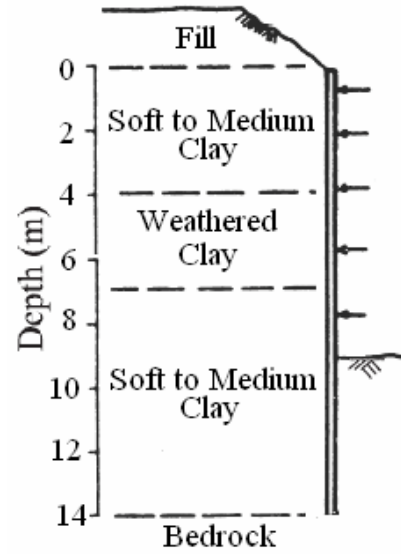
Depth (m)	δ_H (mm)
0.05	1.33
0.68	20.51
1.06	31.47
1.80	52.22
2.20	64.15
2.82	81.00
3.19	91.79
4.04	113.97
4.99	142.01
5.48	156.19
6.46	183.00
7.10	199.78
7.53	209.77
8.23	223.33
8.55	228.88
8.68	228.66
8.91	223.55
9.11	217.55
9.66	197.34
10.01	183.20
10.77	146.15
11.13	128.20
11.71	104.02
12.04	89.03
12.85	57.05
13.01	51.72

Lateral Deformation (mm)
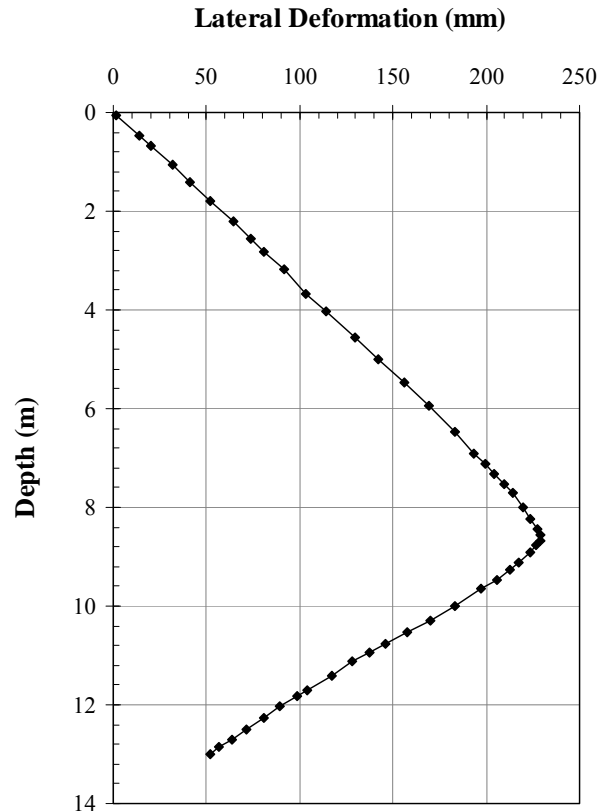
C.3   Case Histories in Soft Clay

So1: Chicago and State Street Excavation in Chicago (Finno et al., 2002)

Wall Type =	Secant Pile
Thickness (m) =	0.9
H (m) =	18.3
H_e (m) =	12.2
B (m) =	22
I (m^4/m) =	0.0607
E (GPa) =	12.65
S_V (m) =	3.8
S_H (m) =	6.1
$\delta_{H(max)}$ $(\delta_{V(max)})$ (mm) =	38.13 (27.43)
$EI/\gamma_w S_V^4$ =	376.08
$\gamma_{s,avg}$ (kN/m^3)=	19.1
s_u (kPa) =	20
FS (Eq. 2-26 and 2-27) =	0.52 and 0.59
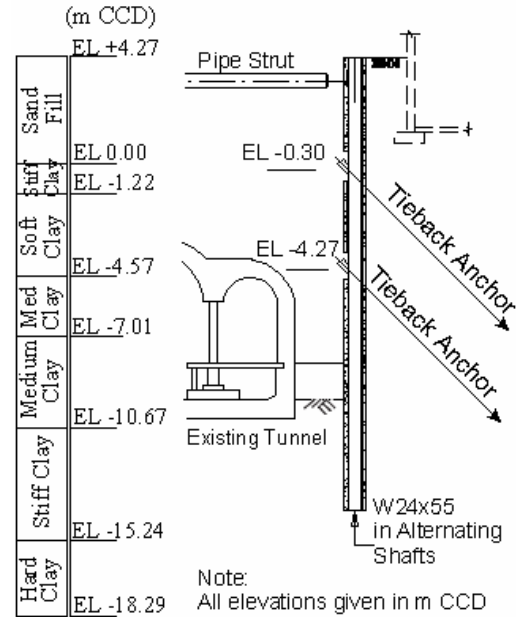
Depth (m)	δ_H (mm)
0.61	10.424
1.219	6.416
1.829	5.258
2.438	7.879
3.048	11.567
4.267	20.406
5.486	26.426
6.096	29.078
7.925	38.13
8.534	37.612
9.144	36.637
10.363	33.117
11.582	29.809
12.192	27.752
12.802	24.902
13.411	22.235
14.63	17.678
15.24	15.408
16.459	10.287
17.069	7.559
18.288	3.658
19.507	1.844
20.117	1.189

Lateral Deformation (mm)
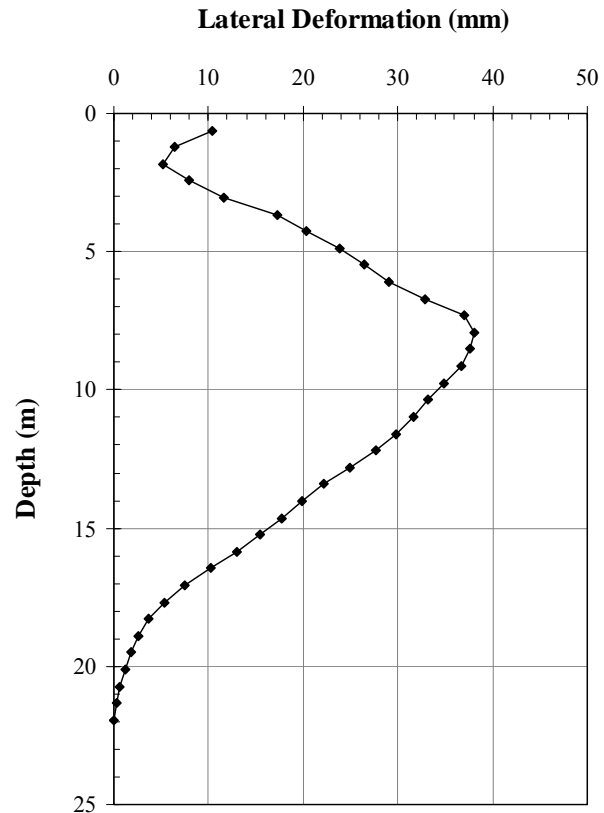
21.946	0

So2: Mass Rapid Transit Line in Singapore (Goh et al., 2003)

Wall Type =	Diaphragm
Thickness (m) =	0.8
H (m) =	31
H_e (m) =	16
B (m) =	20
I (m⁴/m) =	0.0426
E (GPa) =	30
S_V (m) =	2.5
S_H (m) =	9
$\delta_{H(\max)}$ $(\delta_{V(max)})$ (mm) =	38.55 (NA)
$EI/\gamma_w S_V^4$ =	3343.67
$\gamma_{s,avg}$ (kN/m³) =	17.6
s_u (kPa) =	10
FS (Eq. 2-26 and 2-27) =	0.21 and 0.31
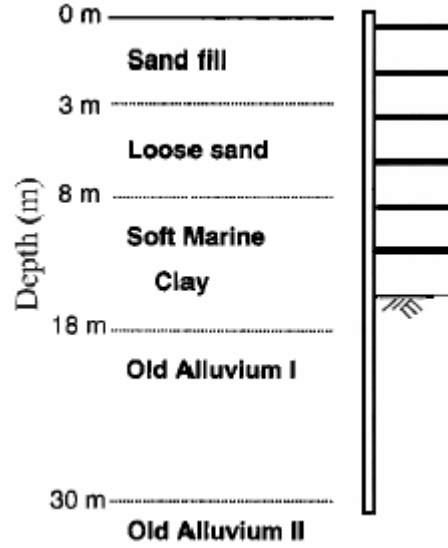
Depth (m)	δ_H (mm)
0.03	14.96
1.72	16.32
2.94	17.92
4.45	21.50
5.88	25.12
7.39	27.65
8.88	30.12
10.17	34.36
11.04	37.36
11.88	38.55
12.58	38.23
13.78	35.04
14.97	30.91
16.51	25.49
18.01	20.14
19.57	15.76
20.91	11.92
22.50	7.91
24.02	5.08
25.61	3.74
28.58	2.65
30.03	2.37
34.48	1.17
39.35	0.84
42.00	0.92

Lateral Deformation (mm)

203
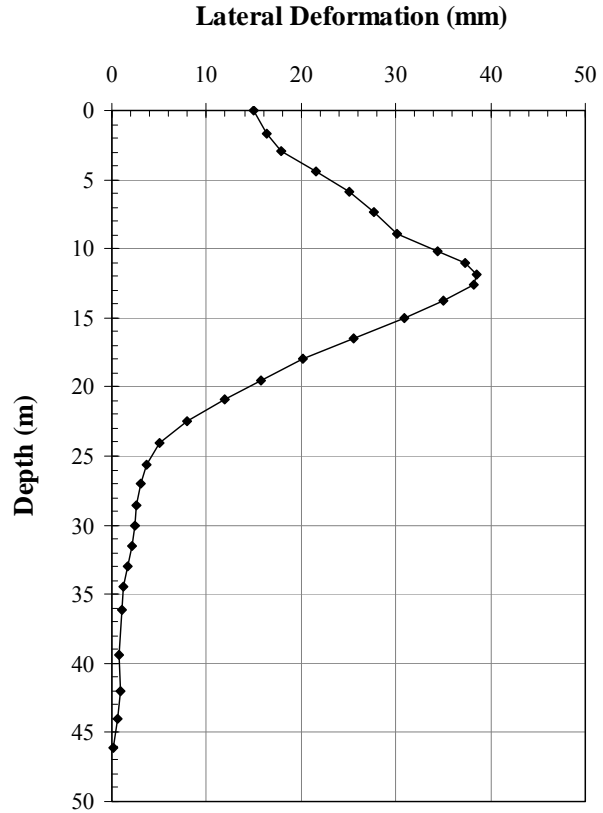
| 46.08 | 0.13 |

So3: Deep Excavation adjacent to the Shanghai Metro Tunnels (Hu et al., 2003)

Wall Type = Diaphragm
Thickness (m) = 0.8
H (m) = 21
H_e (m) = 11.5
B (m) = 28.5
I (m⁴/m) = 0.0426
E (GPa) = 21.7
S_V (m) = 3.5
S_H (m) = 9
$\delta_{H(max)}\ (\delta_{V(max)})$ (mm) = 15.39 (7.0)
$EI/\gamma_w S_V^4$ = 629.58
$\gamma_{s,avg}$ (kN/m³) = 18
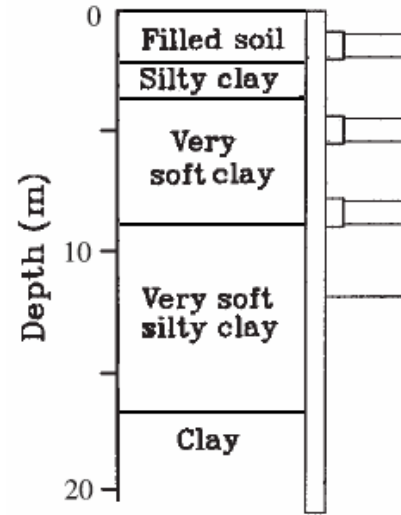s_u (kPa) = 22
FS (Eq. 2-26 and 2-27) = 0.64 and 0.73

Depth (m)	δ_H (mm)
0.00	2.35
1.45	4.51
2.13	5.96
3.28	8.08
4.29	9.52
5.23	10.25
6.15	11.19
7.00	12.22
7.78	13.64
8.53	14.99
9.08	15.31
9.74	15.39
10.33	14.97
10.97	13.94
11.49	13.47
11.67	13.16
12.46	12.10
13.24	11.00
14.33	9.80
15.67	7.69
16.96	5.65
17.72	4.63
18.59	3.56
19.04	3.04
20.73	1.23
21.01	1.00

Lateral Deformation (mm)
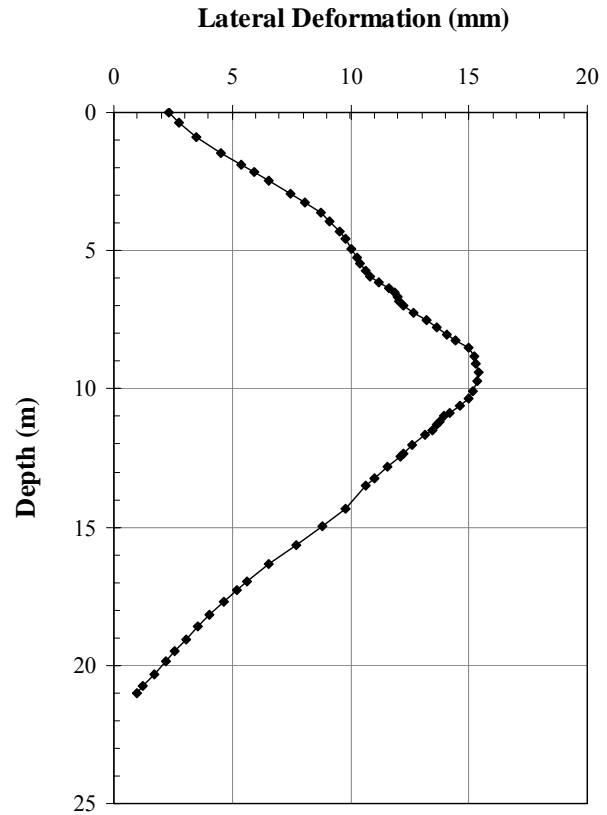
So4: Excavation in Downtown Chicago (Gill and Lukas, 1990)

Wall Type = Sheet Pile
Ref. = NA
H (m) = 16.8
H_e (m) = 7.0
B (m) = ?
EI (kN-m²/m) = 55,250
E (GPa) = 200
S_V (m) = 2.5
S_H (m) = ?
$\delta_{H(\max)}(\delta_{V(max)})$ (mm) = 83.27 (NA)
$EI/\gamma_w S_V^4$ = 144.33
$\gamma_{s,avg}$ (kN/m³) = 19 (assumed)
s_u (kPa) = 22.7
FS (Eq. 2-26 and 2-27) = 1.28 and 1.93

Depth (m)	δ_H (mm)
0.09	14.14
0.35	15.94
0.74	20.74
1.16	26.78
1.34	28.91
2.65	42.42
3.33	50.02
4.48	64.79
5.53	77.16
6.66	83.05
6.73	83.27
7.40	82.14
8.60	72.51
9.67	56.29
10.25	52.03
11.58	36.78
12.53	30.01
13.24	23.94
14.58	13.76
15.77	8.64
16.67	4.94
17.67	2.20
18.02	1.56
19.53	1.01
20.92	0.77
21.90	0.55

Lateral Deformation (mm)

205
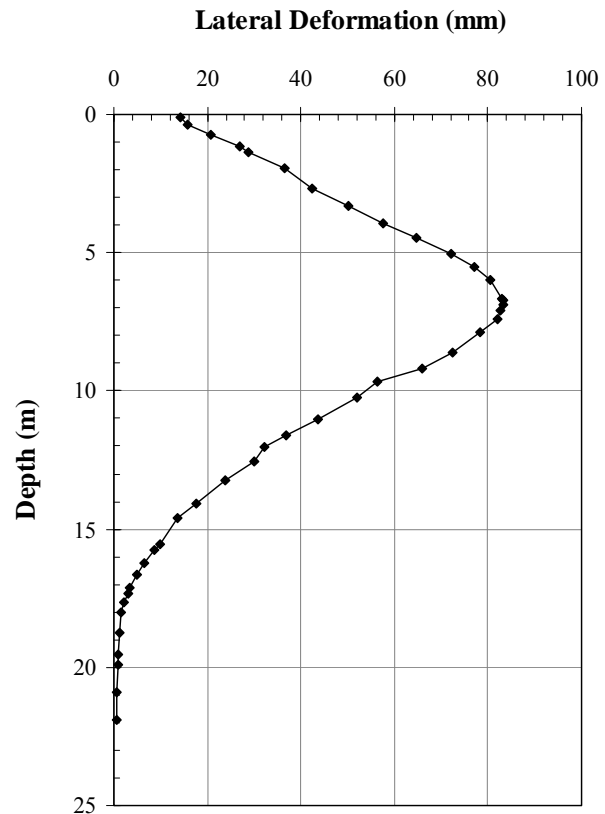
So5: Peninsula Hotel project in Bangkok (Teparaksa, 1993)

Wall Type =	Sheet Pile
Ref. =	FSP Type IV
H (m) =	18
H_e (m) =	8
B (m) =	65
I (m⁴/m) =	0.000252 (assumed)
E (GPa) =	200
S_V (m) =	2.5
S_H (m) =	?
$\delta_{H(\max)}$ $(\delta_{V(max)})$ (mm) =	123.65 (NA)
$EI/\gamma_w S_V^4$ =	131.66
$\gamma_{s,avg}$ (kN/m³)=	16
s_u (kPa) =	10-17
FS (Eq. 2-26 and 2-27) =	0.61 and 0.62
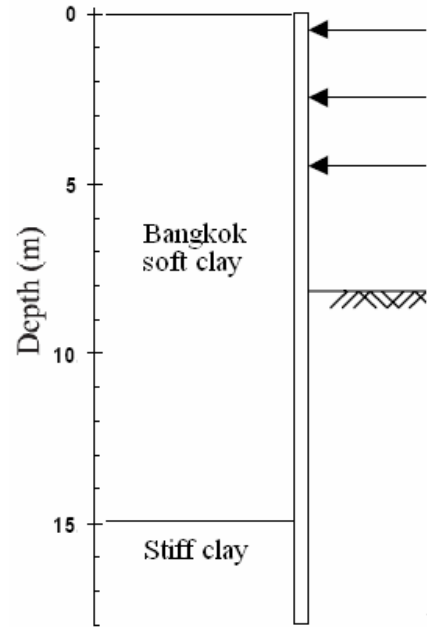
Depth (m)	δ_H (mm)
0.54	28.67
1.05	29.78
1.56	29.78
2.00	31.99
2.59	39.24
3.02	49.82
4.05	80.13
4.57	94.18
5.09	106.34
5.57	115.50
6.08	119.44
6.53	121.66
7.09	122.91
7.58	123.65
8.08	120.67
9.06	106.56
10.05	84.27
11.58	50.59
12.57	33.00
13.56	22.78
14.07	19.66
15.08	11.73
16.08	4.56
17.08	1.56
18.06	2.56
19.04	1.98

Lateral Deformation (mm)

206
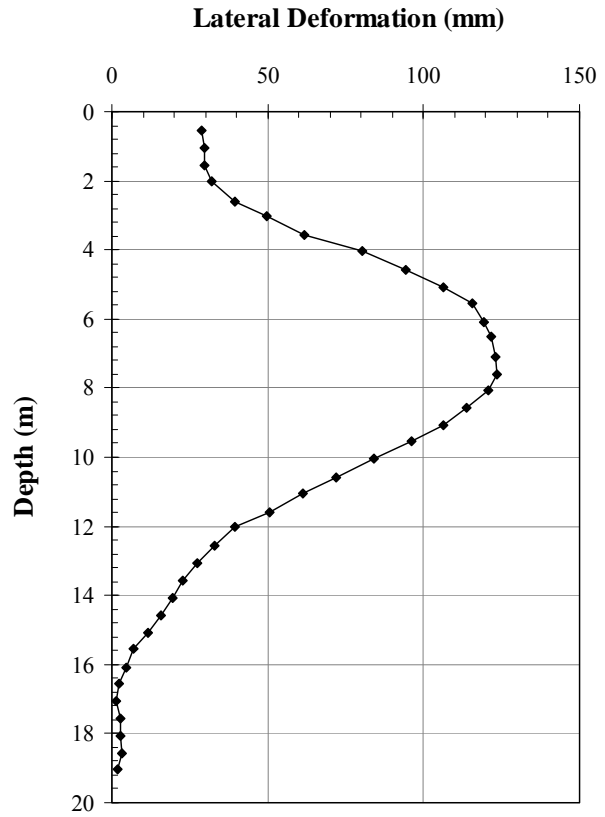
So6: AT&T Corporate Center in Chicago (Baker et al., 1989)

Wall Type = Diaphragm
Thickness (m) = 0.76
H (m) = 18.3
H_e (m) = 8.5
B (m) = 25
I (m⁴/m) = 0.03658
E (GPa) = 26
S_V (m) = 2.75
S_H (m) = ?
$\delta_{H(\max)}\,(\delta_{V(max)})$ (mm) = 37.39 (37.0)
$EI/\gamma_w S_V^4$ = 1696.98
$\gamma_{s,avg}$ (kN/m³) = 19
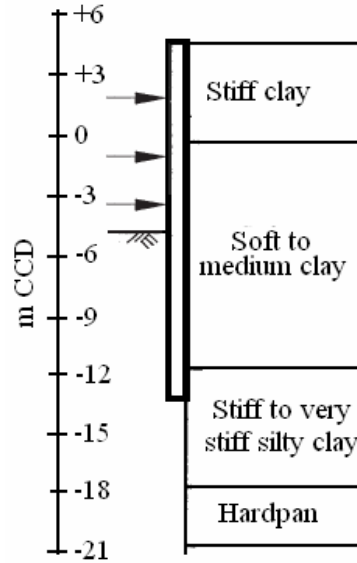s_u (kPa) = 21.5
FS (Eq. 2-26 and 2-27) = 0.81 and 0.93

Depth (m)	δ_H (mm)
0.47	5.42
1.26	7.93
1.37	9.97
1.94	15.20
2.20	18.05
3.07	22.53
4.03	26.73
4.98	30.53
5.41	32.84
6.04	35.22
6.58	37.39
7.37	36.57
8.35	35.01
9.30	33.52
10.06	32.03
11.09	28.88
12.38	25.15
13.38	21.35
14.13	19.15
15.42	14.28
16.50	9.34
17.37	5.08
18.03	3.41
19.14	1.97
20.40	0.37
21.19	0.13

Lateral Deformation (mm)

207
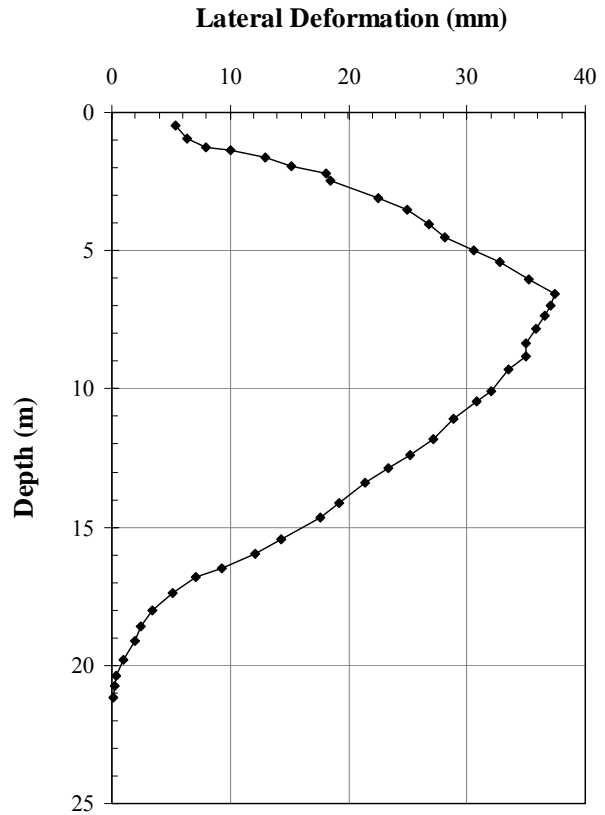
So7: Museum of Science and Industry Parking Garage in Chicago, IL (Konstantakos, 2000)

Wall Type =	Diaphragm
Thickness (m) =	0.76
H (m) =	13.7
H_e (m) =	10.3
B (m) =	85
I (m⁴/m) =	0.03658
E (GPa) =	26
S_V (m) =	3.65
S_H (m) =	?
$\delta_{H(max)}$ ($\delta_{V(max)}$) (mm) =	3.63 (NA)
$EI/\gamma_w S_V^4$ =	546.81
$\gamma_{s,avg}$ (kN/m³) =	19
s_u (kPa) =	45
FS (Eq. 2-26 and 2-27) =	1.36 and 1.25

Lateral Deformation (mm)
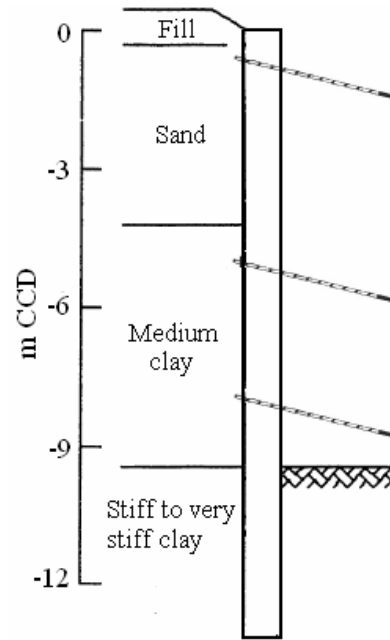
Depth (m)	δ_H (mm)
0.39	0.13
0.81	0.63
1.02	0.99
1.47	1.31
2.09	1.90
2.64	2.40
3.02	2.71
3.52	2.89
4.04	3.04
4.95	3.29
5.38	3.43
5.93	3.63
6.16	3.54
6.42	3.37
6.96	2.99
7.49	2.59
7.92	2.31
8.21	2.19
8.77	1.99
9.47	1.67
10.41	1.22
10.89	0.70
11.79	0.42
12.27	0.25

208
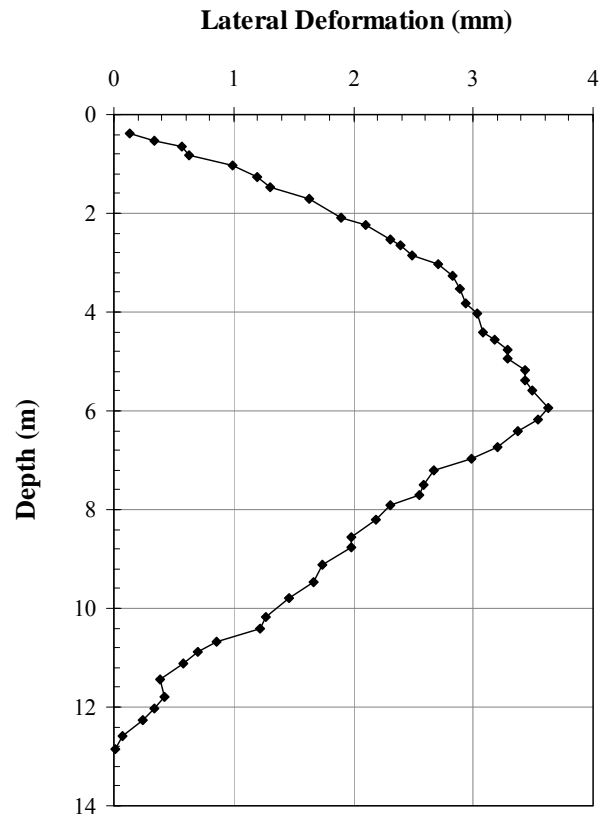
So8: One Market Plaza Building in San Francisco (Clough and Buchignani, 1981)

Wall Type = Soldier Pile
Thickness (m) = 0.75
H (m) = 30.5
H_e (m) = 11
B (m) = ?
I (m⁴/m) = 0.03658
E (GPa) = 26
S_V (m) = 3
S_H (m) = ?
$\delta_{H(max)}$ $(\delta_{V(max)})$ (mm) = 107.06 (NA)
$EI/\gamma_w S_V^4$ = 1151.50
$\gamma_{s,avg}$ (kN/m³) = 17
s_u (kPa) = 25
FS (Eq. 2-26 and 2-27) = 0.94 and 1.69

Lateral Deformation (mm)
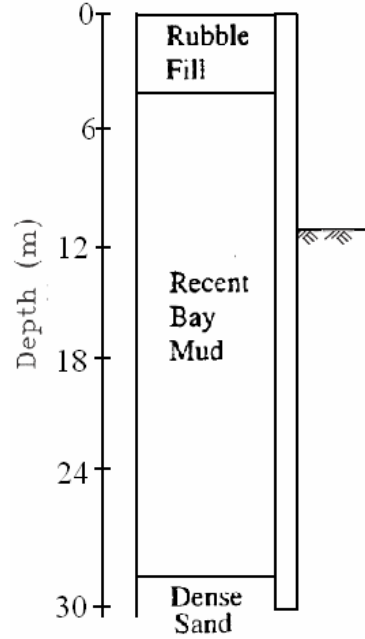
Depth (m)	δ_H (mm)
0.01	12.85
1.22	30.26
2.68	46.43
3.34	53.89
4.11	60.74
5.36	73.17
6.68	84.05
7.37	89.65
8.14	94.94
9.75	102.09
10.63	104.58
11.18	105.82
12.17	107.06
13.64	103.38
14.11	100.19
15.20	94.13
17.21	82.41
18.17	76.48
20.74	58.05
21.59	52.74
22.18	47.74
23.80	37.44
24.49	33.38
27.03	19.64
28.74	12.90
29.80	8.28

209
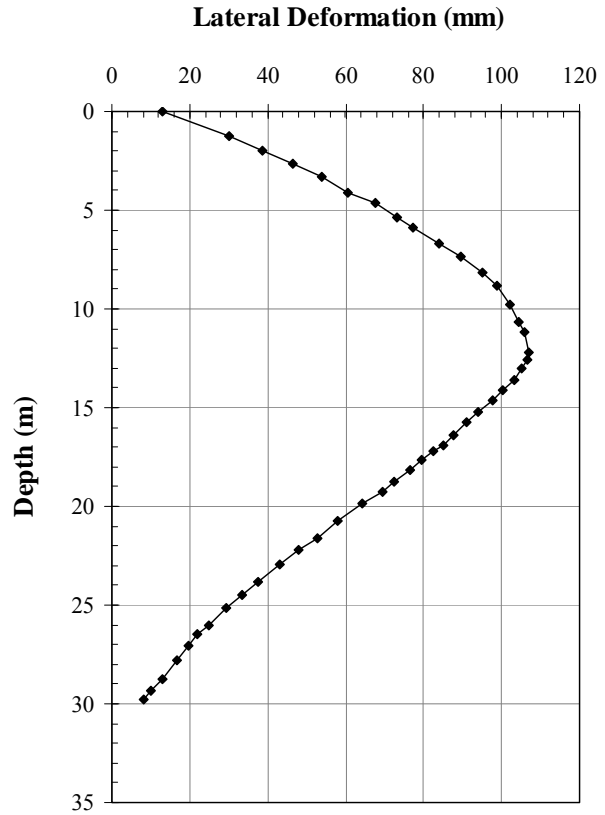
So9: Sheet Pile Wall Field Test in Rotterdam (Kort, 2002)

Wall Type = Sheet Pile
Ref. = AZ13
H (m) = 19
H_e (m) = 8
B (m) = 12.2
EI (kN-m²/m) = 41,370
E (GPa) = 200
S_V (m) = 7.75
S_H (m) = 7.2
$\delta_{H(max)}(\delta_{V(max)})$ (mm) = 385.38
$EI/\gamma_w S_V^4$ = 1.17 (NA)
$\gamma_{s,avg}$ (kN/m³) = 14
s_u (kPa) = 10-30
FS (Eq. 2-26 and 2-27) = 1.22 and 1.63
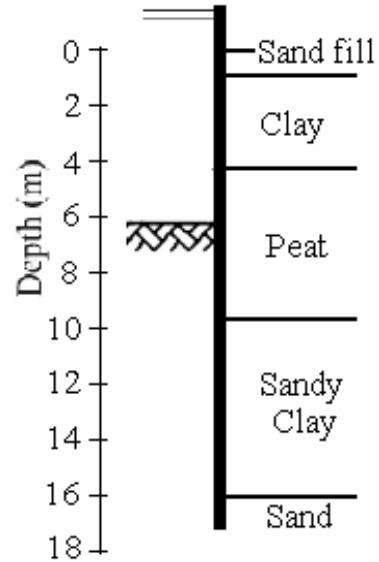
Depth (m)	δ_H (mm)
0.01	13.10
0.68	61.47
1.08	89.55
2.01	154.42
2.64	193.02
3.02	218.77
3.94	270.97
4.53	301.75
5.21	332.20
5.73	353.61
6.72	376.43
7.14	381.57
7.51	383.01
7.94	383.48
8.34	385.38
8.70	381.57
9.17	375.42
10.17	354.55
11.38	317.90
12.22	288.04
13.08	254.46
14.97	175.15
15.86	138.76
16.73	99.57
17.73	58.51
18.78	20.26

Lateral Deformation (mm)
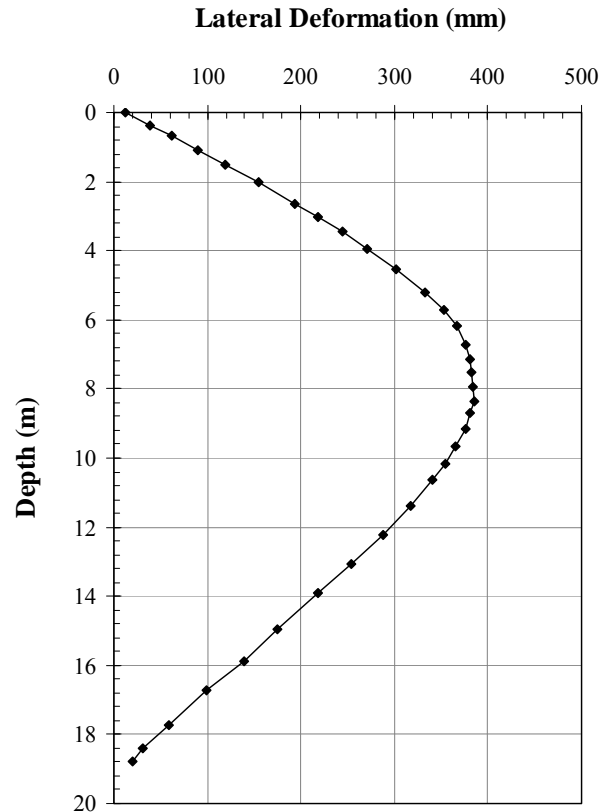
So10: MUNI Metro Turnback Project in San Francisco (Koutsoftas et al., 2000)

Wall Type =	Soldier Pile
Thickness (m) =	0.914
H (m) =	41
H_e (m) =	13.1
B (m) =	16
I (m⁴/m) =	0.0636
E (GPa) =	27.6
S_V (m) =	3.3
S_H (m) =	6
$\delta_{H(max)}$ $(\delta_{V(max)})$ (mm) =	48.10 (30.2)
$EI/\gamma_w S_V^4$ =	1491.32
$\gamma_{s,avg}$ (kN/m³) =	16.5
s_u (kPa) =	25-30
FS (Eq. 2-26 and 2-27) =	0.76 and 1.42
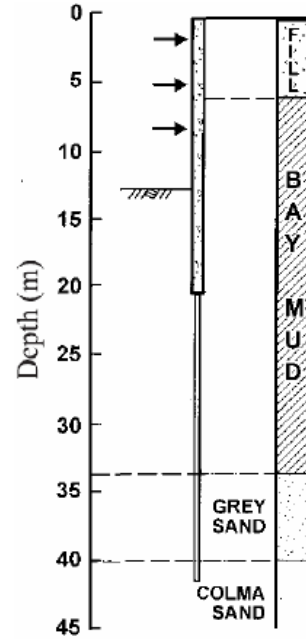
Depth (m)	δ_H (mm)
0.52	0.84
2.56	3.23
3.91	5.99
5.50	8.99
6.97	14.24
8.71	20.57
10.18	25.77
12.32	31.81
13.45	36.81
15.13	40.69
16.74	44.98
18.16	48.04
19.67	48.10
21.14	45.21
24.35	32.51
25.74	26.28
28.77	15.28
30.36	10.63
31.83	7.64
34.78	2.87
36.29	2.66
37.90	2.74
39.26	1.53
42.29	0.30
43.84	0.25

Lateral Deformation (mm)

211
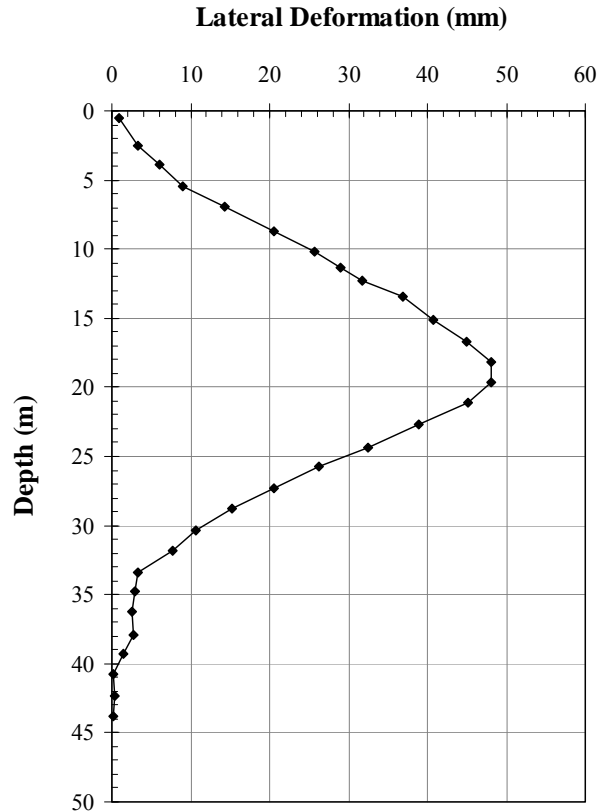
REFERENCES

1. AISC (2001) "*Manual of Steel Construction.*" 3rd edition, American Institute of steel Construction, United States of America.

2. American Petroleum Institute (1987) "*API Recommended Practice for Planning, Designing and Constructing Fixed Offshore Platforms.*" American Petroleum Institute, Washington, D.C.

3. Baker, C. N. Jr., Bucher, S. A., and Baker, W. F. Jr. (1989) "Complex High-Rise Foundation Design and Construction." *Proceedings Foundation Engineering: Current Principles and Practices*, June 25-29, 1989, Evanston, IL. pp. 1445-1458.

4. Becker, J. M., and Haley, M. X. (1990) "Up/Down Construction - Decision Making and Performance." *Proc., ASCE Conf. on Des. and Perf. of Earth Retaining Struct., Geotech. Spec. Publ. No. 25*, ASCE, New York, 170-189.

5. Bjerrum , L., and Eide, O. (1956). "Stability of Strutted Excavation in Clay." *Geotechnique*, Vol 6(1), pp. 32-47.

6. Blackburn, J. T. (2005). "Automated Sensing and Three-dimensional Analysis of Internally Braced Excavations." *PhD Thesis*, Northwestern University, Evanston, IL.

7. Blackburn, J. T., and Finno, R. J. (2006). "Representing Internal Bracing Systems in 3-D Models of Deep Excavations." *Proceedings of GeoCongress 2006: Geotechnical Engineering in the Information Technology Age*, ASCE, Atlanta, GA, pp. 1-6.

8. Brinkgreve, R. B. J. and Broere, W. (2006) "*Finite Element Code for Soil and Rock Analysis.*" PLAXIS 3D FOUNDATION Version 1.5 Manual, A.A. Balkema Publishers.

9. Bryson, L. S. (2002). "Performance of a Stiff Excavation Support System in Soft Clay and the Response of an Adjacent Building." *PhD Thesis*, Northwestern University, Evanston, IL.

10. Burland, J. B., and Hancock, R. J. R. (1977) "Underground Car Park at the House of Commons: Geotechnical Aspects." *The Structural Engineer*, London, Vol. 55(2), pp. 87-105.

11. Calvello, M. (2002) "Inverse Analysis of a Supported Excavation through Chicago Glacial Clays." *PhD Thesis*, Northwestern University, Evanston, IL.

12. Caquot, A. and Kerisel, J. (1948) *"Tables for the Calculation of Passive Pressure, Active Pressure, and Bearing Capacity of Foundations."* Gauthier-Villars, Paris, France.

13. Chew, S. H., Yong, K. Y., and Lim, A. Y. K. (1997). "Three-dimensional Finite Element Analysis of a Strutted Excavation," *Computer Methods and Advances in Geomechanics*, Yuan (editor), Balkema, Rotterdam.

14. Chung, C. K., and Finno, R. J. (1992) "Influence of Depositional Processes on the Geotechnical Parameters of Chicago Glacial Clays." *Eng. Geol. (Amsterdam)*, Vol. 32, pp. 225-242.

15. Clough, G. W., and Buchignani, A. L. (1981) "Slurry Walls in the San Francisco Bay Area." ASCE, Preprint, pp. 81-142.

16. Clough, G. W., and O'Rourke, T. D. (1990). "Construction Induced Movements of In-Situ Walls." Design and Performance of Earth Retaining Structures, *Proceedings of a Specialty Conference at Cornell University*, ASCE, New York, pp. 439-470.

17. Clough, G. W., Smith, E. M., and Sweeney, B. P. (1989). "Movement Control of Excavation Support Systems by Iterative Design." *Current Principles and Practices, Foundation Engineering Congress*, ASCE, Vol. 2, pp. 869-884.

18. Das, B. M. (2007) *"Principles of Foundation Engineering."* 6th Edition, Thompson, Toronto, Ontario, Canada.

19. De Moor, E. K. (1994) "An Analysis of Bored Pile/Diaphragm Wall Installation Effects." *Geotechnique*, Vol. 44(2), pp. 341-347.

20. Fang, H-Y. (1991) *"Foundation Engineering Handbook."* 2nd edition, Van Nostrand Reinhold, New York, NY 10003.

21. Finno, R. J. and Bryson, L. S. (2002) "Response of Building Adjacent to Stiff Excavation Support System in Soft Clay." *Journal of Performance of Constructed Facilities*, ASCE, Vol. 16(1), pp. 10-20.

213

22. Finno, R. J. and Roboski, J. F. (2005) "Three-Dimensional Responses of a Tied-Back Excavation through Clay." *Journal of Geotechnical and Geoenvironmental Engineering*, ASCE, Vol. 131(3), pp. 273-282.

23. Finno, R. J., and Blackburn, J. T. (2006). "Three-Dimensional Modeling of Excavation Sequences." *Proceedings of GeoCongress 2006: Geotechnical Engineering in the Information Technology Age*, ASCE, Atlanta, GA, pp. 1-6.

24. Finno, R. J., Atmatzidis, D. K., and Perkins, S. B. (1989) "Observed Performance of a Deep Excavation in Clay." *Journal of Geotechnical Engineering*, ASCE, Vol. 115(8), pp. 1045-1064.

25. Finno, R. J., Blackburn, J. T., and Roboski, J. F. (2007) "Three-Dimensional Effects for Supported Excavations in Clay." *Journal of Geotechnical and Geoenvironmental Engineering*, ASCE, Vol. 133(1), pp. 30-36.

26. Finno, R. J., Bryson, L. S., and Calvello, M. (2002) "Performance of a Stiff Support System in Soft Clay." *Journal of Geotechnical and Geoenvironmental Engineering*, ASCE, Vol. 128(8), pp. 660-671.

27. Gill, S. A., and Lucas, R. G. (1990). "Ground Movement Adjacent to Braced Cuts." *Proc., ASCE Conf. on Des. and Perf. of Earth Retaining Struct., Geotech. Spec. Publ. No. 25*, ASCE, New York, 471-488.

28. Goh, A. T. C., Wong, K. S., Teh, C. I., and Wen, D. (2003) "Pile Response Adjacent to Braced Excavation." *Journal of Geotechnical and Geoenvironmental Engineering*, ASCE, Vol. 129(4), pp. 383-386.

29. Gourvenec, S. M., and Powrie, W. (1999) "Three-Dimensional Finite-Element Analysis of Diaphragm Wall Installation." *Geotechnique*, Vol. 49(6), pp. 801-823.

30. Gourvenec, S. M., Powrie, W., and De Moor, E. K. (2002) "Three-Dimensional Effects in the Construction of a Long Retaining Wall." *Proceedings of the Institution of Civil Engineers, Geotechnical Engineering*, Vol. 155(3), pp. 163-173.

31. Hsieh, P-G. and Ou, C-Y. (1998). "Shape of Ground Surface Settlement Profiles Caused by Excavation." *Canadian Geotechnical Journal*, Vol. 35(6), pp. 1004-1017.

32. Hu Z. F., Yue Z. Q., Zhou J., and Tham L. G. (2003) "Design and Construction of a Deep Excavation in Soft Soils Adjacent to the Shanghai Metro Tunnels." *Canadian Geotechnical Journal*, Vol. 40(5), pp. 933-948.

33. Jardine, R. J., Potts, D. M., Fourie, A. B. and Burland, J. B. (1986) "Studies of the influence of nonlinear stress-strain characteristics in soil-structure interaction." *Geotechnique*, Vol. 36(3), pp. 377-396.

34. Konstantakos, D. C. (2000) "Measured Performance of Slurry Wall." *PhD Thesis*, Massachusetts Institute of Technology, Cambridge, MA.

35. Kort, D. A. (2002) "Steel Sheet Pile Walls in Soft Soil." *PhD Thesis*, Delft University of Technology, Delft, The Netherlands.

36. Koutsoftas, D. C., Frobenius, P., Wu, C. L., Meyersohn, D. and Kulesza, R. (2000) "Deformations during Cut-and-Cover Construction of MUNI Metro Turnback Project." *Journal of Geotechnical and Geoenvironmental Engineering*, ASCE, Vol. 126(4), pp. 344-359.

37. Lee, F. H., Yong, K. Y., Quan, K. C., and Chee, K. T. (1998) "Effect of Corners in Strutted Excavations: Field Monitoring and Case Histories." *Journal of Geotechnical and Geoenvironmental Engineering*, ASCE, Vol. 124(4), pp. 339-349.

38. Liao, H. J., and Hsieh, P. G. (2002) "Tied-Back Excavations in Alluvial Soil of Taipei." *Journal of Geotechnical and Geoenvironmental Engineering*, ASCE, Vol. 128(5), pp. 435-441.

39. Lin, D. G., Phien-wej, N., and Chung, T. C. (2003) "Quantitative evaluation of corner effect on deformation behavior of multi-strutted deep excavation in Bangkok subsoil." *Journal of the Southeast Asian Geotechnical Society*, Vol. 34(1), pp. 41-57.

40. Lings, M. L., Ng, C. W. W., and Nash, D. F. T. (1994) "The Lateral Pressure of Wet Concrete in Diaphragm Wall Panels Cast Under Bentonite." *Proceedings of the Institution of Civil Engineers Geotechnical Engineering.* Vol. 107(3), pp. 163-172.

41. Long, M. (2001) "Database for Retaining Wall and Ground Movements Due to Deep Excavations." *Journal of Geotechnical and Geoenvironmental Engineering*, ASCE, Vol. 127(3), pp. 203-224.

42. Mana, A. I., and Clough, G. W. (1981). "Prediction of Movements for Braced Cuts in Clays." *Journal of the Geotechnical Engineering Division*, ASCE, Vol. 107(8), pp. 759-777.

43. Miyoshi, M. (1977) "Mechanical Behavior of Temporary Braced Wall." *Proceedings of the 6th International Conference on Soil Mechanics and Foundation Engineering*, Tokyo, Vol. 2(2), pp. 655-658.

44. Moormann, C. (2004) "Analysis of Wall and Ground Movements Due to Deep Excavations in Soft Soil Based on a New Worldwide Database." *Soils and Foundations*, Japanese Geotechnical Society, Vol. 44(1), pp. 87-98.

45. Ng, C. W. W. (1992). "An Evaluation of Soil-Structure Interaction Associated with a Multi-Propped Excavation." *Ph.D. Thesis*, University of Bristol, UK.

46. Ng, C. W. W., and Lings, M .L. (1995) "Effects of Modeling Soil Nonlinearity and Wall Installation on Back-Analysis of Deep Excavation in Stiff Clay." *Journal of Geotechnical Engineering*, ASCE, Vol. 121(10), pp. 687-695.

47. Ng, C. W. W., and Yan, R. W. M. (1998) "Stress Transfer and Deformation Mechanisms around a Diaphragm Wall Panel." *Journal of Geotechnical and Geoenvironmental Engineering*, ASCE, Vol. 124(7), pp. 638-648.

48. Ng, C. W. W., and Yan, R. W. M. (1999) "Three-Dimensional Modeling of a Diaphragm Wall Construction Sequence." *Geotechnique*, Vol. 49(6), pp. 825-834.

49. Ng, C. W. W., Ling, M. L., and Nash, D. F. T. (1995) "An Approximate Analysis of the Three-Dimensional Effects of Diaphragm Wall Installation." *Geotechnique*, Vol. 45(3), pp. 497-507.

50. Ng. C. W. W. and Lei. G. H. (2003) "An Explicit Analytical Solution for Calculating Horizontal Stress Changes and Displacements around an Excavated Diaphragm Wall Panel." *Canadian Geotechnical Journal*, Vol. 40(4), pp. 780-792.

51. Ng. C. W. W., Lings, M. L., and Nash, D. F. T. (1998) "Numerical Analysis of a Multipropped Excavation in Stiff Clay." *Canadian Geotechnical Journal*, Vol. 35(1), pp. 115-130.

52. Norwegian Geotechnical Institute. (1962) "*Measurements at a Strutted Excavation, Oslo Subway, Vaterland 1.*" Norwegian Geotechnical Institute, Technical Report 6.

53. O'Rourke, T. D. (1981). "Ground Movements Caused by Braced Excavation." *Journal of Geotechnical Engineering*, ASCE, Vol. 107(9), pp. 1159-1178.

54. Osman, A. S., and Bolton, M. D. (2004) "A New Design Method for Retaining Walls in Clay." *Canadian Geotechnical Journal*, Vol. 41(3), pp. 451-466.

55. Osman, A. S., and Bolton, M. D. (2006a) "Design of Braced Excavations to Limit Ground Movements." *Geotechnical Engineering*, Vol. 159(3), pp. 197-175.

56. Osman, A. S., and Bolton, M. D. (2006b) "Ground Movement Predictions for Braced Excavations in Undrained Clay." *Journal of Geotechnical and Geoenvironmental Engineering*, ASCE, Vol. 132(4), pp. 465-477.

57. Ou, C. Y. (2006) "*Deep Excavation: Theory and Practice.*" Taylor & Francis/Balkema, The Netherlands.

58. Ou, C. Y., and Chiou, D. C. (1993) "Three-dimensional Finite Element Analysis of Deep Excavation." *Proceedings of 11th Southeast Asian Geotechnical Conf.*, The Institute of Engineers, Malaysia, Kuala Lampur, Malaysia, pp. 769-774.

59. Ou, C. Y., and Shiau, B. Y. (1998) "Analysis of the Corner Effect on Excavation Behaviors." *Canadian Geotechnical Journal*, Vol. 35(3), pp. 532-540.

60. Ou, C. Y., Chiou, D. C., and Wu, T. S. (1996) "Three-dimensional Finite Element Analysis of Deep Excavations." *Journal of Geotechnical and Geoenvironmental Engineering*, ASCE, Vol. 122(5), pp. 473-483.

61. Ou, C. Y., Hsien, P. G., and Chiou, D. C. (1993) "Characteristics of Ground Surface Settlement during Excavation." *Canadian Geotechnical Journal*, Vol. 30(5), pp. 758–767.

62. Ou, C. Y., Liao, J. T., and Lin, H. D. (1998) "Performance of Diaphragm Wall Constructed Using Top-Down Method." *Journal of Geotechnical and Geoenvironmental Engineering*, ASCE, Vol. 124(9), pp. 798-808.

63. Ou, C. Y., Shiau, B. Y., and Wang, I.W. (2000) "Three-Dimensional Deformation Behavior of the Taipei National Enterprise Center (TNEC) Excavation Case History." *Canadian Geotechnical Journal*, Vol. 37(2), pp. 438-448.

64. Padfield, C. J. and Mair, R. J. (1984) "*Design of Retaining Wall Embedded in Stiff Clay.*" CIRIA Report No 104, England, pp. 83-84.

65. Peck, R. B. (1943) "Earth Pressure Measurements in Open Cuts Chicago (III) Subway." *Transactions*, ASCE, Vol. 108, pp. 223.

66. Peck, R. B. (1969). "Deep Excavations and Tunneling in Soft Ground." *Proceedings 7th International Conference on Soil Mechanics and Foundation Engineering*, State-of-the-Art Volume, pp. 225-290.

67. PLAXIS 3D FOUNDATION, Version 1.6 (2006) "*PLAXIS Finite Element Code for Soil and Rock Analysis.*" Delft University of Technology & PLAXIS B.V., Delft, The Netherlands.

68. Poh, T. Y., and Wong, I. H. (1998) "Effects of Construction of Diaphragm Wall Panels on Adjacent Ground: Field Trial." *Journal of Geotechnical and Geoenvironmental Engineering*, ASCE, Vol. 124(8), pp. 749-756.

69. Poh, T. Y., Chee Goh, A. T., and Wong, I. H. (2001) "Ground Movements Associated with Wall Construction: Case Histories." *Journal of Geotechnical and Geoenvironmental Engineering*, ASCE, Vol. 127(12), pp. 1061-1069.

70. Poh, T. Y., Wong, I. H., and Chandrasekaran, B. (1997) "Performance of Two Propped Diaphragm Walls in Stiff Residual Soils." *Journal of Performance of Constructed Facilities*, ASCE, Vol. 11(4), pp. 190-199.

71. Potts, D. M., and Zdravkovic, L. (1999). "*Finite Element Analysis in Geotechnical Engineering: Theory.*" Thomas Telford, London.

72. Rankine, W. M. J. (1857) "On Stability on Loose Earth." *Philosophic Transactions of Royal Society*, London, Part I, pp. 2-27.

73. Roboski, J. F. (2001) "Soil Parameters for Constitutive Models of Compressible Chicago Glacial Clays." *Master Thesis*, Northwestern University, Evanston, IL.

74. Roboski, J. F. (2004) "Three-dimensional Performance and Analyses of Deep Excavations." *PhD Thesis*, Northwestern University, Evanston, IL.

75. Roboski, J. F. and Finno, R. J. (2006) "Distributions of Ground Movements Parallel to Deep Excavations in Clay." *Canadian Geotechnical Journal*, Vol. 43(1), pp. 43–58.

76. Rowe, P. W. (1971) "The Stress-Dilatancy Relation for Static Equilibrium for an Assembly of Particles in Contact." *Proc. Roy. Soc. A.*, Vol. 269, pp. 500-527.

77. Schafer, R. and Triantafyllidis, Th. (2004) "Modeling of Earth and Water Pressure Development during Diaphragm Wall Construction in Soft Clay." *Int. J. Numer. Anal. Meth. Geomech.*, Vol. 28(13), pp. 1305–1326.

78. Schanz, T. and Vermeer, P. A. (1996) "Angles of Friction and Dilatancy of Sand." *Geotechnique*, Vol. 46(1), pp. 145-151.

79. Schanz, T., Vermeer, P. A., and Bonnier, P. G. (1999) "The Hardening Soil Model: Formulation and Verification." *Beyond 2000 in Computational Geotechnics - 10 Years of PLAXIS*. Balkema, Rotterdam.

80. Silva, W. P., and Silva, Cleide M. D. P. S. (2006) "LAB Fit Curve Fitting Software (Nonlinear Regression and Treatment of Data Program) V 7.2.34." online, available from world wide web: <www.labfit.net>, date of access: 2006-06-10.

81. Simpson, B. (1992) "Thirty-Second Rankine Lecture: Retaining Structures: Displacement and Design." *Geotechnique*, Vol. 42(4), pp. 541-876.

82. Teparaksa, W. "Behavior of Deep Excavations Using Sheet Pile Bracing System in Soft Bangkok Clay." *Third International Conference on Case Histories in Geotechnical Engineering*, June 1-6, St. Louis, USA, pp. 745-750.

83. Terzaghi, K. (1943a) "*Theoretical Soil Mechanics.*" John Wiley and Sons, New York.

84. Terzaghi, K. (1943b) "Liner-Plate Tunnels on the Chicago, IL Subway." *Trans.*, ASCE, Vol. 108, pp. 970-1007.

85. Thorley, C. B. B., and Forth, R. A. (2002) "Settlement due to Diaphragm Wall Construction in Reclaimed Land in Hong Kong." *Journal of Geotechnical and Geoenvironmental Engineering*, ASCE, Vol. 128(6), pp. 473-478.

86. Tschebotarioff, G. P. (1951) "*Soil Mechanics, Foundations and Earth Structures.*" McGraw-Hill Book Co., Inc., New York, NY.

87. Ukritchon, B., Whittle, A. J., and Sloan, S. W. (2003) "Undrained Stability of Braced Excavations in Clay." *Journal of Geotechnical and Geoenvironmental Engineering*, ASCE, Vol. 129(8), pp. 738-755.

88. Ulrich, E. J., Jr. (1989) "Tieback Supported Cuts in Overconsolidated Soils." *Journal of Geotechnical Engineering*, ASCE, Vol. 115(4), pp. 521-545.

89. Wang, Z. W., Ng, C. W. W., and Liu, G. B. (2005) "Characteristics of Wall Deflections and Ground Surface Settlements in Shanghai." *Canadian Geotechnical Journal*, Vol. 42(5), pp. 1243-1254.

90. Whittle, A. J., Hashash, Y. M. A., and Whitman, R. V. (1993) "Analysis of Deep Excavation in Boston." *Journal of Geotechnical Engineering*, ASCE, Vol. 119(1), pp. 69-90.

91. Zdravkovic, L., Potts, D. M., and St John, H. D. (2005) "Modeling of a 3D Excavation in Finite Element Analysis." *Geotechnique*, Vol. 55(7), pp. 497-513.

VITA

David Zapata-Medina was born on July 23, 1980 in Medellin, Colombia. He attended the National University of Colombia, School of Mines at Medellin, earning a B.S. in Civil Engineering. After he finished his undergraduate studies, he worked as a research engineer at the National University of Colombia for one year. In 2005, he came to the United States as a research assistant at the Civil Engineering Department of Ohio University (OU). After being at OU for one year, he transferred to the University of Kentucky in order to continue his graduate studies under the advisory of Dr. L. Sebastian Bryson, formerly a Civil Engineering professor at OU.